



HAL
open science

Synthesis, characterization and study of the properties of new exotic lithium ion intercalation compounds

Thomas Marchandier

► **To cite this version:**

Thomas Marchandier. Synthesis, characterization and study of the properties of new exotic lithium ion intercalation compounds. Material chemistry. Sorbonne Université, 2021. English. NNT : 2021SORUS276 . tel-03545622

HAL Id: tel-03545622

<https://theses.hal.science/tel-03545622v1>

Submitted on 27 Jan 2022

HAL is a multi-disciplinary open access archive for the deposit and dissemination of scientific research documents, whether they are published or not. The documents may come from teaching and research institutions in France or abroad, or from public or private research centers.

L'archive ouverte pluridisciplinaire **HAL**, est destinée au dépôt et à la diffusion de documents scientifiques de niveau recherche, publiés ou non, émanant des établissements d'enseignement et de recherche français ou étrangers, des laboratoires publics ou privés.

Sorbonne Université

ED 397-Physique et Chimie des Matériaux

Chimie du Solide et Energie, Collège de France, UMR 8260

Synthesis, characterization and study of the properties of new exotic lithium ion intercalation compounds.

By Thomas Marchandier

Ph.D. thesis of Chemistry of Materials

Supervised by Gwenaëlle Rousse and Jean-Marie Tarascon

Presented and defended publicly on December 10th, 2021

In front of the Jury:

Dr. Montserrat Casas-Cabanas	Group Leader, CIC energiGUNE, Vitoria-Gasteiz	Referee
Dr. Oliver Mentré	Research Director, UCCS, Lille	Referee
Prof. Robert Cava	Professor, Princeton University	Examiner
Prof. Simon Clarke	Professor, Oxford University	Examiner
Dr. Sandrine Ithurria	Associate Professor, LPEM, Paris	Examiner
Dr. Stéphane Jobic	Research Directeur, IMN, Nantes	Invited member
Dr. Gwenaëlle Rousse	Associate Professor, Sorbonne Université, Paris	Director
Prof. Jean-Marie Tarascon	Professor, Collège de France, Paris	Director

Sorbonne Université

ED 397-Physique et Chimie des Matériaux

Chimie du Solide et Energie, Collège de France, UMR 8260

Synthèse, caractérisation et étude des propriétés de nouveaux composés exotiques d'intercalation des ions lithium

Par Thomas Marchandier

Thèse de doctorat en Chimie des Matériaux

Dirigée par Gwenaëlle Rousse et Jean-Marie Tarascon

Présentée et soutenue publiquement le 10 décembre 2021

Devant un jury composé de :

Dr. Montserrat Casas-Cabanas	Group Leader, CIC energiGUNE, Vitoria-Gasteiz	Rapportrice
Dr. Oliver Mentré	Directeur de Recherche, UCCS, Lille	Rapporteur
Prof. Robert Cava	Professor, Université de Princeton	Examineur
Prof. Simon Clarke	Professor, Université d'Oxford	Examineur
Dr. Sandrine Ithurria	Maître de Conférences, LPEM, Paris	Examinatrice
Dr. Stéphane Jobic	Directeur de Recherche, IMN, Nantes	Membre invité
Dr. Gwenaëlle Rousse	Maître de Conférences, Sorbonne Université, Paris	Directrice
Prof. Jean-Marie Tarascon	Professeur, Collège de France, Paris	Directeur

A ma famille, mes amis

Acknowledgment

First of all, I would like to sincerely thank Jean-Marie Tarascon for having welcomed me in his laboratory almost three and a half years ago, first for my master internship and then for my thesis. You have given me your trust, the freedom to work and means to carry out my research beyond what I could have hoped or found elsewhere. Your work force and your passion for research are contagious and have inspired me throughout my PhD thesis. In every respect, these few years spent in the laboratory allowed me to grow and progress and will remain engraved in me as an exceptional experience. Thank you.

I would like to thank Gwenaëlle Rouse (Gwen) who, in addition to sharing her laughter, stories of all kinds, transmitted to me the terrible fever of the crystallographer and of structural resolution. I took a sincere pleasure to learn and progress in crystallography. Finally you managed to change the young rebellious PhD student who (oh misery) dared not to put in italics the letters of the space groups. Beyond my direct supervisors, I would like to deeply thank Sathiya and Quentin Jacquet who, in addition to their friendship, have, at different moments of my thesis, participated in my supervision and have supported my work and my ideas. Outside the walls of the laboratory I had the opportunity to meet and work with many people. Thus, I have a special thought for Artem Abakumov who participated in almost all the works presented in this manuscript and who always brought essential answers to these projects. I also think of the Montpellier theoreticians Marie-Liesse Doublet and Matthieu Saubanère who, beyond the good times spent together, tried to make me understand the mysteries of DFT. Thanks to François Fauth who received me at the Alba Synchrotron twice, to Claire Colin for her help on the D1B line of the ILL and to Maxim Avdeev who accepted to receive my samples in Australia. I have a special thought for Stéphane Jobic, who beyond our common interest for iridium sulfides gave me precious advices and accepted my invitation to my defense. Thanks to the spectroscopists, Antonella Iadecola, Dominique Foix, Bernard Humbert, Jean-Yves Mevellec, Rémi Dedryvère and Moulay Tahar Sougrati who tried to understand the charge compensations in my compounds. Finally, I thank Nicolas Dubouis for having allowed the unlikely scientific collaboration of a solid-state chemist and an electrochemist.

These great years spent in the laboratory owe much to all his residents to whom I address my sincere thanks. In particular, I thank Alexis Grimaud with whom I shared the office,

Acknowledgement

innumerable scientific discussions and others often around a beer. It would not be fair to forget Jiaqiang and Jacques who have more than contributed to the good mood and atmosphere of the office. Thanks to Bernhard, Valentin, Damien, Elisa and all those who participated in our weekly jogging sessions. Thanks to the older members who saw my beginnings in the lab and shared beers (Daniel, Boris, Iban, Claudio, Paul, Quentin, Laurie...) or their advice (Chunzen, Sujoy, Qing...). A big thank you to Jessica Duvoisin for her kindness and her incredible efficiency on all the administrative questions. Finally, of course I thank Pierre, Nicolas, Fanny, Ivette, Léa and Romain without whom these years would not have been the same.

I am very grateful to Montse Casas-Cabanas and Olivier for agreeing to be the referee of this work and to Simon Clarke, Sandrine Ithurria and Robert Cava for being the reviewers. I thank them all for the time they spent on this manuscript and for having accepted to come to my defense, sometimes from far away.

Enfin, bien sûr j'adresse mes remerciements les plus profonds à mes amis et à ma famille pour leur patience, leur compréhension et leur soutien sans faille au cours de ma thèse.

Table of Contents

Acknowledgment	7
General introduction	11
Chapter I: State of the art	15
I.1 Intercalation chemistry: from the synthesis tool to the Li-ion batteries.....	15
I.1.a Intercalation chemistry: definition and principles.....	15
I.1.b Intercalation chemistry: modifications of the physical properties	16
I.1.c Intercalation chemistry to store the energy: Li-ion batteries.....	18
I.2 Design principles of a cathode material	21
I.2. a Tuning the crystal structure.....	21
I.2. b Tuning the redox potential	26
I.2. c Increasing the gravimetric capacity.....	30
I.2 d Redox in high-valence systems.....	32
Chapter conclusion.....	39
Chapter II: Low temperature synthesis of ruthenium ternary oxides .	41
II.0 Introduction	41
II.0.a Low temperature synthesis?.....	41
II.0.b Ruthenium oxides	42
II.1 Synthesis.....	43
II.1.a Hydrothermal synthesis of ternary alkaline-earth ruthenium oxides.	43
II.1.b Low temperature cations exchange	52
II.2 Structural characterisations	55
II.2.a Elemental analysis	55
II.2.a Structural characterisations.....	55
II.3 Physico-chemical properties.....	77
II.3.a Magnetic properties of BaRu ₂ O ₆	77
II.3.a Electrochemical insertion of Li ⁺ in BaRu ₂ O ₆ and SrRu ₂ O ₆	81
Chapter conclusion.....	91
Chapter III: Re-exploration of the transition metals sulfides in the context of anionic redox.....	93
III.0 Introduction	93
III.0.a General Background.....	93

III.0.b How to activate anionic activity in transition metal sulfides?	94
III.1 Study of the Li_3MS_4 family (M = V, Nb or Ta).....	97
III.1.a Synthesis	97
III.1.b Structures	99
III.1.c Electrochemistry	107
III.1.d How to explain the difference in electrochemical behavior of the two polymorphs Li_3NbS_4 polymorphs ?	109
III.1.e Partial conclusion.....	124
III.2 Study of the LiIrS_2 and IrS_2 compounds	125
III.2.a Experimental results:	125
III.2.b Discussion.....	146
Chapter conclusion	150
Chapter IV: Investigation of new chemistries	153
IV.0 Introduction	153
IV.1 Oxysulfides	154
IV.1.a General Considerations.....	154
IV.1.b $\text{Na}_3\text{VS}_{4-x}\text{O}_x$ compounds	155
IV.2 Vanadium halides.....	166
IV.2.a Synthesis.....	166
IV.2.b Structure	167
IV.2.c Lithium intercalation	181
IV.2.d Magnetic properties of the Li_xVX_3 phases (with x = 0 or 1).....	189
Chapter conclusion	197
Conclusion and future work.....	199
Materials and methods	205
Glossary	215
References	217

General introduction

Combating climate change is one of the main challenges of the 21st century and is intimately linked to the way energy is produced and used. Indeed, today's energy mix is still based at 81% on nonrenewable fossil fuels which are responsible of most of the green-house gases, therefore urgent changes are needed to turn the tide. However, in spite of many improvements made on systems able to harvest energy in a “greener” way, most of these alternatives are based on intermittent sources (wind, solar etc...) and call for the development of disruptive storage solutions. To meet the energy grid demands, electrochemical storage devices are among the most promising solutions. Among them batteries can be easily coupled with electrical engine to equip vehicles (the transport sector representing today more than two third of the CO₂ emissions). Out of the existing storage technologies, Li-ion batteries, which have conquered the portative electronic market and are now overwhelming the electrical car market, are a serious contender to help this energetic conversion.

Among all challenges faced by the Li-ion technology such as safety and sustainability or costs, the energy density is probably today the most important issue as it limits the driving distance of electrical cars or the autonomy of portable devices. This essential characteristic being mostly limited by the cathode material, intense research efforts have been made worldwide to synthesize either “practical ” compounds, with a high energetic density, or “model” compounds designed to help understanding the mechanisms occurring upon cycling. The pursuit of the ideal cathode material started in the 70's with layered sulfides, before being replaced barely ten years after by higher voltage oxides. Subsequently in the 90's the crystal chemistry of intercalation materials reached its heights with the beautiful diversity of polyanionics (PO₄³⁻, SO₄²⁻ etc...) compounds. Towards the 2000's great efforts were devoted in pushing the amount of lithium at the expense of the transition metal in layered oxides to further increase their capacity. Although really promising this Li-rich strategy comes up with several roadblocks such as voltage fade and hysteresis induced by the participation of the anionic network to the electrochemical reaction. However, after 40 years of frenetic research and an exhaustive screening of the known strategies, the discovery of new materials has reached a standstill these last years. On this basis, it is worth wondering the role of solid-state chemistry for designing new intercalation compounds in the current Li-ion research context.

The aim of this thesis is to explore several strategies to synthesize new cathode materials of either practical interest or that could serve as model compound to answer specific questions. This manuscript is divided in the following four chapters.

In the first part, we briefly introduce the lithium-ion technology and specify the figures of merits that a cathode material should have. In particular, the factor influencing the materials voltage and capacity will be detailed along with the different strategies to increase them. Through this introduction, we will briefly review the inorganic cathodes materials synthesized so far prior to identify new synthesis routes to obtain new materials: Question such as “1) what can non-conventional synthesis processes bring to the discovery of new material?”; “2) Can we re-investigate old chalcogenides intercalation in the context of the anionic redox?”; “3) Is there still room for exploring new chemistries?” will be discussed.

Afterwards, the second chapter will focus on the low temperature synthesis of ruthenium oxides. Indeed, while ruthenium oxides have been heavily studied for their magnetic behavior, a recent interest for these compounds has emerged from the battery community for their potential use as model material to understand anionic redox process. However, most of the reported compounds have been obtained through high temperature synthesis; here we show a low-temperature hydrothermal synthesis route to obtain new alkaline-earth ruthenates that will be characterized for their electrochemical and magnetic properties.

The third chapter aims to re-investigate transition metal sulfides in the anionic redox context. Indeed, while historically transition metal sulfides have been set aside for the benefit of higher voltage oxides, recent studies demonstrated that anionic redox process could happen in lithium rich sulfides without the main drawbacks such as voltage hysteresis and fade observed for the oxides. Therefore, these materials could be interesting for both the fundamental understanding of the anionic redox mechanisms and as high-energy cathode candidates. Hence our interest to study charge compensation pathways pertaining to the electrochemistry of two Li_xIrS_2 polymorphs through cycling that turns out to be highly dependent of the electronic/crystallographic structure giving clues to a better understanding of hysteresis phenomenon commonly observed concomitantly with anionic redox. Then, the electrochemical performances of Li_3NbS_4 and derivate compounds will be presented to highlight the importance of the structure to trigger the anionic redox.

Finally, the last chapter will deal with a less explored crystal family based on mixed ligands as potential cathode materials. First the structure and electrochemical performances of an oxysulfide family ($\text{Na}_3\text{VS}_{4-x}\text{O}_x$ with $0 \leq x \leq 2$) will be presented prior to focus on the structural, electrochemical and magnetic properties of layered halides VX_3 ($\text{X} = \text{Cl}, \text{Br}, \text{I}$).

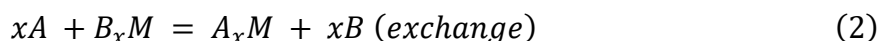
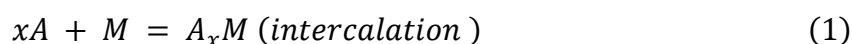
A general conclusion will then sum up the most important results of this work and propose perspectives for a further work.

Chapter I: State of the art

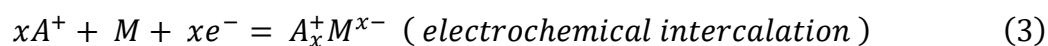
I.1 Intercalation chemistry: from the synthesis tool to the Li-ion batteries

I.1.a Intercalation chemistry: definition and principles

The idyllic vision of the synthesis chemist is an architect of matter, who by controlling physicochemical properties of chemical reactions is able to tune the reaction pathways to obtain any desired compound. If this description suits to some extent the organic chemist, who adjusts and understand most of the reaction steps, the solid-state chemist cannot boast of similar reaction control. Indeed, in spite of general solid state laws such as Pauling rules¹ or dimensionality² considerations, any “sur mesure synthesis” is still today out of the scope of solid state chemistry. However, the intercalation (or insertion) and exchange reactions are probably the only exceptions to this frustrating conclusion (cf. figure I.1).³ Indeed, these reactions consist in either inserting or exchanging a guest (A, B in the equations below) species (molecule, ion) in a host matrix (M) without modifying the structure of the host (topotactic reaction cf. figure I.1), as follows:



While the physicochemical forces driving these reactions are very diverse and depend on the guest/host couple, an important class of intercalation reactions consists in electrochemically reducing the host matrix to insert cations:



The insertion of anions is more anecdotal and is mostly reported in graphite;⁴ while pertinent example of oxygen and sulfur intercalation.^{5,6} are also worth mentioning.

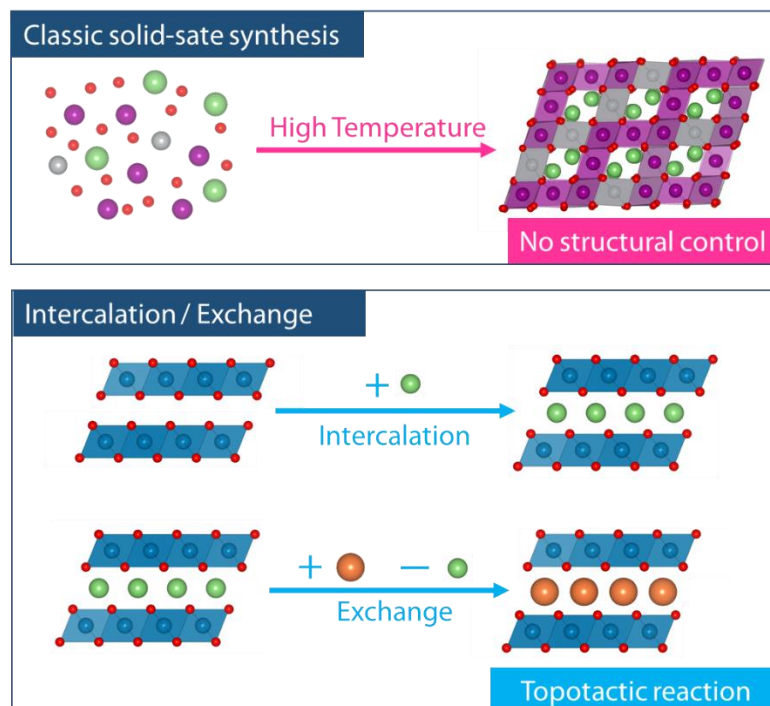


Figure I.1: Schematic drawing of different solid-state reactions. In the “classic” one all the elements are mixed prior to a sintering step at high temperature, leading to a product with non-predictable structure. On the contrary, the intercalation and exchange reactions occur topotactically.

Moreover, beyond their use as synthesis tools, these reactions also alter the properties of the material.^{7,8} For instance, by inducing volume modifications, the intercalated guests can affect the electronic interactions or the phonon modes of the host structure. Thus, by controlling the amount, size or charge of the intercalant these reactions can lead to the design of compounds with exotic thermoelectric, electronic, optic or magnetic properties as described next.

I.1.b Intercalation chemistry: modifications of the physical properties

The insertion of a charged species in a matrix will strongly affect its electronic structure and thus its electronic or magnetic properties. This is nicely exemplified by the semiconductor-to-metal transition observed following the intercalation of alkali cations (Li^+ or K^+) in ZrSe_2 ⁹ or WSe_2 ¹⁰. Equally, the disappearance of the charge density wave (CDW) in TiSe_2 was shown to be suppressed by the insertion of Cu into $\text{Cu}_{0.04}\text{TiSe}_2$ that shows superconductivity.¹¹ Within the same spirit, Guo et al. managed to shift the critical temperature (T_c) of FeSe ¹² from 8 K to 30 K by inserting potassium in the structure ($\text{K}_{0.4}\text{FeSe}$), and Kriener et al. showed that superconductivity could be triggered by copper insertion in Bi_2Se_3 ¹³.

Besides the onset of superconductivity, the intercalation of Cu in Bi_2Se_3 comes along with a drastic change in transmittance¹⁴ (cf. figure I.2). This modification of the optical properties through intercalation has been widely studied to design electrochromic materials. The most noticeable example of that is the Li insertion in WO_3 oxides¹⁵.

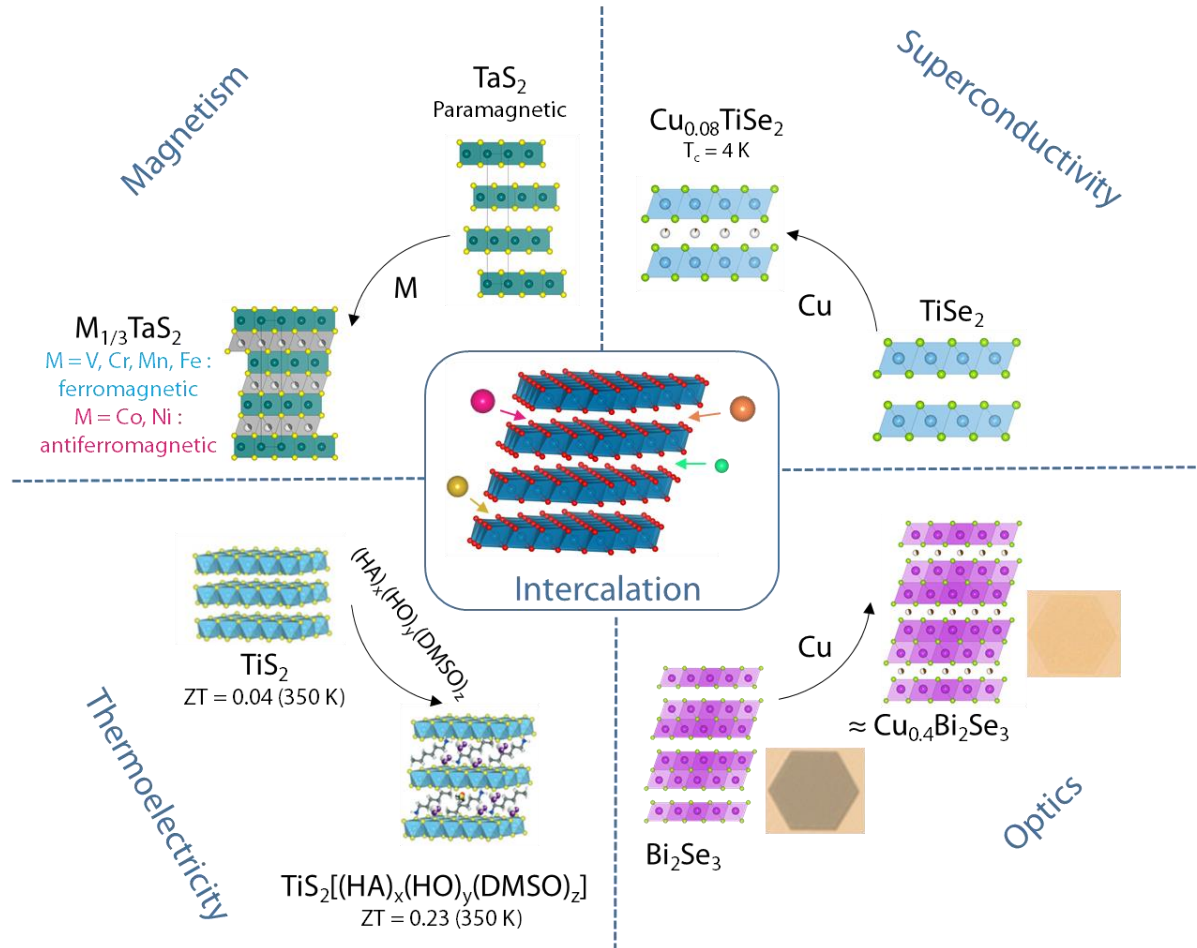


Figure I.2: Schematic drawing of different ways to tune physical properties using intercalation chemistry. The optical transition images of Bi_2Se_3 have been extracted from [14] and those of TiS_2 and $\text{TiS}_2[(\text{HA})_x(\text{HO})_y(\text{DMSO})_z]$ from [19].

Equally, lithium insertion has been shown to be a convenient way to finely tune the magnetic transition temperatures (Curie or Néel) in ferromagnets or antiferromagnets.¹⁶ This is further exemplified in the study of the transition metal intercalation in transition metal dichalcogenides,¹⁷ with for instance M_xTaS_2 being ferromagnetic for $\text{M} = \text{V}, \text{Cr}, \text{Mn}$ and Fe and antiferromagnetic for $\text{M} = \text{Co}, \text{Ni}$.

Finally, intercalation reactions can also affect the thermoelectric properties of an insertion compounds by indirectly affecting their phonon structures that plays a key role in the electronic-thermal conductivity balance that governs the Seebeck coefficient.¹⁸

In short, insertion chemistry is a powerful tool to tune on the demand the electronic and structural properties of materials and therefore their associated physical properties for various applications, with the most famous one within the context of this thesis being energy storage.

I.1.c Intercalation chemistry to store the energy: Li-ion batteries

i) General information on batteries:

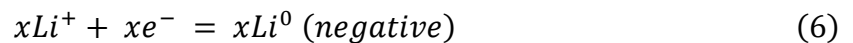
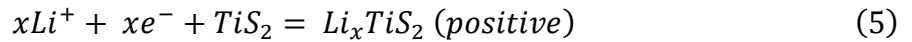
Since the discovery of Volta's cell in 1800, electrochemical devices have been used to store energy. From then, a plethora of systems have been developed, such as the notable Planté batteries, which are the first rechargeable ones. Regardless of the employed technology, all these devices are working on the same principle: two opposite electrodes reacting together through an external circuit. The energy per unit of mass that such a device can store (the energy density) can then be easily estimated as follows:

$$E = \Delta V \times C \quad (4)$$

Where E stands for the energy density, ΔV for the voltage difference between the electrodes and C for the gravimetric capacity that is conventionally expressed in mAh.g⁻¹ (1 mAh/g = 3.6 C.g⁻¹ in S.I) and is proportional to the number of e- that the devices can deliver per unit of mass. The pursuit of the highest energy density system lead naturally to the study of metallic lithium as electrode, seeing as this element combines a low molecular mass (6.94 g.mol⁻¹) and the lowest redox voltage ($E^{\circ}_{\text{Li}^+/\text{Li}} = -3.04 \text{ V vs. SHE}$), which leads to very high theoretical specific capacity (3862 mAh.g⁻¹). Therefore, several primary batteries (non-rechargeable) such as lithium sulfur dioxide (Li:SO₂), lithium-polycarbonmonofluoride (Li:(CF_x)_n) or lithium-manganese oxide (Li:MnO₂) were developed with this element as negative electrode.¹⁹ However, to develop rechargeable devices, it was necessary to use a reversible reaction at the positive electrode. Given the ability of Li⁺ to be intercalated in various structures, it seemed natural think of using electrochemical intercalation reactions for such applications.²⁰

ii) *Rechargeable lithium batteries*

The insertion of alkali ions in the layered titanium disulfide (TiS_2) investigated in the beginning of the 1970's²¹ probably inspired Whittingham to propose in 1976²² a rechargeable battery based on the reversible Li^+ intercalation between a positive TiS_2 electrode and a negative lithium metal electrode. The reactions on both sides read :



This first battery operating at 2 V and around 200 mAh.g⁻¹ reversible capacity showed in addition an excellent match between charge and discharge cycling curves (high-energy efficiency). Following this proof of concept, several other cathode materials were investigated and the first commercial Li-based battery was finally proposed by Moli energy with MoS_2 replacing TiS_2 at the positive electrode and a Li foil at the negative one. Nevertheless, despite the good performance of the system, it encountered safety issues posed by the formation of dendrites. These lithium filaments grow from the lithium electrode through cycling and may cause a short circuit if they end up touching the positive electrode, thereby provoking a short circuit leading to cells that catch into fire. This settled the end of rechargeable Li batteries and the launch of a new research era that led to the Li-ion battery technology.

iii) *Lithium-ion batteries*

Several ideas appeared to overcome the formation of dendrites, the first one consisting of the use of solid electrolytes (polymers) to mechanically block the filament growth. Although rarely used in industry, it is worth mentioning that such technology equipped the Parisian self-service electrical cars developed by the Bolloré group. The second strategy consisted in replacing the metallic lithium anode by another lithium-based material. Lithium alloys (especially with Al) were investigated²⁰ first and solved the dendrite problem but were rapidly abandoned due to large volume changes between charge and discharge. Then came the idea of using lithium intercalation materials at the negative electrode.²³ Graphite was finally chosen²⁴ for the smaller voltage difference to which it leads with respect to metallic lithium (0.3 V). Furthermore, it still

had a high theoretical specific capacity (372 mAh.g⁻¹) coming from the following lithiation reaction:

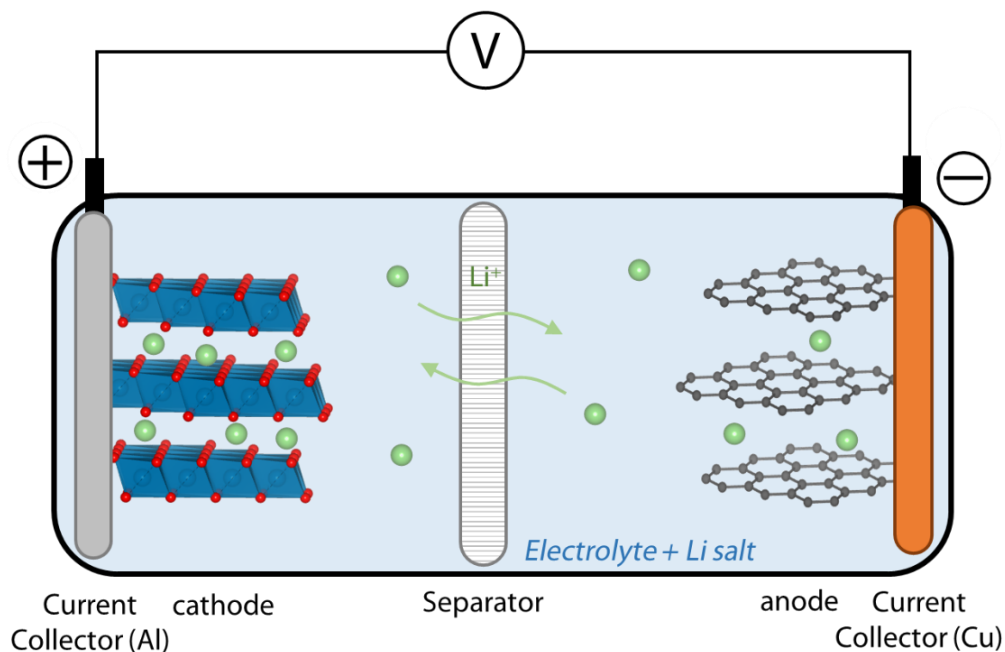


Figure I.3: Schematic drawing of a Li-ion battery device.

This system employing two intercalation materials at both the anode and the cathode (“rocking-chair” principle) defines the Lithium-Ion (Li-Ion) technology. To sum up, a Li-ion device is composed of two-lithium intercalation positive and negative electrodes separated by an electrolyte containing a dissolved lithium salt to ensure ionic conductivity (cf. figure I.3). Moreover, for the sake of simplicity, in the manuscript, the positive electrode (resp. negative), i.e. the electrode with the highest (resp. lowest) electrical potential, will be conventionally called cathode (resp. anode).

As previously mentioned, the batteries’ development is pinned on the improvement of their energy density. Considering all the components of a Li-ion device, it is clear that the intercalation compounds used as cathode are the main elements limiting the capacity and are therefore the ones in need of improvement. To that end, the goal of the following part is to describe various design strategies to increase the energy density of the positive electrode material.

I.2 Design principles of a cathode material

To design ideal cathode material three parameters have to be taken into account:

- 1) The crystal structure to host lithium and to allow its diffusion
- 2) The adequate electronic band structure to tune the redox potential and provide decent electronic conductivity
- 3) The gravimetric capacity directly related to the amount of lithium inside the structure per unit of mass.

The next sections will describe individually the way to tune and optimize these different parameters. However, it is worth mentioning that this manuscript focuses on the “solid state chemistry” point of view of cathode material design, whereas several other aspects such as the cost, toxicity and environmental impact are also of paramount importance, especially when considering the mass production of the compounds.

I.2. a Tuning the crystal structure

i) General considerations

The main specifications of a lithium intercalation structure are first to allow an easy diffusion of the lithium in/out of the structure while preserving the mechanical cohesion of the compound. The compounds can simply be visualized as the interpenetration of a rigid network providing the structural cohesion (anions + transition metal) and of another one composed of lithium atoms or vacant sites ensuring the Li diffusion. It is then possible to classify these compounds according to the dimensionality of the lithium/vacancy¹ network, which can be either monodimensional (yielding channels that have been observed for Nb₃S₄²⁵ or LiFePO₄²⁶), bi-dimensional (layers observed for TiS₂²⁷ and LiCoO₂²⁷) or even three-dimensional (TiS₃²⁸ or Li₃RuO₄²⁹) as shown on figure I.4.

Although no rules exist to directly link the chemical formula to the structure, it is worth noticing that the dimensionality of the lithium (or vacant site) network seems to be related to the Li (or □)/M ratio (M referring here to the non-diffusing cations). This result is in fact intuitive, as the

¹ Both networks being topologically complementary, the dimensionality of the “structural network” varies coherently in the opposite way.

increase of the molar ratio of lithium in a structure should statistically shorten the Li-Li distance, thereby increasing the lithium network dimension.

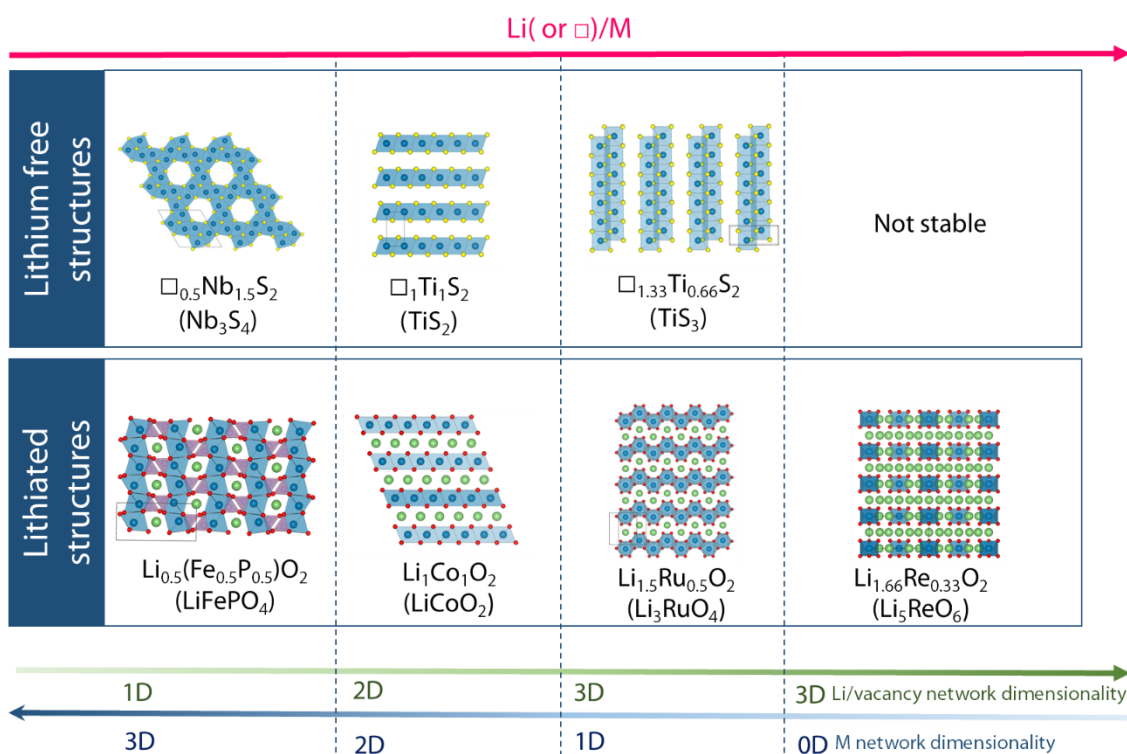


Figure I.4: Schematic drawing of different intercalation compounds with or without lithium in their structure, classified in function of their lithium/vacancy network dimensionality.

The relationship between the Li stoichiometry and the dimensionality of the compounds is convenient for the exploration of new structures. Indeed, low Li/M ratios will prevent good lithium diffusion; contrarily, in lithium super-rich compounds, the 1D/0D dimensionality of the “structural network” will induce structural instability at extended states of charge (lithium extraction).³⁰ Therefore, while there are in theory an infinite number of possible structures, these first considerations already narrow them to a few viable ones. Consequently, the number of structures really considered for Li-ion applications is quite limited and can be mostly split into two families: the transition metal chalcogenides and the polyanionic compounds.³¹

ii) Transition metal chalcogenides:

The transition metal chalcogenides are, as their name implies, simply made of a transition metal cation and a chalcogenide anion ($\text{X} = \text{O}^{2-}, \text{S}^{2-}, \text{Se}^{2-}, \text{Te}^{2-}$). Among this wide family, the structures³² commonly used to intercalate lithium are more specifically closed-packed chalcogenide

arrays of MX_6 octahedrons, the lithium atoms being placed in octahedral or tetrahedral vacant sites. Following these specifications, three main classes of transition metal chalcogenides have been studied: the layered, the spinels and finally the disordered rocksalts.

The layered compounds clearly define the prototypical Li-ion structures, comprising the first historical cathode material TiS_2 as well as LiCoO_2 and $\text{LiNi}_x\text{Mn}_y\text{Co}_z\text{O}_2$ (NMC) that are dominating the market today. In these compounds, the MX_6 octahedra share edges with one another and are organized to form a stack of layers while the lithium atoms are placed in the octahedral vacant sites of the interlayer (cf. figure I.5). These compounds share the general A_xMX_2 ($0 < x < 1$) formula, where A defines the species in the lithium layer (lithium or vacancies), M the species in the transition metal layer and X the chalcogenide. Although simple in theory, the crystallographic structure of these compounds admits several possible variations. For instance, the way the transition metal layers are stacked is not unique, as exemplified by the $\text{TiS}_2/\text{LiCoO}_2$ comparison in figure I.5. Indeed, while the sulfur layers alternate in an ABAB sequence along the c direction in TiS_2 , the oxygen layers in LiCoO_2 follow an ABC sequence. To take this into consideration Delmas³³ proposed a nomenclature of layered materials accounting for the coordination polyhedron of the intercalated cation (O = octahedral, P = prismatic, T = tetrahedral) and the number of layers contained in the unit cell of the compound. Using this system TiS_2 adopts an O1 stacking and LiCoO_2 an O3 stacking, which are the most common ones for lithium layered compounds. Beyond the crystallographic considerations, the understanding of the stacking preference as well as the physics underlying its evolution through cycling are of prime importance for the electrochemical performance.

Moreover, in the so-called lithium-rich layered oxides some of the transition metals are exchanged with lithium atoms. This replacement can in some cases generate an ordered segregation of the lithium and the transition metal within the layer, leading to the formation of a superstructure. The most common one in the lithium-rich oxides is the honeycomb superstructure, where the transition metals define a honeycomb hexagonal network while the lithium atoms are found in the center of the honeycomb void (cf. figure I.5).

In addition to the layered frameworks, the spinel structure has been widely studied in the 1980's and 1990's,³⁴ and sparks renewed interest today.³⁵ These compounds adopt a $\text{A}_x\text{M}_2\text{X}_4$ stoichiometry (where A refers to lithium atoms and/or voids, M to transition metals and X to chalcogenides) and present, similarly to O3 layered compounds, a cubic closed-packed oxygen

framework, where the transition metals are placed in the octahedral sites and the lithium sits in the tetrahedral ones.

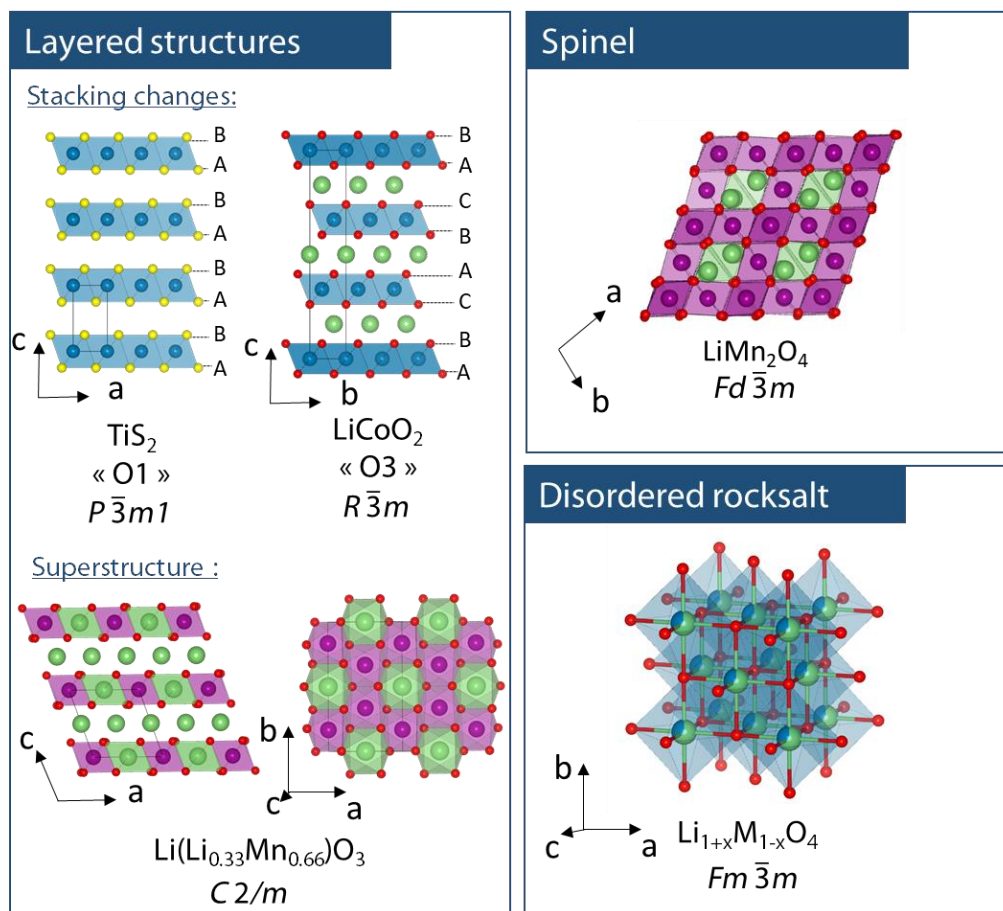


Figure I.5: Schematic drawing of the main transition metal structures used as Li-ion cathodes materials. In particular, some structural variations found in the layered compounds such as stacking sequence change or transition metal layer superstructure are shown.

Finally, the recent interest for the lithium-rich composition lead to the study of the so-called disordered-rocksalts.³⁶ Similarly to the spinels and O3 layered compounds, these compounds present a cubic closed-packed oxygen framework. However, here, the lithium and transition metal atoms are randomly distributed among the octahedral sites of the structure. It is worth mentioning that although incredibly simple the crystallography of these compounds (identical to NaCl from which the compounds got their name) only accounts for an average long range model, while the description of their properties (such as lithium diffusion) calls for a local description and necessitates short range analytical techniques or statistical models³⁷.

iii) Polyanionic compounds

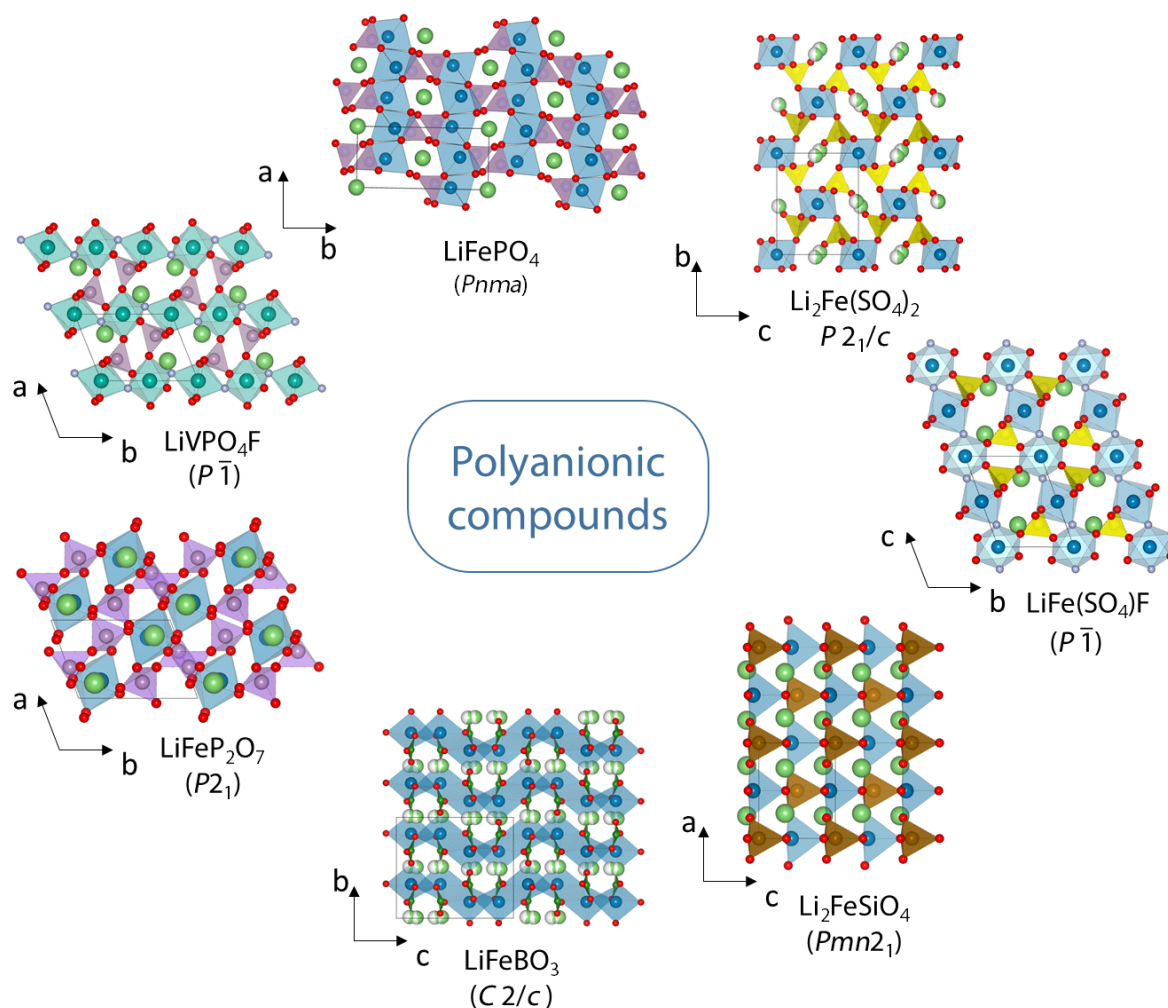


Figure I.6: Schematic drawing of the structural diversity of lithium polyanionic compounds.^{26,38–43}

In the 1990's, John B. Goodenough⁴⁴ showed the possibility to use LiFePO₄ (LFP) as Li-ion cathode material, demonstrating that the single atom anions (chalcogenides, nitrides, halides etc...) were not the only negatively charged building blocks that could be used to design lithium intercalation compounds. This major discovery multiplied the number of possible chemical compositions and opened the way to intensive synthesis and crystallography investigations.^{45–47} Indeed, the replacement of “spherical” single atom anions by tetrahedral (SiO₄⁴⁻, PO₄³⁻, SO₄²⁻), triangular (BO₃³⁻) or even trigonal bipyramidal (P₂O₇⁴⁻) polyanions deeply affects the crystal packing, yielding very different structures (figure I.6).

Considering the large library of available polyanions and the fact that they can be mixed with other anions (F⁻, O²⁻, HO⁻, N³⁻ etc...), the number of possible structure becomes infinite.

However, it is worth noting that, with the exception of LFP and its derivatives, none of these materials have generated much attention for industrial applications of Li-Ion batteries (the situation with Na-ion is different⁴⁸). Indeed, an appropriate crystal structure is necessary but not sufficient to make a suitable cathode material, and voltage as well as capacity have to be optimized as well.

I.2. b Tuning the redox potential

i) *General considerations*

Prior to explaining the relations between cathode material structure and voltage, it is necessary to introduce the difference of potential measured in a Li-ion battery from thermodynamic considerations. Considering a system at temperature T_{ext} , pressure P_{ext} with volume V , according to the first law of thermodynamic, the internal energy variation of this system occurring during an infinitesimal chemical transformation can be written as follows:

$$\delta U = \delta Q + \delta W \quad (8)$$

Here δU , δQ and δW correspond respectively to the variations of internal energy, heat exchanged with the surroundings and work done by the system. The work term can be further decomposed into:

$$\delta W = -P_{ext}dV + \delta W_{elec} \quad (9)$$

Where W_{elec} corresponds to the electrical work. Moreover, according to the second law of thermodynamic, in a system without temperature and pressure variations it is possible to write:

$$\delta Q = T_{ext}(\delta S + \delta_i S) \quad (10)$$

Where δS refers to the exchanged entropy and $\delta_i S$ the created entropy. Besides,

$$dU = T_{ext}dS - P_{ext}dV + Gd\xi \quad (11)$$

G refers here to the Gibbs free energy of the system and ξ to the extent of the chemical reaction. By combining the equations (8) to (11) the following expression is obtained:

$$Gd\xi = T_{ext}\delta_i S + \delta W_{elec} \quad (12)$$

The equation (12) is a general relation for a system undergoing an electrochemical reaction. At this point, we can consider the specific reaction occurring in a Li battery. According to the first part of the chapter, the lithium intercalation in a host matrix (M) can be written as follows:²



For an ideal intercalation we can neglect the irreversibility of this reaction ($\delta_i S = 0$) and express the electrical work as a function of the difference of electrical potential between the lithium anode and the M cathode (ΔE), leading (after integration of (12) over the whole reaction) to the well-known relation:

$$G_{Li_nM} - (nG_{Li} + G_M) = -nF\Delta E \quad (14)$$

With F the Faraday constant. This equation relates the observed cell voltage ΔE and the Gibbs free energies of the Lithium (G_{Li}), the empty host (G_M) and the intercalated host (G_{Li_nM}). At this point, it is common to identify the Gibbs free energies with the more convenient internal energies.⁴⁹ For the sake of simplicity, we will assume it in this section; however, it is worth mentioning that such hypotheses require to ignore the entropy changes, which are not always negligible especially at low or high states of charge.⁵⁰ Moreover, the energy term associated to the lithium being almost constant regardless of the system, we can write a final equation:

$$(U_{Li_nM} - U_M) + cste = nF\Delta E \quad (15)$$

According to this, ΔE is governed by the energy changes of the cathode compound through lithiation. In order to make this relation more intuitive it has been proposed to split this energy difference into an electrochemical and a structural contributions. In other words, it suggests that ΔE could be determined considering independently the redox potentials of the electrochemically active sites (ΔE^M) of the cathode and the energy variations induced by the structural changes through lithiation (ΔE^S). This decomposition ($\Delta E = \Delta E^M + \Delta E^S$) has been rationalized with DFT calculations by Saubanère et al.⁵¹ However, we will just discuss it qualitatively here.

The redox potential of the electroactive metallic center (ΔE^M) can be explained with a simple molecular orbital model. Indeed, in most of the cathode materials described above the transition metal (M) is found octahedrally coordinated by the anions (L= O, S...). It is therefore interesting to first build a molecular orbital diagram of the ML_6 subunit (cf. figure I.7). In this

² For sake of simplicity and because we will focus in this manuscript on the cathode material we consider here the reaction occurring in a lithium cell and not a lithium ion one.

diagram the overlap between the ligand orbitals and M d-orbitals leads to the formation of an antibonding (ψ) and a bonding (ψ^*) molecular orbitals, which are found to be the HOMO (Highest Occupied Molecular Orbital) and HOMO-1. In first approximation, the relative destabilization of the HOMO (β_{\mp}) is given by the following expression:

$$\beta_{\mp} = K \frac{S^2}{\Delta\chi} \quad (16)$$

Where ($\Delta\chi$) represents the energy difference (also referred as the ionicity of the system) between the M d-orbitals and the ligands' orbitals, S is the overlap between these orbitals (S) and K is a proportionality factor. From this orbital diagram of a single ML_6 subunit an approximate band diagram⁵² of the whole crystal structure can be deduced, where the centers of the energy bands correspond to the energy of the discrete orbitals and their width to the overlap between the different molecular orbitals. Using this rough approximation, the position of the Fermi level coincides with the HOMO energy. Therefore, the Fermi level E_F can be express as a function of the energy of the d orbitals of the isolated atom E_M^d as follows:

$$E_F \approx E_M^d + K \frac{S^2}{\Delta\chi} \quad (17)$$

Moreover, the redox potential of the metal (ΔE^M) is proportional to the difference between the Fermi level of the metal and that of the lithium (E_F^{Li}),

$$\Delta E^M \propto E_M^d + K \frac{S^2}{\Delta\chi} - E_F^{Li} \quad (17)$$

Since the more electronegative, the metal the lower E_M^d it is easy to tune ΔE^M via an appropriate choice of the transition metal. For instance, the electronegativity of the 3d transition metals increases when moving from the left to the right of the periodic table (Fe < Mn < Co < Ni) and the redox potential follows the same trend. This has been illustrated using isostructural $LiMPO_4$ with (M = Fe, Mn, Co, Ni) where the redox potential varies from 3.5 V to 4.5 V from Fe to Co^{44,53,54} and even 5.4 V for $LiNiPO_4$ ⁵⁵. The equation (17) also indicates that redox potential can be tuned by playing with the anion. Indeed, by lowering the electronegativity of the ligand the “ionicity” $\Delta\chi$ will increase, ultimately leading to a higher voltage. This justifies historically the transition from the layered sulfur-based materials (TiS_2) to the layered oxides ($LiCoO_2$). The oxygen being more electronegative than the sulfur, the redox potential was drastically increased (2 V²² vs 3.5 V⁵⁶) through this change. Lastly, it also explains the principal interest of the polyanionic compounds. Indeed, by covalently linking the oxygen atoms to a cation C

(Si^{4+} , P^{5+} , S^{6+} etc...), the oxygen orbitals have their energy lowered (cf. figure I.7) and meanwhile, their overlap with the M d-orbitals decreased. These two phenomena leads to increase $\Delta\chi$ and a decrease of S inducing a global increase of ΔE^M . Therefore, the more covalent the C-O cation is, the higher the voltage will be, as exemplified by the comparison of LiFePO_4 (3.5 V) and $\text{Li}_2\text{Fe}(\text{SO}_4)_2$ (3.8 V).⁵⁷

However, as mentioned before, the transition metal redox is not the only parameter to take into account to understand the cathode voltages. Indeed, in LiMn_2O_4 the first lithium removal involves the $\text{Mn}^{3+}/\text{Mn}^{4+}$ redox couple and occurs at 4 V, while the lithium reinsertion involving the same redox couple is observed at 2.9 V. Yet according to the precedent section ΔE^M should be the same between the charge and the discharge. This 1.1 V difference can be solely understood by considering structural parameters (ΔE^S). Indeed, in LiMn_2O_4 the lithium atoms are found initially in high energy tetrahedral sites while upon reinsertion the lithium goes into lower energy octahedral sites⁵⁸.

Finally, following these “rules”, it is possible to synthesize materials with very high redox potentials (nickel based sulfates or spinels). However, electrode materials are limited by the electrolyte’s voltage window, which cannot exceed 5 V,⁵⁹ leading to intensive research efforts in this field today. Waiting for the improvement of electrolytes, the solid chemists can still improve the energy density of the cathode via the capacity as presented in the following section.

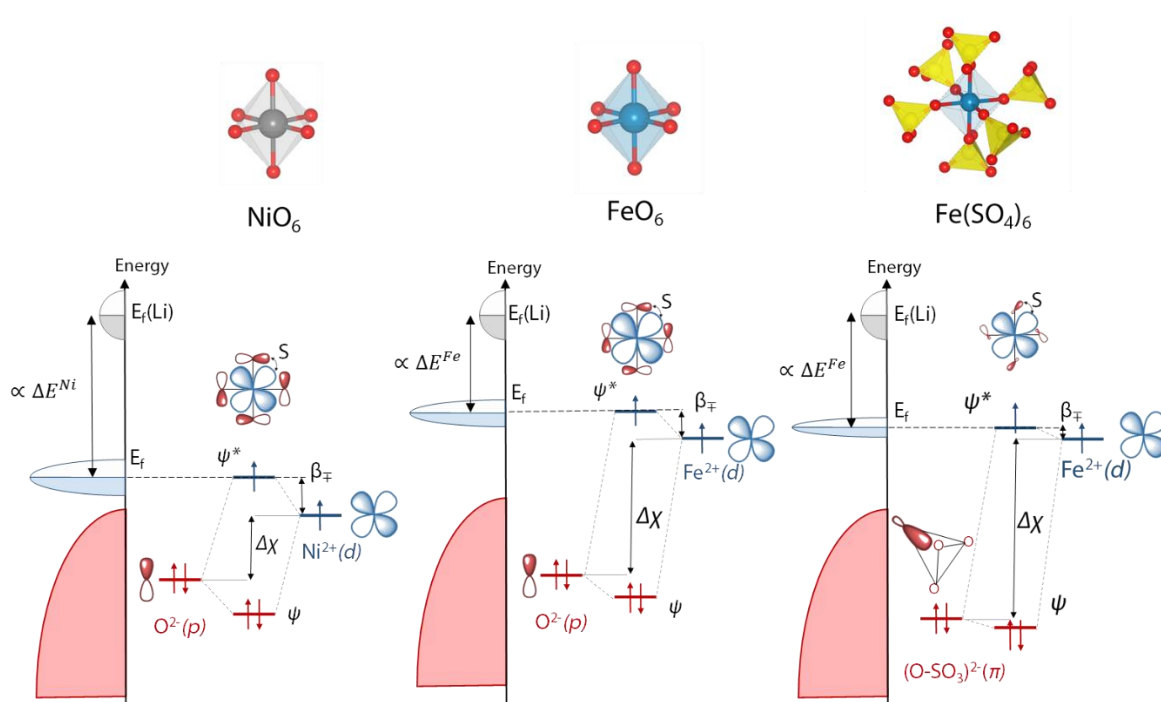


Figure I.7: Schematic drawing of the band diagram of transition metal oxides and polyanionic systems as deduced from local orbital interactions. This figure represents the effect of several parameters (transition metal electronegativity and nature of the anion) on the orbital interaction and further on the band diagram. The energy difference between the Fermi energy of each compounds (E_f) and that of the lithium reflects the variation of the transition metal's redox potential. This figure is freely inspired by [50].

I.2. c Increasing the gravimetric capacity

i) General considerations

As defined in the first part of this chapter the gravimetric capacity (hereafter simply denoted by “capacity”) can be defined as the number of lithium atoms the material can intercalate reversibly per unit of mass. It is possible to express the theoretical capacity in $\text{mAh}\cdot\text{g}^{-1}$ as a function of the number of lithium atoms per formula unit (n_{Li}) and the molar mass (M) of the compound:

$$C = \frac{F}{3.6} \times \frac{n_{\text{Li}}}{M} \quad (18)$$

From this expression, it is clear that in order to increase of the capacity it is necessary to either increase n_{Li} or decrease the molar mass of the compound. It is however important to mention that this simplistic model is not always sufficient to predict the real capacity of layered oxides and, for instance, the experimental reversible capacity of LiCoO_2 is only $140 \text{ mAh}\cdot\text{g}^{-1}$ due to structural instability at a high state of charge. To circumvent these issues cationic substitution

strategies were necessary. They lead to the commercial NMC compounds^{60–62} ($\text{LiNi}_x\text{Mn}_y\text{Co}_z\text{O}_2$) whose capacity can today reach 200 mAh.g^{-1} . Nevertheless, equation (18) remains a convenient tool to predict the viability of a material. For instance, the molar mass term explains the limit of the polyanionic strategy. Indeed, by replacing two O^{2-} anions (32 g.mol^{-1}) atoms by heavier anions like $(\text{PO}_4)^{3-}$ (95 g.mol^{-1}) the capacity decreases from 274 mAh.g^{-1} (for LiCoO_2 theoretically) to 170 mAh.g^{-1} (for LiFePO_4 theoretically). Moreover, it represents another argument in favor of the replacement of sulfur by oxygen. However, the anions molar mass cannot be reduced further significantly. Therefore, to increase the capacity of transition metal oxide a natural strategy is to replace the transition metals by lithium atoms, thereby decreasing the molar mass while increasing n_{Li} . This reasoning historically led to the investigation of the so-called Li-rich oxides,⁶³ derived from $\text{Li}(\text{Li}_{0.33}\text{Mn}_{0.66})\text{O}_2$ (also referred as Li_2MnO_3) and promising more than 300 mAh.g^{-1} capacity. The current record of reversible capacity in a Li-rich oxides has been reached with Li_3IrO_4 ($\text{Li}(\text{Li}_{0.5}\text{Ir}_{0.5})\text{O}_2$) with 340 mAh.g^{-1} .⁶⁴

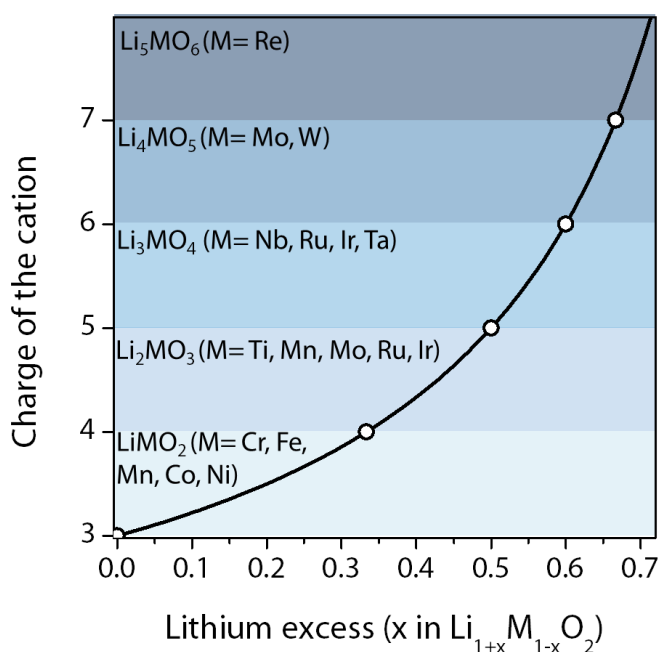


Figure I.8: Evolution of the transition metal valence with lithium enrichment of rocksalt compounds.

Thus, the Li-enrichment is one of the most promising ways to increase cathode capacities. However, this strategy comes with its own downsides. The first one has been mentioned previously: by replacing transition metals by lithium, the dimensionality of the transition metal oxides framework is lowered, leading to structural instabilities (decomposition, dissolution) at higher states of charge. In addition, the replacement of some of the transition metals by lithium atoms increases the transition metal redox state. For instance, moving from LiMnO_2 to Li_2MnO_3

($\text{Li}(\text{Li}_{0.33}\text{Mn}_{0.66})\text{O}_2$) shifts the Mn redox state from 3+ to 4+. This increase in the metal valence already limits the choice of transition metals as exemplified in figure I.8. It is particularly interesting to note that no 3d metal are found in a rocksalt structure with a redox state greater than 4 (V, Cr and Mn can be found with higher valence but not in octahedral sites). Furthermore, these considerations naturally raises the question of electrochemical process occurring through lithium removal (i.e. oxidation) in these compounds. Indeed, naïvely one could expect that through oxidation $\text{Li}_2\text{Mn}^{4+}\text{O}_3$ would first form $\text{LiMn}^{5+}\text{O}_3$ and then eventually $\text{Mn}^{\text{VI}}\text{O}_3$. However, in spite of a first study on this material where such a scenario was proposed,⁶⁵ the poor electrochemical activity and irreversibility of the material already suggested a more complex scenario. The aim of the next section is to describe how the electrochemistry study of high-valent compounds progressively lead to a new paradigm in the battery community.

I.2 d Redox in high-valence systems

i) *The emergence of the anionic redox concept*

Although lithium-rich oxides have been investigated as cathode materials since the 1980's (with for instance Li_2MoO_3 ⁶⁶ or Li_2RuO_3 ⁶⁷) the debate about their charge compensation through oxidation really started with Li_2MnO_3 and its derivatives. Indeed, to improve the electrochemical activity of Li_2MnO_3 , Dahn et al investigated solid solutions of Li_2MnO_3 with LiCoO_2 and MO ($\text{M} = \text{Co}$ or Ni) leading to the formation of the Li-rich compounds. In these compounds, the Ni, Co and Mn atoms are found in the +2, +3 and +4 redox states respectively in the pristine state. Moreover, through oxidation the removal of the first lithium clearly involves $\text{Co}^{3+}/\text{Co}^{4+}$ and $\text{Ni}^{2+}/\text{Ni}^{4+}$ and is reversible.⁶⁸ On the contrary, while further oxidation is possible, it brings strong voltage hysteresis in discharge, and voltage fading cycle after cycle,⁶⁹ which questioned the nature of the associated charge compensators.

This problem generated lots of interest in the community and several studies demonstrated in quick succession the formation of gaseous O_2 as well as the inactivity of the manganese during oxidation.⁷⁰⁻⁷² Altogether, these results rejuvenated the old idea of the participation of the anions through the oxidation process proposed in the early 1980's for layered sulfides⁷³ and in 1999 by Tarascon⁷⁴ et al. for the full oxidation of LiCoO_2 . Finally, Sathiyaraj et al. using a "model compound" $\text{Li}_2\text{Ru}_{1-x}\text{Sn}_x\text{O}_3$,⁷⁵ gave the decisive proof of the participation of the oxygen in the oxidation of lithium rich compounds, supported by X-ray photoelectron spectroscopy (XPS) and electron paramagnetic resonance (EPR) analyses. These first results generated much

interest in the community with the hope to find solutions to the electrochemistry roadblocks encountered by the Li-rich NMC.

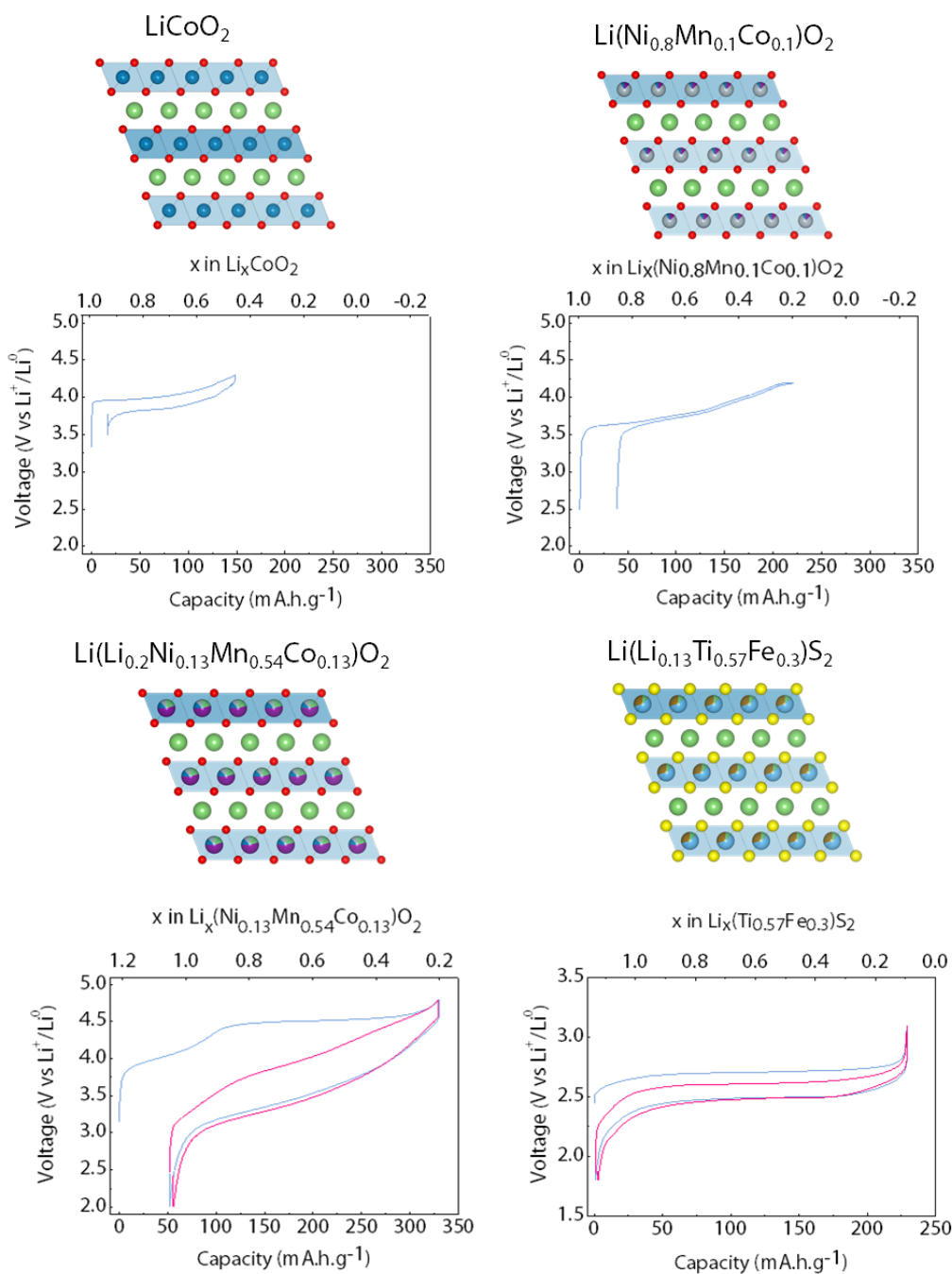


Figure I.9: Structural evolution of layered materials (oxygen, lithium, manganese, cobalt and nickel are represented in red, green, purple, blue and grey respectively) with the corresponding voltage curves.

ii) Solid state chemistry strategies

Of all the strategies that have been implemented, it is worth mentioning the importance of those relying on solid-state chemistry. Indeed, the Li-rich NMC being very complex with several redox centers and structural inhomogeneities, chemists decided to study “model” compounds sharing similar structures but with only one metal center such as Li_2RuO_3 ⁷⁶ or Li_2IrO_3 .^{77,78} Interestingly, contrary to 3d transition metal based oxides the anionic redox process in these systems has been shown to be reversible without oxygen release. This behavior has been rapidly related to the increase of the M-O bond covalency obtained when using 4d and 5d metals instead of 3d metals. Although efficient, this substitution strategy is nevertheless unrealistic from the point of view of potential application due to the cost of the 4d and 5d transition metals. However, to improve the covalency of the metal anion bond it is also possible to play on the anions replacing oxygen by heavier chalcogenides (S, Se or Te). This anion substitution strategy (which will be described in more detail in chapter III) led to the synthesis of Li-rich sulfides derived from the Li_2TiS_3 compound.^{79–81} It has been shown that these materials exhibit anionic redox without the problems observed in oxides (hysteresis, voltage fade etc...) (cf. figure I.9). Although promising, these materials are still limited by a much lower voltage than oxides (2.5 V for $\text{Li}_{1.13}\text{Ti}_{0.57}\text{Fe}_{0.3}\text{S}_2$ ⁸¹) which prevents them for the moment from competing with industrial standards. It is therefore interesting to try either to increase their gravimetric capacity or to find a way to increase the voltage by looking at oxysulfides for example (see chapter IV).

iii) Spectroscopic and theoretical investigations

At this point, it is important to discuss the role of the spectroscopy techniques and theoretical calculations to elucidate the anionic redox mystery. Indeed, while classic solid state structural analyses (X-ray or Neutron diffraction, microscopy) were able to spot structural signatures associated to the anionic redox process (distortions, cation migration etc.)⁷⁷, an arsenal of spectroscopic techniques were used to track any signs of anion oxidation. For instance, XPS studies demonstrated the appearance upon oxidation of an extra signal found at higher binding energy than O^{2-} , which suggested the presence of oxidized anionic species. Nevertheless, as the analysis depth with XPS is limited to a few nanometers from the surface, X-ray absorption spectroscopy (XAS) was massively used to show the involvement of the bulk material in the anionic redox.⁸² To investigate the presence of O-O bonds, Raman spectroscopy was also used.⁸³ Lastly, Gent et al.⁸⁴ compared the Resonant Inelastic X-ray Scattering (RIXS) spectra of several charged cathode materials and peroxides and claimed to have spotted an anionic

redox fingerprint with this technique. However, after almost ten years working on the subject it is worth wondering what these techniques have really brought to our understanding of the anionic redox. Indeed, while there is no longer any doubt about the redox activity of the anionic network, the nature of the oxidized oxygen species is still a complete mystery with many candidates such as “transition metal hybridized O_2^{n-} ($n < 4$)”,^{75,85} O_2^{2-} ,^{83,86} O_2^- ,⁸⁷ O^- ⁸⁸ and even molecular O_2 .⁸⁹ In addition, many theoretical models have emerged over the years, bringing an elementary understanding of the anionic redox process, without however succeeding to unify the field. The aim of the next section is then to describe the basic understanding of the anionic redox process and to discuss the difficulties encountered to build a more complete model.

iv) Fundamentals of the anionic redox

Although now well accepted by the community, the oxidation of the anion network deserves basic explanations. As discussed before, the increase in the cation valence results in an energy decrease of its nd orbitals. At certain oxidation states the partially occupied transition metal orbitals can be pushed below the filled anionic ones (cf. figure I.10 a).⁹⁰ At this point, an internal reduction of the metal by the anion can occur (cf. figure I.10 a). While this simplistic model can be generalized to all systems experiencing anionic redox, an important point specific to the lithium-rich compounds is the presence of non-bonding anionic states. Indeed, in a classic layered material the oxygen atoms are surrounded by three transition metals. Consequently, all the oxygen’s 2p orbitals are involved in bonding or antibonding interactions with the transition metals. Moving to lithium rich compounds, some of the transition metals are replaced by lithium, which does not form bonds with the oxygen, thereby leaving some 2p orbitals non-bonded (cf. figure I.10 b).⁹¹ The resulting non-bonding states are then convenient electron supplies for oxidation, as their removal will not induce any changes in the bonding structure. While the aforementioned points are no longer up for debate, the different scenarios mostly diverge on the evolution of the crystal and electronic structures following the removal of the electrons. In short, it was first suggested that the charge transfer gap between the O-2p and TM-d bands would determine the nature and thus the stability of the oxidized oxygen species.⁶⁹ However, this model was unable to explain different anionic redox behaviors for compounds with similar covalency. In order to address these issues Ben Yahia et al.⁹² considered the number of holes on the oxygen atoms to define the threshold of the anionic redox instabilities. Lastly, several authors opposed to these “rigid structure” models (the redox behavior is discussed considering solely small structural changes) the necessity to take into account

structural changes (cation migration for instance). They proposed several scenarios ranging from the formation of real O_2^{2-} dimers, to that of Mn^{7+} intermediate state^{84,93} and even molecular oxygen, with however no convincing experimental proof.

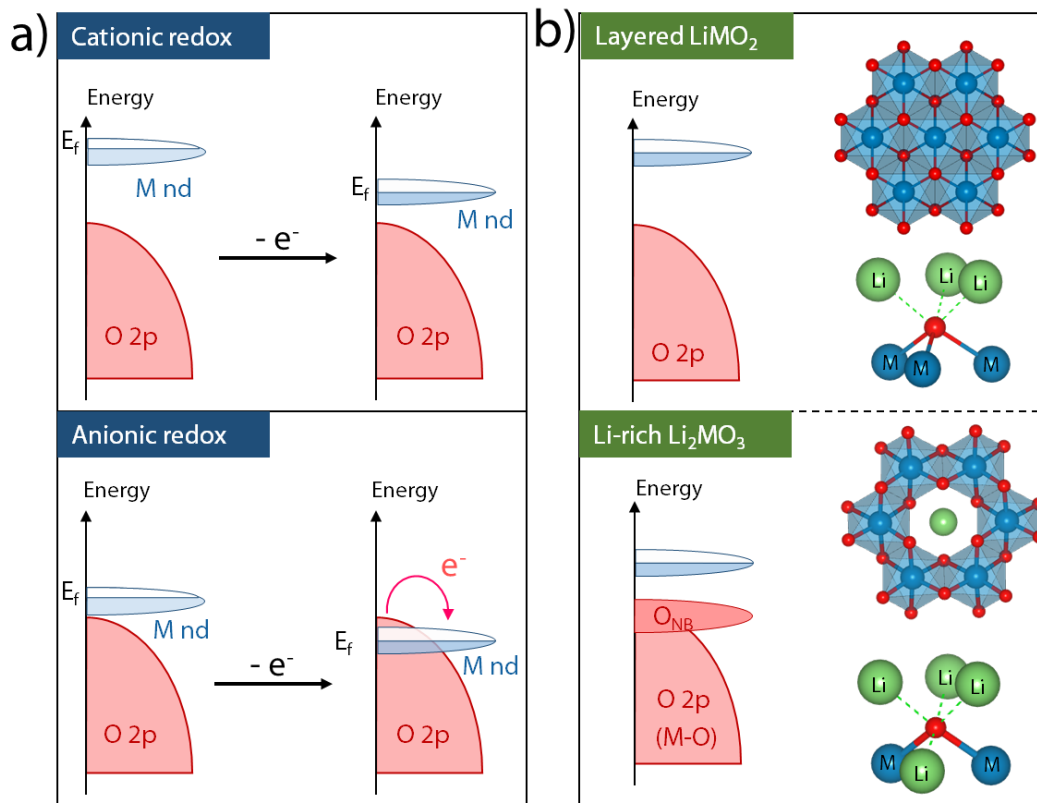


Figure I.10: a) Schematic drawing of the band diagram evolution during reduction in both cationic and anionic redox systems. b) Impact of the Li-enrichment on the band diagram of a layered oxide.

In response to this statement of failure, Gent et al.⁹⁴ highlighted the electrochemical similarities (irreversibility, hysteresis) between anionic redox and systems implying high-valent cations (Cr^{6+} , V^{5+} etc...) and suggested incorporating all these processes into a more general concept of “high-valent redox”. In addition, they proposed, rather than a detailed mechanism, a working framework based on intuitive kinetic and thermodynamic “rules”. Thus, the authors simply suggested that, from the thermodynamic point of view, high-valent species (cation or oxygen) are driven to change their bonding arrangements. Then, motivated by this driving force, the redox process will follow a pathway (kinetic) shaped by the activation energies related to all the different reactions steps. Indeed, a glance at the crystallography databases (and in line with Pauling rules) suggests that highly oxidized cations ($Mn(VII)$, $Cr(VI)$, $V(V)$ or $Mo(VI)$) are more stable in 4 or 5 coordination with oxygen than in 6. Similarly, in line with the octet rule, the oxidized oxygen atoms are always found in nature bonded to other elements. Thus, the

electrochemical formation of the high-valent species should induce a driving force prone to rearrange the material (such as coordination polyhedron distortion or cation migration). The example of the layered LiCrO_2 nicely exemplifies this point. Indeed Komaba and co-workers demonstrated that through lithium removal the chromium atoms, rather than forming Cr^{4+} , undergo a segregation leading to the presence of Cr^{3+} and Cr^{6+} in a 2/3:1/3 ratio, with the Cr^{6+} species found in the tetrahedral sites of the interlayer, thereby leading to cycling irreversibly.^{95,96}

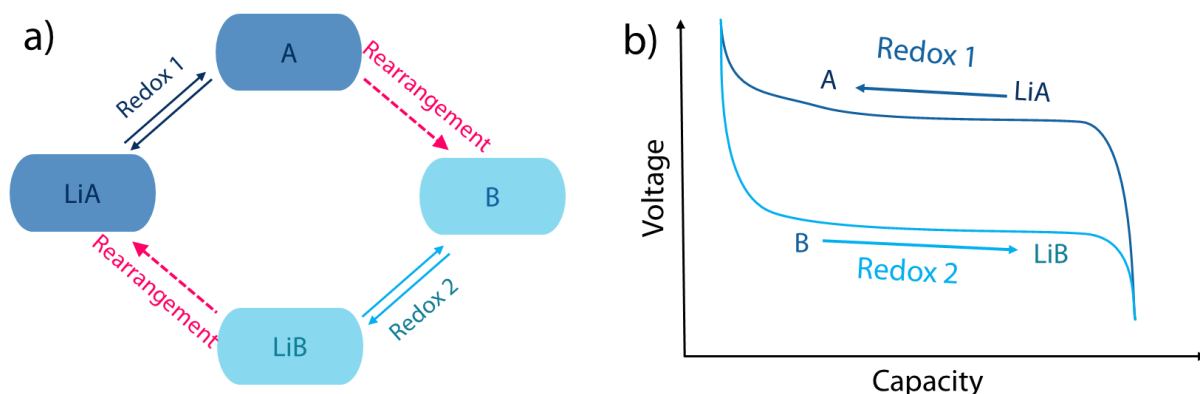


Figure I.11: a) Multistep “square scheme” as proposed by Assat et. al.⁹⁷ In this model the anionic redox process is decomposed into a purely redox process (without electronic/crystallographic structural changes) and slower reorganizations steps. This results in different electrochemical pathways in charge and discharge as represented on b).

To push this framework further, it is interesting to make a parallel with a mechanism proposed by Assat et al.⁹⁷ Indeed, based on micro calorimetry these authors suggested that, contrary to cationic redox, the anionic redox should occur in two steps, the first one corresponding to an electrochemical reaction with few crystallographic/electronic reorganization, and the second one consisting in the structural reorganization (cf. figure I.11). The decoupling of a fast rigid electrochemical reaction and slower reorganization steps is commonly observed in electrochemical systems^{98,99} and is pinned on Marcus theory. Therefore, by combining these two frameworks, it is possible to describe the behavior of high-valent redox systems as follows:

-Similarly to cationic redox, the electrochemical delithiation occurs first with minor crystallographic/electronic structural changes (rigid structure). However, the high-valence state formed in such a way necessitates structural reorganization to be stabilized.

-Driven by this thermodynamic force, the compound then evolves following the chemical pathways dictated by the activation energies of the different reactions steps.

-A similar scenario would occur in discharge.

Thus, while this model does not make any assumption on the nature of the oxidized species or reorganization steps it introduces an asymmetry between the electrochemical reactions in charge and discharge, thereby providing an explanation for the voltage hysteresis observed between charge and discharge in most anionic redox systems. Moreover, in spite of its simplicity, this general model still gives us information as to how the design of cathode materials can be optimized. For instance, according to the multistep mechanism detailed above, it is clear that the hysteresis could be avoided if the reorganization step following the oxidation one were blocked. This can be achieved by stabilizing the compounds that are formed just after the reorganization and/or by slowing down this step. Recent studies by Yamada's and Van der Ven's groups agreed on this point as they showed that the hysteresis-free compounds Li_2IrO_3 and $\text{Na}_2\text{Mn}_3\text{O}_7$ cycled with minimal structural changes.^{100,101} Moreover, in line with this mechanism, it is worth mentioning that no cation migration nor dimer formation has been observed during the cycling of the hysteresis-free $\text{Li}_{1.13}\text{Ti}_{0.57}\text{Fe}_{0.3}\text{S}_2$. In my personal opinion, the strength of such a picture is to give intuitive tools to understand more globally the behavior of a compound undergoing high-valent redox without having to delve into technical details. Such "details" will however need to be addressed eventually in order to understand completely the cycling behavior of the compounds.

Thus, although lot of research efforts have been devoted to anionic redox, the underlying mechanisms are still far from being fully understood and further synthesis, theoretical, and spectroscopic investigations are needed.

Chapter conclusion

This chapter has been devoted to the presentation of intercalation chemistry and more precisely of its use to electrochemically store energy in Li-ion battery devices. It has been highlighted that the cathode material is today the main component that limits energy density of such cells, which calls for further investigations in synthesis. The different strategies and classes of materials contemplated throughout the years to meet these challenges have been described, thereby revealing that the lithium enrichment of transition metal oxides is one of the most interesting strategies to improve the energy density. However, such an approach comes along with several difficulties generated by the high-valent redox process, which have not been solved yet in spite of intense research efforts. The contribution of the solid-state chemist to this technology is then to synthesize new materials with better performance or specifically designed to understand fundamental questions.

However, following the intense research effort to find the best materials carried out these last 40 years, a notable decrease in publications describing new cathode compounds is now observed. Thus, a natural question arises: is there still room for new cathode material designs? Facing this discouraging ascertainment, the aim of this thesis is to investigate original strategies for synthesizing compounds that intercalates lithium. While an impressive amount of lithiated chemical compositions have been studied to store lithium, most of these compounds are thermodynamically stable phases obtained at high temperature, which leaves the field open for the investigation of metastable compositions. Moreover, as presented in this chapter, the new paradigm of the anionic redox rejuvenated the interest for sulfide materials. The re-investigation of this field –that had fallen into oblivion- in the light of the lessons brought by decades of cathode studies is quite exciting. Moreover, although the most well-known families of compounds have been seriously exhausted, there is fortunately plenty of room to dream about unexplored chemistries.

Finally, it is worth remembering that intercalation, before being a way of storing energy, was a fabulous synthesis tool used to tune the physicochemical properties of various compounds as pioneered by F.R. Gamble and T.H. Geballe searching for superconductivity.¹⁰² The following chapters will therefore be a good opportunity to mention the magnetic properties of the newly synthesized materials.

Chapter II: Low temperature synthesis of ruthenium ternary oxides

II.0 Introduction

II.0.a Low temperature synthesis?

As stated in the first chapter of this thesis, these last 50 years have seen an intensive research effort to unearth the best cathode materials. Such strategy seriously narrows down today's possibility to find new compounds and especially oxides using conventional methods. However, until now most of the lithium-based oxides have been prepared via ceramic processes enlisting high temperature (or high pressure) to facilitate the diffusion of chemical elements in the solid state. These *modus operandi* present the advantages of reducing the number of steps, of co-reactants and allow the production of large amounts of pure crystalline products with high reproducibility. Nevertheless, these drastic conditions lead solely to thermodynamically stable compounds (cf. figure II.1). In order to develop more “eco-friendly” processes and enable the synthesis of metastable phases, low-temperature processes (sol-gel, hydrothermal, co-precipitation etc...) have been developed over the last twenty years.

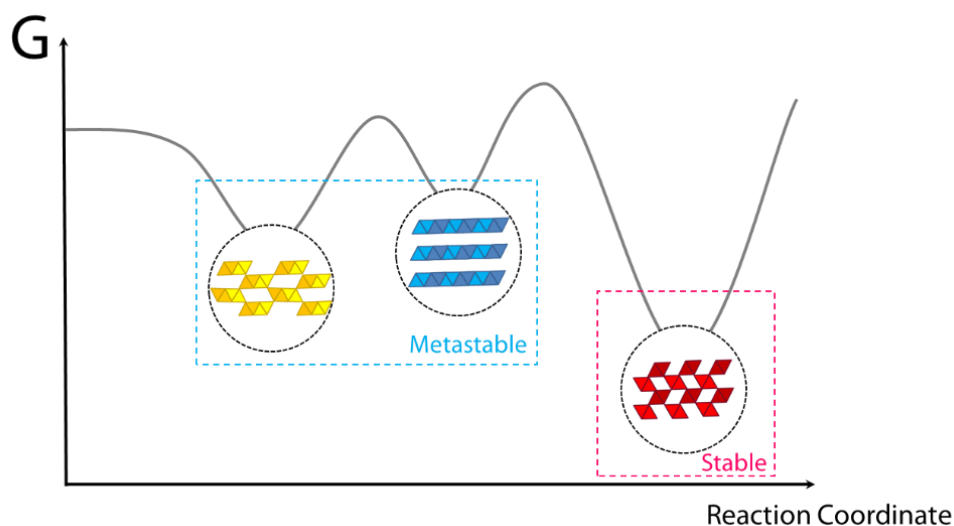


Figure II.1: Schematic drawing of a reaction pathway, with G being the Gibbs free energy. This emphasizes that while the thermodynamically stable compound is unique, several metastable phases can be isolated by controlling the reaction parameters.

These low temperature synthesis approaches, also referred as "chimie douce", involve multiple chemical steps such as oxydoreduction, proton transfers, and/or cluster formation. Although such reactions proceed via complex nucleation-growth mechanisms, they offer many opportunities to tune the reaction pathway and obtain different materials playing with physico-chemical tools (pH, temperature, reactant ratio...). The literature is rich of elegant studies showing how the control of solvated species or reaction kinetics steps can lead to the oriented synthesis of vanadium binary oxides¹⁰³ or the polymorphic control of TiO₂¹⁰⁴ or FeS₂¹⁰⁵, to name only a few.

II.0.b Ruthenium oxides

In the Li-ion battery field, ruthenium oxides have been studied since the 1980 with Li₂RuO₃,⁶⁷ but solely regains full interest with the emergence of the anionic redox concept. In particular the Li₂Ru_{1-x}M_xO₃ (M=Sn, Ti, Mn...) ¹⁰⁶⁻¹⁰⁸ compositions have enabled the stability of anionic redox process with 4d metals but also the origin of the voltage fade upon cycling. Finally, the limits of anionic redox in compounds extra-rich in lithium ions have been studied with Li₃Ru_{1-x}M_xO₄ compounds (with M being Ir, Nb, Sb or Ta).^{32,109,110} In a more general way, ruthenium oxides have been widely studied in several research fields due to their panoply of unique electrical and magnetic properties. For instance, ruthenium dioxide (RuO₂) is known to be the most efficient electrocatalyst for water splitting¹¹¹. Among all the ternary combination, alkaline-earth ruthenates are the most studied for their magnetic properties. Indeed, Sr₂RuO₄ sparked considerable attention for its unconventional spin-triplet superconductivity¹¹² and more recently SrRu₂O₆ has been found to be an antiferromagnet with high Néel temperature (565 K).¹¹³ Owing to such a continuous interest, there is a need to enlarge the Ru-based oxides family members via additional chemical exploration.

Therefore, in light of the benefits provided by the "chimie douce", some authors have decided to implement it to the synthesis of ruthenium oxides with high ruthenium redox state (greater than IV). The hydrothermal approach with either high temperature or pressure was first tried but success had been limited^{7,114,115} to the synthesis of three new metastable ruthenium(V)/alkaline-earth oxides by Hiley *et al.* in 2014 using mild temperature synthetic conditions (200°C).¹¹⁶ The novelty in their approach relies in the use of a highly oxidized ruthenium salt (KRu^{VII}O₄) which is reduced during the reaction, rather than in the oxidation of a ruthenium precursor having a low (+IV) oxidation state as previously. Following this work several other ruthenium (+V) phases were obtained using the same chemical trick.^{117,118,119}

Surprisingly, none of these studies went into a deep understanding of the reacting paths by which these new phases were formed. Progress in this direction, however, cannot be uncoupled from a deeper appreciation of the means by which the reduction and precipitation steps are affected by various physico-chemical parameters.

This chapter will be divided into three parts, the first one will deal with the different synthesis processes of new ruthenium oxides, the second one will describe the structure of the compounds thus formed and, finally, the magnetic and electrochemical properties of two phases in particular (BaRu_2O_6 and SrRu_2O_6) will be studied.

II.1 Synthesis

II.1.a Hydrothermal synthesis of ternary alkaline-earth ruthenium oxides.

As mentioned in the introduction, Hiley et al.¹¹⁶ proposed a hydrothermal process to synthesize ruthenium oxides, the aim of this first part is to deepen the understanding of this reaction procedure and see how the structure of the synthesis products depends on the physico-chemical reaction parameters.

For all the synthesis described in the following sections, we used KRuO_4 (Alfa Aesar), $\text{BaCl}_2 \cdot 2\text{H}_2\text{O}$ (Alfa Aesar), and $\text{Sr}(\text{NO}_3)_2$ (Sigma Aldrich) as sources of Ru, Ba and Sr, respectively. To prepare the aqueous alkaline solutions, extra pure KOH (> 99.98 metal basis, Alfa Aesar) was used, as well as NaOH (98% metal basis, Sigma-Aldrich) and LiOH (98% metal basis, Alfa Aesar). The synthesis consists in reacting a ruthenium (VII) salt (KRuO_4) with alkaline-earth (BaCl_2 , $\text{Sr}(\text{NO}_3)_2$) salts in aqueous alkaline hydroxides solution (KOH, NaOH or LiOH) at 200°C. Our synthesis procedure throughout this manuscript, if not otherwise mentioned, consists in i) mixing of 5 mg ($2.45 \cdot 10^{-2}$ mmol) of KRuO_4 with the desired amount of alkaline-earth salt in 1 mL of aqueous solution of alkaline hydroxide with controlled concentration, ii) pouring the mixtures into a hermetically sealed tailor made 2 mL Teflon-lined steel autoclave and iii) placing the autoclave at 200°C in a preheated chamber furnace for 72 hours. After the reaction, powders are cleaned three times: twice with 5 mL of a 10^{-2} M solution of HCl and then with water before being dried at 100°C overnight. The resulting powder was then characterized for phase purity and composition. Hydrothermal syntheses being known as

extremely sensitive to physico-chemical parameters such as pH, reactant ratio, cations in solution or temperature, a survey of these various parameters has been undertaken.

i) Impact of KOH concentration and reactant ratio: speciation diagram

For guidance purpose speciation diagrams were first experimentally drawn (cf. figure II.2 and II.3) as function of the KOH concentration and of the $\text{MX}_2/\text{KRuO}_4$ ratio (with $\text{MX}_2 = \text{BaCl}_2$ or $\text{Sr}(\text{NO}_3)_2$). To build these diagrams, three different molar ratios of $\text{BaCl}_2/\text{KRuO}_4$ reactants (0.5, 1 and 2) were studied. For each of these ratios, nine concentrations of KOH ranging from 0 to 8 mol.L⁻¹ were considered (cf. figure II.2 a)). The same ratios were used for $\text{Sr}(\text{NO}_3)_2/\text{KRuO}_4$, with seven concentrations of KOH ranging from 0 to 3 mol.L⁻¹ (cf. figure II.2 b)). We observed that the higher KOH concentration is, the lower the amount of powder is formed at the end of the reaction (after 72 hours) and this depends on the nature of alkaline earth cation. Consequently, no KOH concentration greater than 8 M and 3 M will be studied from now on for the barium/ruthenium and strontium/ruthenium systems, respectively. The resulting samples from such a survey that correspond to symbols in the diagram (cf. figure II.3) were analysed for phase purity by XRD and single phase domains are defined by different colours. For multiphase samples, the relative ratios are not given, as they slightly fluctuate from one experiment to the other.

For the barium/ruthenium system with a $\text{BaCl}_2/\text{KRuO}_4$ ratio of 1 we observed the formation of five phases (cf. figure II.3 a) upon increasing KOH concentration: BaRu_2O_6 ($[\text{KOH}] < 1\text{M}$), $\text{Ba}_2\text{Ru}_3\text{O}_9(\text{OH})$ ($1\text{M} < [\text{KOH}] < 4\text{M}$), $\text{Ba}_2\text{Ru}_3\text{O}_{10}$ ($4\text{M} < [\text{KOH}] < 6\text{M}$), $10\text{H-Ba}_5\text{Ru}_4\text{O}_{15}$ ($6\text{M} < [\text{KOH}] < 7\text{M}$), and finally the layered perovskite $\text{Ba}_4\text{Ru}_3\text{O}_{10.2}(\text{OH})_{1.8}$ for $[\text{KOH}] > 7\text{M}$. Note that BaRu_2O_6 , $\text{Ba}_2\text{Ru}_3\text{O}_{10}$ and $10\text{H-Ba}_5\text{Ru}_4\text{O}_{15}$ are new phases obtained in pure form except for $10\text{H-Ba}_5\text{Ru}_4\text{O}_{15}$ which was contaminated with traces of either $\text{Ba}_2\text{Ru}_3\text{O}_{10}$ or $\text{Ba}_4\text{Ru}_3\text{O}_{10.2}(\text{OH})_{1.8}$. This contrasts with the strontium/ruthenium system with $\text{Sr}(\text{NO}_3)_2/\text{KRuO}_4$ of 1 for which we solely found (cf. figure II.3 b) three different phases which are in the order of increasing the KOH concentration : SrRu_2O_6 , $\text{Sr}_2\text{Ru}_3\text{O}_9(\text{OH})$ and $\text{Sr}_2\text{Ru}_3\text{O}_{10}$, respectively. Interestingly, none of the isolated phase have the same M/Ru ratio whatever the alkaline earth cation ($\text{M} = \text{Ba}$ or Sr). Moreover, this ratio is not distributed randomly within the diagram but increases with the KOH concentration taking the values of 0.5, 0.66, 1.1, 1.25, 1.3 for BaRu_2O_6 , $\text{Ba}_2\text{Ru}_3\text{O}_9(\text{OH})$, $\text{Ba}_4\text{Ru}_3\text{O}_{10.2}(\text{OH})_{1.8}$, $10\text{H-Ba}_5\text{Ru}_4\text{O}_{15}$, $\text{Ba}_4\text{Ru}_3\text{O}_{10.2}(\text{OH})_{1.8}$. The same trend applies as well for the strontium/ruthenium system and this is not fortuitous as discussed latter.

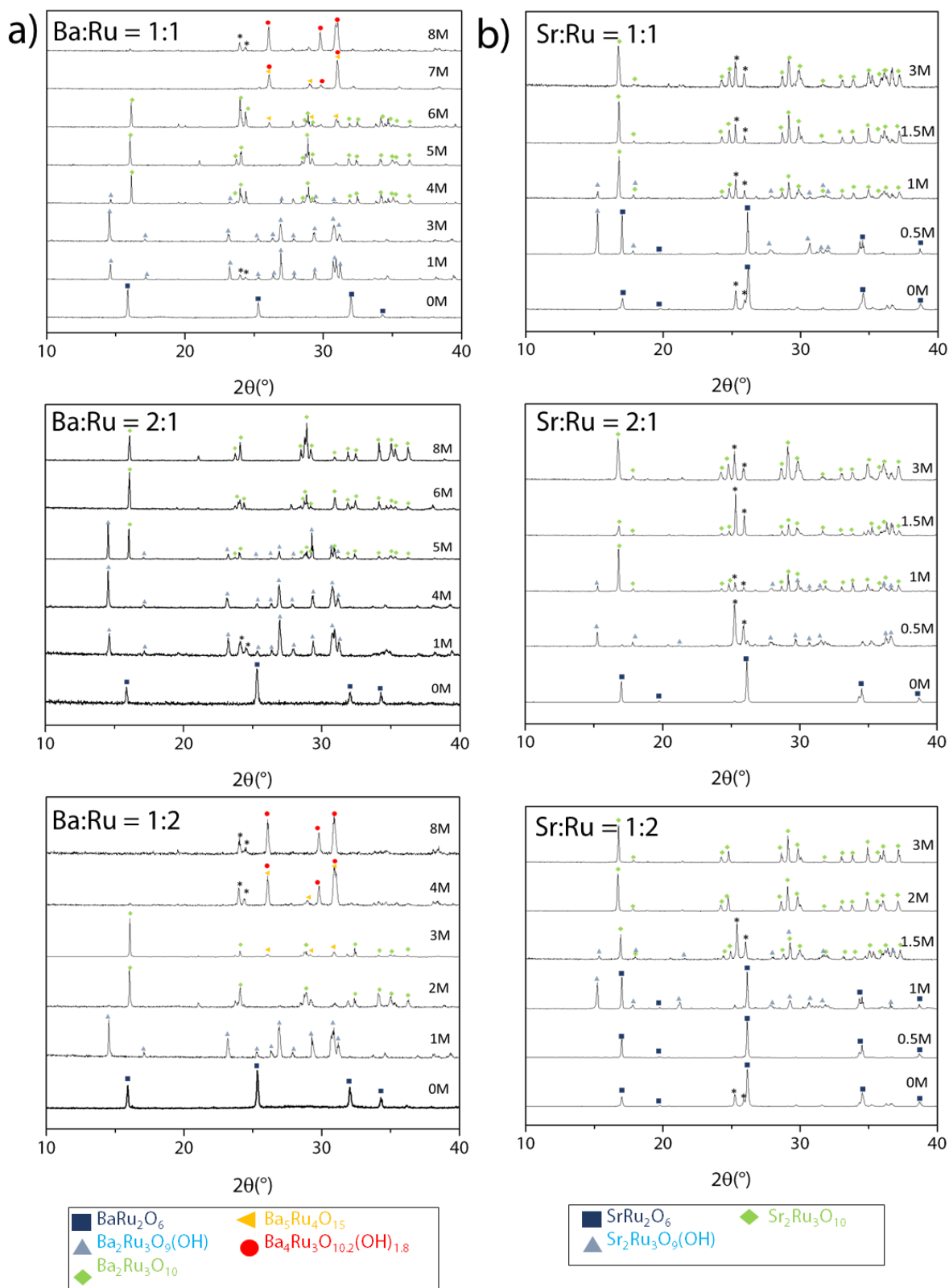


Figure II.2: X-ray diffraction patterns of powders obtained at different KOH concentrations using various a) $\text{BaCl}_2:\text{KRuO}_4$ or b) $\text{Sr}(\text{NO}_3)_2:\text{KRuO}_4$ ratios at 200°C . The different diagrams are indexed using a color code described in the figure legend. Peaks corresponding to barium or strontium carbonate impurities (sample not washed with acid) are indexed using (*).

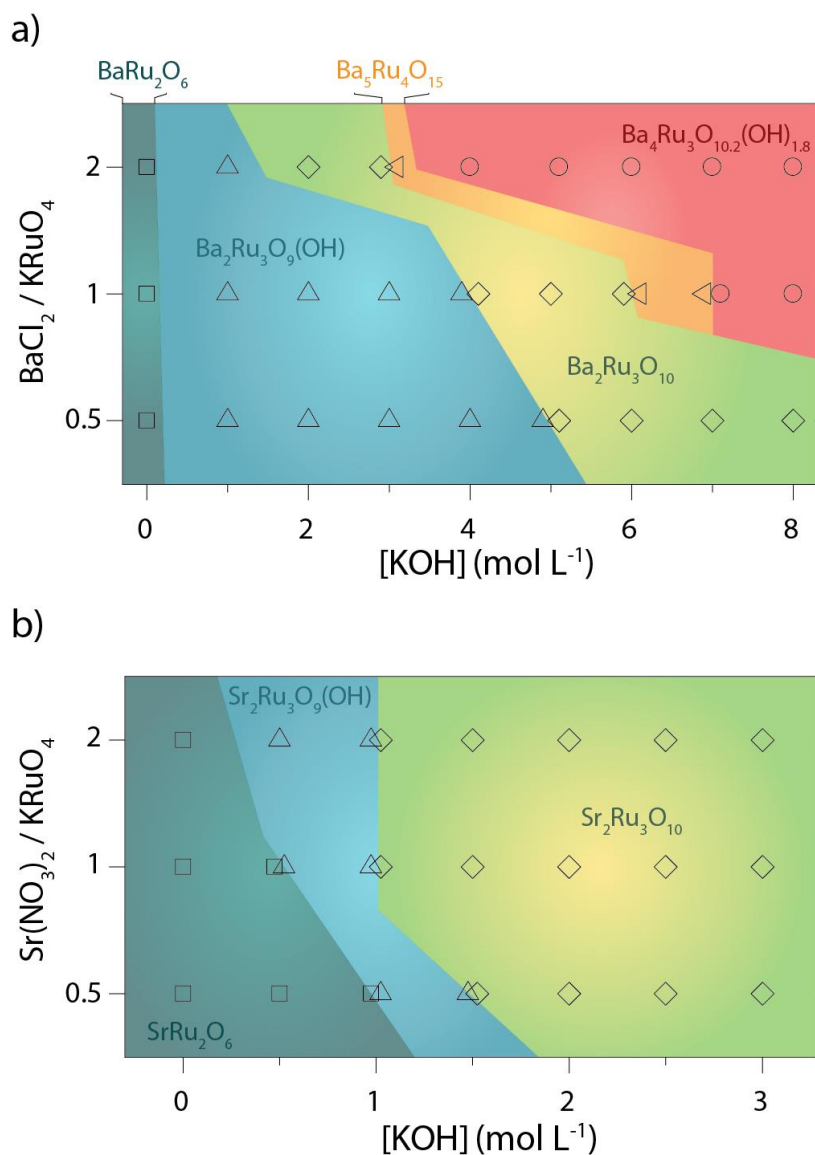


Figure II.3: Speciation diagram of ruthenium oxides as a function of the initial KOH concentration and reactant molar ratios. a) Speciation diagram of the ruthenium/barium system, symbols correspond to experimental points: BaRu_2O_6 (\square), $\text{Ba}_2\text{Ru}_3\text{O}_9(\text{OH})$ (\triangle), $\text{Ba}_2\text{Ru}_3\text{O}_{10}$ (\diamond), $10\text{H-Ba}_5\text{Ru}_4\text{O}_{15}$ (\triangleleft), $\text{Ba}_4\text{Ru}_3\text{O}_{10.2}(\text{OH})_{1.8}$ (\circ). b) Speciation diagram of the ruthenium/strontium system, symbols correspond to experimental points: SrRu_2O_6 (\square), $\text{Sr}_2\text{Ru}_3\text{O}_9(\text{OH})$ (\triangle), $\text{Sr}_2\text{Ru}_3\text{O}_{10}$ (\diamond). Colored areas are a visual help for the reader to apprehend the domains of formation for each compound.

Our results further indicate that the M/Ru ratio in the obtained phases greatly differs from the reactant ratio. Nevertheless, the fact remains that this reactant ratio impacts considerably the domain of OH concentrations, that is the pH, over which these phases are forming as shown in figure II.3 a) and b). For example, when the reactants are alkaline-earth rich ($\text{MX}_2/\text{KRuO}_4 > 1$), phases richer in alkaline earth are formed in a broader [KOH] range (red and orange colours), while such phases cannot even form when the reactants are alkaline-earth poor. The inverse

observation is made with alkaline-earth poor reactants (i.e $\text{MX}_2/\text{KRuO}_4 < 1$) (see green and blue domains figure II.3 a)).

ii) Impact of the counter cation

Having explored the impact of KOH concentration on the nature of the synthesis products within the Ba-Ru and Sr-Ru systems, we next check the importance of the nature of counter cation (K^+). New syntheses were performed by replacing KOH by NaOH and LiOH while keeping $\text{BaCl}_2/\text{KRuO}_4$ and $\text{Sr}(\text{NO}_3)_2/\text{KRuO}_4$ precursor ratios of 1. For the strontium/ruthenium couple, whatever the alkaline hydroxides used, the obtained phases remain the same. This is not any longer true in presence of the barium/ruthenium couple for hydroxides concentrations greater than 1M since with NaOH and LiOH, we obtained the $\text{NaBa}_4\text{Ru}_3\text{O}_{12}$ and $\text{LiBa}_4\text{Ru}_3\text{O}_{12}$ phases, respectively as opposed to $\text{Ba}_2\text{Ru}_3\text{O}_{10}$, $10\text{H-Ba}_5\text{Ru}_4\text{O}_{15}$ and $\text{Ba}_4\text{Ru}_3\text{O}_{10.2}(\text{OH})_{1.2}$ for $[\text{KOH}] > 1 \text{ M}$, as previously described. Let's recall that the aforementioned Li and Na-based compounds are not new since they have been previously reported using ceramic high temperature process (800°C).¹²⁰ For completeness we also examined the influence of counter ion concentration, replacing KOH with KCl. Whatever the added KCl concentration we only obtained BaRu_2O_6 . Therefore, the hydroxide ions are essential to guide the reaction. Altogether these results show that the hydroxide counter ions can modify the speciation diagram leading to new compounds in which they could become a component of the structure.

iii) Impact of the temperature

Temperature is another parameter that we have investigated as it is of paramount importance in controlling reaction pathways. Figure II.4 represents XRD patterns of the phases resulting from heating precursor mixtures ($\text{BaCl}_2:\text{KRuO}_4 = 1:1$ at $[\text{KOH}] = 4 \text{ M}$) at four different temperatures ranging from 120°C to 220°C . Crystalline phase are solely obtained for $T > 120^\circ\text{C}$. The phase formed at 175°C (red diamonds) can easily be identified as $\text{Ba}_2\text{Ru}_3\text{O}_{10}$. With increasing temperature to 200°C , there is the appearance of a second phase $\text{Ba}_2\text{Ru}_3\text{O}_9(\text{OH})$ (blue triangles) which grows at the expense of the first one and becomes single phase as the temperature reaches 220°C . This indicates a well-pronounced influence of the temperature on the speciation diagrams and may explain, based on the temperature inhomogeneity of our furnaces, the occasional irreproducibility of the synthesis.

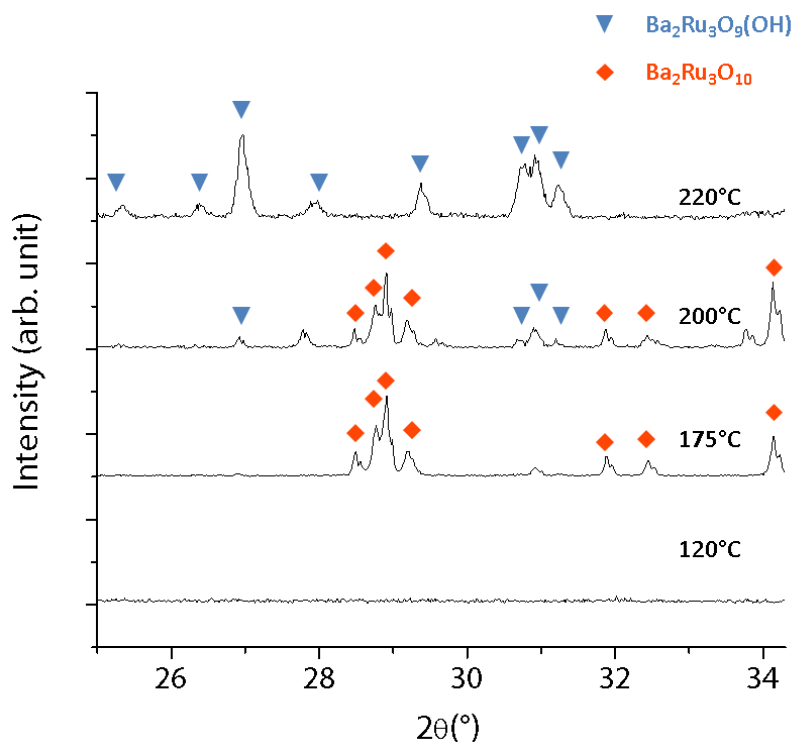


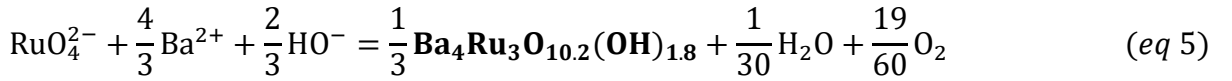
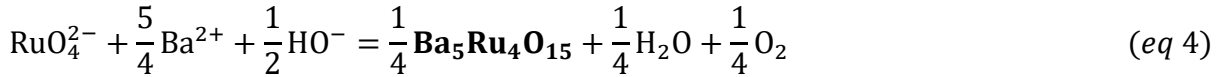
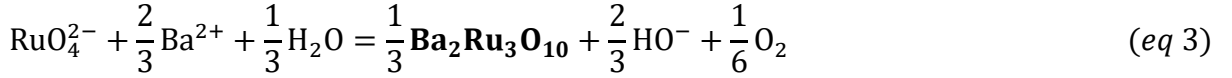
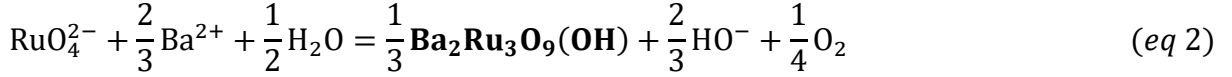
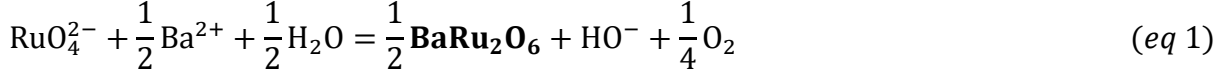
Figure II.4: X-ray diffraction patterns of powders obtained at different temperatures using $\text{BaCl}_2:\text{KRuO}_4 = 1:1$ at $[\text{KOH}] = 4$ M. Blue triangles represent $\text{Ba}_2\text{Ru}_3\text{O}_9(\text{OH})$ peaks whereas red diamonds represent $\text{Ba}_2\text{Ru}_3\text{O}_{10}$ peaks.

Overall, we have shown that the low temperature solution process leading to the formation of new Ru-based binary oxides is sensitive to many parameters, namely, reactant ratio/concentration, temperature and particularly pH. Interestingly, we experienced a positive synergetic effect between the various parameters for synthesising pure phases as opposed to contaminated phases by acting on a single parameter. For instance, by acting on the pH alone the obtained BaRu_2O_6 , and $10\text{H-Ba}_5\text{Ru}_4\text{O}_{15}$ are always contaminated by minute amounts of RuO_2 , $\text{Ba}_2\text{Ru}_3\text{O}_{10}$ and $\text{Ba}_4\text{Ru}_3\text{O}_{10.2}(\text{OH})_{1.2}$. This synergetic effect is a gift for preparing new phases but a nightmare when attempt to rationalize the synthetic process as described next.

iv) *Mechanism investigations*

A grasp to understand such reaction can be provided by considering reactant and products and using the guidance from the Pourbaix diagram (cf. figure II.5). It indicates that, using the synthesis concentrations described above, KRuO_4 , dissolved into K^+ and RuO_4^- , is reduced by water to form water stable $\text{Ru}^{\text{VI}}\text{O}_4^{2-}$ species. According to the redox state of the final compound

obtained (+V or +VI), this implies that RuO_4^{2-} is then reduced by water from its +VI to +V oxidation state. Using these simple deductions, one can write the global reaction equations for the formation of the different compounds:

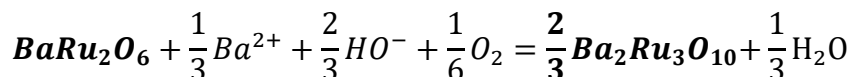


Postulating that these reactions are equilibrium one can write the equilibrium constant associated using the general formula:

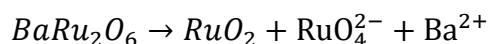
$$K = \frac{[\text{HO}^-]^a P_{\text{O}_2}^c}{[\text{RuO}_4^{2-}][\text{Ba}^{2+}]^b}$$

Where a , b and c depend on the compound formed, and a is positive (eq 1 to 3) or negative (eq 4 and 5) depending on the reaction (for instance $a = 1$, $b = 0.5$ and $c = 0.25$ for BaRu_2O_6). According to these simple equations, the influence of the reactant ratio and the hydroxide concentration is highlighted. Indeed, structures associated with small a values (in particular for negative ones) would be more favorised at higher hydroxide concentration. Identically, phase for which b is high would be more favorised at high $[\text{Ba}^{2+}]$ values. This result is consistent with the experimental speciation diagram drawn in figure II.3 as it predicts the order of appearance of the different materials with pH. For instance, BaRu_2O_6 associated to the larger a value ($a = 1$) is formed at the lowest $[\text{OH}^-]$ whereas $\text{Ba}_4\text{Ru}_3\text{O}_{10.2}(\text{OH})_{1.8}$, associated to the smallest a ($a = -0.66$) is formed for the highest hydroxide concentration. It is important to note, that this simple reasoning doesn't take into account free energy of formation of solid phase which would be essential to simulate a rigorous phase diagram.

This thermodynamic approach is based on the assumption that all the equations written above are equilibrium. It should then be possible to transform one phase to another playing with $[\text{OH}^-]$ and/or $[\text{Ba}^{2+}]$. For instance, BaRu_2O_6 should be changed into $\text{Ba}_2\text{Ru}_3\text{O}_{10}$ according to:



To investigate this point $\mathbf{BaRu_2O_6}$ was heated at 200°C in 5 M $[\mathbf{OH}^-]$ with 0.1 M \mathbf{Ba}^{2+} . After 5 days of reaction, the solution turned orange (characteristic to the presence of $\mathbf{RuO_4}^{2-}$ in solution) and $\mathbf{Ba_2Ru_3O_{10}}$ and $10\mathbf{H-Ba_5Ru_4O_{15}}$ are formed. These observations are perfectly consistent with a thermodynamic scenario, as $\mathbf{BaRu_2O_6}$ is supposed to dissolve into $\mathbf{RuO_4}^{2-}$ according to the equations above, and the formation of the two phases at this hydroxide concentration is in line with the speciation diagram described in figure II.3. However, the presence of $\mathbf{RuO_4}^{2-}$ in solution necessitates the oxidation of the ruthenium specie, the implication of dissolved oxygen to do it is doubtful as the experiment has been reproduced bulling argon in the autoclave before heating and it led to the same results. A disproportionation of Ru(V) can be then suggested following:



No $\mathbf{RuO_2}$ has been clearly seen on XRD pattern but amorphous phase is likely. This prevents to go from one phase to another just playing with pH.

Nevertheless, as mentioned in the synthesis part, we observed that increasing $[\mathbf{OH}^-]$ results in lowering the amount of powder formed at the end of the reaction (after 72 hours). This observation can be proved considering the concentration of $[\mathbf{RuO_4}^{2-}]$ at the end of the reaction. Solutions of this anion are deep orange, we can observe that for low $[\mathbf{OH}^-]$ the final solutions are colourless, indicating that all $[\mathbf{RuO_4}^{2-}]$ is consumed whereas at higher $[\mathbf{OH}^-]$ final solution remain deep orange. This result contradicts the pure thermodynamic scenario as the equilibrium constant predicts (with “a” being negative) that the higher $[\mathbf{OH}^-]$ is the lower $[\mathbf{RuO_4}^{2-}]$ should be. This result let think that kinetic could be implied in this reaction as well, especially, it seems that hydroxides slow down the global reaction rate. Moreover, one can argue that the equilibrium constant of formation of $\mathbf{Ba_2Ru_3O_9(OH)}$ and $\mathbf{Ba_2Ru_3O_{10}}$ are identically impacted by $[\mathbf{OH}^-]$ as a is identical for both ($a = 2/3$). However, these phases are formed in distinct pH domains, which is in contradiction with the pure thermodynamic scenario. In this case, the role of reaction kinetics has probably to be taken into account.

Finally, the experimental speciation diagrams can mostly be rationalized using a simple thermodynamic approach, however the engagement of reaction kinetics is proved in this system. Understanding the precise impact of $[\mathbf{OH}^-]$ on reaction kinetics deals with mechanism investigation. A likely scenario consists in two steps that enlist first the thermal reduction in

solution of Ru(VI) into an hypothetical Ru(V) entity and then the precipitation of this entity with alkaline-earth cations. The implication of hydroxide concentration in one of this step could explain the observations described above. Better understanding of the different steps implied in the process is primordial to fully understand the hydrothermal process and then to obtain other new phases.

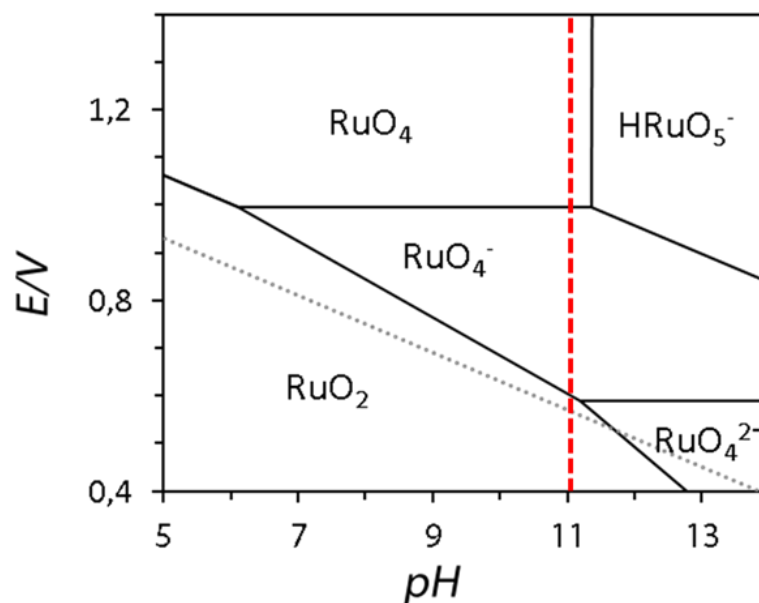


Figure II.5: Reduced Pourbaix diagram of Ruthenium/ H_2O for $[\text{Ru}] = 10^{-2} \text{ mol.L}^{-1}$. This diagram was built using data found in reference [120]. Grey dotted line represents the water oxidation line. The red dotted line represents the pH obtained after the dissolution of KRuO_4 in the reaction concentrations.

In short, these results indicate that this hydrothermal process is highly tunable using different physico-chemical parameters. Furthermore, thermogravimetric analysis (TGA) measurements (cf. figure II.6) indicate that all the new compositions reported here decompose in argon around 600°C confirming that these compounds are metastable. Consequently, none of these compositions could have been obtained by high temperature synthesis validating even more the interest of this process. However, with the exception of Ca^{2+} and Ag^+ forming the previously reported $\text{Ca}_{1.5}\text{Ru}_2\text{O}_7$ and AgRuO_3 ,^{116,118,119} our attempts to extend this process to other cations such as Li^+ , Na^+ , K^+ , Mg^{2+} or Zn^{2+} failed. While the inability to precipitate alkali-based ruthenium oxides is probably related to the low complexation strength of these cations, the failures with divalent cations are more surprising. It is worth then mentioning a recent study of Burnett et al, who investigated a similar process with several divalent cations (Mg, Zn, Cu, Ni, Co) that leads according to the authors to a rutile RuO_2 structure with part of the ruthenium atoms replaced by the abovementioned cations.¹²² Motivated by the idea of obtaining other

divalent cation based ruthenium oxides, another low temperature strategy was investigated and is presented in the next section.

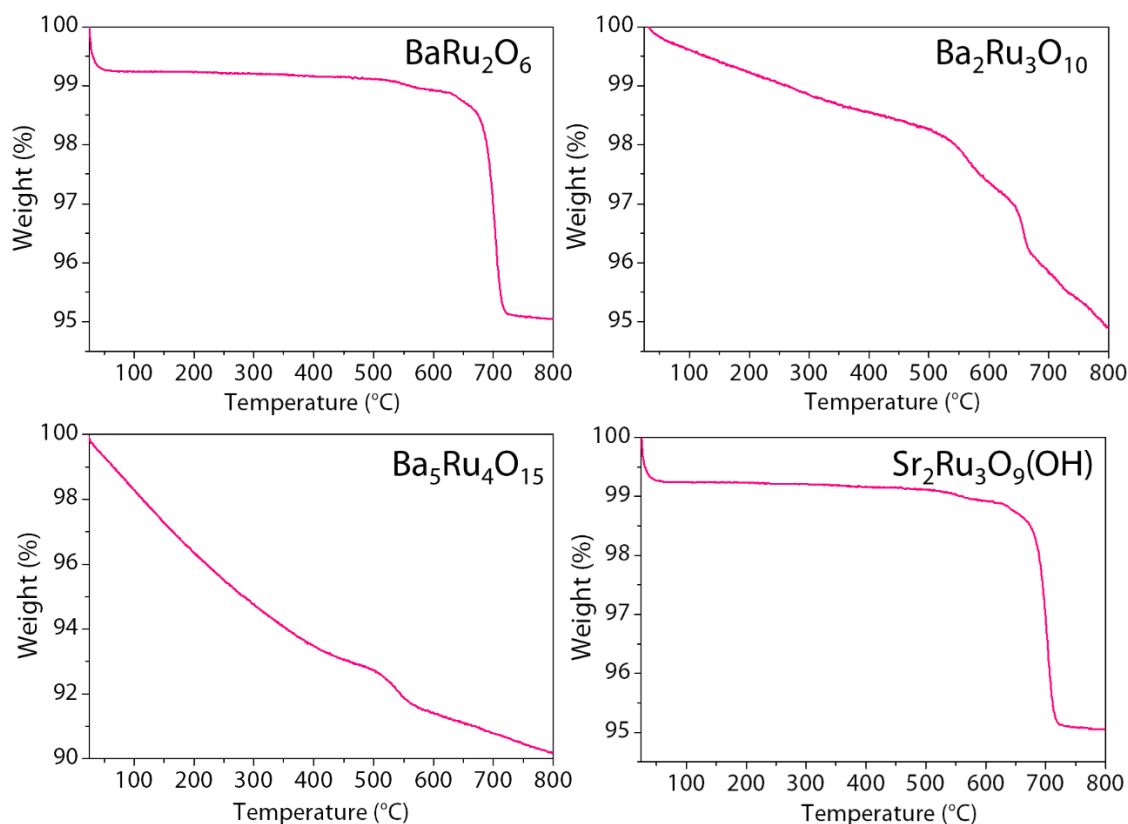
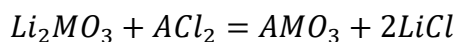


Figure II.6: Thermogravimetric analysis of BaRu_2O_6 , $\text{Ba}_2\text{Ru}_3\text{O}_{10}$, $\text{Ba}_5\text{Ru}_4\text{O}_{15}$ and $\text{Sr}_2\text{Ru}_3\text{O}_9(\text{OH})$ performed under argon with a heating rate of 5°C per minute.

II.1.b Low temperature cations exchange

Recent studies have reported the low temperature synthesis of the AMO_3 compounds (with $\text{A} = \text{Mg}$ or Zn and $\text{M} = \text{Mn}$ or Ir). It consists in exchanging the lithium atoms of the lamellar compounds Li_2MO_3 with divalent cations by the following metathesis reaction^{123,124}:



The thermodynamic driving force of this reaction has to our knowledge not been discussed, although it is clear that the consumption of an equivalent of ACl_2 to form two LiCl entropically favors the reaction. Therefore, inspired by these studies, we attempted to synthesize ZnRuO_3 and MgRuO_3 which could exhibit interesting magnetic properties or possibly be candidates as cathode materials for Zn or Mg-ion based batteries.

Experimentally, these reactions must take place in the complete absence of an oxygen source to avoid the formation of the inert zinc or magnesium oxides. Therefore, the hygroscopic halides (ZnCl_2 , MgCl_2 , etc...) have been bought ultra-dried. The Li_2RuO_3 precursor has been synthesized inspired by already reported procedure:⁷⁶ an appropriate amount of RuO_2 (Alfa Aesar 99.9%) was mixed with a 10% wt excess (to compensate the volatilization at high temperature) of Li_2CO_3 (Sigma Aldrich 99.0 %) with a mortar and pestle and then ball milled (SPEX). The mixture was then transferred to an alumina crucible and heated to 900° for 12 h using a heating and cooling rate of $2^\circ\text{C}\cdot\text{min}^{-1}$. Then, to perform the cation exchange, Li_2RuO_3 as well as the magnesium (zinc) precursor were mixed in an argon-filled glove box before being transferred in a quartz tube and subsequently sealed under high vacuum. The resulting sealed tube was then placed in a box furnace at the required temperature for 60 hrs. After the reaction, the quartz tube was opened in air and the resulting powder was rinsed once with water and a second time with 0.1 M HCl solution with centrifugation steps in between, the washed powders were finally dried in an oven at 110°C for 24 hours.

i) MgRuO_3

The lithium/magnesium exchange was carried out according to the protocol mentioned above using ultra dried MgCl_2 (Alfa Aesar 99.99%) in a molar ratio $\text{Li}_2\text{RuO}_3:\text{MgCl}_2$ of 1:2 and with a heating temperature of 350°C . XRD analysis (cf. next section) suggests the synthesis of a pure compound with minute amounts of crystallized RuO_2 .

ii) ZnRuO_3

Cation exchange was first attempted using the same conditions as for MgRuO_3 ; however, it led to the formation of two phases. Of these, one was identified as the expected layered ZnRuO_3 and the other one could be indexed with a F-centered cubic unit cell ($a = 8.4278(8) \text{ \AA}$) and could refer to a spinel (Zn_2RuO_4 , ZnRu_2O_4 ?). In order to obtain the pure ZnRuO_3 phase, the heating temperature was first varied from 200°C to 450°C in 50°C steps. While no sign of intercalation was observed for syntheses performed below 300°C , the best ZnRuO_3 /"cubic phase" ratio was obtained at 300°C (cf. figure II.7) and any increase in temperature clearly favored the growth of the "cubic phase" at the expense of ZnRuO_3 (cf. figure II.7). Following this first test, different reactions parameters were investigated. Briefly, the Zn/Ru ratio in the reagents was changed (from 1:2 to 10:1), ZnCl_2 was then replaced by ZnBr_2 or ZnI_2 and lastly Na_2RuO_3 has been tried instead of Li_2MnO_3 without much success. At this point, we have not found a way to obtain

pure ZnRuO_3 and the best remaining strategy is probably to understand the nature of the “cubic” phase (XRD, EDX) to determine the physicochemical levers available to obtain the desired phase.

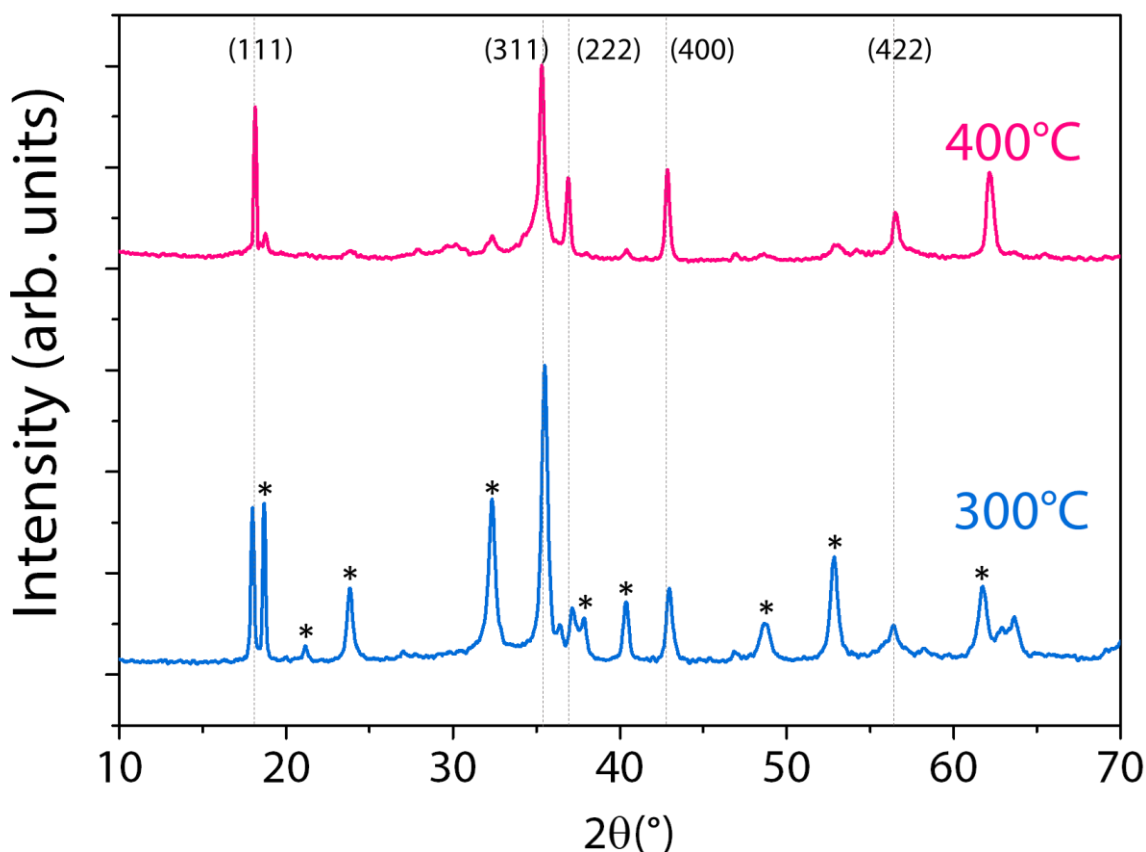


Figure II.7: X-ray diffraction patterns of powders obtained after reaction of Li_2RuO_3 with ZnCl_2 in a 1:2 ratio at 300°C (blue) or 400°C (pink). The pattern at 400°C can be indexed with a F-centered cubic unit cell with $a = 8.4278(8) \text{ \AA}$. The vertical grey dashed lines highlight the positions of reflections from this “cubic phase” with the corresponding indexations; the other reflections observed in the 300°C pattern can be indexed by the expected layered ZnRuO_3 structure and are highlighted by an asterisk.

Now that the various synthetic processes have been described, the next section focuses on describing the structure of the as-synthesized compounds.

II.2 Structural characterisations

II.2.a Elemental analysis

The atomic ratio of Ru/M (where M= Sr/Ba) were determined using energy dispersive X-ray spectrometry (EDX) and are reported in the table II.1. ICP-Ms analysis attempts were done to determine the stoichiometry of the compounds, but the phases described above were found to form RuO₂ after acidic treatment (aqua regia or HCl 37%). RuO₂ is insoluble in acidic media and then the analyses were not convincing.

EDX analysis

Phase	Theoretical Ru/M (M= Ba, Sr)	Experimental Ru/M
Ba ₅ Ru ₄ O ₁₅	0.8	0.9(0.1)
Ba ₂ Ru ₃ O ₁₀	1.5	1.4 (0.1)
BaRu ₂ O ₆	2	1.9 (0.1)
Sr ₂ Ru ₃ O ₉ (OH)	1.5	1.6 (0.1)
Sr ₂ Ru ₃ O ₁₀	1.5	1.7 (0.1)

Table II.1: EDX analysis of different compounds synthesized using hydrothermal process

II.2.a Structural characterisations

In the following section, unless otherwise stated the synchrotron X-ray diffraction measurements (SXRD) were performed on the 11-BM beamline of the Advanced Photon source at Argonne National Laboratory, with a wavelength at 0.413 Å (the exact wavelength for each materials is given with the refinement). Laboratory powder XRD measurements were performed with a Bruker D8 Advance diffractometer as described in the materials and methods section. Finally, single crystal X-ray diffraction (SCXRD) data were collected at the X-ray diffraction platform of IMPMC, on a Rigaku MM007HF diffractometer equipped with a RAXIS4++ image plate detector, a Mo rotating anode ($\lambda = 0.71073$ Å, Varimax multilayer optics) at 293 K (cf. details in the materials and methods).

The crystal structures of 10H-Ba₅Ru₄O₁₅, Sr₂Ru₃O₁₀, Ba₂Ru₃O₁₀, Sr₂Ru₃O₉(OH) and BaRu₂O₆ were determined while the MgRuO₃ one is discussed at the end of the section. For sake of clarity, we will handle each compound separately by first reporting the exact synthesis process of the powders used for carrying the structural determination.

i) *Structure of 10H-Ba₅Ru₄O₁₅*

About 100 mg of pure 10H-Ba₅Ru₄O₁₅ was obtained by mixing K₂RuO₄ with BaO₂ (1:2 molar ratio) with 1 mL of distilled water in a 10 mL silicon carbide vessel, which was subsequently heated to 200°C in three minutes and hold at 200°C for three hours in a microwave oven. To wash the powder, the protocol described in the synthesis part is used. Note that caution has to be taken with acidic conditions, as the material deteriorates within 10 to 20 minutes in 1 M HCl.

The synchrotron powder XRD pattern of the resulting powder is plotted in figure II.8. At a first glance, it is very similar to what was observed by Ogawa et al¹²⁵ for 10H-BaRuO₃ (where H refers to the hexagonal symmetry of underlying close packing of the BaO₃ layers). However, the pattern can be indexed with the *P6₃/mmc* space group and lattice parameters $a = 5.792187(14)$ Å and $c = 23.53579(16)$ Å, which are noticeably different from the unit cell parameters of 10H-BaRuO₃ ($a = 5.756(2)$ Å, $c = 23.727(8)$ Å). Moreover, the Rietveld refinement using the structural model for 10H-BaRuO₃ leads to inappropriate intensities for some reflections. These two observations indicate that our synthesized compound differs from 10H-BaRuO₃. The refinement can indeed be greatly improved by introducing vacancies at the Ru1 site, as shown in figure II.8.a, and is in agreement with the possibility of Ru vacancies that was suggested by Ogawa from single crystal structure investigations.¹²⁵ In our case, the chemical composition, obtained after refinement of the Ru1 occupancy, corresponds to the BaRu_{0.88}O₃ formula (cf. table II.2). However, despite improving the refinement, this model does not take into account the pronounced asymmetry on the main (110) reflection. This indicates the presence of microstructural defects such as stacking faults.

The 10H-BaRuO₃ ideal structure consists of a (*chhch*)₂ stacking of close-packed BaO₃ hexagonal layers along the *c*-direction, where “*h*” and “*c*” stand for the “hexagonal” (i.e. occurring in the *hcp* ...ABAB... structure) and “cubic” (i.e. occurring in the *fcc* ...ABC... structure) layers, respectively. The ruthenium cations occupy interstitial octahedral sites leading to alternate face-sharing Ru₂□O₁₂ (□ - Ru vacancy) trimers and Ru₂O₉ dimers, where face-sharing occurs at the “*h*”-type close-packed layers (cf. figure II.9.a). In our case, the asymmetry of the (001) peak and the clear presence of Ru vacancies on the central octahedron in the Ru₂□O₁₂ trimers encouraged us to explore 10H-BaRu_{0.88}O₃ at a local scale using electron diffraction (ED) patterns, high angle annular dark field scanning transmission electron microscopy (HAADF-STEM) images and atomic resolution energy dispersive X-ray maps.

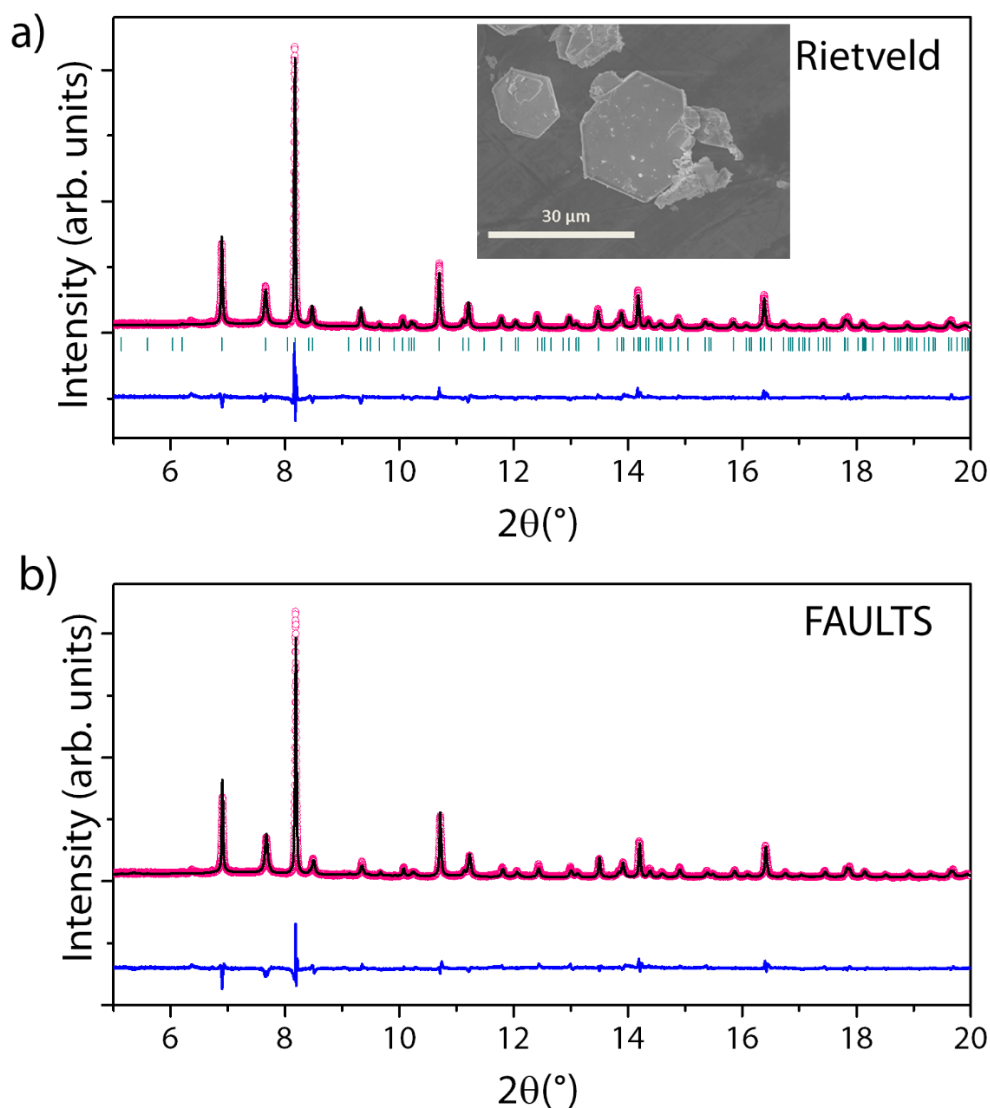


Figure II.8: Refinement of synchrotron X-ray diffraction patterns of $10\text{H-Ba}_5\text{Ru}_4\text{O}_{15}$ ($\lambda = 0.412763 \text{ \AA}$) using a) Rietveld refinement b) the FAULTS program. The pink circles, black continuous line, and bottom blue line represent the observed, calculated, and difference patterns, respectively. Vertical green tick bars stand for the Bragg positions. Insert: SEM picture of $10\text{H-Ba}_5\text{Ru}_4\text{O}_{15}$ crystals.

The $[001]$ ED pattern of $\text{BaRu}_{0.88}\text{O}_3$ (cf. figure II.10) is in good agreement with the close-packed structure of the BaO_3 layers. The $[-120]$ and $[-110]$ ED patterns, showing the $h0l$ and hhl reciprocal lattice rows, demonstrate that the stacking sequence of the BaO_3 layers is faulted. The reflection sequence associated with the 10H structure of $\text{BaRu}_{0.88}\text{O}_3$ with the c parameter of $\sim 23.5 \text{ \AA}$ is present (marked with brackets in figure II.10), but always together with other reflections corresponding to different stacking periodicities.

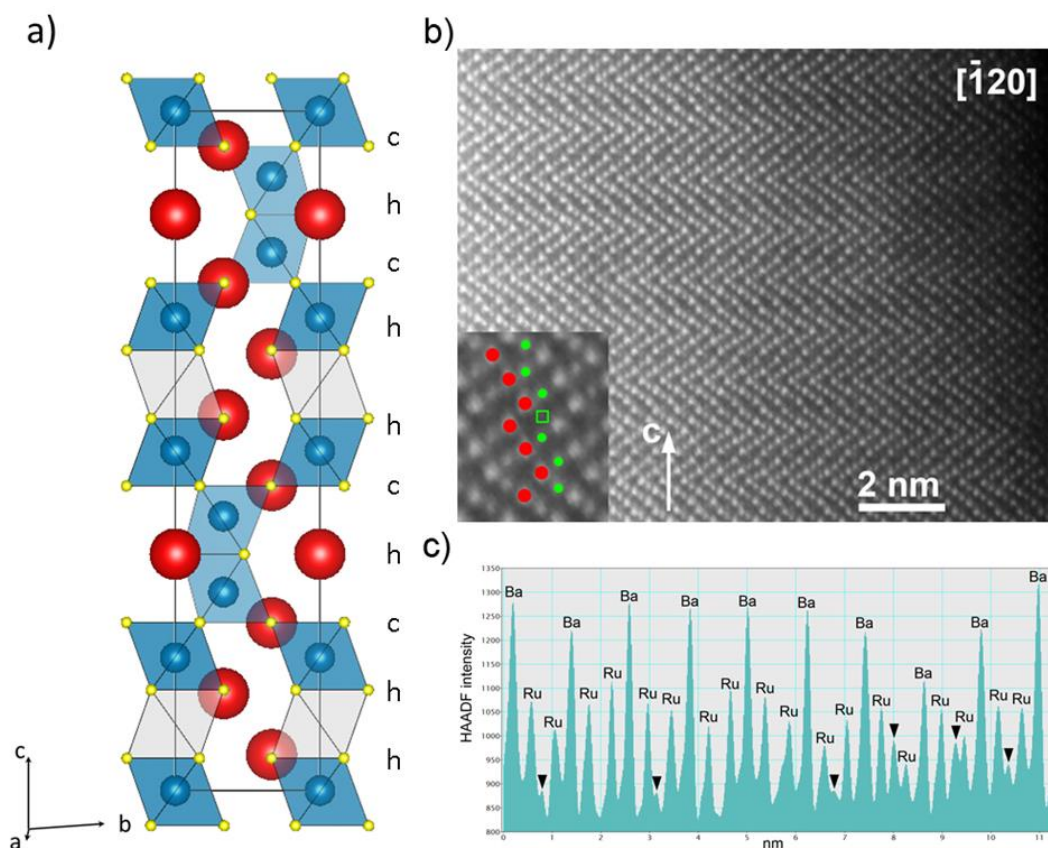


Figure II.9 : a) The structure of $\text{Ba}_5\text{Ru}_4\text{O}_{15}$ viewed along the a direction. Ba atoms are in red and RuO_6 octahedra are in blue with Ru atoms in blue and O atoms in yellow, grey octahedron represents the vacant octahedral sites. Stacking type is given on the right. b) $[-120]$ HAADF-STEM image of the $10\text{H-Ba}_5\text{Ru}_4\text{O}_{15}$ structure showing the assignment of the Ba (red) and Ru (green) atomic columns. The Ru vacancy is denoted with a green square. c) HAADF intensity profile along the $\text{Ru}_2\text{□O}_{12}$ trimers. Note variable intensity at the place of the vacant octahedron (black arrowheads) indicating its random population with Ru cation and vacancy. The Ru cations are randomly shifted from the centers of these octahedral.

HAADF-STEM image of the $10\text{H } (chhch)_2$ stacking sequence clearly demonstrates that the material is Ru-deficient and the Ru vacancies are located in the mid octahedron of the $\text{Ru}_2\text{□O}_{12}$ trimers (cf. figure II.9.b). However, profiling the HAADF intensity along the $\text{Ru}_2\text{□O}_{12}$ trimers shows that the central octahedron is not always vacant and sometimes can be randomly populated with the adjacent Ru cations (cf. figure II.9.c). Interestingly, this Ru cation does not sit at the center of the mid octahedron being shifted towards either the first or the third octahedron of the trimer by $\sim 0.35 \text{ \AA}$. The HAADF-STEM image in figure II.11.b sheds light on the most abundant stacking faults showing thin lamella of the $4\text{H } (ch)_2$ stacking sequence embedded into the $10\text{H } (chhch)_2$ matrix. This lamella in fact corresponds to the 4H-BaRuO_3 structure (has already been reported¹²⁶) forming a coherent intergrowth with the $10\text{H-BaRu}_{0.88}\text{O}_3$ structure. Additionally, the assignment of the atomic columns has been confirmed

with the atomic resolution EDX mapping at the interface between 4H-BaRuO₃ and 10H-Ba₅Ru_{5-x}O₁₅.

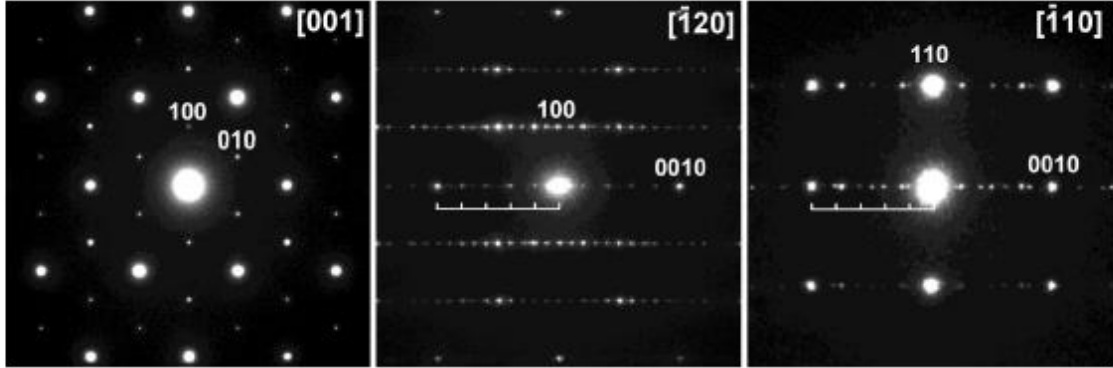


Figure II.10: ED patterns of Ba₅Ru₄O₁₅. The brackets mark reflections from 10H-Ba₅Ru₄O₁₅.

<i>P6₃/mmc</i>		<i>R_{Bragg} = 5.2%</i>		<i>χ² = 3.17</i>		
<i>a = 5.79219(11) Å</i>		<i>c = 23.53580(15) Å</i>		<i>Vol = 683.824 Å³</i>		
<i>Atom</i>	<i>Wyckoff Position</i>	<i>x/a</i>	<i>y/a</i>	<i>z/c</i>	<i>B_{iso} (Å²)</i>	<i>Occupancy</i>
Ru1	2a	0	0	0	0.73 (4)	0.4
Ru2	4e	0	0	0.09782(10)	0.73 (4)	1
Ru3	4f	2/3	1/3	0.69426 (9)	0.73 (4)	1
Ba1	2b	0	0	1/4	1.166(19)	1
Ba2	4f	2/3	1/3	0.14884(8)	1.166(19)	1
Ba3	4f	1/3	2/3	0.04491(7)	1.166(19)	1
O1	6h	0.477(2)	0.954(4)	1/4	0.49(8)	1
O2	12k	0.1688(15)	0.338(3)	0.1495 (3)	0.49(8)	1
O3	12k	0.1666 (17)	0.333(3)	0.5502 (3)	0.49(8)	1

Table II.2: Crystallographic data and atomic positions of Ba₅Ru₄O₁₅ determined from Rietveld refinement of its XRD synchrotron pattern.

To the best of our knowledge, it is the first time that a 10H-Ba₅Ru₄O₁₅ compound is reported, but unfortunately our trials to obtain it without any 4H-BaRuO₃ domains failed, whatever the synthesis conditions we tried. This highlights the ability of such structures to accommodate stacking faults.

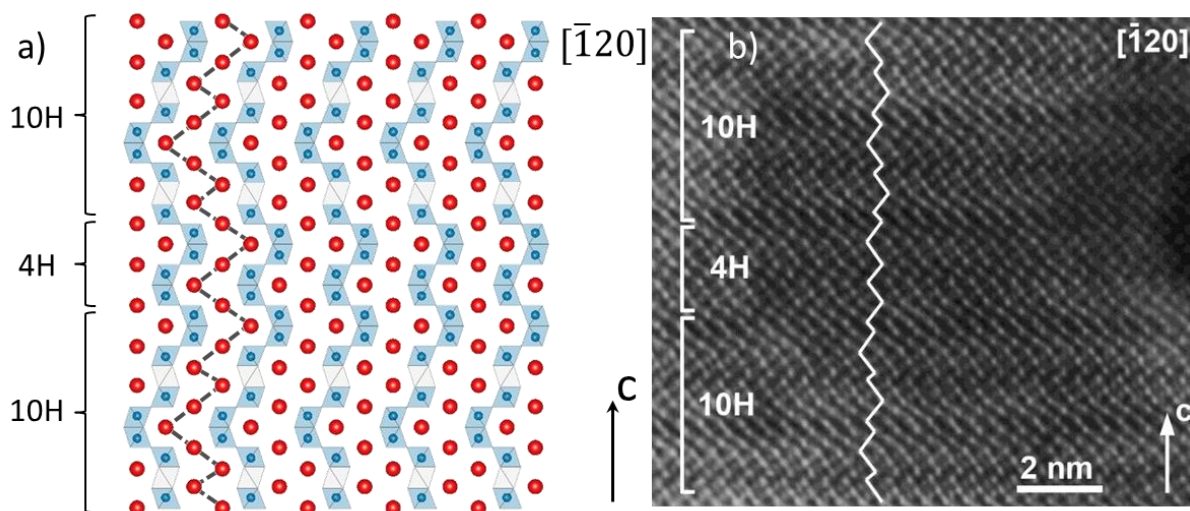


Figure II.11: a) Representation of the stacking faults, in the 10H-Ba₅Ru₄O₁₅ seen from the [-120] direction, Ba atoms are in red and RuO₆ octahedrons are in blue. The black dotted line shows the sequence of BaO₃ layer. b) [-120] HAADF-STEM image showing thin lamella of 4H (ch)₂ stacking in the 10H (chhch)₂. The sequence of the BaO₃ layers is traced with the white zig-zag line, where the kinks stand for the h-type layers.

To complete the structural study on this material and according to the TEM results, the effect of introducing 4H-BaRuO₃ stacking faults on the 10H-Ba₅Ru₄O₁₅ XRD pattern was studied. Using the FAULTS program,¹²⁷ one can indeed create structures built on two different sequences of layers (in our case 10H-Ba₅Ru₄O₁₅ and 4H-BaRuO₃), and one can define between these layers one or several stacking vectors, each one being associated with a stacking probability (P). With this approach, one can simulate a pure 4H-BaRuO₃ structure with stacking probabilities $P_{10H \rightarrow 4H} = 1$ and $P_{4H \rightarrow 10H} = 0$. Identically, a pure 10H-Ba₅Ru₄O₁₅ can be obtained with $P_{10H \rightarrow 4H} = 0$ and $P_{4H \rightarrow 10H} = 1$. In our case, we have considered all possibilities in between with the additional constraint that $P_{10H \rightarrow 10H} = 1 - P_{4H \rightarrow 4H} = P$, that corresponds of having no correlation between two successive layers. XRD patterns were simulated varying P from 1 (which correspond to pure 10H-Ba₅Ru₄O₁₅) to 0 (which correspond to pure 4H-BaRuO₃ layers) and are compared against the experimental XRD pattern on figure II.12.

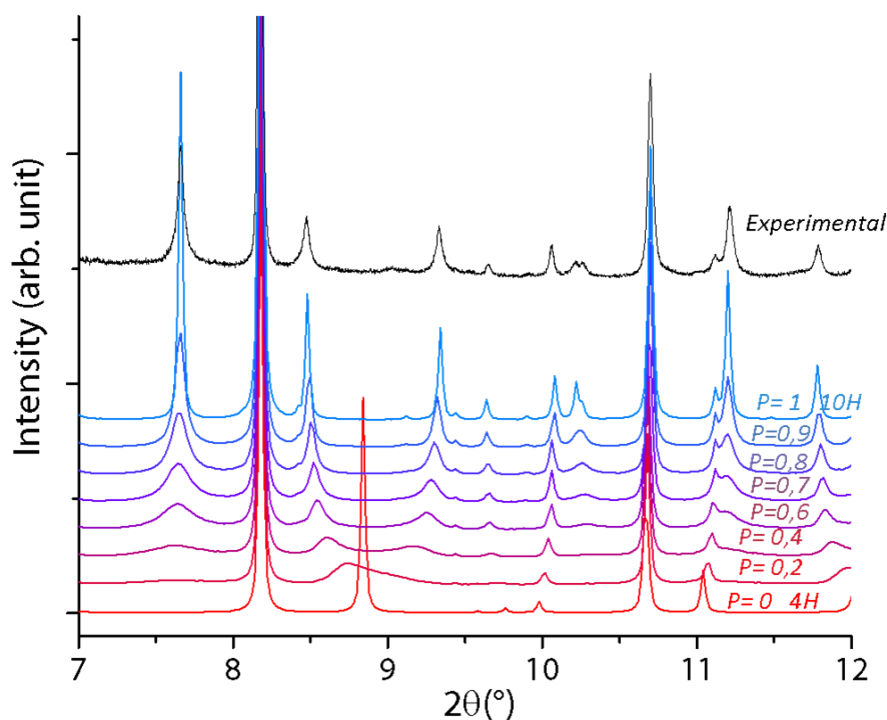


Figure II.12: Comparison between experimental synchrotron XRD pattern (top black line) and simulated XRD patterns of 10H-Ba₅Ru₄O₁₅ with 4H-BaRuO₃ stacking faults, using different 4H to 10H stacking probabilities (P), from pure 4H-BaRuO₃ (P = 0) to pure 10H-Ba₅Ru₄O₁₅ (P = 1).

These simulations show large differences in peak intensities, peak shapes and peak positions, even if P is only slightly modified. Our experimental XRD pattern looks close to the pattern simulated for P = 0.9, and this value was used as a starting point for the refinement of our synchrotron pattern using FAULTS. The results of the refinement is presented in figure II.8 and shows an improvement compared to the Rietveld refinement previously discussed (cf. figure II.8 top); it leads to a stacking probability of 91(2)%, which indicates that the 4H-BaRuO₃ interlayers occupy 9(2)% of the 10H-Ba₅Ru₄O₁₅ structure. This example shows the importance of taking into account stacking faults, especially if the intergrowth layers have a different stoichiometry than the host structure.

Finally this 10H-Ba₅Ru₄O₁₅ compound is different from 10H-BaRuO₃ reported previously.¹²⁵ As previously mentioned, lattice parameters are different (maybe resulting from the different Ru content), and moreover, 10H-Ba₅Ru₄O₁₅ presents Ru in the +V oxidation state while it is Ru(IV) for 10H-BaRuO₃.

ii) *Structure of $Sr_2Ru_3O_{10}$*

$Sr_2Ru_3O_{10}$ phase has been previously obtained impure using high temperature and pressure hydrothermal synthesis (480–650°C, 1800–2100 bars)¹¹⁴ here we report a process to obtain it pure. In a 20 mL Teflon-lined steel autoclave, 200 mg of $KRuO_4$, 207.3 mg of $Sr(NO_3)_2$ (1:1 molar ratio) are mixed in 10 mL of 3M KOH aqueous solution and heated to 200°C in a preheated fan oven for 72 hours. The powder is then washed using the protocol described in the synthesis part. SEM micrographs show the formation of rectangular faceted micrometer-sized platelets (cf. figure II.13).

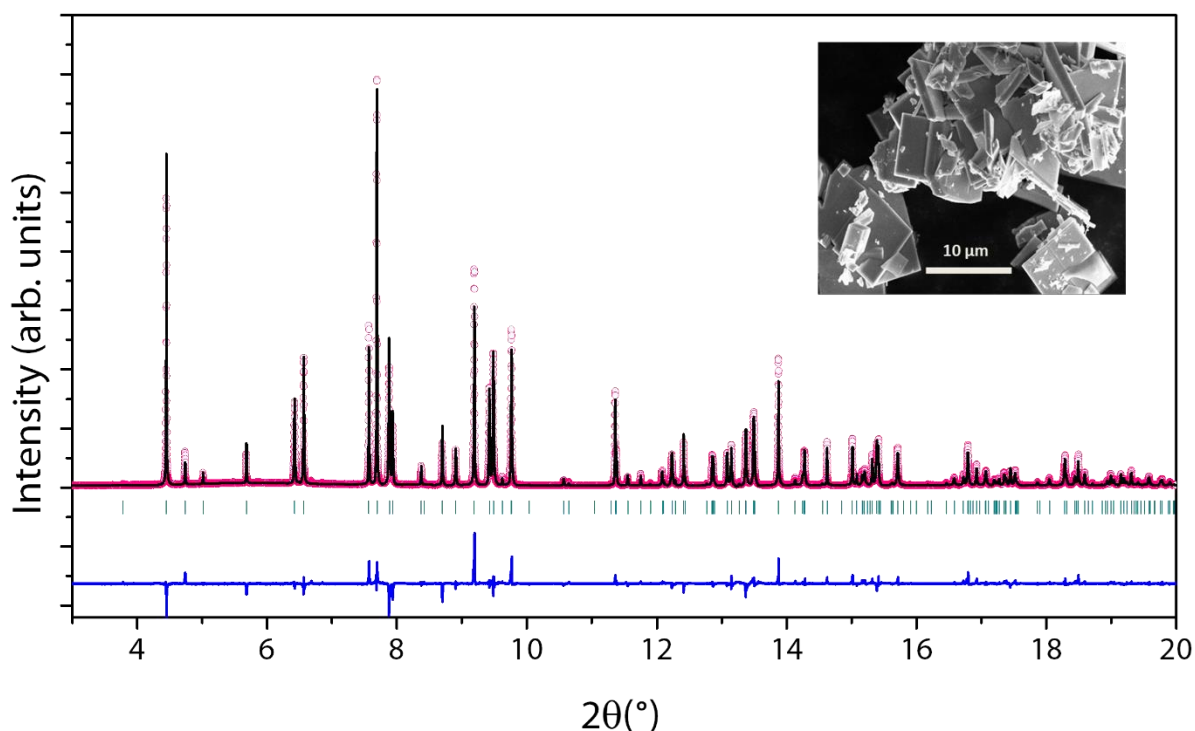


Figure II.13 : Rietveld refinement of synchrotron and neutron diffraction patterns of $Sr_2Ru_3O_{10}$. The pink circles, black continuous line, and bottom blue line represent the observed, calculated, and difference patterns, respectively. Vertical green tick bars stand for the Bragg positions. Insert: SEM picture of $Sr_2Ru_3O_{10}$ crystals.

The synchrotron x-ray pattern was refined using previous work structural model. In this crystal structure represented in Figure II.14 ruthenium atoms are found in two different Wyckoff sites and are octahedrally coordinated by oxygen atoms. Using the notation found in table II.3 $Ru(2)O_6$ octahedra share edges to form chains running along $[010]$, and these chains are connected one to each other by $Ru(1)O_6$ octahedra through corners. This creates Ru layers

stacked along [100]. Strontium atoms are located in the interlayer space and coordinated to nine oxygen atoms.

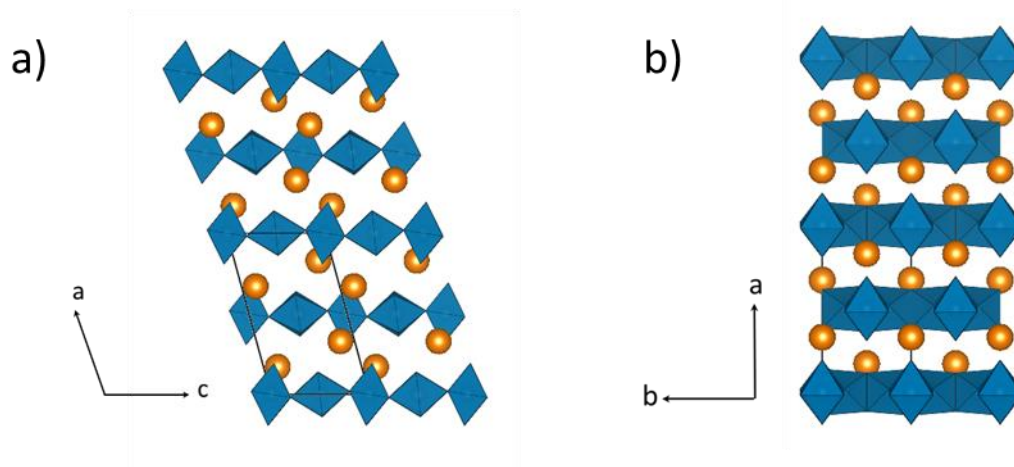


Figure II.14: The structure of $\text{Sr}_2\text{Ru}_3\text{O}_{10}$, Sr atoms are in orange and RuO_6 octahedrons are in blue a) seen from the a direction b) seen from the c direction.

<i>C2/m</i>		$R_{\text{Bragg}} = 5.38\%$		$\chi^2 = 3.88$		
$a = 11.03163(2) \text{ \AA}$	$b = 5.65362(2) \text{ \AA}$	$c = 6.48815(2) \text{ \AA}$		$\beta = 105,4421(2)^\circ$		$\text{Vol} = 390.049 \text{ \AA}^3$
Atom	Wyckoff Position	x/a	y/b	z/c	$B_{\text{iso}} (\text{\AA}^2)$	Occupancy
Ru1	$2a$	0	0	0	0.353(5)	1
Ru2	$4h$	0	0.23237(11)	1/2	0.353(5)	1
Sr1	$4i$	0.67113(5)	0	0.14399(9)	0.125(6)	1
O1	$8j$	0.9782(2)	0.2417(5)	0.1871(4)	0.94(3)	1
O2	$4i$	0.1924(3)	0	0.1176(5)	0.94(3)	1
O3	$4i$	0.3759(4)	0	0.4703(6)	0.94(3)	1
O4	$4i$	0.8624(3)	0	0.4614(6)	0.94(3)	1

Table II.3 : Crystallographic data and atomic positions of $\text{Sr}_2\text{Ru}_3\text{O}_{10}$ determined from Rietveld refinement of its XRD synchrotron pattern.

iii) Structure of $Ba_2Ru_3O_{10}$

Pure $Ba_2Ru_3O_{10}$ powder was obtained by scaling up the process described in the synthesis part. In a 20 mL Teflon-lined steel autoclave, 50 mg of $KRuO_4$, 59.8 mg of $BaCl_2 \cdot 2H_2O$ (1:1 molar ratio) are mixed in 10 mL of 5 M KOH aqueous solution and heated to 200°C in a preheated fan oven for 72 hours. The powder is then washed using the protocol described in the synthesis part. SEM micrographs show the formation of rectangular faceted micrometer-sized platelets (cf. figure II.15).

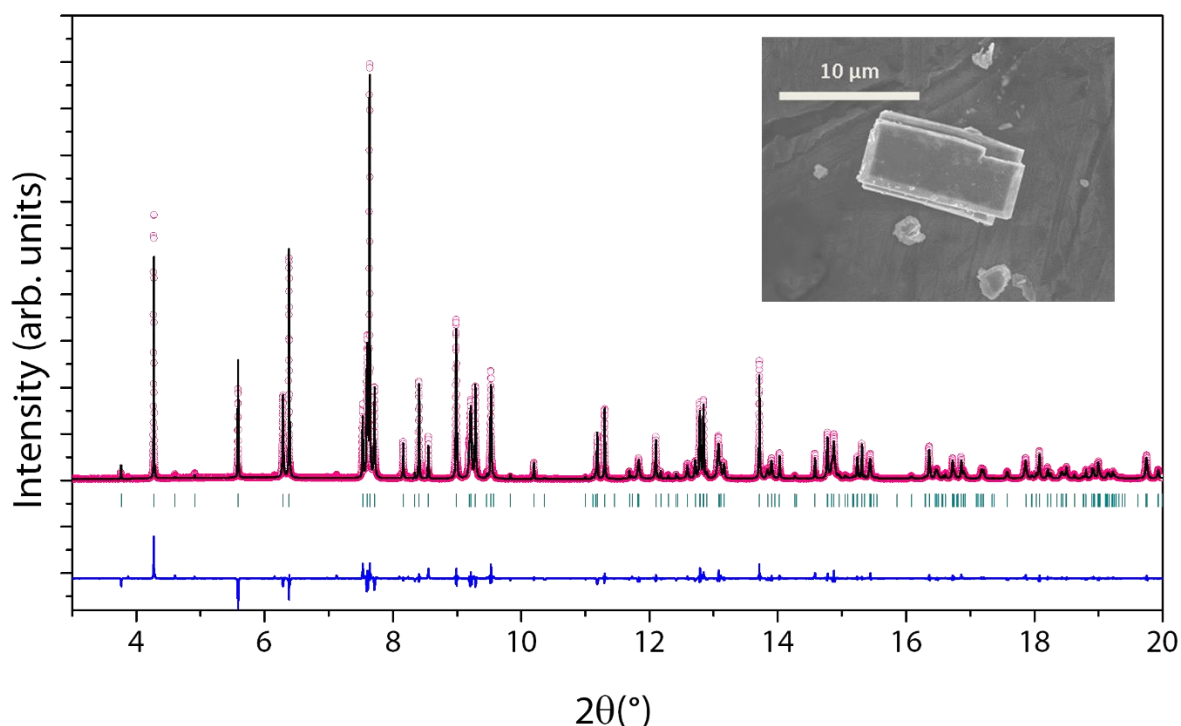


Figure II.15: Rietveld refinement of synchrotron X-ray diffraction patterns of $Ba_2Ru_3O_{10}$ ($\lambda = 0.412763$ Å). The black circles, red continuous line, and bottom blue line represent the observed, calculated, and difference patterns, respectively. Vertical green tick bars are the Bragg positions. Insert: SEM picture of $Ba_2Ru_3O_{10}$ crystals.

The powder X-ray synchrotron diffraction pattern of $Ba_2Ru_3O_{10}$ was indexed using the DICVOL program^{128,129} in a monoclinic unit cell with the following lattice parameters $a = 11.45979$ Å, $b = 5.80123$ Å, $c = 6.50785$ Å, $\beta = 105.44^\circ$ (Vol = 418.005 Å³). These results coupled with the EDX measurements (which indicated Ba/Ru = 2/3 ratio) lead us considering $Sr_2Ru_3O_{10}$ as initial structural model, and replacing Sr with Ba. Positions of all atoms were then refined using the Rietveld method. The refinement showed in figure II.15 presents good

reliability parameters ($\chi^2 = 4.08$ and $R_{\text{Bragg}} = 4.87\%$) and structural parameters are gathered in Table II.4 while the crystal structure is represented in figure II.16.

Bond valence calculations show different redox states for the two crystallographic sites of ruthenium: 5.4 for the $4h$ site (Ru2) and 5.1 for the $2a$ site (Ru1). This leads to an average oxidation state of 5.3^+ , in full agreement with the one expected from the charge neutrality (5.33^+).

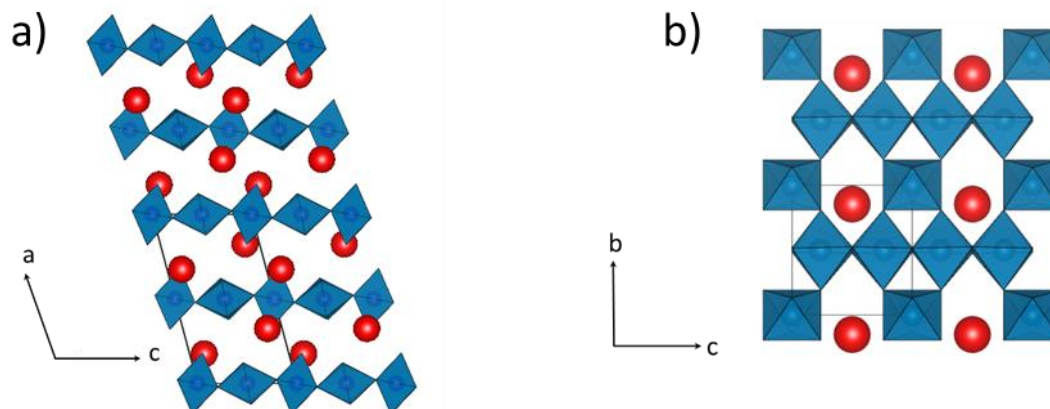


Figure II.16: The structure of $\text{Ba}_2\text{Ru}_3\text{O}_{10}$ Ba atoms are in red and RuO_6 octahedrons are in blue a) seen from the b direction b) seen from the a direction.

$C2/m$		$R_{\text{bragg}} = 4.87\%$			$\chi^2 = 4.08$	
$a = 11.45981(1) \text{ \AA}$	$b = 5.80123(1) \text{ \AA}$	$c = 6.50787(1) \text{ \AA}$		$\beta = 104.9487(1)^\circ$	$\text{Vol} = 418.008 \text{ \AA}^3$	
Atom	Wyckoff Position	x/a	y/b	z/c	$B_{\text{iso}} (\text{\AA}^2)$	Occupancy
Ru1	$2a$	0	0	0	0.109 (11)	1
Ru2	$4h$	0	0.23634(9)	1/2	0.109(11)	1
Ba1	$4i$	0.67499(3)	0	0.14776(5)	0.971(5)	1
O1	$8j$	0.9797(2)	0.2390(4)	0.1930(3)	0.95(3)	1
O2	$4i$	0.1776(3)	0	0.1339(5)	0.95(3)	1
O3	$4i$	0.3937(3)	0	0.4745(5)	0.95(3)	1
O4	$4i$	0.8778(3)	0	0.4833(5)	0.95(3)	1

Table II.4: Crystallographic data and atomic positions of $\text{Ba}_2\text{Ru}_3\text{O}_{10}$ determined from Rietveld refinement of its XRD synchrotron pattern.

iv) *Structure of $Sr_2Ru_3O_9(OH)$*

Around 15 mg of the pure material has been synthesized using the process described in the synthesis part. In a 20 mL Teflon-lined steel autoclave, 15 mg of $KRuO_4$ and 15.6 mg of $Sr(NO_3)_2$ (1:1 molar ratio) are mixed in 5 mL of 0.5 M KOH aqueous solution and heated to 200°C for 72 hours in a preheated chamber furnace. The powder is then washed using the protocol described in the synthesis part. SEM micrographs show the formation of rhombic platelets (inset of figure II.17).

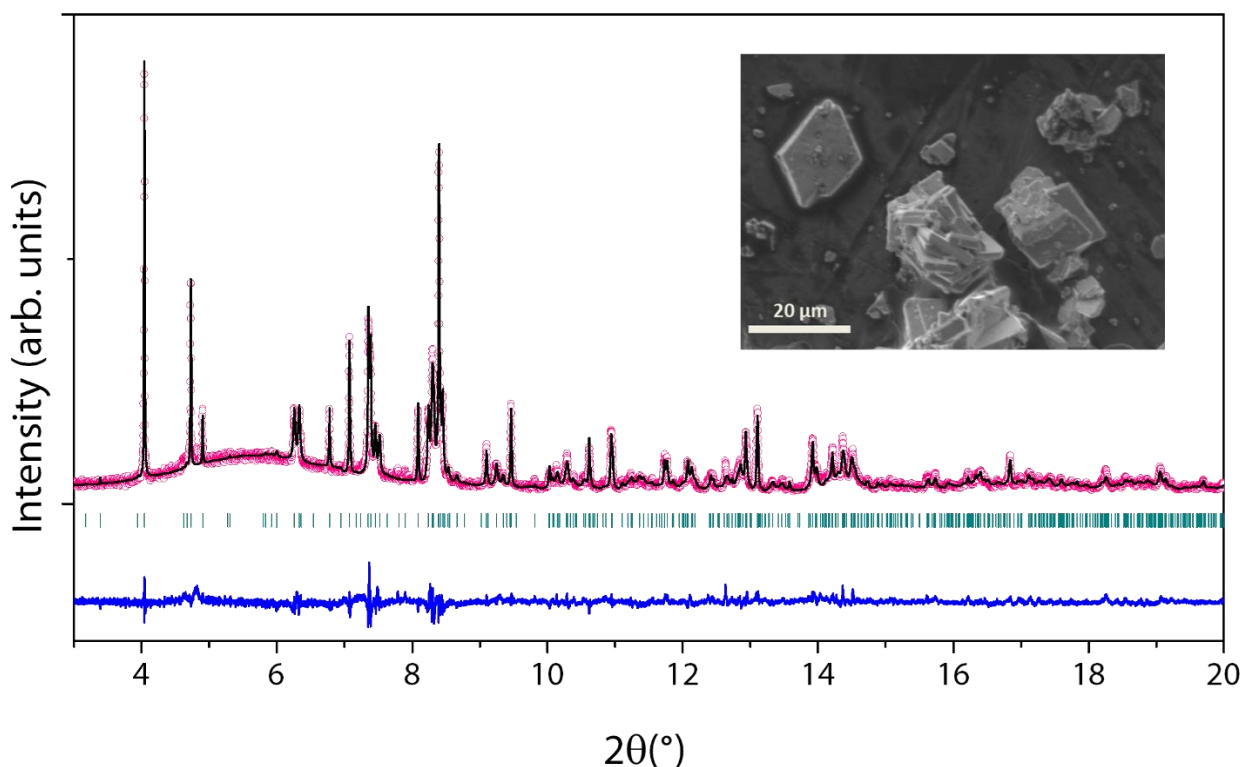


Figure II.17: Rietveld refinement of synchrotron X-ray diffraction patterns of $Sr_2Ru_3O_9(OH)$ ($\lambda = 0.412763 \text{ \AA}$). The black circles, red continuous line, and bottom blue line represent the observed, calculated, and difference patterns, respectively. Vertical green tick bars are the Bragg positions. Insert: SEM picture of $Sr_2Ru_3O_9(OH)$ crystals.

Indexation (using DICVOL program) of the powder X-ray diffraction pattern leads to a monoclinic unit cell with the following lattice parameters $a = 6.98239(6) \text{ \AA}$, $b = 11.70400(10) \text{ \AA}$, $c = 9.65014(7) \text{ \AA}$ and $\beta = 90.7798(11)^\circ$ ($V = 788.55 \text{ \AA}^3$), with possible space group $P2_1/c$ or one of its subgroups. The unit cell and stoichiometry shows strong similarities with $Ba_2Ru_3O_9(OH)$, which was reported to crystallize in the orthorhombic $P2_12_12_1$ space group with lattice parameters $a = 12.1967 \text{ \AA}$, $b = 9.8791 \text{ \AA}$ and $c = 7.0616 \text{ \AA}$ ($V = 850.87 \text{ \AA}^3$)¹¹⁶. This accounts for the smaller ionic radius for Sr compared to Ba. At this stage, two strategies can be

followed: the first one consists in starting from the structural model reported for $\text{Ba}_2\text{Ru}_3\text{O}_9(\text{OH})$ ¹¹⁶, replace Ba with Sr and decrease the symmetry into a monoclinic subgroup. This would indicate that $\text{Sr}_2\text{Ru}_3\text{O}_9(\text{OH})$ crystallizes in the $P2_1$ space group. The second strategy would be to solve the structure from scratch. For this, a single crystal was peaked and the structural model was solved from single crystal diffraction in the $P2_1/c$ space group. Using this structural model, the synchrotron x-ray diffraction pattern was refined using the Rietveld method (Figure II.17). Both structural models, in $P2_1$ or $P2_1/c$, just differ by the hydrogen positions of the hydroxyl groups, which are not accessible from XRD; moreover, the highest symmetry ($P2_1/c$) leads to similar reliability factors, whatever for powder or single crystal refinements. As for $\text{Ba}_2\text{Ru}_3\text{O}_9(\text{OH})$, the structure (cf. figure II.18 and Table II.5) consists in trimers of edge-sharing RuO_6 octahedra linked together by corners and forming corrugated layers stacked along the c -direction. Strontium atoms are in the interlayer. Note that a bond valence sum analysis (BVS) supports our preliminary localization of hydrogen atoms in the structure because the BVS on both O2 and O4 are closer to -1 rather than -2, which does not come as a surprise since O2 and O4 are the only oxygen atoms not being linked to two ruthenium atoms. However, to confirm the space group assignment and obtain accurate proton positions, neutron diffraction would be highly desirable, provided the synthesis can be scaled up.

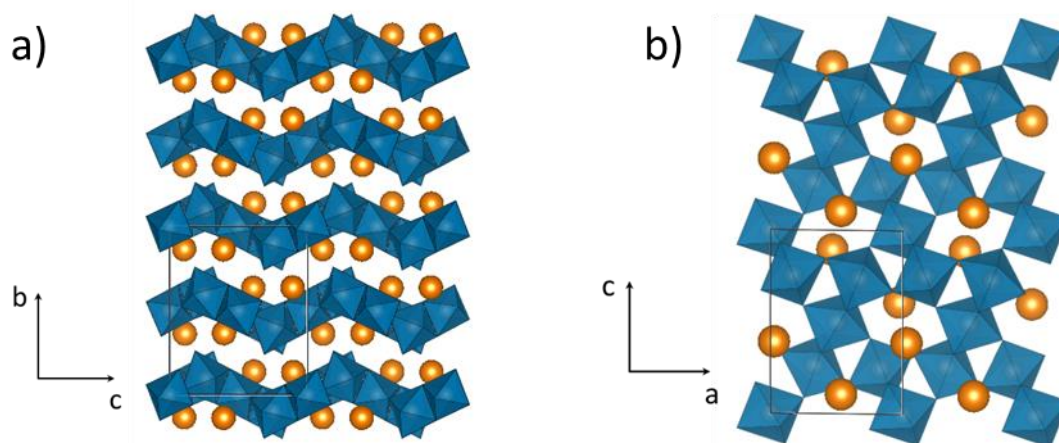


Figure II.18: The structure $\text{Sr}_2\text{Ru}_3\text{O}_9(\text{OH})$, Sr atoms are in orange and RuO_6 octahedrons are in blue a) seen from the a direction b) seen from the b direction.

To conclude, $\text{Sr}_2\text{Ru}_3\text{O}_9(\text{OH})$ presents a small monoclinic distortion compared to the orthorhombic $\text{Ba}_2\text{Ru}_3\text{O}_9(\text{OH})$. This distortion is due to a slight shift in the stacking of RuO_6 layers, which is made possible by less efficient screening of O layers repulsion by the small Sr ions.

$P2_1/c$		$R_{\text{Bragg}} = 6.65\%$		$\chi^2 = 1.68$		
$a = 6.98239 (6) \text{ \AA}$		$b = 11.70400 (10) \text{ \AA}$		$c = 9.65014 (7) \text{ \AA}$		$\beta = 90.7798(11)^\circ$
				$\text{Vol} = 788.552 \text{ \AA}^3$		
Atom	Wyckoff Position	x/a	y/b	z/c	$B_{\text{iso}} (\text{\AA}^2)$	Occupancy
Sr1	4e	0.9747(6)	0.3642(5)	0.1113(6)	3.62(7)	1
Sr2	4e	0.4709(6)	0.1355(5)	0.8953(5)	3.62(7)	1
Ru1	4e	0.1713(6)	0.5971(3)	0.2527(5)	0.873(18)	1
Ru2	4e	0.3231(6)	0.4061(3)	0.7604(5)	0.873(18)	1
Ru3	2a	0	1/2	1/2	0.873(18)	1
Ru4	2d	1/2	1/2	0	0.873(18)	1
O1	4e	0.961(3)	0.6284(16)	0.134(2)	0.021(14)	1
O2	4e	0.423(3)	0.2382(15)	0.7011(19)	0.021(14)	1
O3	4e	0.747(3)	0.5450(17)	0.403(2)	0.021(14)	1
O4	4e	0.241(3)	0.7495(18)	0.1429(19)	0.021(14)	1
O5	4e	0.187(3)	0.4438(18)	0.329(2)	0.021(14)	1
O6	4e	0.338(3)	0.5644(18)	0.826(2)	0.021(14)	1
O7	4e	0.417(3)	0.3382(18)	0.938(2)	0.021(14)	1
O8	4e	0.903(3)	0.3355(19)	0.560(2)	0.021(14)	1
O9	4e	0.242(3)	0.5163(19)	0.097(2)	0.021(14)	1
O10	4e	0.428(3)	0.5891(17)	0.344(2)	0.021(14)	1

Table II.5: Crystallographic data and atomic positions of $\text{Sr}_2\text{Ru}_3\text{O}_9(\text{OH})$ determined from Rietveld refinement of its XRD synchrotron pattern.

v) Structure of $BaRu_2O_6$

The synthesis of pure $BaRu_2O_6$ has been carried modifying slightly the hydrothermal protocol reported in the synthesis section. Indeed, about 100 mg of this compound was obtained by mixing $KRuO_4$ with BaO_2 (2:1 molar ratio) with 1 mL of distilled water in a 10 mL silicon carbide vessel, which was subsequently heated to 200°C in three minutes and hold at 200°C for three hours in a microwave oven. The obtained powder is then washed using the protocol described in the synthesis part.

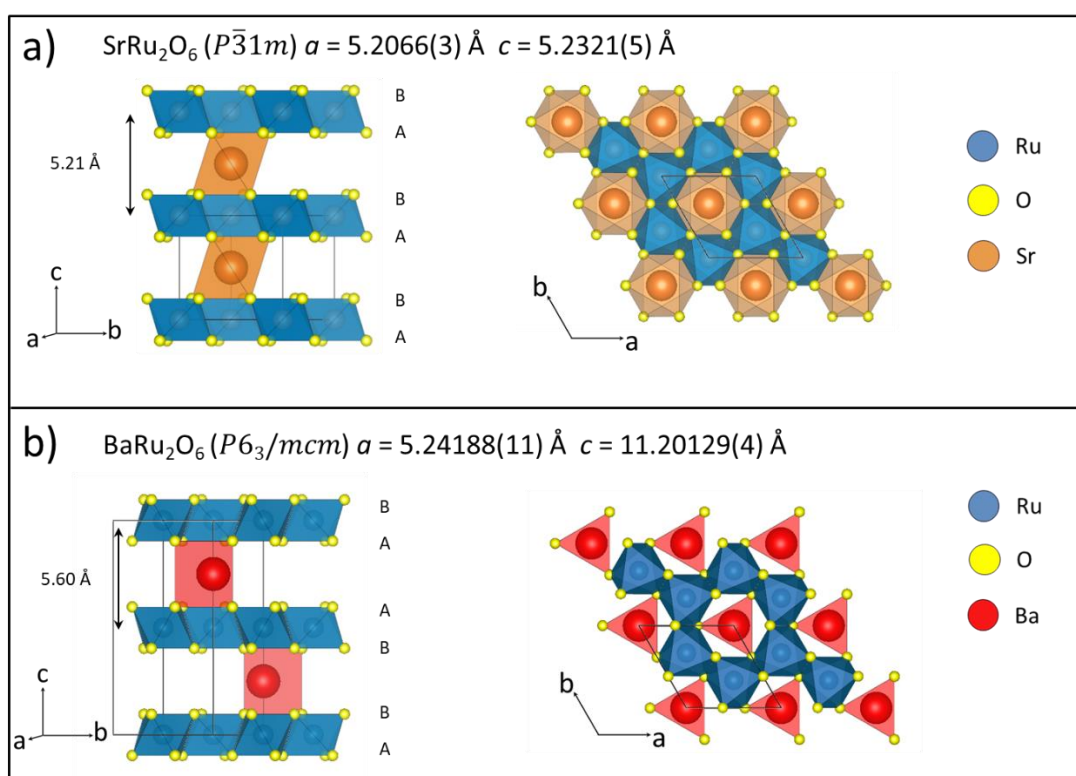


Figure II.19: Structures of $SrRu_2O_6$ (a) and $BaRu_2O_6$ (b). The letters next to the oxygen layers represent the stacking sequence: ABAB for O1 ($SrRu_2O_6$) and ABBA for P2 ($BaRu_2O_6$). Barium, ruthenium and oxygen atoms are coloured in red, blue and yellow, respectively.

The structural analysis of $BaRu_2O_6$ was first carried out by synchrotron X-ray diffraction (SXR) done either on the 11-BM line of Argonne national laboratory or on the MSPD line of the Alba (Barcelona, Spain) synchrotron. Refining the SXR pattern using a structural model alike for $SrRu_2O_6$ (Figure II.19.a) (O1 type structure, $P\bar{3}1m$ space group) and replacing Sr^{2+} by larger Ba^{2+} cation leads to a decent fit ($a = 5.24188(11) \text{ \AA}$ and $c = 5.60065(2) \text{ \AA}$) which at first could suggest that $BaRu_2O_6$ and $SrRu_2O_6$ are isostructural (Figure II.20.a). The quality of the fit is however far to be perfect since several peaks with limited intensities remain unindexed

(marked with stars in inset of Figure II.20.a). This mismatch between the calculated and experimental patterns is heightened in the neutron powder diffraction data (recorded on the D2B diffractometer at ILL). Figure II.20b reveals that using a O1 structural model similar to SrRu_2O_6 to fit the neutron diffraction pattern is not suitable, as the tiny non-indexed peaks observed on the SXRD pattern have non-negligible neutron intensities. These additional peaks can be fully indexed by doubling the c lattice parameter to obtain $a = 5.24188(11) \text{ \AA}$, $c = 11.20129(4) \text{ \AA}$. This doubling was confirmed by electron diffraction (cf. figure II.21) for which the reflection condition $h0l$, $l = 2n$ suggests $P6_3/mcm$ as the most symmetric space group with the feasibility of $P-6c2$, $P6_3cm$, $P-3c1$, $P3c1$ as possible subgroups.

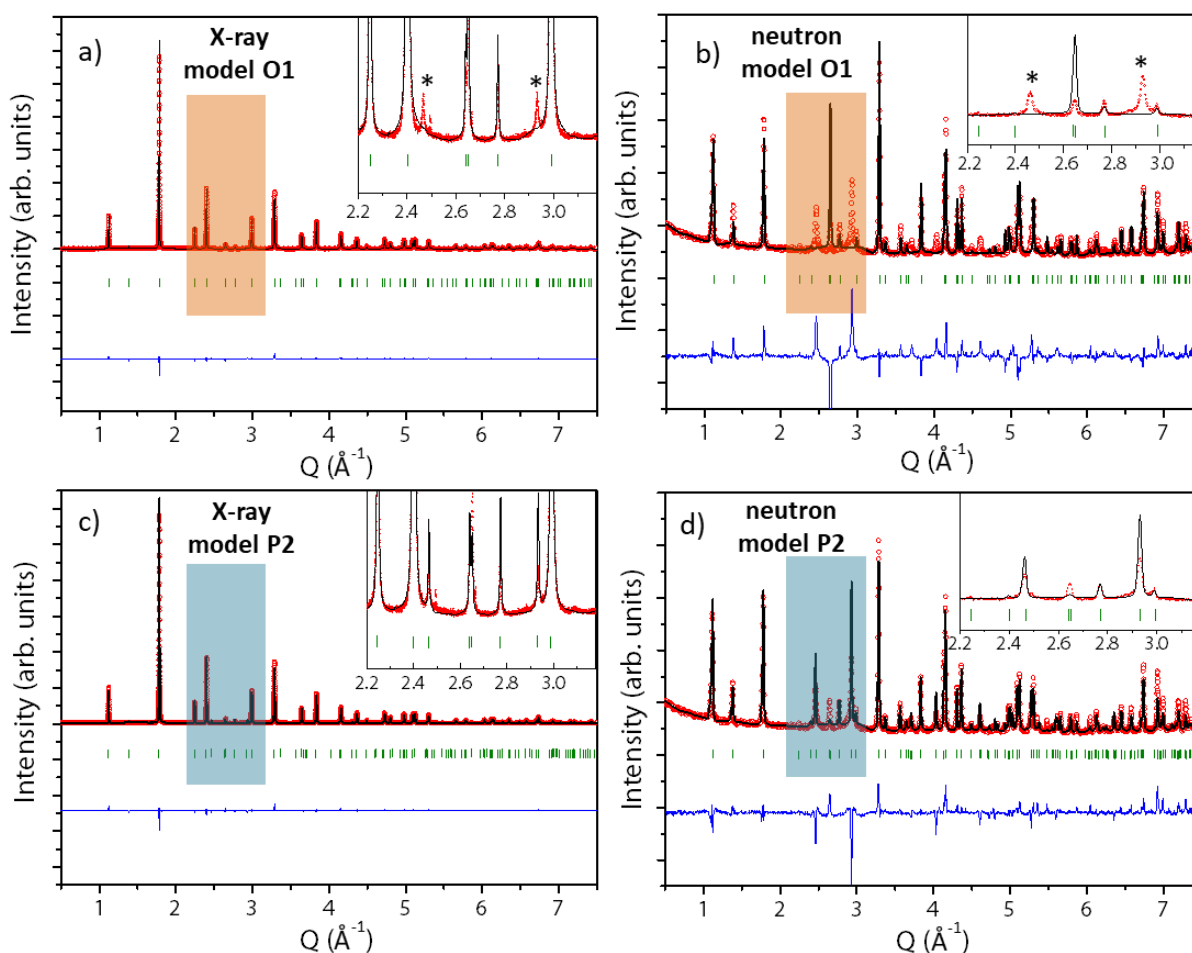


Figure II.20: Rietveld refinement of BaRu_2O_6 synchrotron X-ray ($\lambda = 0.4128 \text{ \AA}$) and neutron diffraction patterns ($\lambda = 1.5940 \text{ \AA}$), using the O1 type structural model (a, b) or the P2 type structural model with a doubled cell (c, d). The red circles, black continuous line, and bottom blue line represent the observed, calculated, and difference patterns, respectively. Vertical green tick bars are the Bragg positions. The inset in each picture refers to a zoom of the coloured areas. Stars in the (a) and (b) panels refer to the peaks non indexed with the O1 structural model but indexed with the P2 one.

In light of such difference between the X-ray and neutron refinements, we hypothesized Ru and Ba atoms to be correctly placed in the O1 model deduced by XRD while the oxygen sublattice, almost transparent to XRD in presence of Ba and Ru, needs to be modified in order to account for neutron intensities. A structural model was thus built using the doubled cell with Ba and Ru positioned as in SrRu_2O_6 , in agreement with the HAADF-STEM images (cf. figure II.21 d and e), and the oxygen atomic positions deduced from a simulated annealing optimization procedure. A reasonable fit (cf. figure II.20.c and d) was achieved in the $P6_3/mcm$ space group, by placing Ba in $2a$, Ru in $4d$ and O in $12k$ Wyckoff sites. The obtained structural model is shown in Figure II.19.b.

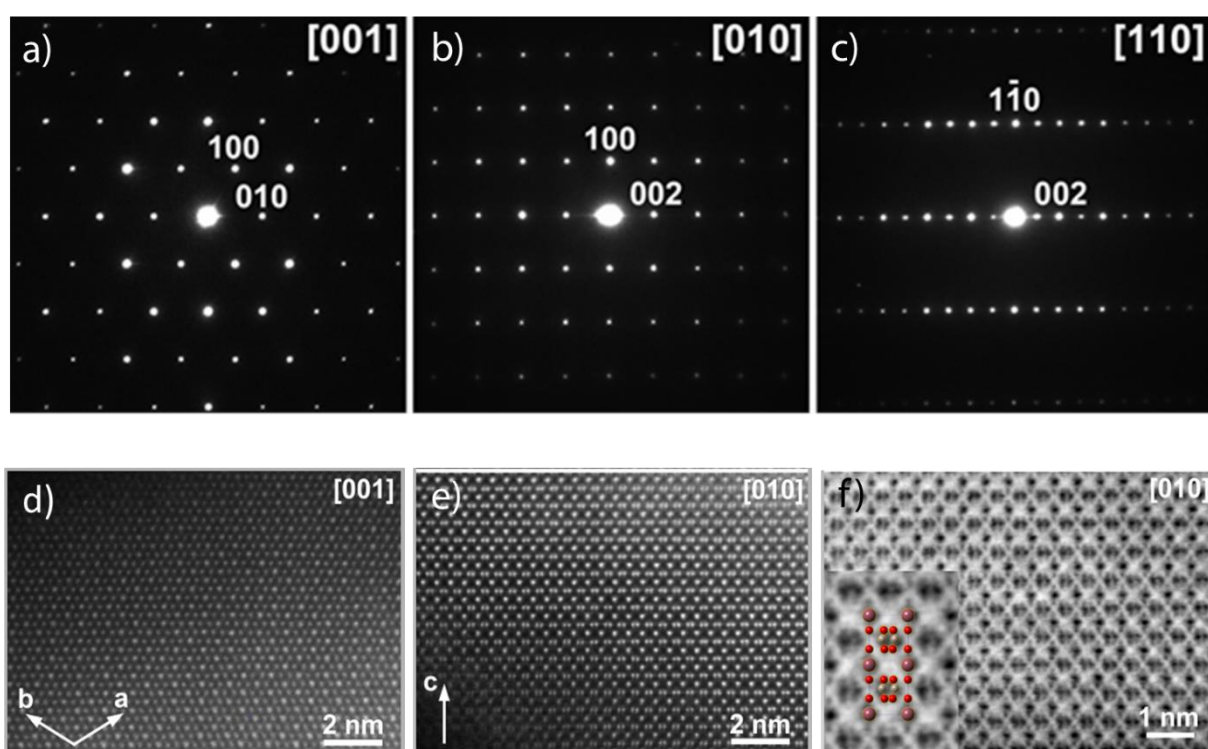


Figure II.21: (a-c) Electron diffraction (ED) patterns of BaRu_2O_6 . The ED patterns can be indexed with a hexagonal unit cell with $a \approx 5.2 \text{ \AA}$, $c \approx 11.2 \text{ \AA}$. The reflection condition $h0l$, $l = 2n$ corroborates $P6_3/mcm$, $P-6c2$, $P6_3cm$, $P-3c1$, $P3c1$ as possible space groups. HAADF -STEM images of BaRu_2O_6 along $[001]$ (d) and $[010]$ (e) directions; (f) $[010]$ ABF-STEM image of BaRu_2O_6 . The insert shows the enlarged image with the projected crystal structure overlaid (Ru – yellow, Ba – brown, O – red).

Alike SrRu_2O_6 , it consists of “honeycomb” layers of edge sharing RuO_6 octahedra stacked along the c axis with barium in the interlayer space. However, this model differs from SrRu_2O_6 in the oxygen positions that lead to a trigonal prismatic site for Ba (against octahedral coordination for Sr). BaRu_2O_6 therefore adopts a P2-type structure. Note that the NPD pattern refinement could be further improved by considering besides the oxygen position found by simulated annealing, an additional oxygen position partially occupied (labelled O2 in Table II.6 and in

Figure II.22.b). The final combined X-ray/neutron diffraction refinement is shown in Figure II.22.a with crystallographic parameters reported in Table II.6. The O1 oxygen position corresponds to the trigonal prismatic coordination for Ba, and results in the P2 stacking mentioned above, while O2 corresponds to an octahedral coordination and corresponds to the O1-type structure described in a doubled cell. This result suggests a possible intergrowth of two BaRu₂O₆ polymorphs: one crystallizing in the O1 structure (O1-BaRu₂O₆) and the other in the P2 structure (P2-BaRu₂O₆).

BaRu ₂ O ₆		P6 ₃ /mcm		R _{Bragg} = 7.66 %	χ ² = 4.51		
a = 5.24188(1) Å		c = 11.20129(4) Å				Vol = 265.355(7) Å ³	
Atom	Wyckoff Position	x/a	y/b	z/c	B _{iso} (Å ²)	Occupancy	
Ba	2a	0	0	1/4	1.211(12)	1	
Ru	4d	1/3	2/3	0	0.022(6)	1	
O1	12k	0.3851(4)	0.3851(4)	0.5936(2)	1.22(7)	0.823(3)	
O2	12k	0.3748(18)	0.3748(18)	0.0891(11)	1.22(7)	0.177(3)	

Table II.6: Crystallographic data and atomic positions of BaRu₂O₆ determined from combined Rietveld refinement of its synchrotron X-ray and neutron diffraction patterns.

To check this hypothesis, the patterns of structures with P2-BaRu₂O₆ and O1-BaRu₂O₆ as building layers were simulated using the FAULTS program.¹²⁷ This software allows to describe structures as a stack of layers by defining as input the structure of the different layers, the stacking vectors between these layers and the probabilities for these stacking to occur. Thus we built two blocks, one corresponding to a O1 type layer and the other to a P2 type layer with the following stacking vectors : $\mathbf{V}_{O1 \rightarrow O1} = (0 \ 0 \ 0.5)$; $\mathbf{V}_{O1 \rightarrow P2} = (0 \ 0 \ 0.5)$; $\mathbf{V}_{P2 \rightarrow O1} = (0 \ 0 \ 1)$; $\mathbf{V}_{P2 \rightarrow P2} = (0 \ 0 \ 1)$. For each stacking vectors, a stacking probability is associated with $P_{i \rightarrow j}$ being the probability to stack a layer j on a layer i. Obviously these four probabilities can be reduced into two as $P_{P2 \rightarrow P2} + P_{P2 \rightarrow O1} = 1$ and $P_{O1 \rightarrow O1} + P_{O1 \rightarrow P2} = 1$. Both the vectors and the probabilities can then be adjusted or refined.

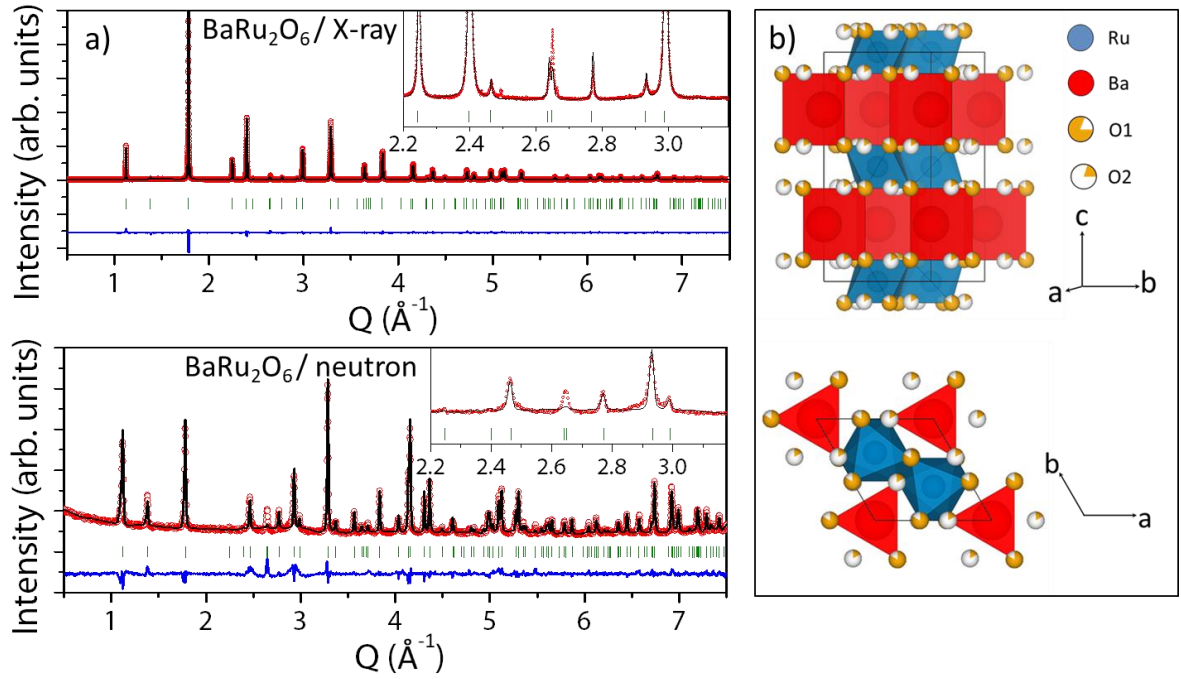


Figure II.22: a) Combined XRD/neutrons Rietveld refinement of BaRu_2O_6 corresponding of the structural model in Table II.6. Wavelengths for synchrotron X-ray and neutrons are $\lambda = 0.4128 \text{ \AA}$ and $\lambda = 1.5940 \text{ \AA}$, respectively. The red circles, black continuous line, and bottom blue line represent the observed, calculated, and difference patterns, respectively. Vertical green tick bars stand for the Bragg positions. b) Structure of BaRu_2O_6 . Barium, ruthenium and oxygen atoms are coloured in red, blue and yellow, respectively, and vacancies on oxygen sites are represented in white. The yellow-white colour proportion corresponds to the site's occupancies.

The comparison between experimental and simulated neutron pattern with different O1 vs P2-type layer proportion (P_{O1}) is represented in Figure II.23.b. These simulations confirm that the introduction of O1 type layers in the P2 structure is pertinent for reproducing the experimental neutron diffraction pattern. The FAULTS refinement of both neutron and X-ray diffraction patterns (cf. figure II.24) indeed shows an improvement compared to the previous model, especially to fit the peaks in the $2.2\text{-}3.2 \text{ \AA}^{-1}$ region, confirming our hypothesis (cf. figure II.23.c). Moreover, the refined stacking probabilities allow calculating the proportion P_{O1} and P_{P2} of the two layers types in the crystallites¹²⁷.

$$P_{O1} = \frac{1 - p_{P2 \rightarrow P2}}{(2 - p_{O1 \rightarrow O1} - p_{P2 \rightarrow P2})}$$

and

$$P_{P2} = \frac{1 - p_{O1 \rightarrow O1}}{(2 - p_{O1 \rightarrow O1} - p_{P2 \rightarrow P2})}$$

This indicates that around 25% of the barium atoms are in octahedral sites (cf. Table II.7). This proportion is consistent with the structural model used for Table II.6, where 18 % of the oxygen are found in the O2 sites that correspond to the octahedral coordination of the barium.

Interestingly, electron diffraction of BaRu_2O_6 powders does not show reflection broadening nor diffuse intensity along the c^* axis which could correspond to a high concentration of stacking faults. The STEM images do not indicate any noticeable variation in the interlayer distances. This is in agreement with X-ray and neutron diffraction for which no noticeable anisotropic peak broadening was observed. This indicates the closeness of the interlayer distances for the O1 and P2 stackings in BaRu_2O_6 . This feature is unique since intergrowth of O-type and P-type layers are known to lead to substantial variations of the interlayer distance, as for example in Na-based layered oxides.¹³⁰

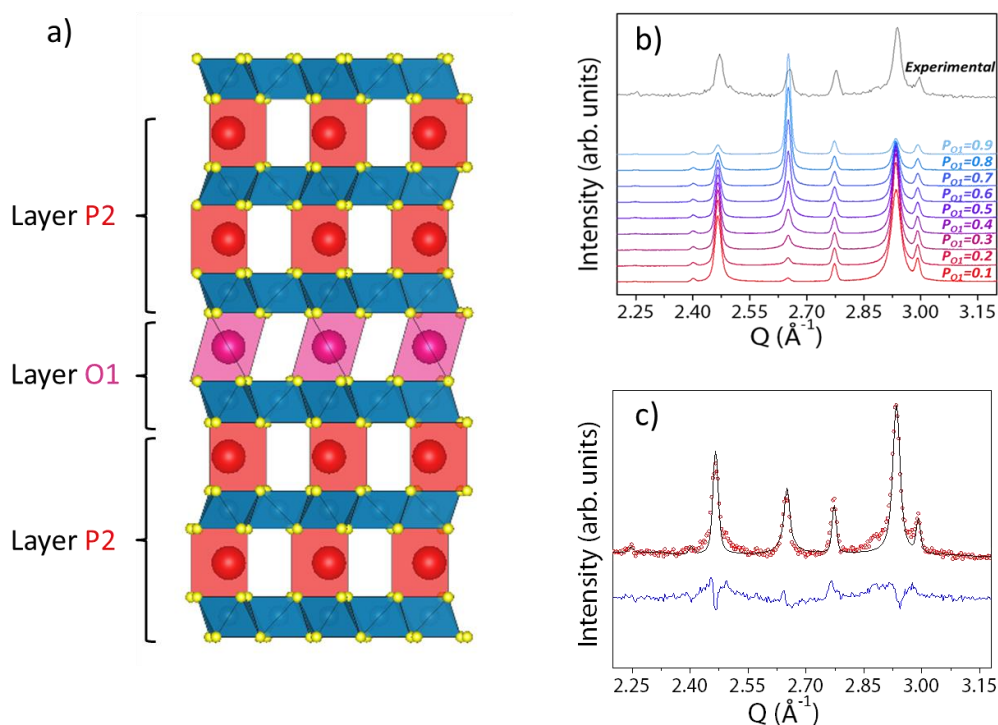


Figure II.23: a) Representation of stacking along the c direction of O1 and P2 layers for BaRu_2O_6 . b) Comparison of the experimental neutron diffraction pattern (on top in gray) and simulated patterns varying the proportion of O1 layer (P_{O1}). c) FAULTS refinement of the neutron diffraction pattern of BaRu_2O_6 ($\lambda = 1.5940 \text{ \AA}$), focused on the $2.2\text{-}3.2 \text{ \AA}^{-1}$ area. The red circles, black continuous line, and bottom blue line represent the observed, calculated, and difference patterns, respectively.

Lastly, another interesting aspect of BaRu_2O_6 is the coexistence of two barium coordination sites (octahedral and trigonal prismatic) while Sr^{2+} in SrRu_2O_6 occupies exclusively octahedral sites. The larger size of Ba^{2+} (1.38 \AA) as compared to Sr^{2+} (1.18 \AA) could account for such a difference. DFT calculations were conducted to check this possibility. Two sets of structures

were considered with the cation being either in an octahedral or in a prismatic coordination, and the structures were relaxed to obtain their energy per unit cell. We found that for the strontium counterpart, the octahedral site is stabilized against the prismatic site by 13 meV/unit cell, whereas the energy of the octahedral stacking for BaRu₂O₆ is solely 5 meV/unit cell higher than the energy of the prismatic one. Such a small difference most likely explains the formation of O1-P2 intergrowth in BaRu₂O₆ and our encountered difficulty in preparing this phase free of intergrowth whatever the synthesis conditions we have tried. Attempts to follow the structural evolution of this phase as function of temperature did not provide any clues regarding the kinetics of the intergrowth process, but solely a decomposition of the material starting at 400°C.

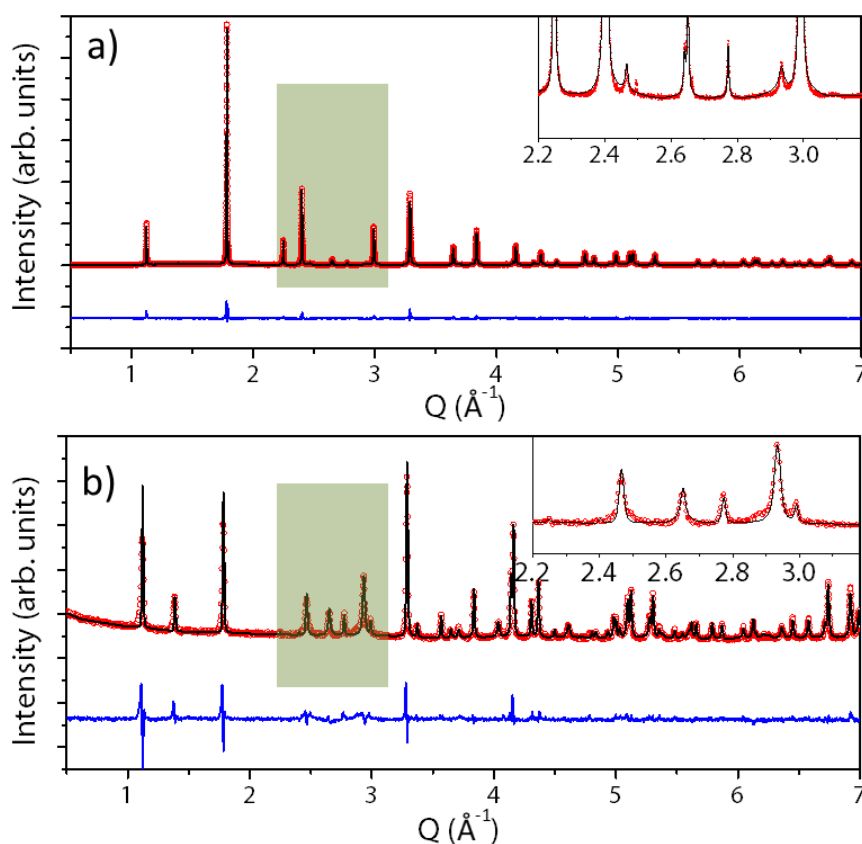


Figure II.24: FAULTS refinement of the (a) synchrotron X-ray diffraction pattern ($\lambda = 0.4128 \text{ \AA}$), (b) neutron diffraction pattern ($\lambda = 1.5940 \text{ \AA}$) of BaRu₂O₆. The red circles, black continuous line, and bottom blue line represent the observed, calculated, and difference patterns, respectively. The insets refer to a zoom of the green areas.

Parameter	a	b	c	α	β	γ
Refined value	5.23420(1) \AA	5.23420(1) \AA	11.09905(1) \AA	90°	90°	120°
Parameter	$p_{O1 \rightarrow O1}$	$p_{O1 \rightarrow P2}$	$p_{P2 \rightarrow O1}$	$p_{P2 \rightarrow P2}$	R_f	χ^2
Refined value	0.86038(1)	0.13962(1)	0.10524(1)	0.89476(1)	5.61454 %	7.5156

Table II.7: Structural parameters refined with FAULTS program

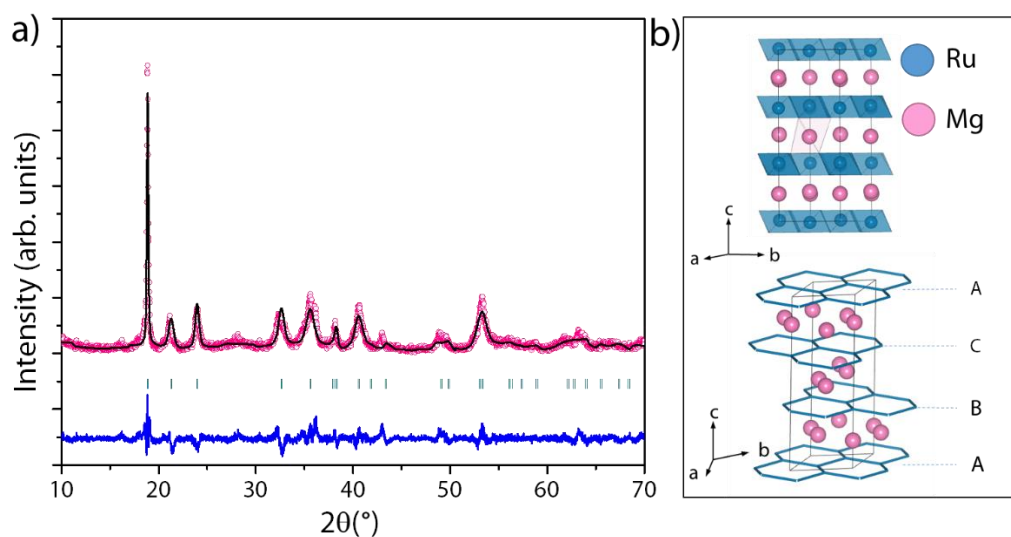
vi) Structure of MgRuO_3 

Figure II.25: a) XRD Rietveld refinement of MgRuO_3 corresponding of the structural model in Table II.8. ($\lambda_1 = 1.540562 \text{ \AA}$ and $\lambda_2 = 1.544390 \text{ \AA}$) The pink circles, black continuous line, and bottom blue line represent the observed, calculated, and difference patterns, respectively. Vertical green tick bars stand for the Bragg positions. b) Structure of MgRuO_3 . Magnesium and ruthenium are coloured in pink and blue, the RuO_6 octaedron are represented in blue.

MgRuO_3		$R\bar{3}$	$R_{\text{Bragg}} = 8.95 \%$	$\chi^2 = 2.65$		
$a = 5.0471(6) \text{ \AA}$		$c = 14.1303(23) \text{ \AA}$		$\text{Vol} = 311.72(7) \text{ \AA}^3$		
Atom	Wyckoff Position	x/a	y/a	z/c	$B_{\text{iso}} (\text{\AA}^2)$	Occupancy
Ru	6c	0	0	0.3413(5)	2.8(3)	1
Mg	6c	0	0	0.165(3)	6.0(9)	1
O	18f	0.3702(2)	0.0281(2)	0.2695(2)	3.0(10)	1

Table II.8: Crystallographic data and atomic positions of MgRuO_3 determined from Rietveld refinement of its X-ray diffraction pattern.

Refinement of the X-ray diffraction pattern performed starting from the structural model proposed for MgIrO_3 lead to a decent fit (cf. figure II.25.a). Within this structure ($R\bar{3}$, $a = 5.0471(6) \text{ \AA}$, $c = 14.1303(23) \text{ \AA}$) the RuO_6 octahedra are arranged in honeycomb layers, themselves stacked one above the other following an ABC sequence and with the magnesium atoms placed in the octahedral vacant sites of the interlayer. However, with respect to data quality, a synchrotron diffraction pattern would be required before further confirming this model, especially considering the positions of the oxygen and magnesium atoms whose contributions to the diffraction pattern may be masked by ruthenium as discussed previously.

II.3 Physico-chemical properties

Having described the synthesis of new ruthenium oxides, it is now interesting to investigate their physicochemical properties. Among them SrRu_2O_6 is known to be antiferromagnetic¹¹⁶ with one of the highest Néel temperature (565 K) reported for a 4d transition metal-based oxide. Therefore, the magnetic investigation of quasi-isostructural BaRu_2O_6 came as an evidence and will be a first part of this section. In a second part, the ability of SrRu_2O_6 and BaRu_2O_6 to insert lithium atoms will be studied.

II.3.a Magnetic properties of BaRu_2O_6

As mentioned above, the aim of this section is to use our new BaRu_2O_6 phase as a model compound to better understand the origin of the unusually high Néel temperature (565 K) displayed by SrRu_2O_6 . Indeed BaRu_2O_6 presents a similar Ru framework than SrRu_2O_6 , but with a larger interlayer distance, so that intra and interplane couplings may be slightly modified. The evolution of the magnetic susceptibility as a function of temperature for BaRu_2O_6 and SrRu_2O_6 , as obtained via SQUID magnetometry from 2 K to 350 K under zero field cooled (ZFC) conditions with an applied magnetic field of 10 kOe, is displayed in figure II.26.a. Our data shows a profile alike the one reported for SrRu_2O_6 ¹¹⁶, with a susceptibility decrease until 100 K and increase above 300 K with however a lower molar magnetic susceptibility for the Ba compound. The low temperature magnetic behaviour may be attributed to a small amount of RuO_2 impurities undetected by diffraction, whereas the susceptibility upturn after 300 K could suggest, similarly to SrRu_2O_6 , an antiferromagnetic behavior in BaRu_2O_6 . In parallel, high intensity neutron powder diffraction (D1B, ILL) measurements were carried out from 2 K to 570 K to check for the eventual presence of magnetic peaks.¹³¹ The pattern collected at 2 K reveals the presence of a small peak at $Q = 1.52 \text{ \AA}^{-1}$ which was barely seen at 300 K using the high angular resolution D2B diffractometer; this peak disappears above 525 K and reappears on cooling (cf. figure II.26.b), suggesting the presence of a long range ordering of the ruthenium magnetic moments. Moreover, this reflection can be indexed with the propagation vector $\mathbf{k} = (0, 0, 0)$ which means that the magnetic and nuclear cells are identical (however this peak was not indexed in the $P6_3/mcm$ space group pertaining to the nuclear structure). The magnetic structure was examined with the help of the Isodistort program^{132,133} and was solved in the $P6_3/m'cm$ magnetic space group. Figure II.26.d shows the magnetic contribution to the neutron pattern at 2 K around the 1.52 \AA^{-1} peak, and the whole refinement is shown in figure II.27.

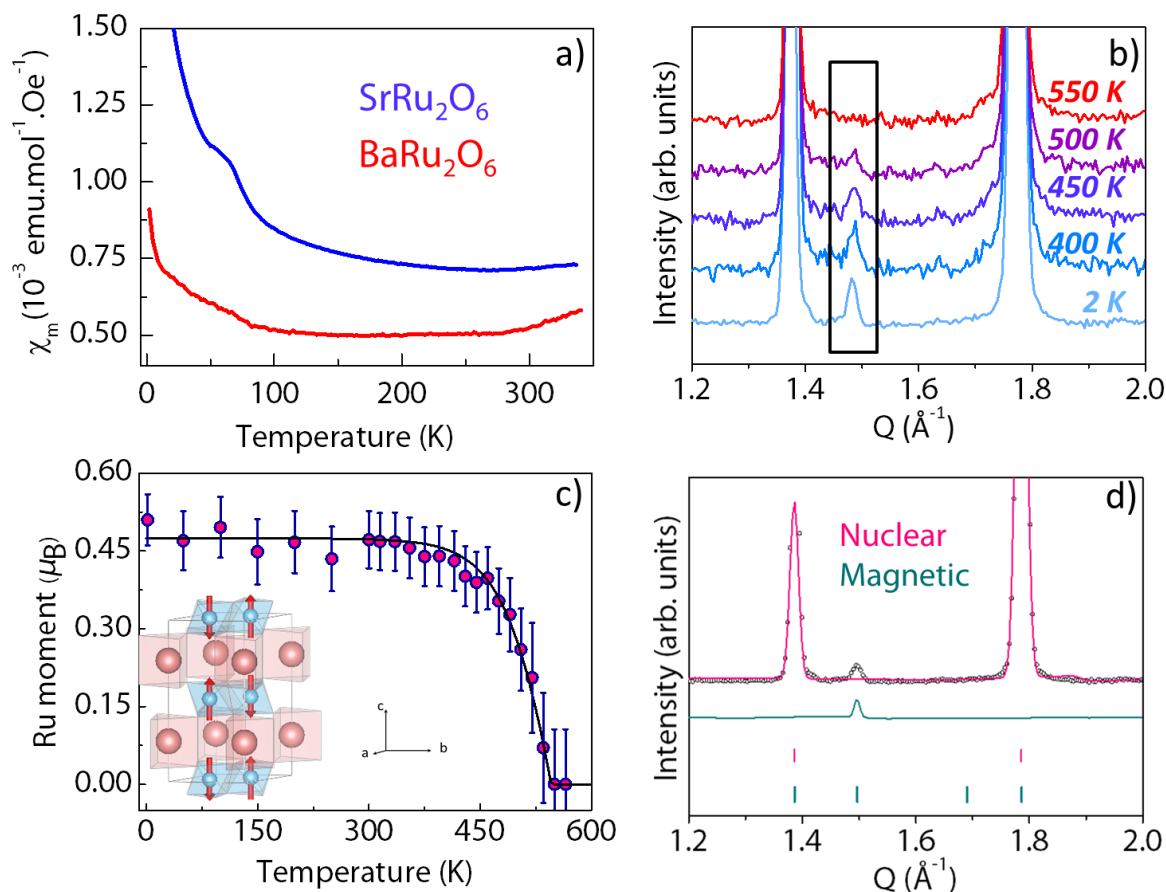


Figure II.26: a) Magnetic susceptibility of SrRu_2O_6 and BaRu_2O_6 as a function of temperature. Data were collected at 10 kOe under zero field cooled (ZFC) conditions. b) Evolution of the neutron powder patterns of BaRu_2O_6 , between 2 K and 550 K. The black rectangle marks the evolution of the most intense magnetic peak with the temperature. c) Refined Ru magnetic moment as a function of temperature. Inset shows the magnetic cell, with red Ba^{2+} and blue Ru^{5+} (the oxygen atoms are suggested by the coordination polyhedra of the cations); spin orientations are represented with red arrows. d) Comparison between the experimental neutron diffraction patterns of BaRu_2O_6 measured at 2 K (black dots) and the nuclear (pink line) and magnetic (blue line) contributions obtained by Rietveld refinement.

All Ru magnetic moments are oriented along [001], as imposed by symmetry, and they are all antiparallely oriented (inset of Figure II.26.c), so that both inter and intra-layer antiferromagnetic interactions are expected. The magnetic structure of BaRu_2O_6 is therefore exactly the same as the one reported for SrRu_2O_6 .¹¹³ The ordered magnetic moment on ruthenium, determined from neutron diffraction (figure II.27) at 2 K was found to be $M_{\text{Ru}} = 0.51(8) \mu_{\text{B}}$ (cf. Table II.9) as compared to $M_{\text{Ru}} = 1.425(10) \mu_{\text{B}}$ in SrRu_2O_6 .¹¹³ Such values are quite lower than the one of $3 \mu_{\text{B}}$ expected for Ru^{5+} (d^3). Among the possible reasons to account for such a difference, we could invoke a strong spin-orbit coupling, a slight increase of Ru-O bond covalency or with the emergence of magnetic disorder due to the presence of stacking faults, which are not observed for SrRu_2O_6 . By plotting the variation of the magnetic moment

as a function of temperature (figure II.26.c), a Néel temperature of 525 K was determined for BaRu₂O₆. Altogether, these results confirm that the magnetic ordering exists with the alignment of the magnetic moments along the **c** direction for both compounds with however a slightly lower T_N in BaRu₂O₆ ($T_N = 525$ K) as compared to SrRu₂O₆ ($T_N = 565$ K).

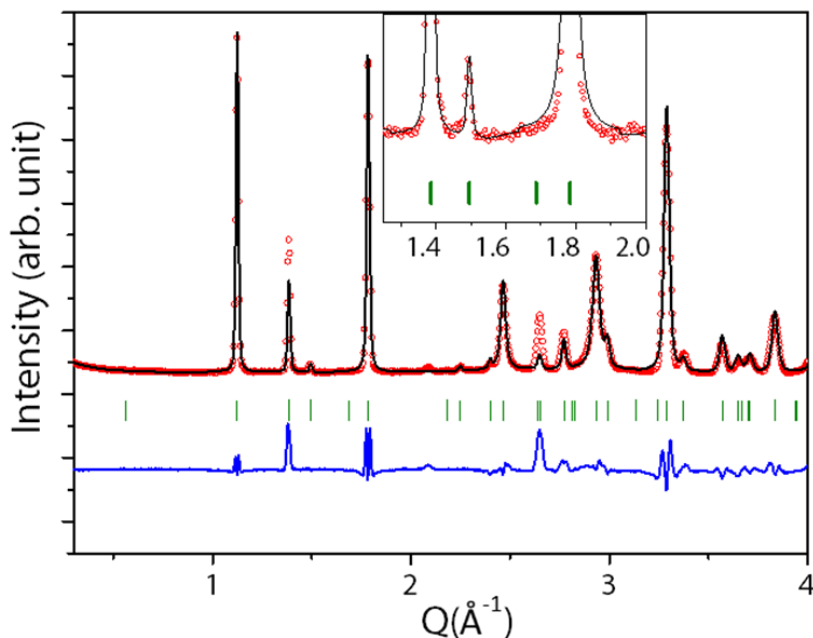


Figure II.27: Rietveld refinement of the nuclear and magnetic structure of BaRu₂O₆ from 2 K neutron diffraction pattern ($\lambda = 2.5297$ Å). The red circles, black continuous line, and bottom blue line represent the observed, calculated, and difference patterns, respectively. Vertical green tick bars are the Bragg positions.

Previous experimental and theoretical magnetic studies^{113,134} in these two-dimensional honeycomb phases revealed an antiferromagnetic coupling of the Ru moments both in-plane and out-of-plane with however quite weaker inter-plane than intra-plane interactions. Moreover, using Monte-Carlo simulations, it was shown¹³⁴ that a decrease of the out-of-plane coupling would lower the Néel temperature while an increase of the in-plane coupling would have the opposite effect. This implies a delicate balance between the interlayer distance that controls the out-of-plane coupling and the Ru-O covalence and Ru-O-Ru angle (e.g superexchange) that governs the in-plane one. On that basis, the lower Néel temperature observed for BaRu₂O₆ as compared to SrRu₂O₆ could simply be explained by a larger interlayer distance in BaRu₂O₆ (5.60 Å vs 5.23 Å) which implies a weaker out-of-plane coupling but we couldn't rule out completely the fact that O1 and P2 layers may have different superexchange paths. However, the smallness of the T_N difference between BaRu₂O₆ and SrRu₂O₆ may be nested in

the out-of-plane interaction that is counter-balanced by the in-plane interaction due to an increase of the Ru-O covalence (e.g increase of T_N). This is supported by the shortening of the Ru-O distances for the Ba-based phase as compared to the Sr one as well as a flattening of the Ru-O-Ru angles, which indicate a slightly greater super exchange. The greater covalency is most likely rooted in the larger chemical pressure induce by the bulky Ba^{2+} cations.

BaRu ₂ O ₆ magnetic structure				
Magnetic space group: $P6_3/m'cm$		Lattice parameters: $a = 5.2365(2) \text{ \AA}$ $c = 11.1728(8) \text{ \AA}$		
Atom	x/a	y/b	z/c	M_z
Ru1	1/3	2/3	0	0.51(8) μB
Ru2	2/3	1/3	0	-0.51(8) μB
Ru3	1/3	2/3	1/2	-0.51(8) μB
Ru4	2/3	1/3	1/2	0.51(8) μB

Table II.9: Magnetic structure parameters of BaRu₂O₆.

Besides their interest in terms of magnetism, layered-type compounds are also of paramount importance as electrode materials in today's lithium-ion batteries, hence our exploration of their electrochemical behaviour against lithium as described next.

II.3.a Electrochemical insertion of Li^+ in BaRu_2O_6 and SrRu_2O_6

At this stage of the manuscript it is clear for the reader that layered materials are among the most studied positive electrode compounds for metal-ion batteries. In contrast, studies dealing with the insertion of divalent cations into layered oxides are relatively rare.¹³⁵ However, in the case of MRu_2O_6 , the divalent interlayer cations are too bulky and too highly charged to be mobile in the structure. Thus, these phases can be considered as ideal model materials to study the effect of interlayer pillars on lithium insertion as well as on layers gliding often observed when alkali cations are intercalated.

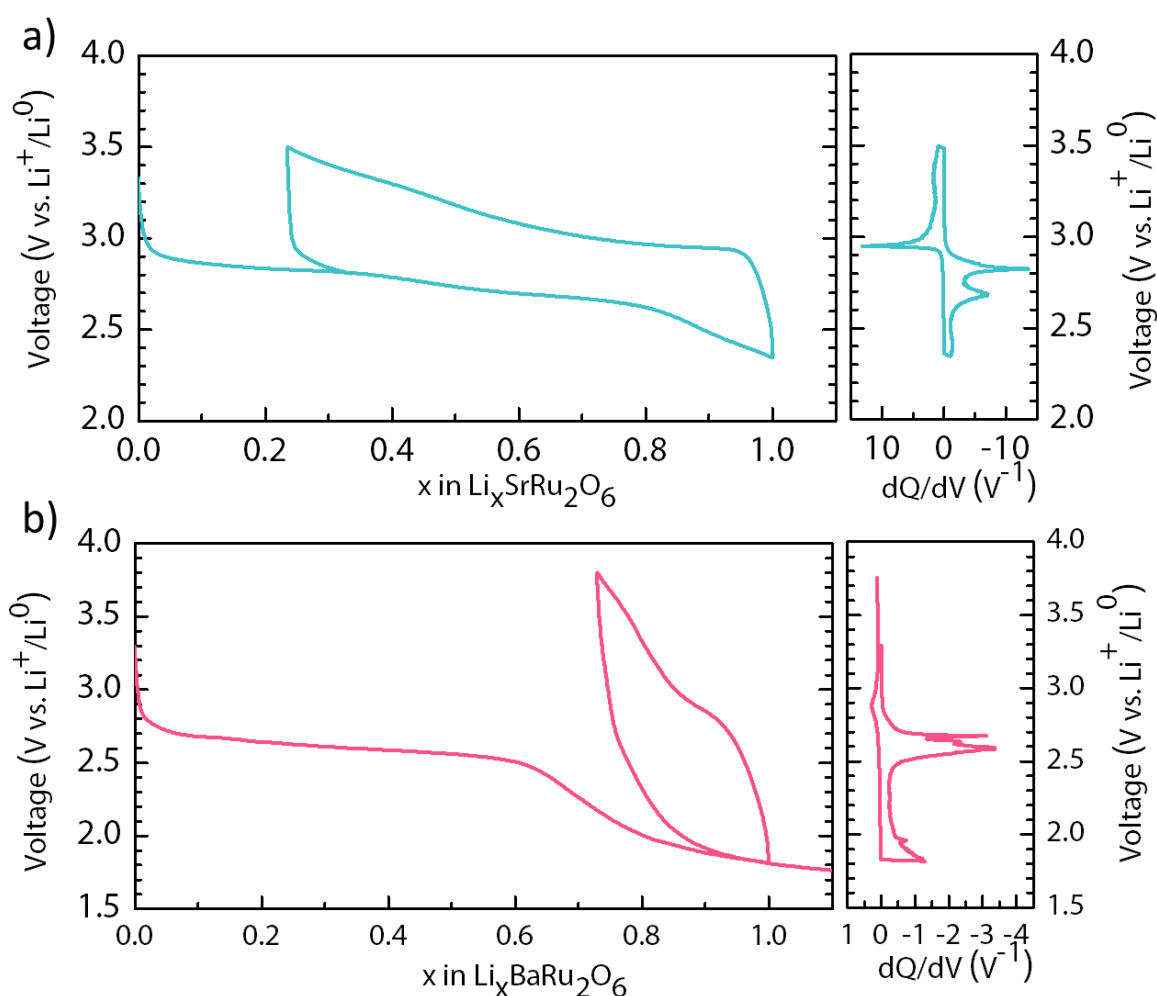


Figure II.28: Voltage–composition trace and derivative curves of SrRu_2O_6 (a) and BaRu_2O_6 (b) cycled at C/20 started with reduction.

Swagelok-type cells using BaRu_2O_6 and SrRu_2O_6 at positive electrode and lithium metal as negative electrode were assembled to perform electrochemical tests. The composition-voltage profile for $\text{Li}/\text{BaRu}_2\text{O}_6$ and $\text{Li}/\text{SrRu}_2\text{O}_6$ cells cycled at C/20 rate are shown in figure II.28 together with their corresponding derivative plots. Nearly one lithium is inserted into the

SrRu_2O_6 structure upon discharge through two voltage plateaus having an amplitude of 0.25 and 0.5 Li^+ , respectively, with an extra 0.25 Li^+ be uptake through a continuous drop in voltage. Out of the one inserted Li^+ , nearly 0.8 can be removed on the subsequent charge. The corresponding derivative plot (right panel) highlights two reduction peaks, corresponding to the two voltage insertion plateaus located at 2.82 and 2.65 V, that transform into a single one located at 2.95 V on charge (oxidation). Such a difference implies that the Li uptake and removal processes are different. We could extend the lithium insertion beyond $x = 1$, but it is of no interest since it triggers a drastic loss of reversibility (cf. figure II.29).

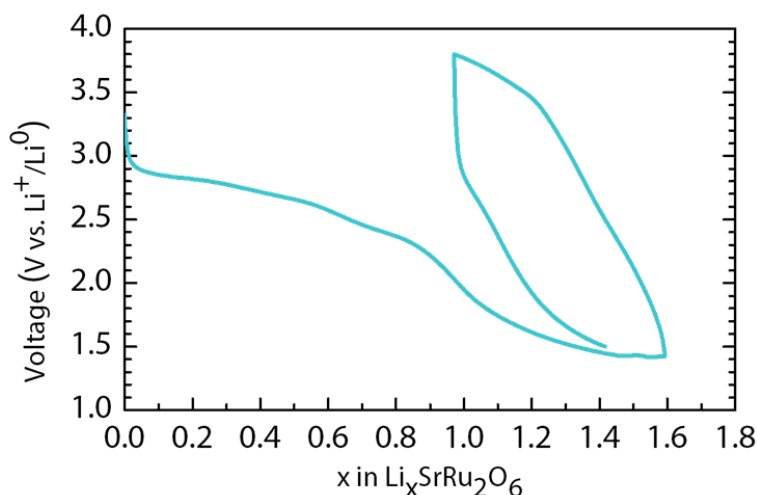


Figure II.29: Voltage–composition trace for SrRu_2O_6 for lithium insertion above $x = 1$. The compound was cycled at $C/20$.

Turning to BaRu_2O_6 , it uptakes 0.7 lithium through a staircase voltage profile, but the process is mostly irreversible as only 0.2 Li can be removed upon subsequent charge irrespective of the different voltage windows we have tried. To elucidate these different electrochemical behaviours and to understand the structural changes upon lithium insertion, we carried out operando XRD measurements.

A $\text{Li}/\text{SrRu}_2\text{O}_6$ cell was cycled at a $C/20$ rate and XRD patterns were collected for every change in lithium stoichiometry of 0.05 in $\text{Li}_x\text{SrRu}_2\text{O}_6$ (Figure II.30). Our data reveals an initial shift of peak ($2\theta \approx 17^\circ$) to higher angle till a Li content of $x = 0.25$ indicating a contraction in c lattice parameter.

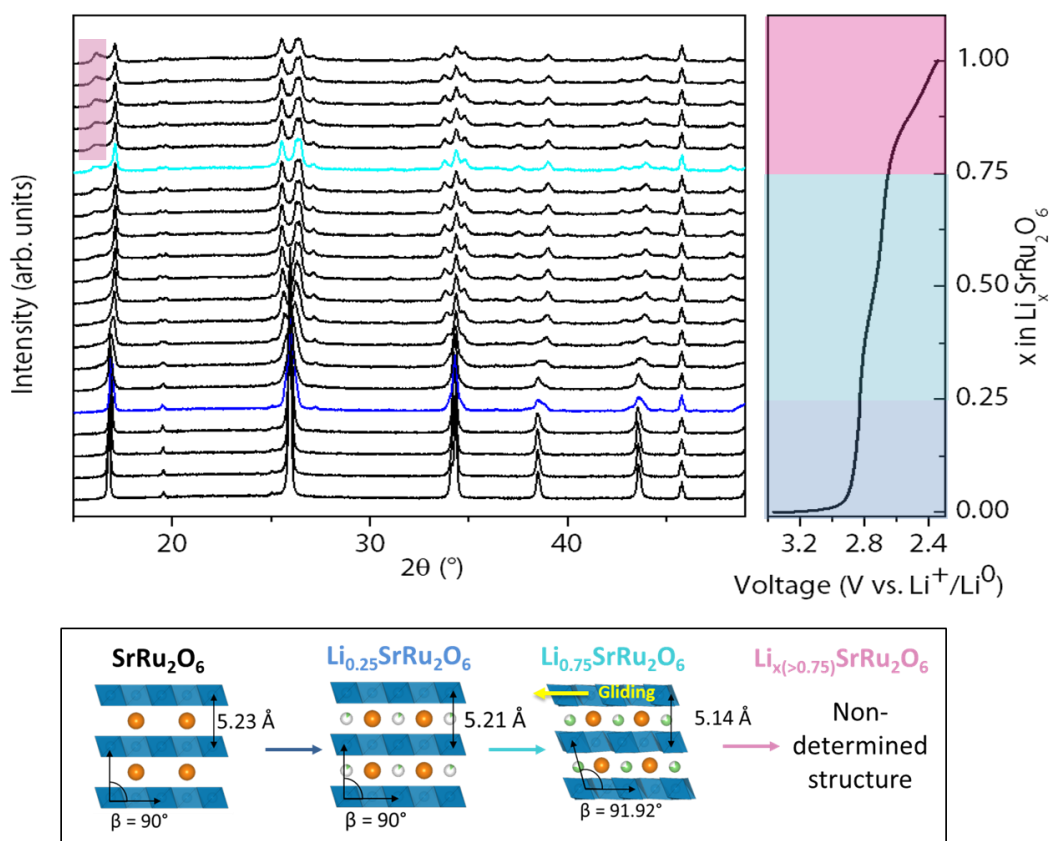


Figure II.30: (Top) Operando XRD patterns during the reduction of SrRu_2O_6 with the corresponding galvanostatic curve. The compound is discharged at $C/20$ and the XRD patterns are measured for 1 h. On the galvanostatic curve, the different structural evolution domains are indicated and the patterns corresponding to $\text{Li}_{0.25}\text{SrRu}_2\text{O}_6$ and $\text{Li}_{0.75}\text{SrRu}_2\text{O}_6$ are respectively plotted in dark and light blue. The pink rectangle underlines the region where extra peaks are growing at the end of the discharge. (Bottom) Principal steps of the lithiation of SrRu_2O_6 are summed up. RuO_6 octahedra, strontium and lithium atoms are represented in blue, orange and green, respectively.

Upon further lithiation ($0.25 < x < 0.75$), some of the main peaks, namely at $2\theta = 26^\circ$ and $2\theta = 34^\circ$ start to split so that the patterns cannot any longer be indexed with the pristine structural model. A monoclinic distortion ($P2_1/c$ space group) was required to satisfactorily index all the reflections. This phase persists until $x = 0.75$. Beyond and concomitantly with a voltage drop, there is the appearance of new extra peaks with the most prominent be located near $2\theta = 15^\circ$ (highlighted in figure II.30). These peaks belong to a lithiated phase, which appears at the end of discharge, but obtaining a complete structural model is difficult because this phase could never be obtained as a pure phase. To make easier the comparison of the lattice parameters at each lithiation stage, all the XRD pattern obtained during operando measurement were refined using the ($P2_1/c$) model. It worth reminding that the pristine unit cell ($P\bar{3}1m$) can be represented in the $P2_1/c$ space group via the linear transformations:

$$P\bar{3}1m \xrightarrow{\begin{pmatrix} 1 & -1 & 0 \\ 1 & 1 & 0 \\ 0 & 0 & 1 \end{pmatrix}} C2/m \xrightarrow{\begin{pmatrix} 1 & 0 & 0 \\ 0 & 1 & 0 \\ 0 & 0 & 2 \end{pmatrix}} P2_1/c$$

The lattice vectors of the targeted space group (\mathbf{a}' , \mathbf{b}' , \mathbf{c}') are deduced from the starting one (\mathbf{a} , \mathbf{b} , \mathbf{c}) by the following expression: $(\mathbf{a}' \ \mathbf{b}' \ \mathbf{c}') = (\mathbf{a} \ \mathbf{b} \ \mathbf{c})\mathbf{P}$, with \mathbf{P} the transformation matrix (given above the arrows in the previous expression). Finally, the evolution of the lattice parameters of $\text{Li}_x\text{SrRu}_2\text{O}_6$ with the inserted lithium amount is represented in figure II.31.

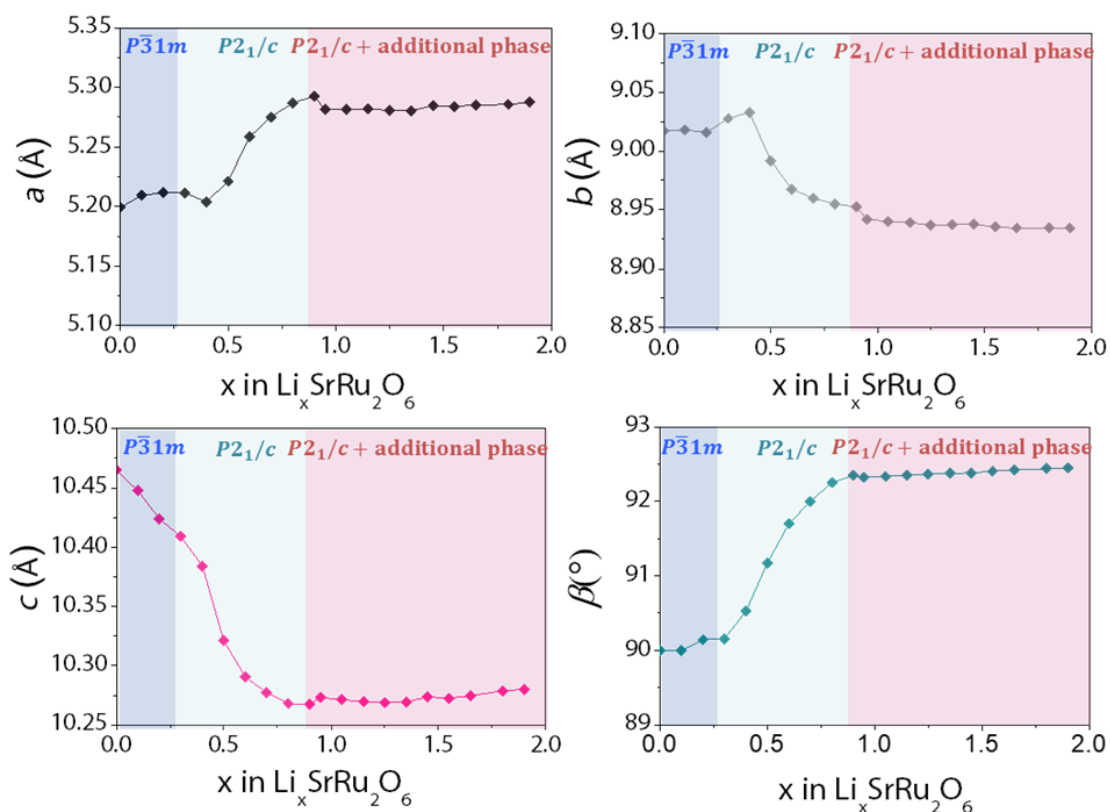


Figure II.31: Evolution of the lattice parameter of $\text{Li}_x\text{SrRu}_2\text{O}_6$ with the inserted Li amount. All the lattice parameters were obtained by refining the operando patterns with the $P2_1/c$ structural model.

Then, to interrogate the position of the Li^+ ions in the monoclinic phase, the structure of the lithiated $\text{Li}_{0.25}\text{SrRu}_2\text{O}_6$ and $\text{Li}_{0.75}\text{SrRu}_2\text{O}_6$ were determined by complementary SXRD and NPD measurements (cf. figure II.32). $\text{Li}_{0.25}\text{SrRu}_2\text{O}_6$ can be described using the same structural model as the pristine phase but with a smaller c parameter ($P\bar{3}1m$, $a = 5.21034(11)$ Å, $c = 5.21148(4)$ Å). By combining bond valence energy landscape maps (BVEL) with the Rietveld refinement of NPD patterns (cf. figure II.32.a), we show that each octahedral site in the $\text{Li}_{0.25}\text{SrRu}_2\text{O}_6$

interlayer is occupied by a lithium atom with a 0.125 occupancy (cf. figure II.33.a and Table II.10).

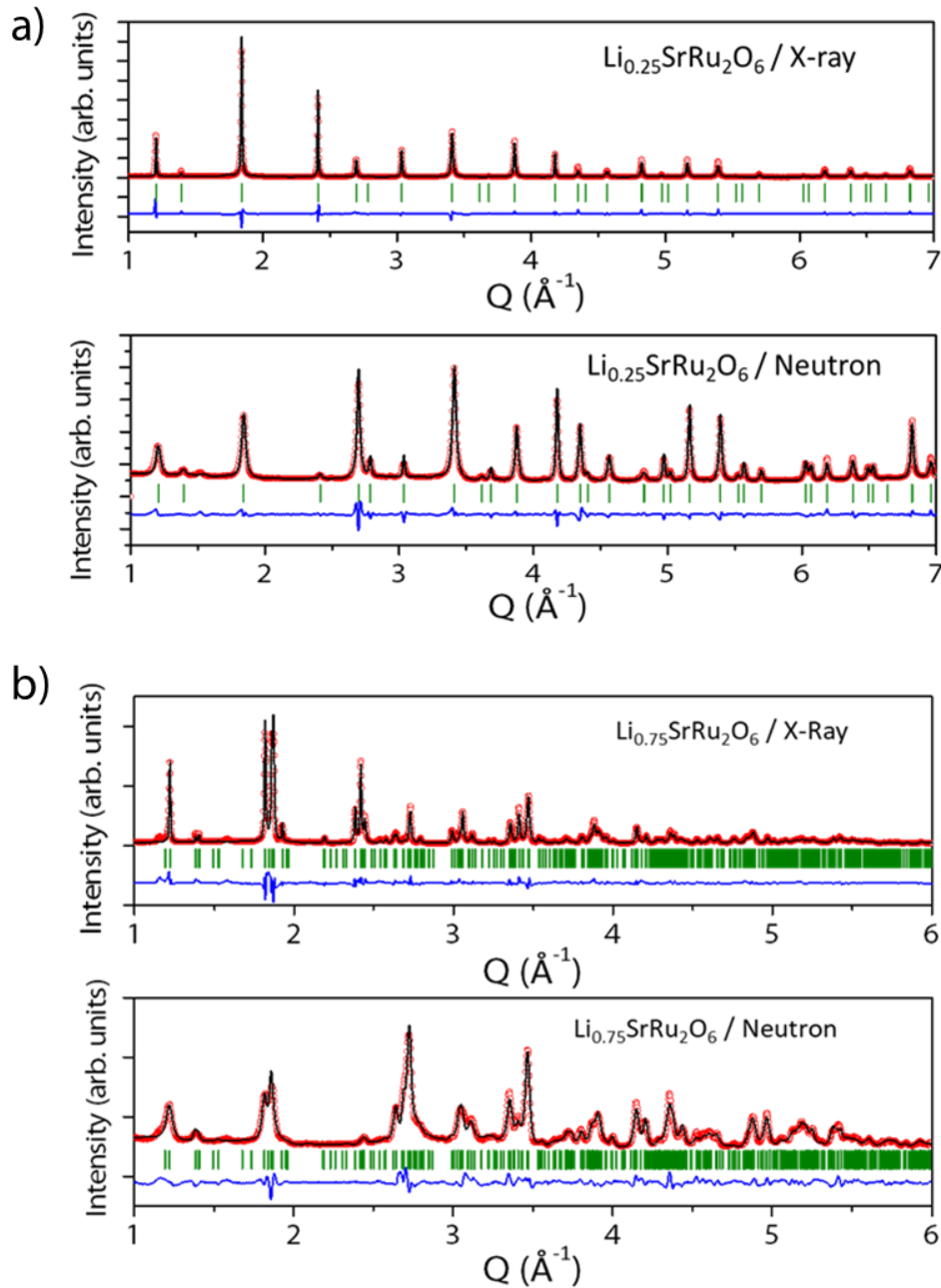


Figure II.32: Combined XRD/neutron Rietveld refinement of $\text{Li}_{0.25}\text{SrRu}_2\text{O}_6$ a) and $\text{Li}_{0.75}\text{SrRu}_2\text{O}_6$ b) using structural model of Table II.10 and II.11 respectively. Wavelengths for synchrotron X-ray and neutrons are $\lambda = 0.4128 \text{ \AA}$ and $\lambda = 1.5940 \text{ \AA}$, respectively. The red circles, black continuous line, and bottom blue line represent the observed, calculated, and difference patterns, respectively. Vertical green tick bars are the Bragg positions.

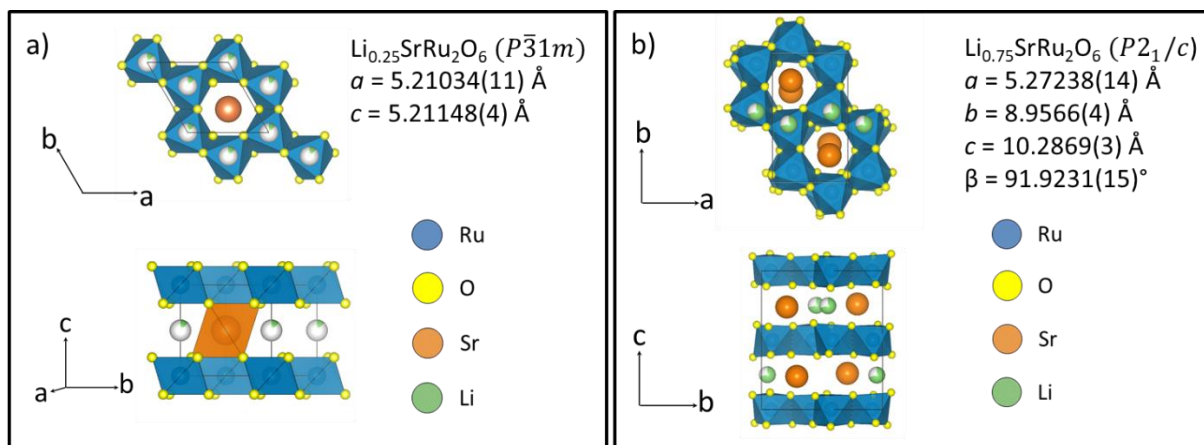


Figure II.33: Structures of $\text{Li}_{0.25}\text{SrRu}_2\text{O}_6$ (a) and $\text{Li}_{0.75}\text{SrRu}_2\text{O}_6$ (b). RuO_6 octahedra, strontium and lithium atoms are represented in blue, orange and green, respectively.

Turning to the $\text{Li}_{0.75}\text{SrRu}_2\text{O}_6$ phase, it was indexed using the $P2_1/c$ space group with lattice parameters $a = 5.27238(14) \text{ \AA}$, $b = 8.9566(4) \text{ \AA}$, $c = 10.2869(3) \text{ \AA}$ and $\beta = 91.9231(15)^\circ$. It can be described as a distortion of the pristine structure with a slight gliding of the ruthenium layers in the a direction (indicated by the yellow arrow in figure II.30) that is concomitant to a displacement of the Sr atoms out of the centers of the “honeycomb” rings (cf. figure II.33.b).

$\text{Li}_{0.25}\text{SrRu}_2\text{O}_6$		$P\bar{3}1m$	$R_{\text{Bragg}} = 4.87 \%$	$\chi^2 = 4.08$		
$a = 5.21034(11) \text{ \AA}$		$c = 5.21148(4) \text{ \AA}$		$\text{Vol} = 122.525(5) \text{ \AA}^3$		
Atom	Wyckoff Position	x/a	y/b	z/c	$B_{\text{iso}} (\text{Å}^2)$	Occupancy
Sr	$1a$	0	0	0	1.20(5)	1
Ru	$2d$	$1/3$	$2/3$	$1/2$	0.28(2)	1
O	$6k$	$0.3778(2)$	0	$0.2964(4)$	0.56(3)	1
Li	$2c$	$1/3$	$2/3$	0	3.1(10)	0.125

Table II.10: Crystallographic data and atomic positions of $\text{Li}_{0.25}\text{SrRu}_2\text{O}_6$ determined from a combined Rietveld refinement of its synchrotron X-ray and neutron diffraction patterns.

Finally, BVOL calculations followed by Rietveld refinement demonstrated that lithium atoms do not equally occupy all the octahedral interlayer sites in $\text{Li}_{0.75}\text{SrRu}_2\text{O}_6$ as they do for $\text{Li}_{0.25}\text{SrRu}_2\text{O}_6$. Indeed, in $\text{Li}_{0.75}\text{SrRu}_2\text{O}_6$, owing to the displacement of the strontium atoms out of the honeycomb centers, the octahedral interstitial sites split into two non-equivalent Li positions referred as Li1 and Li2 in figure II.34. The Li1 site being further away from the strontium atoms than the Li2 site, it is more stable from an electrostatic point of view and thus occupied (cf. Table II.11).

$\text{Li}_{0.75}\text{SrRu}_2\text{O}_6$		$P2_1/c$	$R_{\text{Bragg}} = 5.37\%$	$\chi^2 = 12.2$		
$a = 5.27238(14) \text{ \AA}$		$b = 8.9566(2) \text{ \AA}$	$c = 10.2869(3) \text{ \AA}$	$\beta = 91.9231(15)^\circ$	$\text{Vol} = 486.74(7) \text{ \AA}^3$	
Atom	Wyckoff Position	x/a	y/b	z/c	$B_{\text{iso}} (\text{\AA}^2)$	Occupancy
Sr	4e	0.761(2)	0.2911(4)	0.4978(13)	2.16(10)	1
Ru1	4e	0.7156(13)	0.5886(5)	0.7467(6)	0.039(15)	1
Ru2	4e	0.2213(13)	0.4216(6)	0.7529(6)	0.039(15)	1
O1	4e	0.617(3)	0.764(2)	0.6568(13)	0.47(9)	1
O2	4e	0.429(3)	0.568(2)	0.8598(14)	0.47(9)	1
O3	4e	0.881(3)	0.745(2)	0.8646(13)	0.47(9)	1
O4	4e	0.016(3)	0.5611(16)	0.6629(12)	0.47(9)	1
O5	4e	0.496(3)	0.4609(17)	0.6312(12)	0.47(9)	1
O6	4e	0.890(3)	0.425(3)	0.8662(15)	0.47(9)	1
Li	4e	0.7178(14)	0.5776(6)	0.016(2)	1.19(9)	0.75

Table II.11: Crystallographic data and atomic positions of $\text{Li}_{0.75}\text{SrRu}_2\text{O}_6$ determined from the combined Rietveld refinement of its synchrotron X-ray and neutron diffraction patterns.

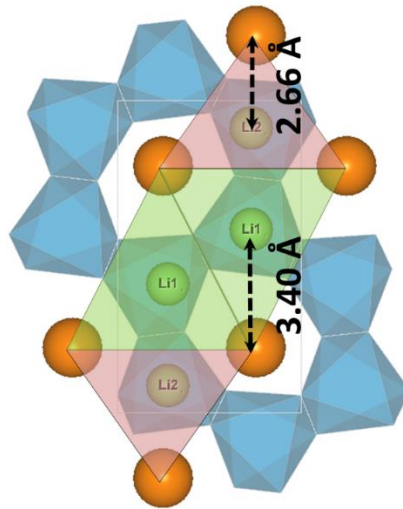


Figure II.34: Representation of the two possible sites for Li in $\text{Li}_{0.75}\text{SrRu}_2\text{O}_6$. The colored triangles point out the distance between each lithium site and their neighboring strontium atoms. This picture shows that the Li1 position is further away from strontium than Li2.

The Li-insertion in BaRu_2O_6 (cf. figure II.35) was also studied by *operando* XRD. A small shift of the $2\theta \approx 16^\circ$ peak to higher angle, indicative of a small decrease of the interlayer spacing, is observed upon the insertion of 0.6 lithium in the structure, alike in SrRu_2O_6 . Upon further

lithiation, the voltage drops with the concomitant appearance of extra peaks (highlighted in figure II.35) that can be indexed in the same space group ($P6_3/mcm$) as for BaRu_2O_6 but with a smaller c lattice parameter (figure II.36). Finally, BVEL calculations suggest that the lithium atoms could be located in the interlayer trigonal prismatic sites. However, since prismatic coordination is very unusual for lithium atoms, additional NPD measurements are needed to verify this assignment.

Altogether, these results unambiguously prove the reversible insertion of Li in SrRu_2O_6 , which occurs via a monoclinic distortion. However, a remaining question regards its incompleteness that we try to rationalise via chemical considerations. First, let us recall that layer oxides are well known to undergo phase transitions associated to layer gliding upon lithium uptake/removal, one of the most common being the O3 to O1 transition. In the O3 (resp. O1) structure, the interlayer alkali octahedra share edges (resp. faces) with the transition metal octahedra. At low alkali concentration and in the presence of transition metal honeycomb ordering, the O1 structure is preferred due to the presence of electrostatically favoured alkali sites sharing faces with transition metal vacancies, i.e. Sr in SrRu_2O_6 . However, at high alkali concentration the O3 structure becomes more stable than the O1 because the overall distances between alkali and transition metal cations are maximized (edge sharing in O3 compared to face sharing in O1).^{76,136,137} The fact that the full lithiation of SrRu_2O_6 (until $\text{Li}_2\text{SrRu}_2\text{O}_6$) is not observed experimentally is proposed to be due to the inability of the structure to undergo the expected O1 to O3 transition because of the presence of the large Sr^{2+} (1.18 Å radius) acting as pillars and providing structural rigidity. Bearing the same reasoning, it does not come as a surprise that the use of bulkier Ba^{2+} (1.35 Å radius) fully blocks the translation motion of the layer and by the same token the distortion. Lastly, an obvious experiment to check for this hypothesis could consist in the use of the smaller Ca^{2+} as pillar, but so far, we have not succeeded in preparing this phase.

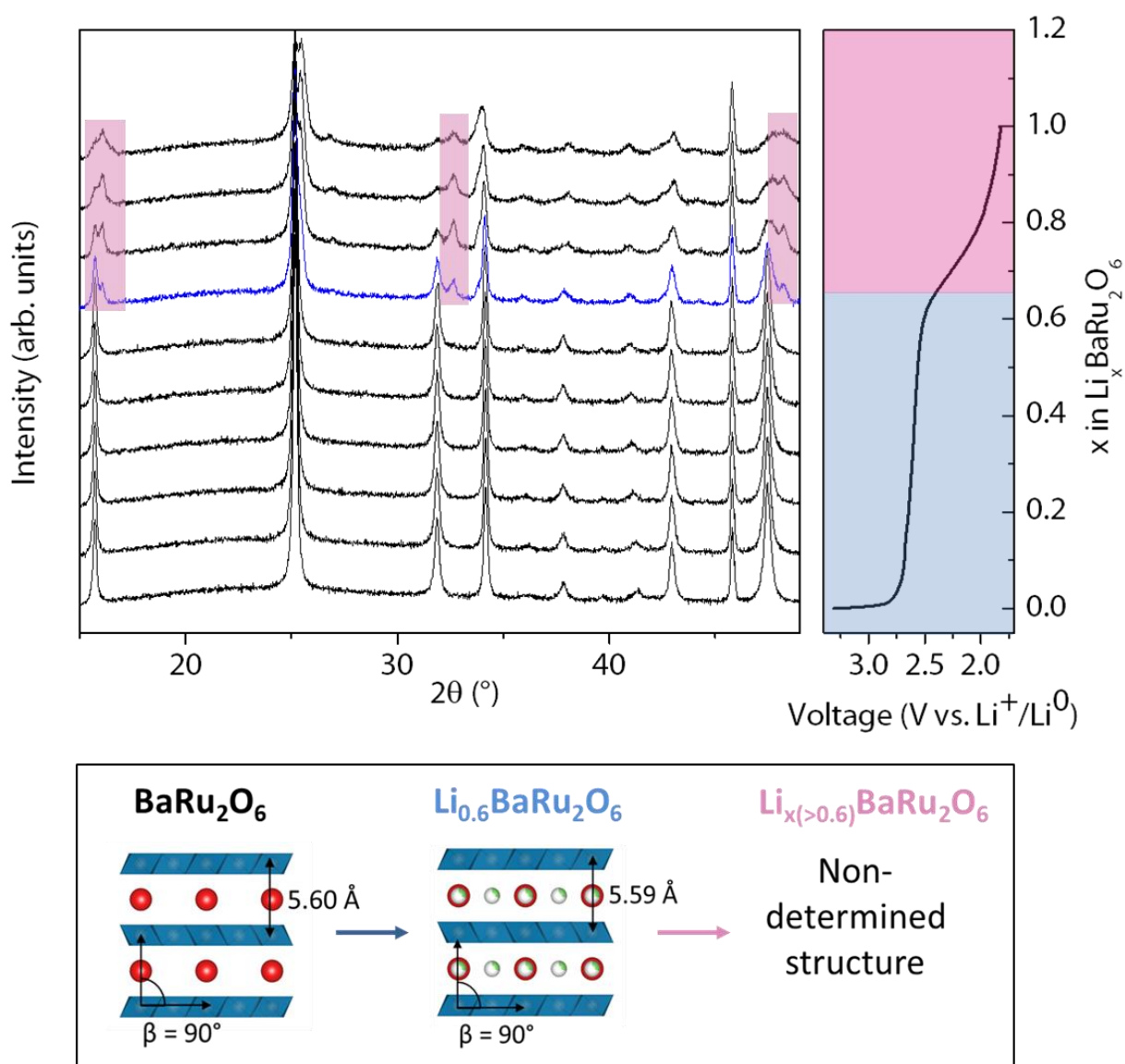


Figure II.35: (Top) Operando XRD patterns during the reduction of BaRu_2O_6 with the corresponding galvanostatic curve. The compound is discharged at $C/20$ and the XRD patterns are taken at intervals of 1 h. On the galvanostatic curve, the different structural evolution domains are indicated and the patterns corresponding to $\text{Li}_{0.6}\text{BaRu}_2\text{O}_6$ is plotted in blue. Pink rectangles underline the regions where extra peaks are growing at the end of the discharge. (Bottom) Principal steps of the lithiation of BaRu_2O_6 are summed up. RuO_6 octahedra, barium and lithium atoms are represented in blue, red and green, respectively.

Lastly, electrochemistry can also be a powerful technique to tune the magnetic properties of the parent SrRu_2O_6 phase by modifying the delicate balance between the in-plane and out-of-plane interactions via the insertion of extra ions (Li^+) or electrons via the reduction of Ru^{5+} in Ru^{4+} . Along that line, we investigated the magnetic measurements of partially lithiated $\text{Li}_x\text{SrRu}_2\text{O}_6$ ($x = 0.25, x = 0.75$). Preliminary results suggest that $\text{Li}_{0.25}\text{SrRu}_2\text{O}_6$ presents at 300 K a magnetic

structure similar to SrRu_2O_6 with, however, a smaller Ru magnetic moment and a lower Néel temperature.

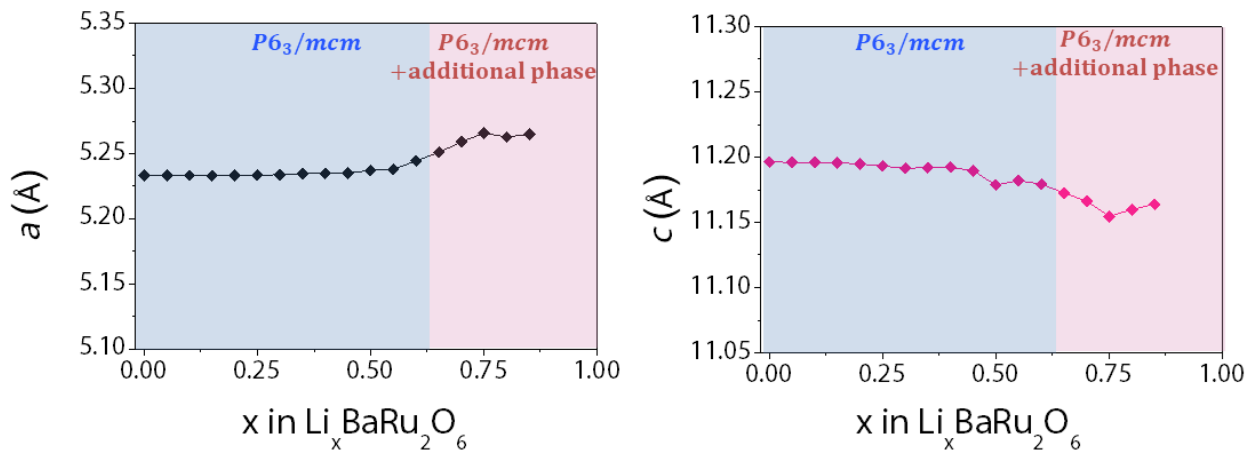


Figure II.36: Evolution of the lattice parameter of $\text{Li}_x\text{BaRu}_2\text{O}_6$ with the Li amount.

Chapter conclusion

In this chapter, we have explored the potential of low temperature synthesis processes to obtain new ruthenium oxides. In particular, using solutions of a strongly oxidized ruthenium salt (KRuO_4) and alkaline earth salts of barium or strontium and adjusting the pH, we have shown that a wide variety of alkaline earth ruthenate oxides can be synthesized. Five different barium ruthenates (BaRu_2O_6 , $\text{Ba}_2\text{Ru}_3\text{O}_9(\text{OH})$, $\text{Ba}_2\text{Ru}_3\text{O}_{10}$, $\text{Ba}_5\text{Ru}_4\text{O}_{15}$, and $\text{Ba}_4\text{Ru}_3\text{O}_{10.2}(\text{OH})_{1.8}$) and three strontium ruthenates (SrRu_2O_6 , $\text{Sr}_2\text{Ru}_3\text{O}_9(\text{OH})$, $\text{Sr}_2\text{Ru}_3\text{O}_{10}$) were obtained, four of which are reported here for the first time. This example demonstrates that the control of reaction kinetics could allow to shape the reaction pathways, which is a forward step towards tailor made new compounds. Thus, future research could aim at replacing ruthenium by other cheaper elements, notably Mn. Interestingly, the reduction of KMnO_4 in water has already been used to form manganese oxides¹³⁸ and, like KRuO_4 , KMnO_4 can also be thermally reduced by water. In addition, an exchange reaction to obtain other ruthenium oxides based on divalent cations (Zn^{2+} , Mg^{2+}) was briefly outlined. Although not yet fully mastered, this reaction could allow the formation of original compositions with an interesting layered structure for magnetism or as a model cathode material for post-Li-ion batteries.

In a second step, in order to push further the proof of concept, we showed that among these metastable oxides, SrRu_2O_6 and BaRu_2O_6 presented interesting physico-chemical properties. Indeed, like SrRu_2O_6 , BaRu_2O_6 was found to be antiferromagnetic with one of the highest Neel temperature reported for a 4d metal (525 K vs 565 K for SrRu_2O_6). Furthermore, we have shown the feasibility of reversible intercalation of 0.75 Li in SrRu_2O_6 and irreversible insertion of 0.6 Li in BaRu_2O_6 . Thus, although these materials are not of practical interest as cathode materials, they are interesting model materials to understand the impact of pillars in the interlayer on the electrochemical performance. Finally, although little explored in this manuscript, lithiation intercalation in these compounds could prove to be an ideal tool to fine tune their magnetic properties.

More generally, the characterization and control of the various reaction steps enabled by low temperature processes is currently one of the most exciting challenges in solid state chemistry. Such a success may one day allow reaching a level of control equivalent to that of organic chemistry, thus giving access to the infinite possibilities of metastable compounds and their properties. I hope this wish to come true in my future research endeavours.

Chapter III: Re-exploration of the transition metals sulfides in the context of anionic redox

III.0 Introduction

III.0.a General Background

As mentioned in the introduction, transition metal sulfides were the first intercalation compounds used as cathodes for Li-Ion batteries before being supplanted by oxides, which allowed to obtain higher voltages. Today, however, in the context of anionic redox, these materials may well get back in the spotlight. Indeed, we have seen that during the anionic redox process in oxides, the instability of the oxidized oxygen species leads to a severe deterioration of the cathode material and thus of the battery performances. On the contrary, oxidized species of sulfur such as $(S_2)^{2-}$ dimers are extremely common in nature and are known to be stable.^{25,139} These differences with oxygen come from two factors: a greater chemical softness (i.e. the capacity of an atom to lose/gain an electron without strongly impacting its stability) and a lower electronegativity of sulfur compared to oxygen. Thus, being less hard than oxygen, the atoms of sulfur are less destabilized by the departure of an electron. Moreover, by being less electronegative than oxygen, the 3p levels of sulfur are higher in energy and thus closer to the nd levels of transition metals. Therefore, the metallic levels are found under the anionic levels at oxidation degrees much lower than in the case of oxides. This phenomenon has been particularly studied by Rouxel and his collaborators and is well illustrated by the study of the MS_2 family (where M is a transition metal).¹⁴⁰ Indeed, this family of compounds is decomposed into two distinct groups depending on the position of the transition metal in the periodic table (cf. figure III.1 bottom). Thus, for the most electropositive metals (Ti, V, Nb, Ta etc...) the MS_2 compounds are lamellar with S^{2-} ions (and a transition metal that is hexacoordinated in an octahedral or prismatic way), thereby leading to the following charge decomposition: $M^{4+}(S^{2-})_2$. On the contrary, for the most electronegative metals (Fe, Mn, Co, Ru etc...) the nd levels of the cations with a +4 oxidation degree would be below the 3d level of the sulfur. Consequently, the obtained compounds are found with oxidized sulfur atoms and a respectively reduced transition metal (cf. figure III.1 top). The most frequent crystallographic structures for these compounds are the pyrite and marcasite ones containing $(S_2)^{2-}$. Faced with this

observation, it is natural to wonder about the electrochemical behavior of materials with a redox process involving sulfur. For this, it is important to explain first how to design such compounds.

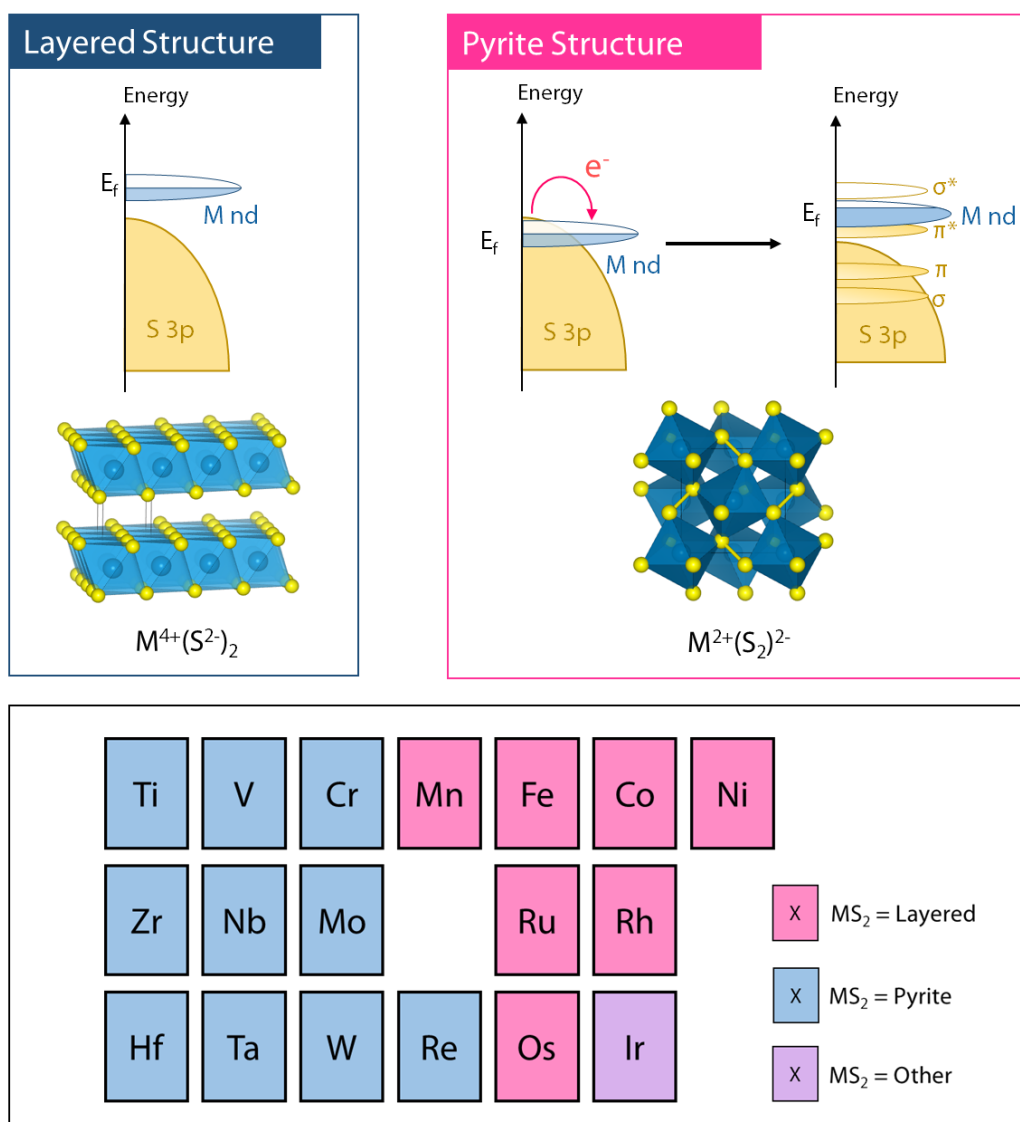


Figure III.1: (Top) Electronic and crystallographic structures of layered and pyrite structures. (Bottom) Classification of the transition metal dichalcogenides MX_2 based on their structure.

III.0.b How to activate anionic activity in transition metal sulfides?

To activate the anionic redox in sulfides one can be inspired by what has been done in oxides (cf. figure III.2). Thus, we can direct our attention to "d⁰" compounds, i.e. compounds where the nd metal levels are empty, which leaves no other choice than to involve the anions in the oxidation process. Another possibility is to start from a compound whose cationic levels are close to the anionic ones, so that we observe an energy inversion of these levels during oxidation.

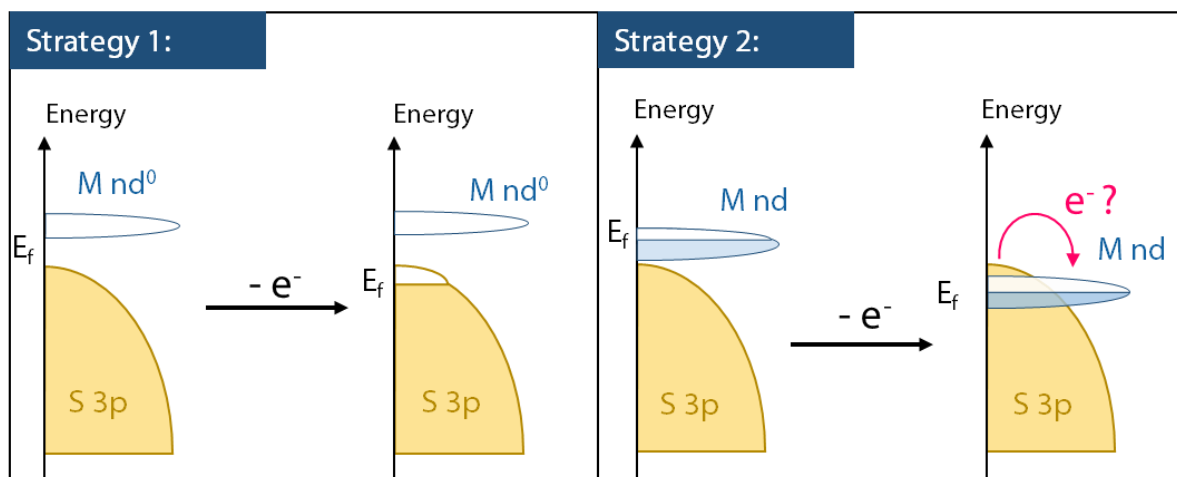


Figure III.2: Schematic drawing of the two strategies contemplated to design anionic active transition metal chalcogenides. The first one (left panel) consists in working with d^0 transition metal to constrain the oxidation to happen on the sulfur. The second strategy consists in synthesizing a lithiated compound with the nd transition metal band just above the sulfur $3p$ band.

i) Strategy 1: Synthesis of lithiated “ d^0 ” transition metal sulfides

In oxides, many “ d^0 ” compounds have been studied using very high valence cations like Ti^{4+} , Nb^{5+} , Ta^{5+} , Mo^{6+} or W^{6+} .^{79,83,141–143} However, those very high oxidation degrees lead to very low-energy nd orbitals. Therefore, these oxidation states are more difficult to reach in sulfides where the $3p$ orbitals of sulfur are high in energy. Despite these difficulties, it was possible to synthesize Li_2TiS_3 ,⁷⁶ a lamellar compound isostructural to Li_2MnO_3 . However, like Li_2MnO_3 , Li_2TiS_3 is mostly electrochemically inactive, and a cation substitution strategy was undertaken to activate it. Thus, $LiTiS_2$ - Li_2TiS_3 ,⁸⁰ Li_2TiS_3 - CoS ⁷⁹ and Li_2TiS_3 - FeS ⁸¹ solid solutions were shown to be able to activate the electrochemical lithium disinsertion in this compound. Interestingly, although spectroscopic and theoretical investigations undoubtedly demonstrated the involvement of sulfur in the redox process, the bottlenecks inherent to the anionic redox in oxides (voltage fade upon cycling and hysteresis) were not observed in these compounds. Nevertheless, in spite of the high reversible capacity of these compounds ($250 \text{ mAh}\cdot\text{g}^{-1}$ for $Li_{1.13}Ti_{0.57}Fe_{0.3}S_2$), the average voltage (2.5 V) induced by the sulfur limits the energy density and therefore the interest of these materials.⁸¹ We can then wonder if by increasing the capacity, i.e. by looking for lithium “super-rich” sulfides, it is possible to obtain even higher capacities that will perhaps allow to compete with the current standards of the industry. So similarly to what has been done for the oxides,⁶⁴ it is interesting to move from the Li-rich Li_2MS_3 composition to a Li-super rich Li_3MS_4 one. The first part of this chapter will therefore focus on

the synthesis of Li_3MS_4 compounds ($M = \text{V}, \text{Nb}$ or Ta) with a particular attention for the Li_3NbS_4 compound.

ii) *Strategy 2: Triggering the anionic redox through band position engineering*

To try to activate the redox activity of the anions during the withdrawal of lithium, the periodic table of figure III.1 can give us some clues. Indeed, considering the possibility of using transition metals that lead to MS_2 structures containing dimers, it may be interesting to try to synthesize Li_xMS_2 lithiated structures and to look at their oxidation behavior. This idea is not new and the electrochemistry of Li_2FeS_2 and Na_2FeS_2 compounds has already been studied.^{144–150} However, although it has been shown that dimers can be formed upon oxidation, the structural evolution during lithium removal leads to a drastic decrease of the long range order that limits the structural study of these compounds and thus the full understanding of their behavior. Inspired by this work, we will focus in the last part of the chapter on the electrochemical properties of both the lamellar compound LiIrS_2 and the $(\text{S}_2)^{2-}$ dimer-containing compound IrS_2 .

III.1 Study of the Li_3MS_4 family (M = V, Nb or Ta)

III.1.a Synthesis

A quick search in crystallographic databases shows that Li_3MS_4 compounds have been very little studied in contrast to their oxide equivalents (Li_3VO_4 ,¹⁵¹ Li_3NbO_4 ¹⁵² and Li_3TaO_4 ¹⁵³) or Na-based counterparts (Na_3VS_4 ,¹⁵⁴ Na_3NbS_4 ¹⁵⁵ and Na_3TaS_4 ¹⁵⁵). Indeed, to our knowledge no study of these materials has been reported except for a mechanical synthesis of Li_3NbS_4 with a disordered rock salt structure.¹⁵⁶ We have therefore undertaken to synthesize these materials by ceramic or mechanical means.

i) Ceramic synthesis

The ceramic synthesis of all the Li_3MS_4 (M= V, Nb and Ta) compounds was attempted following a similar protocol whatever the transition metal. About 500 mg of Li_3MS_4 was targeted by mixing in an Ar-filled glovebox stoichiometric proportions of vanadium (or niobium or tantalum) powder (Alfa-Aesar, 99.99 %), lithium sulfide (Alfa-Aesar, 99.9 %) and elemental sulfur (Sigma-Aldrich, 99.998 %). It is worth noting that the Li_3NbS_4 was obtained by using a 10% excess of Li_2S over the stoichiometry. Then, the reagents were transferred into a carbon coated quartz ampoule and subsequently sealed under dynamic vacuum ($\sim 10^{-3}$ mbar). The resulting ampoule was then placed in an oven at 650 °C for 60 hours before being opened in a glove box under argon atmosphere. The collected powder was then stored as such.

ii) Mechanic synthesis

For mechanic synthesis, the same procedure was followed to get the precursor mixture, but instead of transferring the reagents into a quartz tube, the hand grinding mixture was placed in a 45 mL zirconia jar with 11 zirconia balls (10 mm diameter, 2.4 gram weight) and ball milled using a Pulverisette 7 instruments at 550 rpm for 60 hrs. After the reaction, the jar was opened in an Ar-filled glovebox and the powders collected and stored as such.

iii) *Results*

Whatever the synthesis method, we did not succeed in obtaining Li_3VS_4 . Indeed, at high temperature (we tried different temperatures 650, 550, 600 or 700°C) the synthesis leads ineluctably to the formation of LiVS_2 , with Li_2S and S as impurities. Similarly, after mechanical synthesis the powder obtained is amorphous. This difficulty to form the compound could come from an energetic position of the hypothetical V^{5+} d levels lower than the sulfur bands of preventing its formation. However, it is important to note that the compound Na_3VS_4 exists (it is described in detail in chapter IV); with however in this case vanadium atoms in tetrahedral coordination which perhaps allows to stabilize this V^{5+} . If this is true, lithium exerting a chemical pressure weaker than Na could then be unable to stabilize VS_4 tetrahedra and prevent the formation of the compound. Thus, a Li_3VS_4 compound is probably thermodynamically unstable. It is important to note, however, that low-temperature routes can truly form this compound. Indeed, Clare Gray's group by lithiating the VS_4 compound discusses the formation of an amorphous Li_3VS_4 phase.¹⁵⁷ One can also imagine a Na/Li exchange in solution at low temperature from Na_3VS_4 to obtain Li_3VS_4 .

On the contrary, Li_3NbS_4 and Li_3TaS_4 compounds are formed whatever the synthesis process with however different structures depending on the method used. Thus mechano-synthesis leads systematically to the formation of disordered rocksalt structures whereas ceramic synthesis forms rocksalt structures with a cationic order between lithium and the transition metal, this order being different between Li_3NbS_4 and Li_3TaS_4 (cf. Table III.1). For the sake of clarity, in the following, the prefix d-(resp. o-) will be used to designate a disordered (resp. ordered) Li_3MS_4 phase and their structures are described in the next section.

	V	Nb	Ta
Mecanosynthesis	Amorphous	d- Li_3NbS_4	d- Li_3TaS_4
Ceramic synthesis	$\text{LiVS}_2 + \text{Li}_2\text{S} + \text{S}$	o- Li_3NbS_4	o- Li_3TaS_4

Table III.1: Summary table of the results of the synthesis of Li_3MS_4 compounds by ceramic route or by mechanical grinding. The prefix d- (resp. o-) corresponds to a disordered (resp. ordered) rocksalt structure.

III.1.b Structures

NB: In this study the synchrotron XRD patterns were all collected at the 11-BM beamline of the Advanced Photon Source (Argonne National Laboratory) (cf. materials and methods).

i) *d-Li₃NbS₄* and *d-Li₃TaS₄*

A Rietveld refinement of the X-ray diffraction pattern of the mechanically synthesized *d*-Li₃NbS₄ compound confirmed the disordered rocksalt-type cubic structure ($Fm\bar{3}m$, $a = 5.1412(2)$ Å) described by Sakuda et al.¹⁵⁶ (cf. figure III.3 and Table III.2). Moreover, transmission electron microscopy images showed that the sample consists in clusters of crystalline nanoparticles of 5 to 10 nm in diameter (cf. figure III.4d), which is consistent with the width of the peaks observed in X-ray diffraction. Finally, an EDX analysis (cf. figure III.4b) of the sample confirmed the expected Nb/S = 4 ratio for this compound.

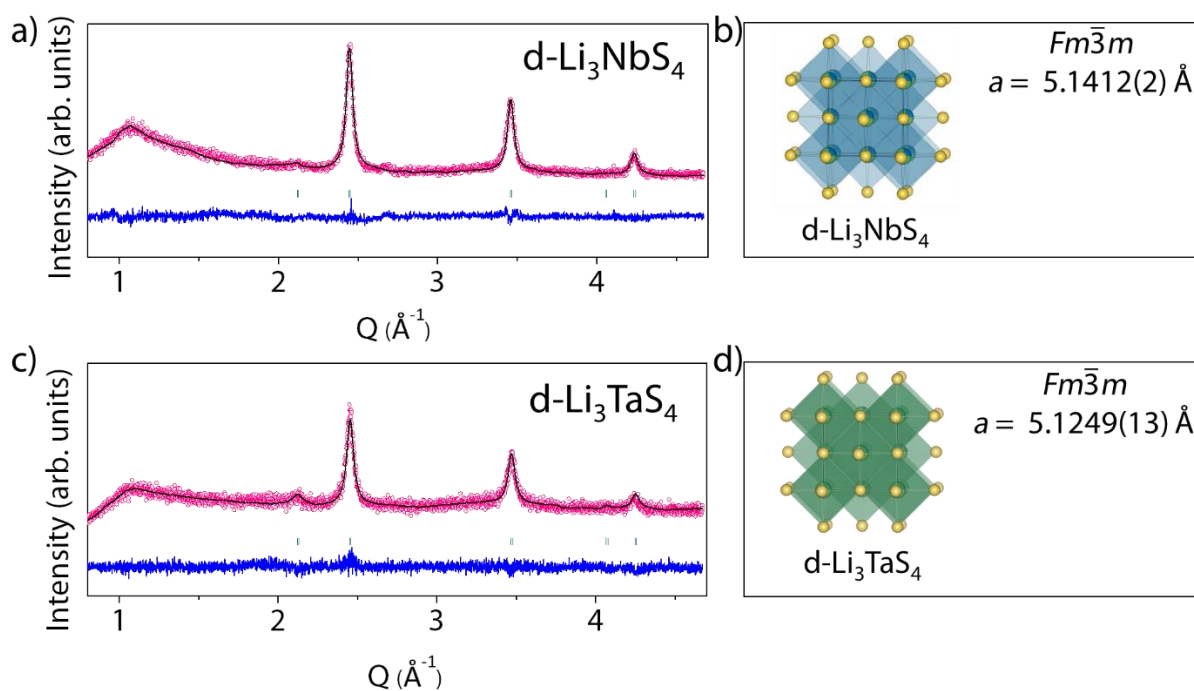


Figure III.3: (a) resp. (c) X-ray Rietveld refinement of *d*-Li₃NbS₄ resp. Li₃TaS₄ XRD patterns at 300 K. The pink circles, black continuous line, and bottom blue line represent the observed, calculated, and difference patterns, respectively. Vertical green tick bars stand for the Bragg positions. (b) resp. (d) Structure of *d*-Li₃NbS₄ resp. *d*-Li₃TaS₄, the lithium, niobium, tantalum and sulfur atoms are represented in light green, blue, dark green and yellow respectively.

Similarly a disordered rocksalt structure is obtained by replacing niobium by tantalum with a slightly smaller lattice parameter ($a = 5.1249(13) \text{ \AA}$) (cf. figure III.3 and Table III.3) which is counter intuitive due to the ionic radius of the tantalum atom being larger than that of the niobium atom. This could come from a Li/Ta understoichiometry.

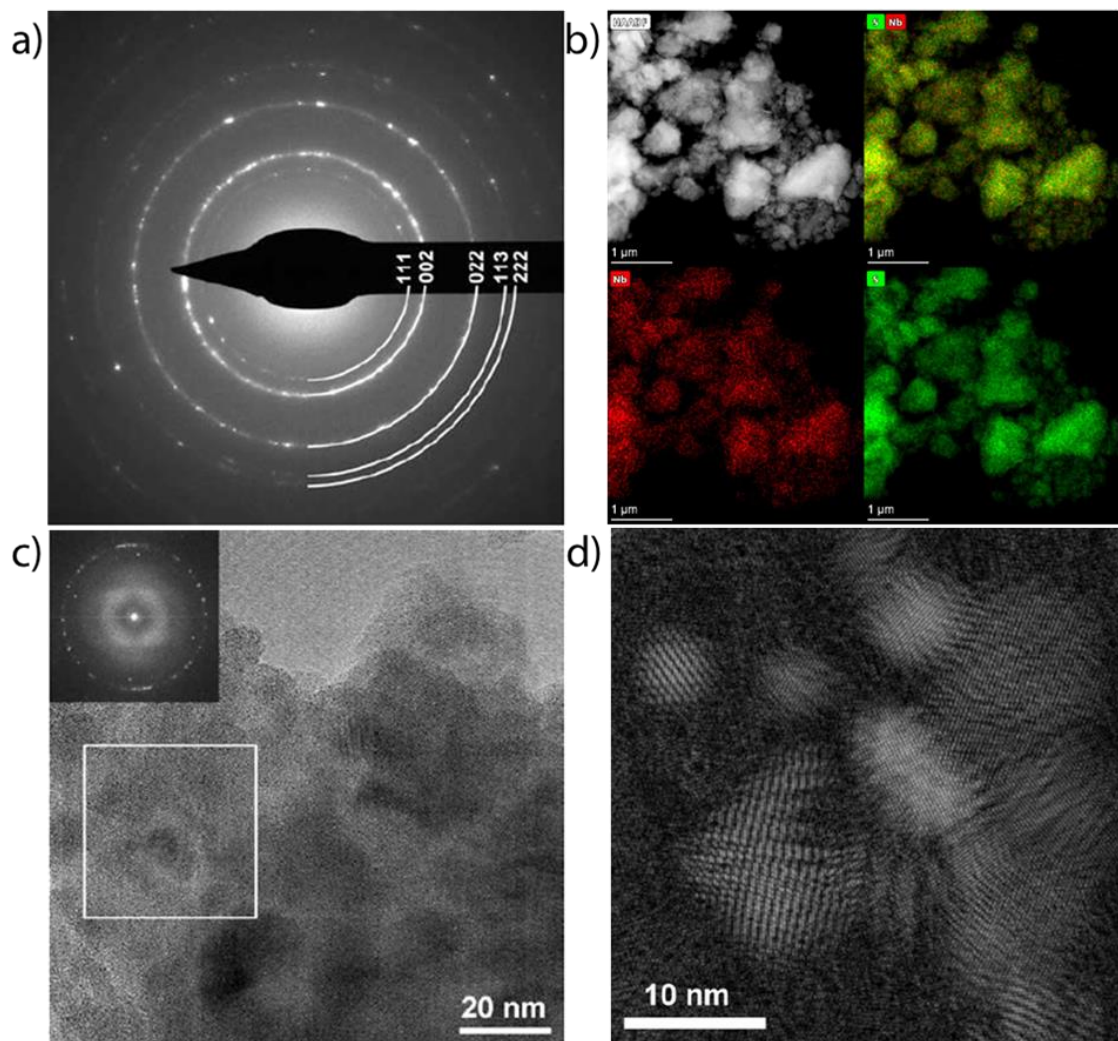


Figure III.4: (a) Ring electron diffraction pattern of d- Li_3NbS_4 . (b) HAADF-STEM image mixed color-coded compositional Nb/S map and individual Nb and S EDX maps. (c) HR-TEM image of the agglomerated nanoparticles in the BM- Li_3NbS_4 sample. Fourier transform in the upper left corner confirms that the nanoparticles are crystalline. (d) The Fourier-filtered enlarged image of the outlined area of panel c shows crystalline nanoparticles of 5-10 nm in size.

<i>d-Li₃NbS₄</i>		<i>Fm$\bar{3}$m</i>		$R_{bragg} = 9.94\%$		$\chi^2 = 1.64$	
$a = 5.1412(2) \text{ \AA}$						$Vol = 135.894(8) \text{ \AA}^3$	
<i>Atom</i>	<i>Wyckoff Position</i>	<i>x/a</i>	<i>y/a</i>	<i>z/a</i>	$B_{iso} (\text{\AA}^2)$	<i>Occupancy</i>	
S1	4b	1/2	1/2	1/2	0.92(21)	1	
Nb1	4a	0	0	0	1*	1/4	
Li1	4a	0	0	0	1*	3/4	

Table III.2: Crystallographic data and atomic positions for d-Li₃NbS₄ at 300 K using the complete model determined from Rietveld refinement of its X-ray diffraction pattern.

<i>d-Li₃TaS₄</i>		<i>Fm$\bar{3}$m</i>		$R_{bragg} = 13.6\%$		$\chi^2 = 1.37$	
$a = 5.1249(13) \text{ \AA}$						$Vol = 134.60(6) \text{ \AA}^3$	
<i>Atom</i>	<i>Wyckoff Position</i>	<i>x/a</i>	<i>y/a</i>	<i>z/a</i>	$B_{iso} (\text{\AA}^2)$	<i>Occupancy</i>	
S1	4b	1/2	1/2	1/2	2.7(3)	1	
Ta1	4a	0	0	0	1*	1/4	
Li1	4a	0	0	0	1*	3/4	

Table III.3: Crystallographic data and atomic positions for d-Li₃TaS₄ at 300 K using the complete model determined from Rietveld refinement of its X-ray diffraction pattern.

ii) *o*-Li₃NbS₄

Contrary to d-Li₃NbS₄ the *o*-Li₃NbS₄ polymorph, as far as we know, has never been reported and thus required structural resolution. A first indexation of the synchrotron XRD (SXR) pattern suggested a cubic lattice with an I centering and electron diffraction confirmed the space group $I\bar{4}3m$ with $a = 10.2973(2)$ Å. This similarity with the Li₃NbO₄ oxide naturally led to the proposal of an identical structural model, later confirmed by the Rietveld refinement of the SXR pattern (cf. Figure III.5a and table III.4).

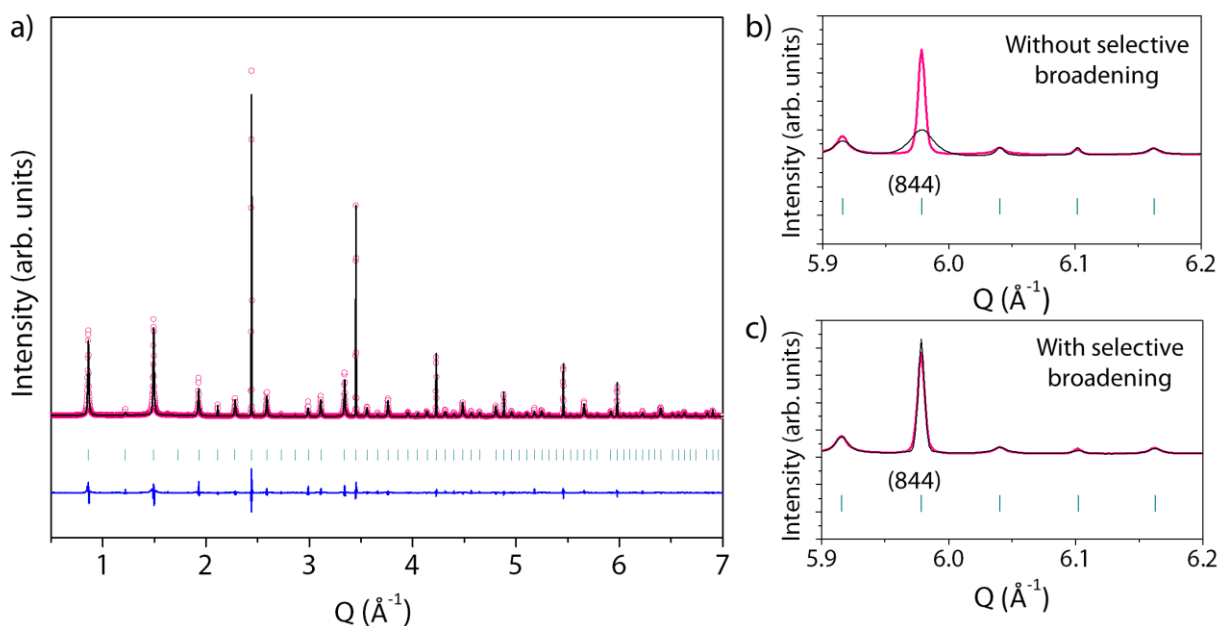


Figure III.5: (a) X-ray Rietveld refinement of *o*-Li₃NbS₄ at 300 K. The wavelength used for synchrotron X-ray is $\lambda = 0.4137$ Å. The pink circles, black continuous line, and bottom blue line represent the observed, calculated, and difference patterns, respectively. Vertical green tick bars stand for the Bragg positions. (b) Rietveld refinement of *o*-Li₃NbS₄ performed without using selective broadening conditions. We notice that the reflection (844) for example is poorly taken into account. (c) On the contrary, by using selective broadening conditions (the reflection with $h/2$, $k/2$, and $l/2$ integer and same parity, are kept sharp, and the other broadened), this reflection is well taken into account.

Structurally, *o*-Li₃NbS₄ shares with d-Li₃NbS₄ the same close-packed arrangement of cations and anions but differs from the disordered polymorph by a segregation of lithium and niobium crystallographic sites (cf. figure III.6a). Indeed, the NbS₆ octahedra in *o*-Li₃NbS₄ are linked to each other by the edges to form isolated Nb₄S₁₆ tetramers (cf. figure III.6b and c), the lithium atoms occupying the octahedral spaces left vacant. However, it is important to note that at first the refinement did not allow a decent fit of some reflections (cf. Figure III.5b). In order to understand the origin of this problem, a complementary transmission electron microscopy study was conducted.

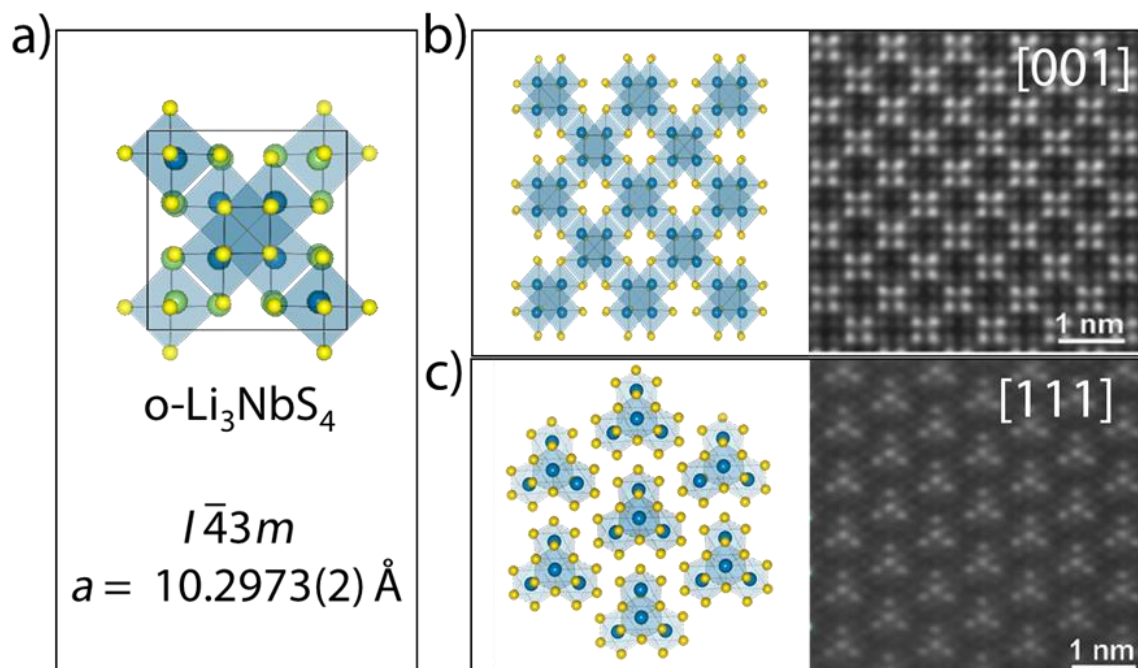


Figure III.6: (a) Structure of $o\text{-Li}_3\text{NbS}_4$. The lithium, niobium and sulfur atoms are represented in light green, blue and yellow respectively. (b) and (c) high resolution HAADF-STEM image of the ordered Li_3NbS_4 along either [001] or [111] direction and the corresponding structural scheme.

$o\text{-Li}_3\text{NbS}_4$ $a = 10.2973(2) \text{ \AA}$	$I\bar{4}3m$	$R_{\text{bragg}} = 3.99\%$	$\chi^2 = 31.8$	$\text{Vol} = 1091.874(5) \text{ \AA}^3$		
Atom	Wyckoff Position	x/a	y/a	z/a	$B_{\text{iso}} (\text{\AA}^2)$	Occupancy
S1	8c	0.8866(3)	0.8866(3)	0.8866(3)	1.492(20)	1
S2	24g	0.1206(2)	0.1206(2)	0.3633(2)	1.492(20)	1
Nb1	8c	0.1398(2)	0.1398(2)	0.1398(2)	1.186(10)	1
Li1	24g	0.3582(8)	0.3582(8)	0.1259(10)	0.50(14)	1

Table III.4: Crystallographic data and atomic positions for $o\text{-Li}_3\text{NbS}_4$ at 300 K using the complete model determined from Rietveld refinement of its synchrotron X-ray diffraction pattern.

Thus, HAADF-STEM images demonstrated presence of antiphase boundaries (APBs) (cf. Figure III.7) which arise when one ordered domain is shifted over $a/4$ with respect to another, closely resembling those previously observed in $\text{Li}_3\text{Ru}_{0.1}\text{Nb}_{0.9}\text{O}_4$.¹⁵⁸ Thus, this phenomenon was taken into account in the refinement, using selective broadening conditions dependent of the h, k, l indexes (the reflection with $h/2, k/2,$ and $l/2$ integer and same parity, are kept sharp, and the other broadened), and lead to a significant improvement of the fit (cf. Figure III.5c).

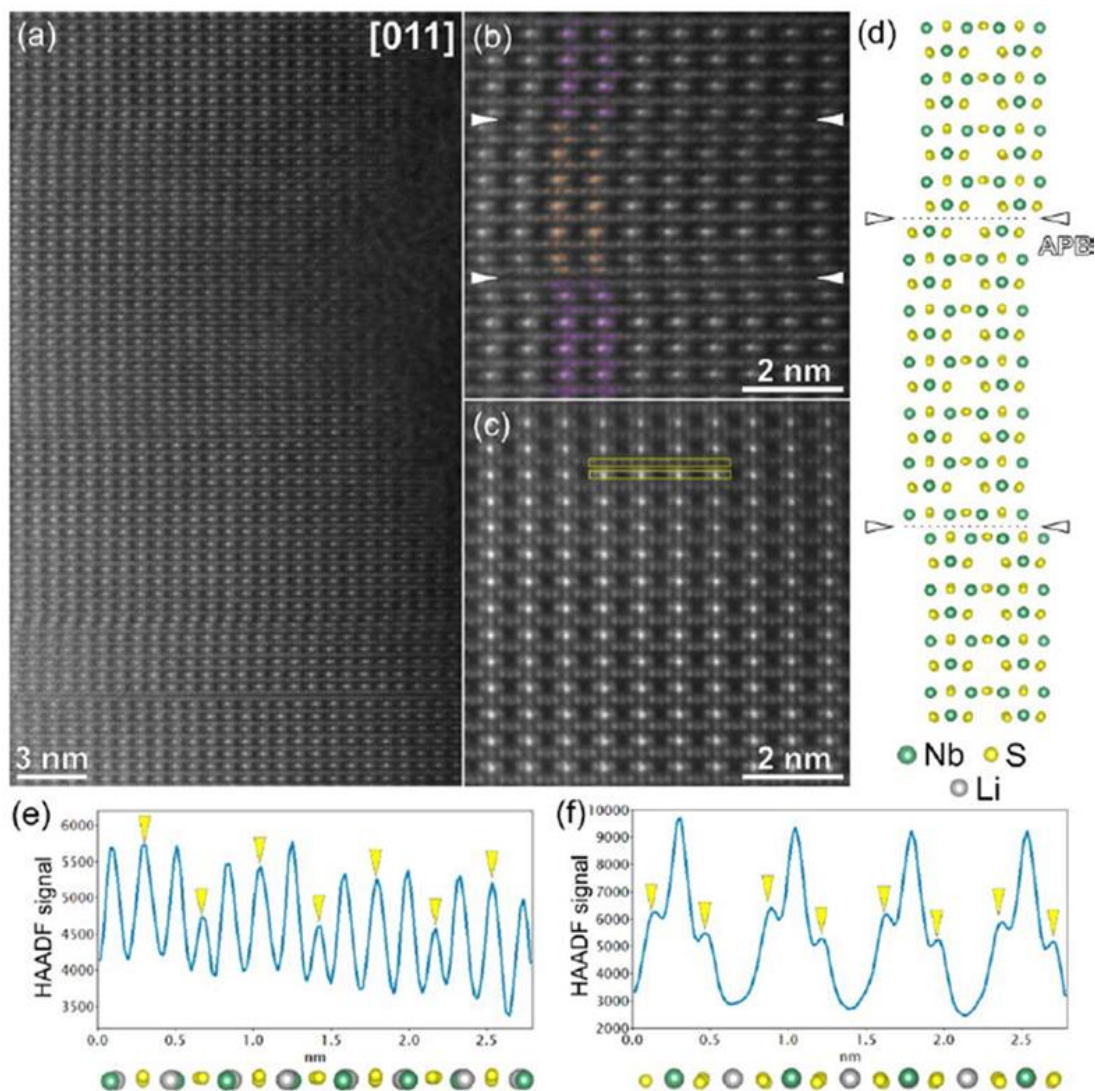


Figure III.7: [011] HAADF-STEM image of $o\text{-Li}_3\text{NbS}_4$ (a-c) showing that domains with ordered structure are separated by APBs marked with white arrowheads. Colored areas clearly illustrate the shift of the structure domains across the APB. Intensity profiles (e, f) along the structure fragments marked with yellow rectangles in (c), indicating the presence of Li/Nb mixing. Yellow arrowheads indicate the position of “pure” S atomic columns.

iii) *o*-Li₃TaS₄

As for *o*-Li₃NbS₄, there is to our knowledge no report of a structure of *o*-Li₃TaS₄ and an ab-initio resolution is necessary. Thus, a rough indexation of the reflections observed on the synchrotron X-ray pattern suggest a cubic lattice (*P*4₁32 with $a = 10.3184(3)$ Å). However, looking at the details of the diagram reveals a multitude of slight peak splitting (cf. inset of figure III.8) and a more accurate indexation indicates an orthorhombic lattice ($a = 10.3259(2)$ Å; $b = 7.2801(2)$ Å; $c = 7.3066(2)$ Å). Moreover, an analysis of the extinction conditions suggests to consider the *P*2₁22 space group. From this it is then necessary to build a structural model. Starting from the reasonable assumption that the structure could be derived from a rocksalt, a model was obtained by performing a symmetry lowering from the *Fm* $\bar{3}$ *m* cubic unit cell obtained for *d*-Li₃TaS₄ to the *P*2₁22 cell determined by reflections indexing using the following transformation:

$$(\mathbf{a}_o \quad \mathbf{b}_o \quad \mathbf{c}_o) = (\mathbf{a}_c \quad \mathbf{b}_c \quad \mathbf{c}_c) \begin{pmatrix} 2 & 0 & 0 \\ 0 & 1 & -1 \\ 0 & 1 & 1 \end{pmatrix}$$

Where the *o* and *c* subscripts refer to orthorhombic and cubic respectively.

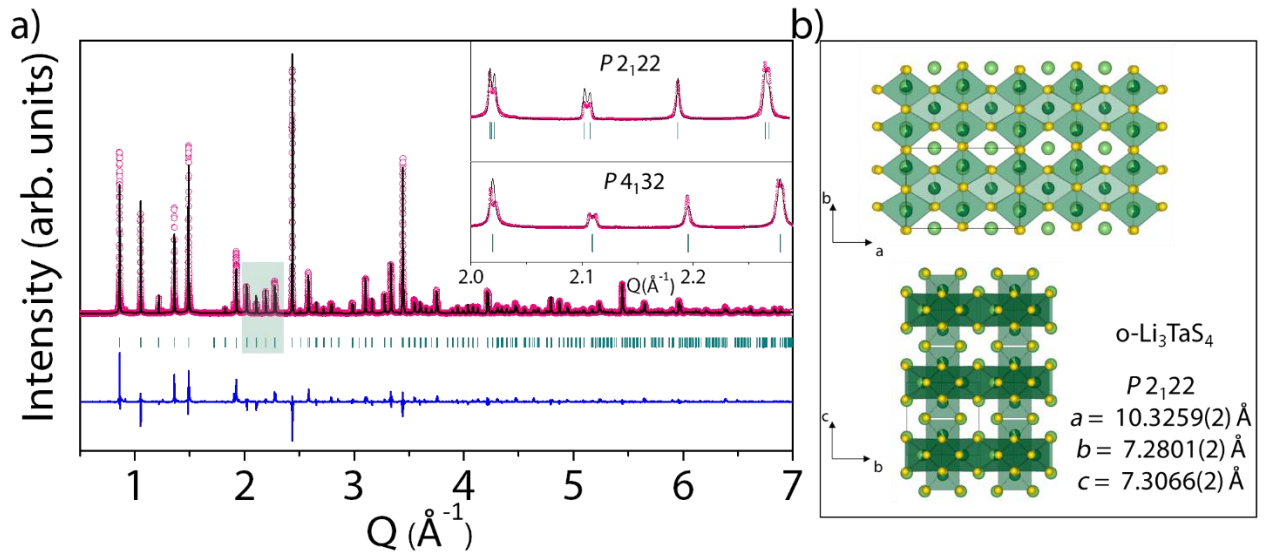


Figure III.8: (a) X-ray Rietveld refinement of *o*-Li₃TaS₄ at 300 K. The wavelength used for synchrotron X-ray is $\lambda = 0.4581$ Å. The pink circles, black continuous line, and bottom blue line represent the observed, calculated, and difference patterns, respectively. Vertical green tick bars stand for the Bragg positions. The upper inset refers to a zoom of the colored areas and the lower one represents a LeBail fit of the same *Q* region using a cubic unit cell. (b) Corresponding structure, the lithium, tantalum and sulfur atoms are represented in light green, dark green and yellow respectively.

At this stage, the atoms are approximately positioned in a cell of good size and symmetry, however the lithium and tantalum atoms are still randomly located on the same sites. By refining the occupation of the cationic positions under the constraint of a Li/Ta ratio around 3, we have achieved a satisfactory but not optimal refinement of the XRD pattern (cf. figure III.8a and table III.5).

$\alpha\text{-Li}_3\text{TaS}_4$		$P2_122$		$R_{\text{bragg}} = 15.3\%$		$\chi^2 = 21.4$	
$a = 10.3259(2) \text{ \AA}$		$b = 7.2801(2) \text{ \AA}$		$b = 7.3066(2) \text{ \AA}$		$\text{Vol} = 549.266(3) \text{ \AA}^3$	
Atom	Wyckoff Position	x/a	y/b	z/c	$B_{\text{iso}} (\text{\AA}^2)$	Occupancy	
S1	4e	0.9905(4)	0.9774(6)	0.7766(5)	0.49(3)	1	
S2	4e	0.5143(4)	0.5040(8)	0.2207(5)	0.49(3)	1	
S3	4e	0.2555(6)	0.2707(4)	0.0017(7)	0.49(3)	1	
S4	4e	0.7289(4)	0.7365(5)	0.4774(6)	0.49(3)	1	
Ta1	2d	1/4	1/2	0.7212(2)	1.51(13)	0.928(2)	
Ta2	2d	3/4	1/2	0.7221(8)	1.51(13)	0.192(2)	
Ta3	2a	1/2	0.7789(4)	0	1.51(13)	0.648(2)	
Ta4	2a	0	0.7803(6)	0	1.51(13)	0.454(2)	
Li1	2d	1/4	1/2	0.7212(2)	1.51(13)	0.072(2)	
Li2	2c	3/4	0	1/4	1.51(13)	1	
Li3	2d	3/4	1/2	0.7221(8)	1.51(13)	0.808(2)	
Li4	2c	1/4	0	1/4	1.51(13)	1	
Li5	2a	1/2	0.7789(4)	0	1.51(13)	0.352(2)	
Li6	2b	0	1/4	1/2	1.51(13)	1	
Li7	2a	0	0.7803(6)	0	1.51(13)	0.546(2)	
Li8	2b	1/2	1/4	1/2	1.51(13)	1	

Table III.5: Crystallographic data and atomic positions for $\alpha\text{-Li}_3\text{TaS}_4$ at 300 K using the complete model determined from Rietveld refinement of its synchrotron X-ray diffraction pattern.

According to the refinement, this compound would adopt a specific layered rocksalt structure with sulfur atoms in a cubic close-packed arrangement, and all the octahedral sites occupied with Li/Ta atoms. The cations are organized into pure Li 1D channels in the three space directions surrounded by a Li/Ta frameworks where the cations are randomly distributed. However, as mentioned above, the refinement remains largely perfectible and it is possible that

the simulated presence of tantalum and lithium atoms on certain crystallographic sites is only an artifact of the refinement induced by crystal defects (stacking faults etc...). An electron microscopy study and neutron diffraction experiments are progress to complete the XRD analysis.

Once the structures of Li_3MS_4 compounds are known, it is interesting to evaluate their electrochemical properties.

III.1.c Electrochemistry

Next, the electrochemical properties of the Li_3NbS_4 and Li_3TaS_4 polymorphs as cathodes for lithium batteries were studied (cf. figure III.9 a and b). As previously reported,^{156,159} it is possible to reversibly remove 2.5 lithium atoms from the d- Li_3NbS_4 compound on first charge in which ~ 2 lithium is re-inserted with a potential difference of 0.65 V between charge and discharge.

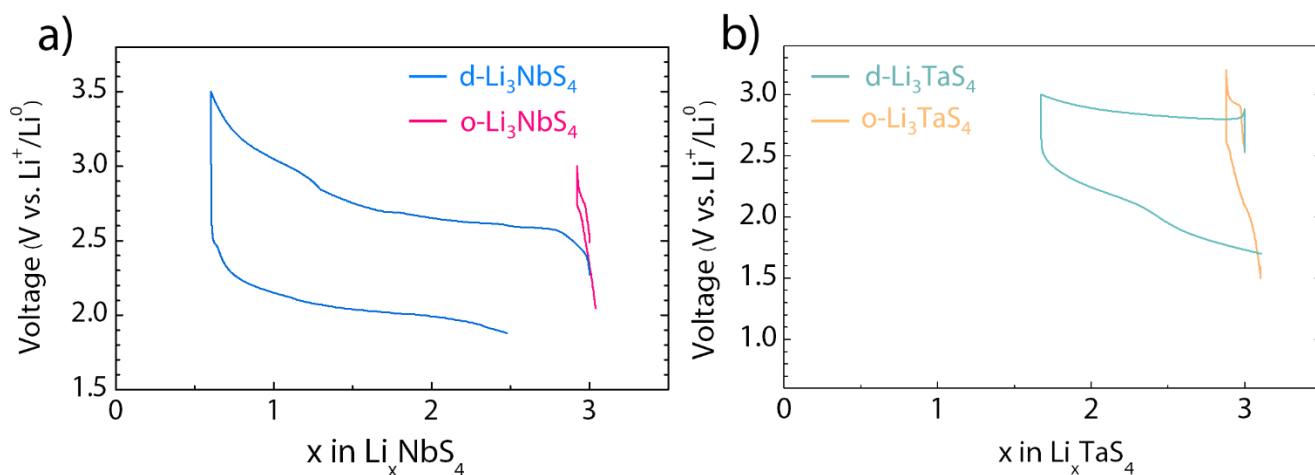


Figure III.9: (a) First cycle voltage–composition trace of d- Li_3NbS_4 (blue) and o- Li_3NbS_4 (pink) starting with oxidation and cycled at $C/20$. (b) First cycle voltage–composition trace of d- Li_3TaS_4 (green) and o- Li_3TaS_4 (orange) starting with oxidation and cycled at $C/20$.

Moreover, the reversible capacity decreases rapidly on cycling and becomes negligible after 5 cycles (cf. Figure III.10). On the contrary, it is nearly impossible to remove lithium from o- Li_3NbS_4 polymorph and the compound presents no electrochemical activity within the tested potential window of 2-3 V.

The Li_3TaS_4 polymorphs behave alike with the ordered compound having no electrochemical activity in oxidation unlike the disordered compound. It is however important to note that the

amount of lithium that can be removed from d- Li_3TaS_4 (= 1 Li) is much less than that of d- Li_3NbS_4 (= 2.5 Li).

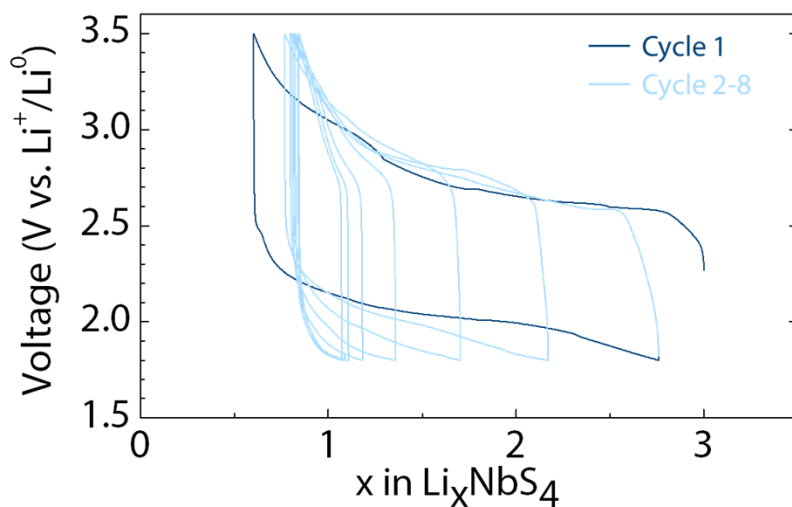


Figure III.10: Voltage–composition trace of d- Li_3NbS_4 . The first cycle is represented in navy blue and the cycles 2 to 8 in light blue.

In view of the observed drastic difference in electrochemical behavior of the Li_3NbS_4 polymorphs, which have yet the same chemical composition, it is natural to wonder about the origin of the difference between these two compounds that differ by their crystal structure and in their physico-chemical characters due to the used synthesis protocols. This is addressed in the next section.

III.1.d How to explain the difference in electrochemical behavior of the two polymorphs Li_3NbS_4 polymorphs ?

i) Effect of particle size and cationic disorder on the electrochemical behavior

It is well accepted in literatures that reducing the particle size of the material can enhance its electrochemical reactivity.^{141,142} d- Li_3NbS_4 being synthesized by high energy ball-milling exhibits nano-sized particles (10-15 nm) in contrary to the micron sized particles obtained for o- Li_3NbS_4 (0.5-1 μm). Therefore, to deeper investigate the effect of particle size on electrochemical behavior, the d- Li_3NbS_4 compound was annealed for 12 hours at different temperatures ranging from 100°C to 450°C in vacuum inside sealed quartz ampoule. The samples were analyzed by XRD for the crystal structure and particle size (cf. figure III.11). With increasing annealing temperature, two main effects were observed. On one hand, a progressive sharpening of the diffraction peaks is observed and on the other hand, beyond 400°C the appearance of superstructure peaks is noted. This indicates an increase in crystallite size/ crystallinity of the material and a progressive ordering of the lithium and niobium atoms through heating, respectively. The annealed samples were then studied for their electrochemical activity in Li-cells and the voltage vs composition figures were shown in Figure III.11b. A clear reduction in capacity is observed with increasing annealing temperature and the material heated at 450 °C showed almost no electrochemical activity. Finally, in order to link the structural evolution with the electrochemical properties, each of the X-ray pattern was refined according to the Rietveld method which allowed to extract the apparent size of the crystallites as well as the percentage of disorder of the cationic sites (the percentage of disorder is defined as the percentage of niobium atoms effectively occupying the niobium sites of the fully ordered phase). It is worth mentioning that the size of the crystallites obtained from XRD for the pristine d- Li_3NbS_4 (not sintered) is in good agreement with the one measured with TEM. Thus, using these results the evolution of the electrochemical capacity (number of lithium extracted on the first charge) of the materials together with the size of the crystallites and cationic disorder were plotted as function of annealing temperature in Figure III.11c. From this, it is clear that the decrease of the reversible capacity with annealing is closely associated to the increase of the crystallite size and to the appearance of a crystallographic order between the cations. However, it is difficult to separate these two effects.

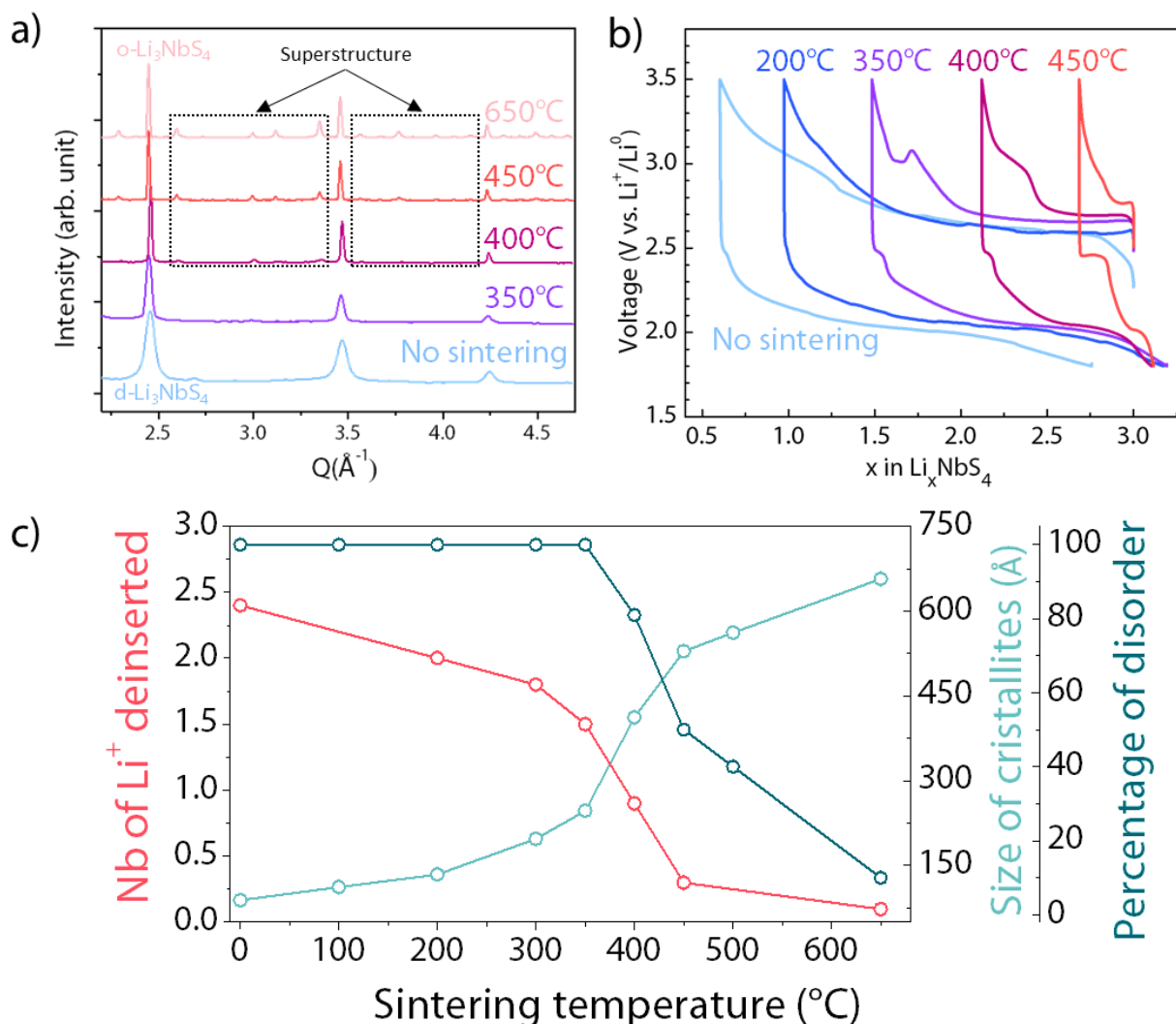


Figure III.11: (a) X-ray diffraction pattern of d-Li₃NbS₄ powders annealed for 12 hours at different temperatures. The Q regions where the superstructure peaks appear are highlighted. (b) First cycle voltage–composition trace of the annealed powders. (c) Evolution of the number of lithium deinserted during the first charge, of the size of the crystals determined by refinement of the X-ray diagrams and of the percentage of cation disorder as a function of the sintering temperature of d-Li₃NbS₄.

At this stage, we tried to understand the inactivity of the o-Li₃NbS₄. Similar electrochemical inactivity was already reported with isostructural Li₃NbO₄ that was described to be associated with the insulating behavior of the material due to d⁰ Nb⁵⁺ ions with empty 4d bands.¹⁴¹ By making them slightly conductive with Ru⁴⁺ substitution, the resulting Li₃Nb_{0.9}Ru_{0.1}O₄ was possible notably to insert lithium atoms in the structure.¹⁵⁸ In order to analyze this electronic conductivity effect, since we cannot remove lithium from o-Li₃NbS₄, we tried the inverse to insert lithium into the o-Li₃NbS₄, and the cycling figure is shown in Figure III.12a.

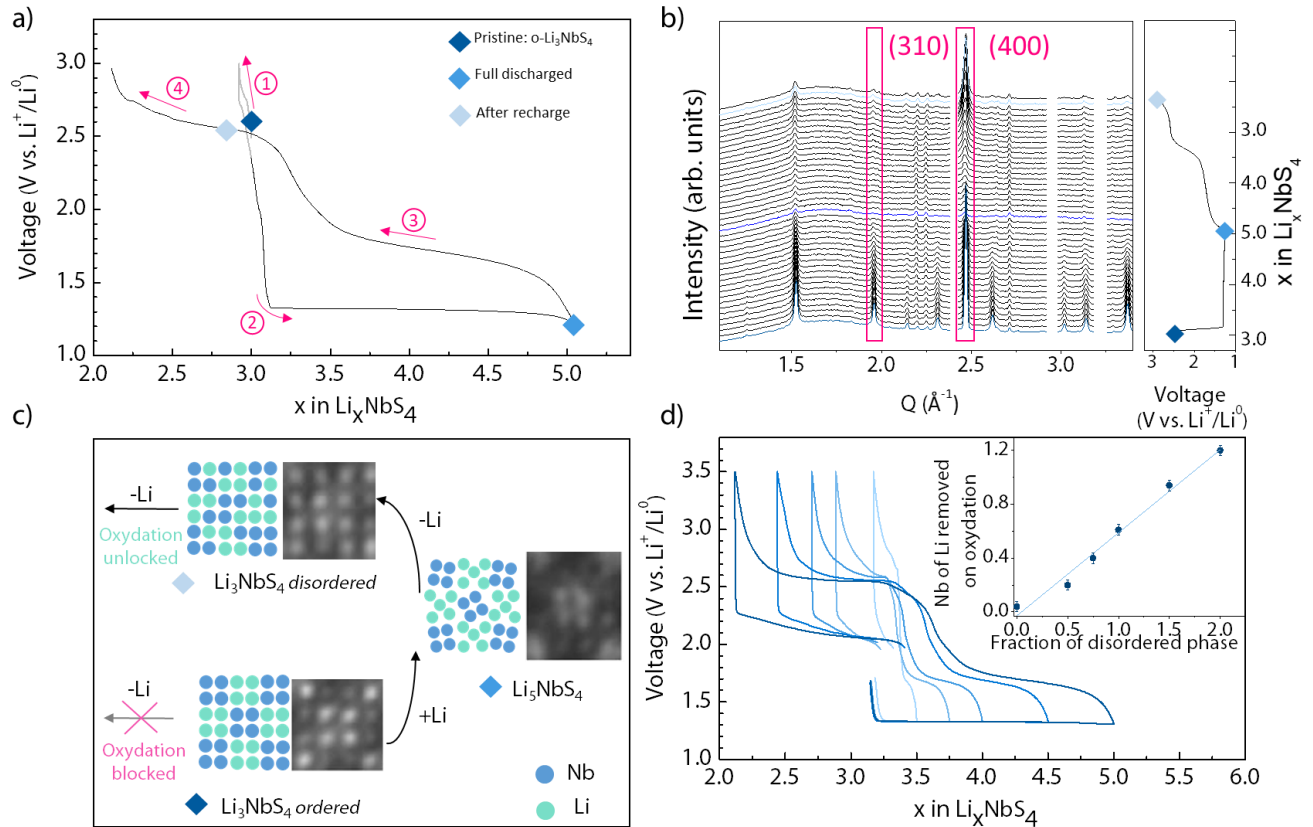


Figure III.12: (a) First cycle voltage–composition trace of $o\text{-Li}_3\text{NbS}_4$ starting in reduction. The pink arrows indicate the direction of cycling. (b) Operando XRD patterns during the first cycle of $o\text{-Li}_3\text{NbS}_4$ starting with reduction with the corresponding galvanostatic curves in the right panel. The compounds are cycled at $C/20$ and the XRD patterns were measured for every 1 h (0.05 Li insertion/ removal). The XRD patterns corresponding to $o\text{-Li}_3\text{NbS}_4$, Li_5NbS_4 and $r\text{-Li}_3\text{NbS}_4$ are plotted in navy, sky and light blue respectively. The (310) and (400) reflections are framed in pink color to highlight the evolution of the intensity ratio between the $o\text{-Li}_3\text{NbS}_4$ and the $r\text{-Li}_3\text{NbS}_4$. (c) Schematic of the structural evolution of Li_3NbS_4 during lithium insertion/disinsertion. HAADF-STEM images of the Nb_4S_{16} tetramers are represented for each steps of the mechanism. (d) Evolution of the voltage–composition trace of $o\text{-Li}_3\text{NbS}_4$ as a function of the number of lithium initially inserted. The insert represents the evolution of the number of lithium extracted by the 2.6 V electrochemical process as a function of the number of lithium initially inserted in $o\text{-Li}_3\text{NbS}_4$.

ii) Insertion of Lithium in $o\text{-Li}_3\text{NbS}_4$

From Figure III.12a, it can be seen that nearly two lithium can be inserted into the $o\text{-Li}_3\text{NbS}_4$ indicating that this compound is not electronically insulating (which is coherent with its brownish color). The lithiation happens through a reduction plateau at 1.3 V until $x = 5.0$ (with x the number of lithium in Li_xNbS_4). The subsequent charge operates by a different electrochemical process at 1.7 V until $x = 3.2$ and beyond this point a new plateau is observed at around 2.6 V until $x = 2.1$. This last process is reversible in discharge with a polarization between oxidation and reduction of 0.5 V (see Figure III.13). In short, once the lithiation of Li_3NbS_4 is carried out, it activates the lithium removal on subsequent charge. To understand

the origin of this phenomenon, an operando X-ray experiment has been performed (cf. Figure III.12b).

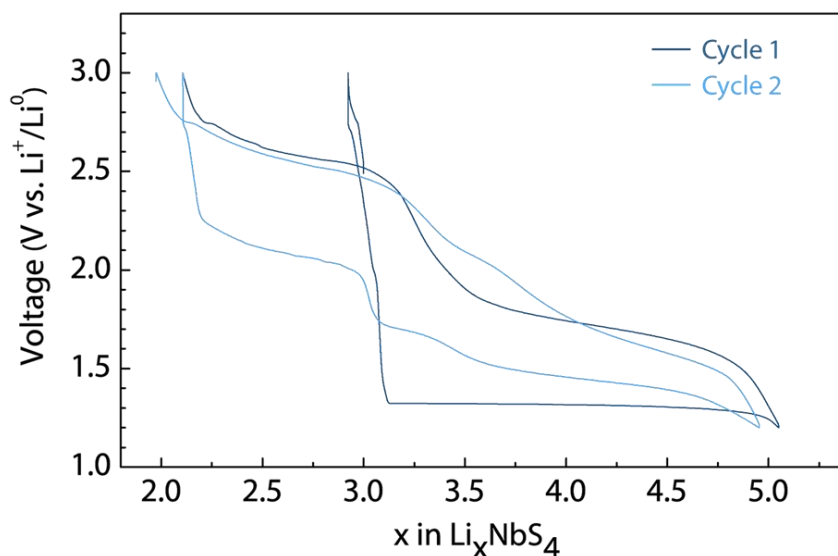


Figure III.13: Voltage–composition trace of o-Li₃NbS₄. The first cycle is represented in navy blue and the second one in light blue.

A biphasic process is observed during discharge throughout the 1.3 V plateau, where the intensity of the reflections associated with pristine disappears in favor of an amorphous or poorly crystallized phase. In recharge, peaks reappear progressively whose positions correspond to those of pristine with nevertheless very different relative intensities, indicating a probable modification of the cationic order. This last hypothesis was verified by a Rietveld refinement of the pattern measured at $x = 3.2$, which indicated a percentage of disorder of 84% between niobium and lithium atoms. Upon further lithium removal (from $x = 3.2$ to $x = 2.5$), no big changes in the XRD patterns are observed.

These results coupled with those of the previous section strongly suggest that the activation of the oxidation of the compound below $x = 3$ is directly related to the cationic disorder obviously generated by the preliminar insertion step. To clarify this, and, in particular, to better understand the structural process involved in the first oxidation plateau, a complementary TEM study was carried out.

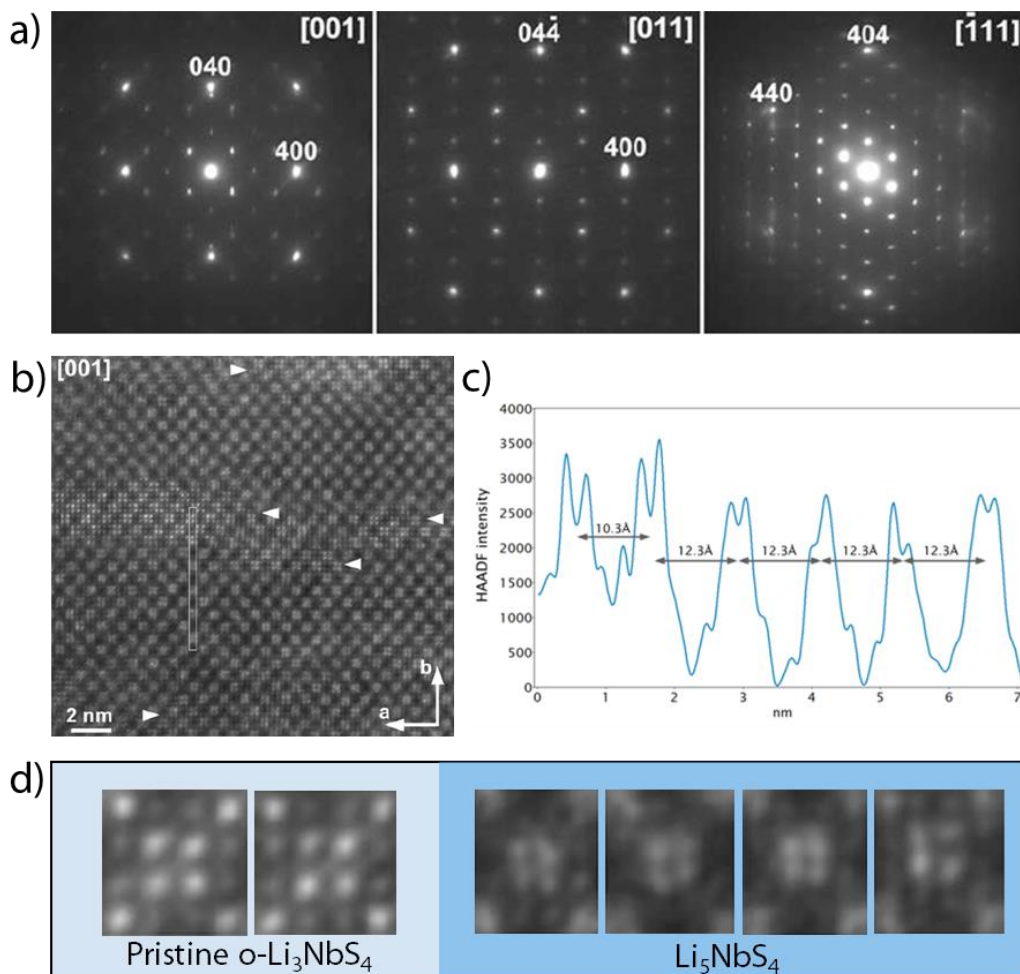


Figure III.14: (a) Electron diffraction patterns of Li_5NbS_4 taken along the main zone axes of the I-centred cubic unit cell. (b) [001] HAADF-STEM image of Li_5NbS_4 . The domains of the pristine phase are marked with arrowheads. (c) The HAADF intensity profile along the area selected in panel c crossing the pristine and lithiated domains. The Nb_4S_{16} clusters appear as double peaks in the profile. These peaks are well-defined in the pristine phase (left) and separated by 10.3 Å. The peaks in the lithiated phase are smeared and separated by 12.3 Å. (d) Comparison of the atomic arrangements in the randomly picked up Nb_4S_{16} clusters (four central dots) in the pristine and lithiated phases. Note perfect positional order in the pristine phase and random atomic displacements in the lithiated phase.

The Li_5NbS_4 compound was first studied. In spite of apparent absence of sharp reflections in the powder XRD pattern, its crystallites demonstrate well-defined electron diffraction patterns (cf. figure III.14a). In addition, HAADF-STEM images (cf. figure III.14 b-d) indicates the co-existence of two crystalline phases one cubic with $10.3 \times 10.3 \text{ \AA}$ ab mesh that is equivalent to pristine o- Li_3NbS_4 and the other one lithiated and distorted with the $10.3 \times 12.3 \text{ \AA}$ ab mesh. At crystallite level, the lithiated phase is then fragmented into small domains being interrupted with lamellas of the pristine phase of 3-5 nm in width (cf. figure III.14b). Structurally, the main difference between pristine and lithiated compound comes from the Nb_4S_{16} tetramers. Indeed,

perfect positional order is maintained in the pristine phase, whereas random atomic displacements appear in the lithiated phase (cf. Figure III.12c and III.14d). Although the clusters appear to perfectly follow the $10.3 \times 12.3 \text{ \AA}$ lattice, the exact atomic positions within the clusters lose periodicity resulting in quasi-amorphous state observed on XRD.

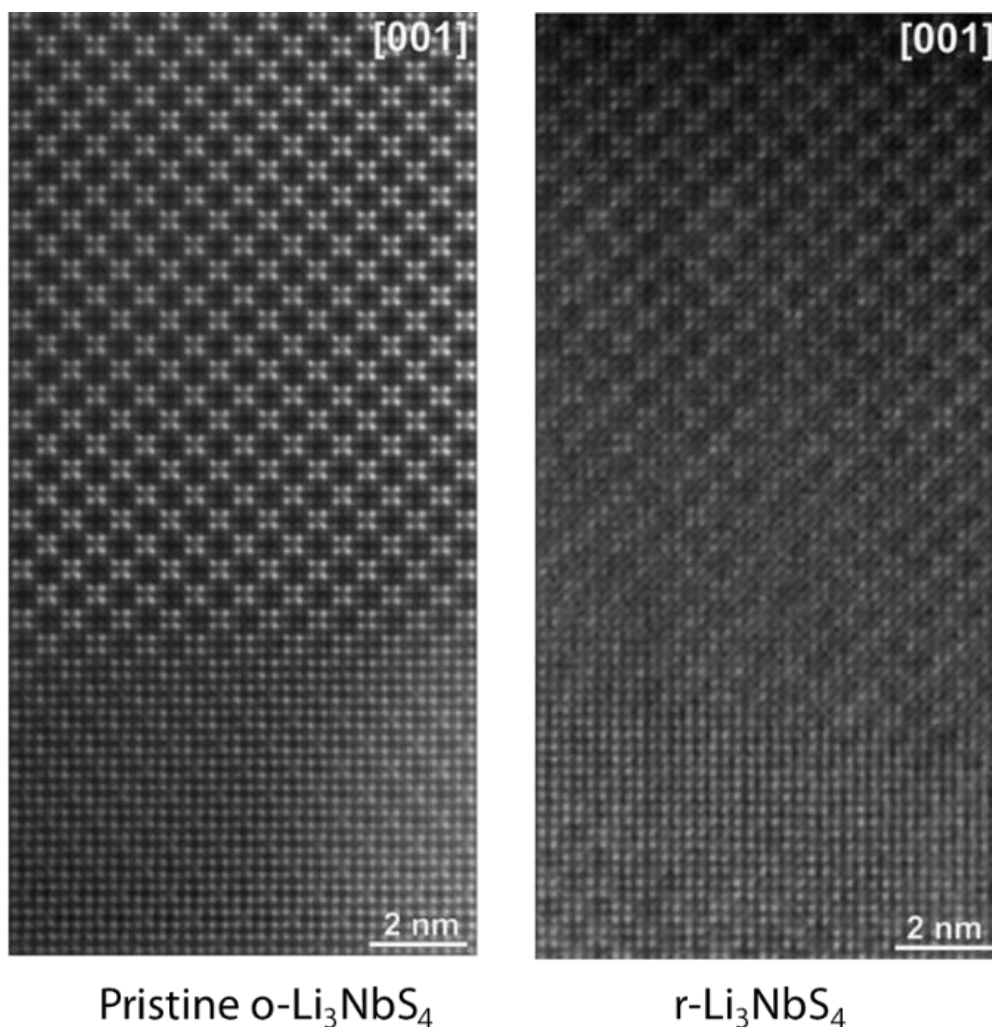


Figure III.15: [001] HAADF-STEM images of o-Li₃NbS₄ and r-Li₃NbS₄, illustrating the presence of disordered nanosized domains in the two structures.

In a second step, TEM analysis of the compound obtained after the removal of about 2 lithium from Li₅NbS₄ (referred as recharged-Li₃NbS₄ or r-Li₃NbS₄ in the following text) confirms an increase of the cationic disorder (cf. figure III.15). Within the particle, this disorder is expressed in a biphasic way with an inter-growth of o-Li₃NbS₄ and d-Li₃NbS₄. It is reasonable to think that the cationic disorder observed in this phase is a direct consequence of the atomic position disorder observed in the Li₅NbS₄ phase. Moreover, in comparison with pristine, the successive

lithium insertion/removal processes do not seem to have a significant effect on the particle size. Thus, these results suggest that the activation of the oxidation of o-Li₃NbS₄ comes only from the Nb/Li disorder. To highlight this, we studied the charge capacity evolution as a function of the amount of lithium inserted in o-Li₃NbS₄ ($x = 3.5, 4.0 \dots$) (cf. figure III.12d). The results shown in figure III.12d indicate that the charge capacity increases with the conversion rate of o-Li₃NbS₄ to Li₅NbS₄ in a linear way. It demonstrates that the activation of Li₃NbS₄ oxidation is directly related with the amount of disordered regions created in the material. Altogether these results show unambiguously the primordial role of the cationic disorder in triggering the electrochemical activity of Li₃NbS₄ in oxidation (deinsertion of lithium).

At this stage, it remains to understand the charge compensation mechanism and how the cation disordering helps in triggering the electrochemical activity of o-Li₃NbS₄ and d-Li₃NbS₄. To do this, we carried out XPS analyses of the o- and d-Li₃NbS₄ at different stages of oxidation and reduction, and the results are discussed next.

iii) Charge compensation mechanisms

XPS spectra of Nb 3d and S 2p were collected for both polymorphs at different states of charge (cf. figure III.16b) and the evolution of the proportion of charged species is shown in figure III.16c.

Starting with o-Li₃NbS₄, the analysis of the spectra indicates that the pristine is mainly composed of Nb⁵⁺ and S²⁻ with traces of Nb⁴⁺ and oxidized sulfur referred as Sⁿ⁻ in the following text. The trace amount of Nb⁴⁺ and Sⁿ⁻ could be related with the surface reactivity of the material during synthesis and/or on exposure to air. By insertion of lithium (Li₄NbS₄ and then Li₅NbS₄), the Nb⁵⁺/Nb⁴⁺ ratio decreases while the S²⁻/Sⁿ⁻ remains constant indicating a mainly cationic reduction process. Nevertheless, it is interesting to note that the S2p spectra of Li₄NbS₄ and Li₅NbS₄ are marked by a significant amount of highly oxidized Sⁿ⁻-sulfur species. However, the quantification on the Li/Nb ratio and further analyses on the spectra indicate that such increase in oxidized sulfur is probably due to a conversion reaction in competition with the insertion one forming elemental sulfur or polysulfides on the surface of the particles themselves.

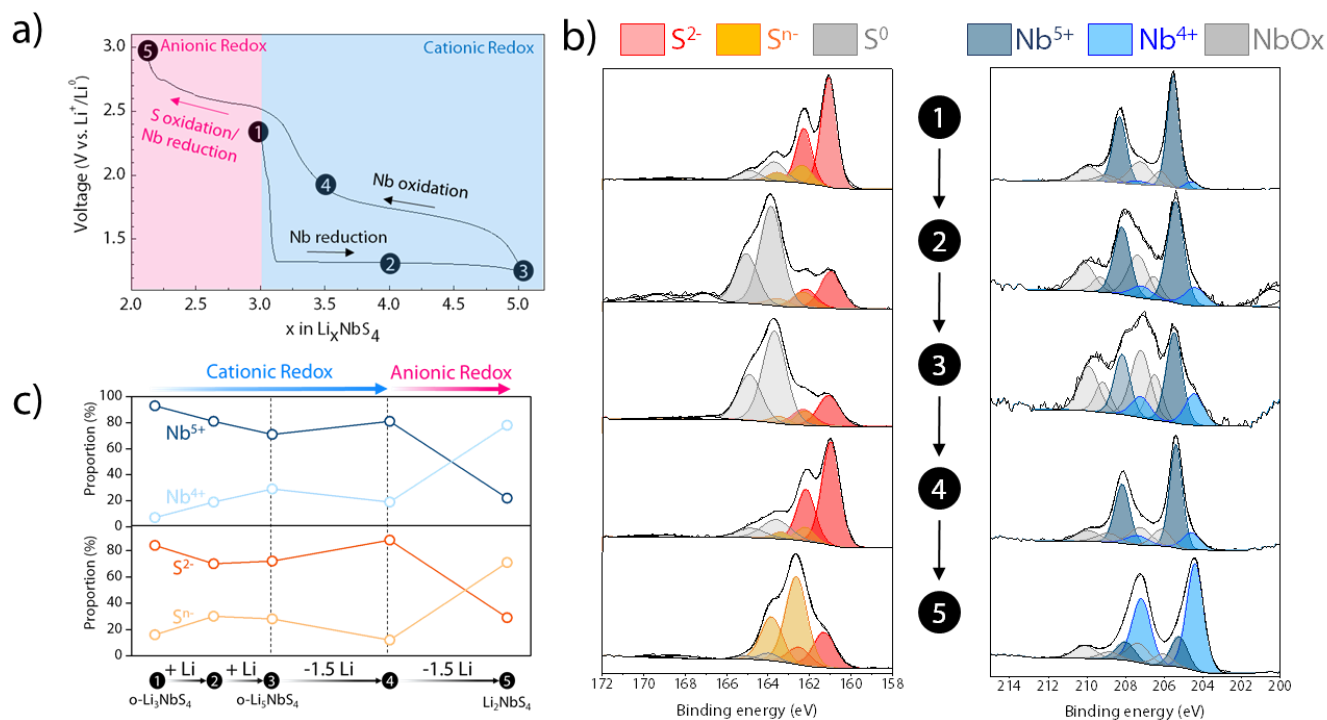


Figure III.16: (a) Electrochemical curve of $o\text{-Li}_3\text{NbS}_4$; the numbered points correspond to the ex-situ samples prepared for XPS analysis. The blue area corresponds to the mainly cationic electrochemical process, while the pink area corresponds to the anionic redox process. (b) S 2p resp. Nb 3d XPS spectra. The S 2p resp. Nb 3d spectra have been decomposed in several components: S^{2-} , $\text{S}^{\text{n-}}$ and a surface contribution of elemental sulfur S^0 resp. Nb^{5+} , Nb^{4+} and some surface oxides NbO_x . (c) Evolution of $\text{Nb}^{5+}/\text{Nb}^{4+}$ and $\text{S}^{2-}/\text{S}^{\text{n-}}$ species as deduced from XPS analysis.

Upon recharge, the XPS spectra of $\text{Li}_{3.5}\text{NbS}_4$ (point 4 in Figure III.16a) are very similar to those of the pristine particles, with mainly S^{2-} and Nb^{5+} , indicating that the electrochemical behavior is reversible from the point of view of charge compensators. Lastly upon further oxidation (up to Li_2NbS_4) the redox process is marked by a sharp decrease of S^{2-} species to the benefit of $\text{S}^{\text{n-}}$ ones indicating sulfur oxidation; while surprisingly the $\text{Nb}^{5+}/\text{Nb}^{4+}$ ratio decreases significantly. To better understand this apparent contradictory behavior, a count of Nb and S charges evolution (considering S^- as the oxidized sulfur species) during this last oxidation step has been done and indicates that the negative charge brought by Li removal and Nb reduction are well compensated by sulfur oxidation. This confirms that sulfur oxidation and niobium reduction are concomitant and refers to reductive coupling mechanism as already observed in oxides. A similar charge evolution is observed with XPS spectra of $d\text{-Li}_3\text{NbS}_4$ upon oxidation (cf. figure III.17). S 2p and Nb 3d spectra of the pristine are found close to the ordered polymorph ones with however a $\text{S}^{2-}/\text{S}^{\text{n-}}$ ratio slightly smaller for $d\text{-Li}_3\text{NbS}_4$. Upon lithium removal, a sharp oxidation of S^{2-} into $\text{S}^{\text{n-}}$ with a concomitant reduction of Nb^{5+} into Nb^{4+} is observed. On subsequent discharge the Niobium redox state is almost found unchanged while the sulfur is

only slightly reduced, therefore, this mechanism does not seem, at least in appearance, reversible.

In short, the XPS results demonstrate that lithium insertion in o- Li_3NbS_4 occurs mainly through cationic redox while removal in both polymorphs occurs through anionic redox with participation of the cation via reductive coupling mechanism. Thus, these results indicate that the inactivity of o- Li_3NbS_4 in oxidation is related to the anionic nature of this process. In other words, the disordering of the compound seems to activate the anionic redox.

At this stage, it is interesting to see whether the similar anionic redox process could be activated by another way. The numerous works reported in Li_2MnO_3 or Li_2TiS_3 compounds utilized substitution of redox inactive $\text{Ti}^{4+}/\text{Mn}^{4+}$ by redox active cation such as Fe^{2+} , Ti^{3+} etc to activate anionic redox process.^{79–81} With this idea in mind, we embarked on synthesis exploration of substituted Li_3NbS_4 phases.

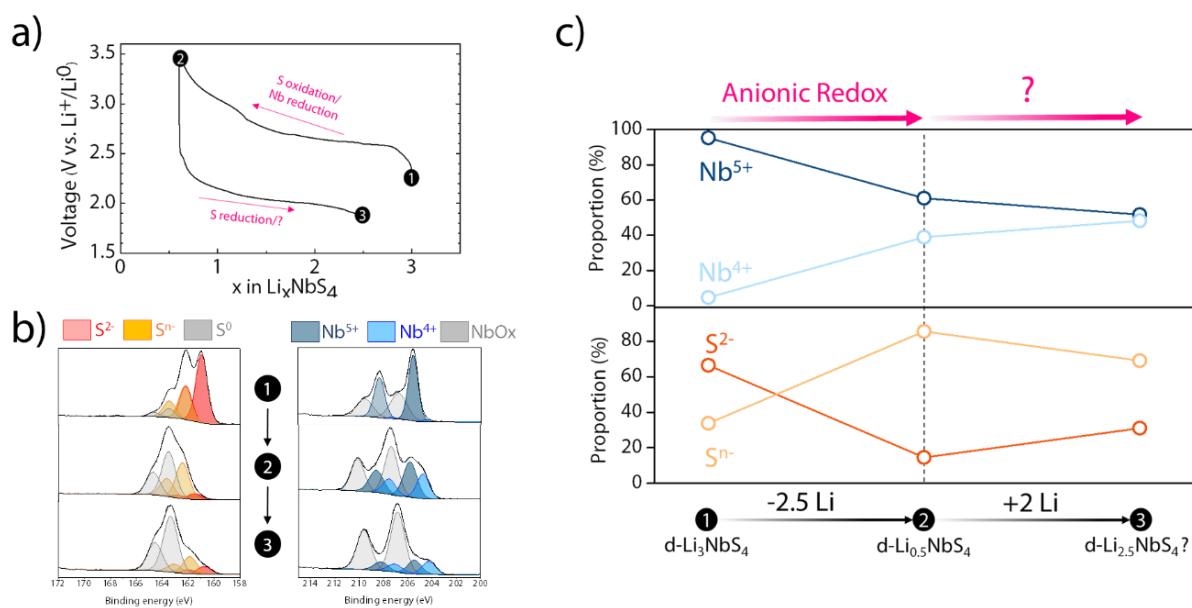


Figure III.17: (a) Electrochemical curve of d- Li_3NbS_4 ; the numbered points correspond to the ex-situ samples prepared for XPS analysis. The blue area corresponds to the mainly cationic electrochemical process, while the pink area corresponds to the anionic redox process. (b) S 2p resp. Nb 3d XPS spectra. The S 2p resp. Nb 3d spectra have been decomposed in several components: S^{2-} , S^n and a surface contribution of elemental sulfur S^0 resp. Nb^{5+} , Nb^{4+} and some surface oxides NbO_x . (c) Evolution of $\text{Nb}^{5+}/\text{Nb}^{4+}$ and S^{2-}/S^n species as deduced from XPS analysis.

iv) Cationic substitution

Different Li_3NbS_4 -MS solid solutions has been investigated ($M = \text{V}, \text{Cr}, \text{Mn}, \text{Fe}$ or Co). Among all syntheses trials, only two compounds with a cationic mixture could be obtained pure: $\text{Li}_{1.2}\text{Nb}_{0.4}\text{Fe}_{0.4}\text{S}_2$ and $\text{Li}_{1.12}\text{Nb}_{0.38}\text{Mn}_{0.5}\text{S}_2$. The synthesis of these two compounds were performed using niobium powder, lithium sulfide, iron sulfide/ manganese sulfide (Alfa-Aesar, 99.9 %) and elemental sulfur in stoichiometric amounts and following the same procedure as for $\text{o-Li}_3\text{NbS}_4$.

It is interesting to note that these two materials have a different structure (cf. figure III.18a). While the Mn-substituted material crystallizes in the form of a disordered rocksalt, the iron compound adopts a lamellar O3-type structure similar to $\text{Li}_{1.13}\text{Ti}_{0.57}\text{Fe}_{0.3}\text{S}_2$ (LTFS).⁸¹ This difference in structure between the two Nb-based compounds could be related to the different size of the Fe^{2+} and Mn^{2+} atoms. Fe^{2+} being closer in ionic radius to that of Nb^{5+} could stabilize the layered structure, whereas Mn^{2+} whatever the spin state, has an ionic radius about 10% larger than iron and stabilize disordered rocksalt structure. However, such conclusion requires further theoretical investigations.

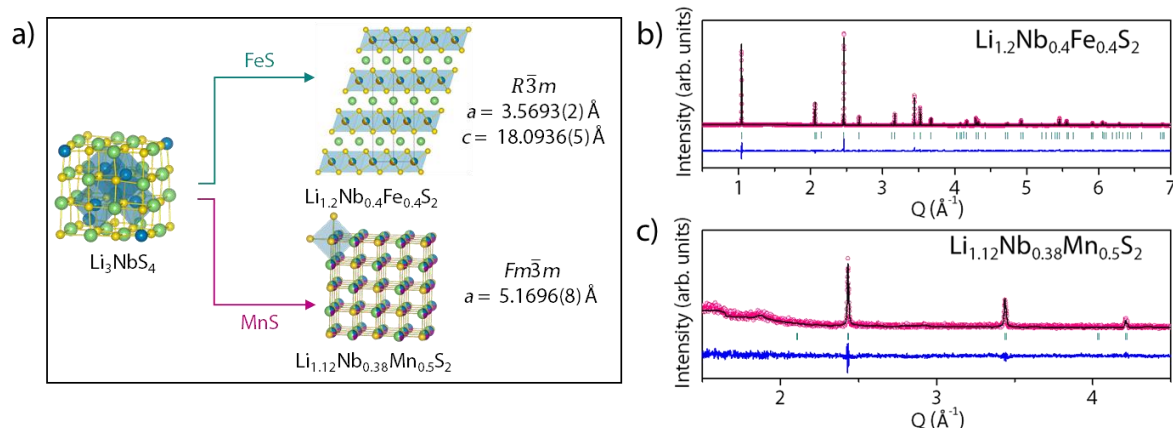


Figure III.18: (a) Structure of LNFS and LNMS. (b) resp. (c) X-ray Rietveld refinement of LNFS resp. LNMS XRD patterns at 300 K. The pink circles, black continuous line, and bottom blue line represent the observed, calculated, and difference patterns, respectively. Vertical green tick bars stand for the Bragg positions.

To study the redox activity of these materials, electrochemical cells were assembled and the electrochemical traces for the two first cycles of these materials are represented on figure III.19 a and b. It is possible to remove 0.9 lithium per formula unit from $\text{Li}_{1.2}\text{Nb}_{0.4}\text{Fe}_{0.4}\text{S}_2$ (LNFS) with an electrochemical process around 2.45 V in a reversible way, hence having another sulfide system besides $\text{Li}_{1.13}\text{Ti}_{0.54}\text{Fe}_{0.33}\text{S}_2$ in which electrochemical activity is triggered by adding Fe^{+2} . On the contrary, $\text{Li}_{1.13}\text{Nb}_{0.38}\text{Mn}_{0.5}\text{S}_2$ (LNMS) is found mostly inactive. Such inactivity of the

disordered rocksalt phases is frequently observed with compounds having reduced Li/transition metal ratio (poor lithium stoichiometry) and explained to be associated with the limited lithium percolation pathway for the Li-removal. Here the composition is particularly poor in lithium and the particles formed at high temperature are much larger than those obtained by mechanical synthesis. The combination of these two effects probably explains the lack of activity of this compound.

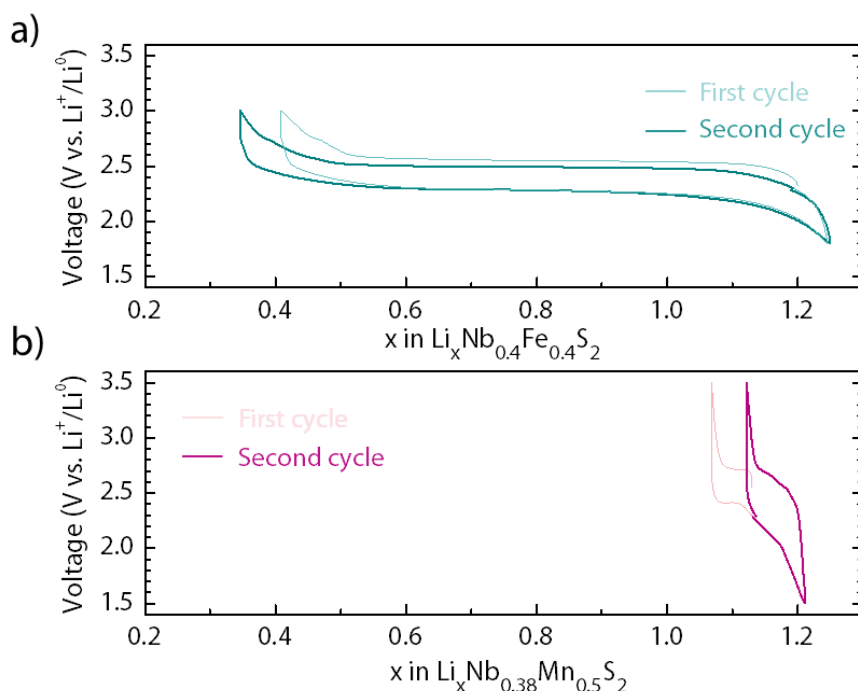


Figure III.19: (a) (resp. (b)) First and second cycle voltage composition trace of LNFS (resp. LNMS). It is worth mentioning that the amount of reversibly inserted lithium in LNFS increases even slightly on cycling probably due to an electrochemical milling effect.

Due to the electrochemical inactivity of the Mn-substituted Li_3NbS_4 , we then focused on solely studying $\text{Li}_{1.2}\text{Nb}_{0.4}\text{Fe}_{0.4}\text{S}_2$. The operando XRD analysis of LNFS showed a biphasic process upon charge which is reversible on discharge (cf. figure III.20).

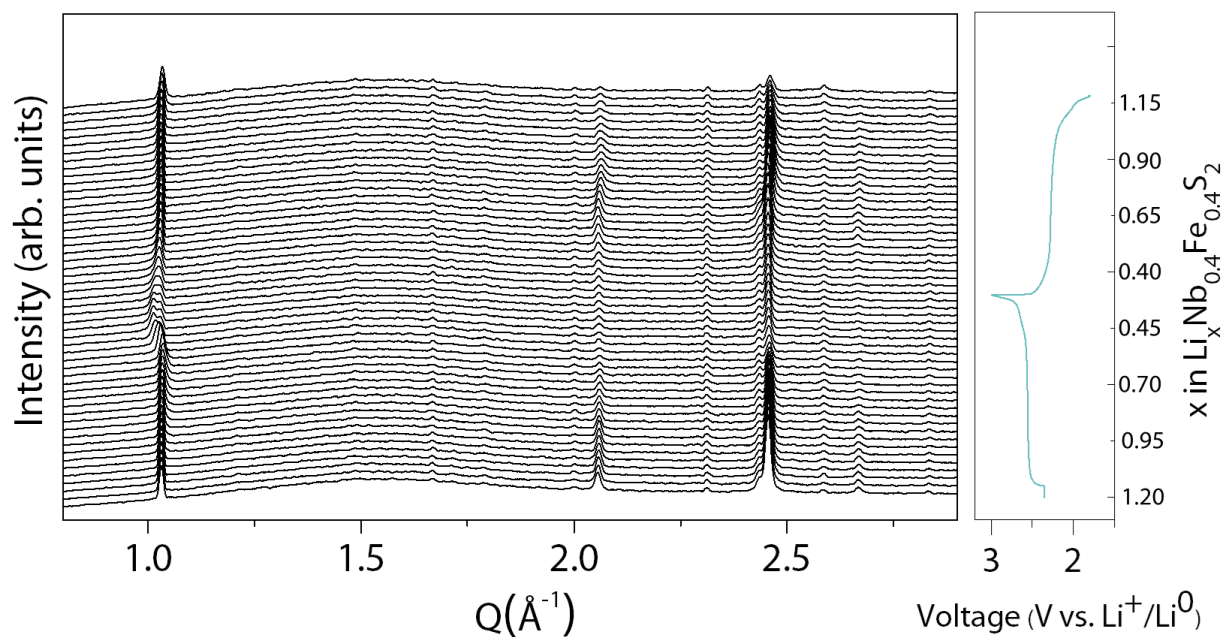


Figure III.20: Operando XRD patterns during the first cycle of LNFS with the corresponding galvanostatic curves in the right panel. The compounds are cycled at C/20 and the XRD patterns were measured for every 1 h (0.05 Li insertion/ removal).

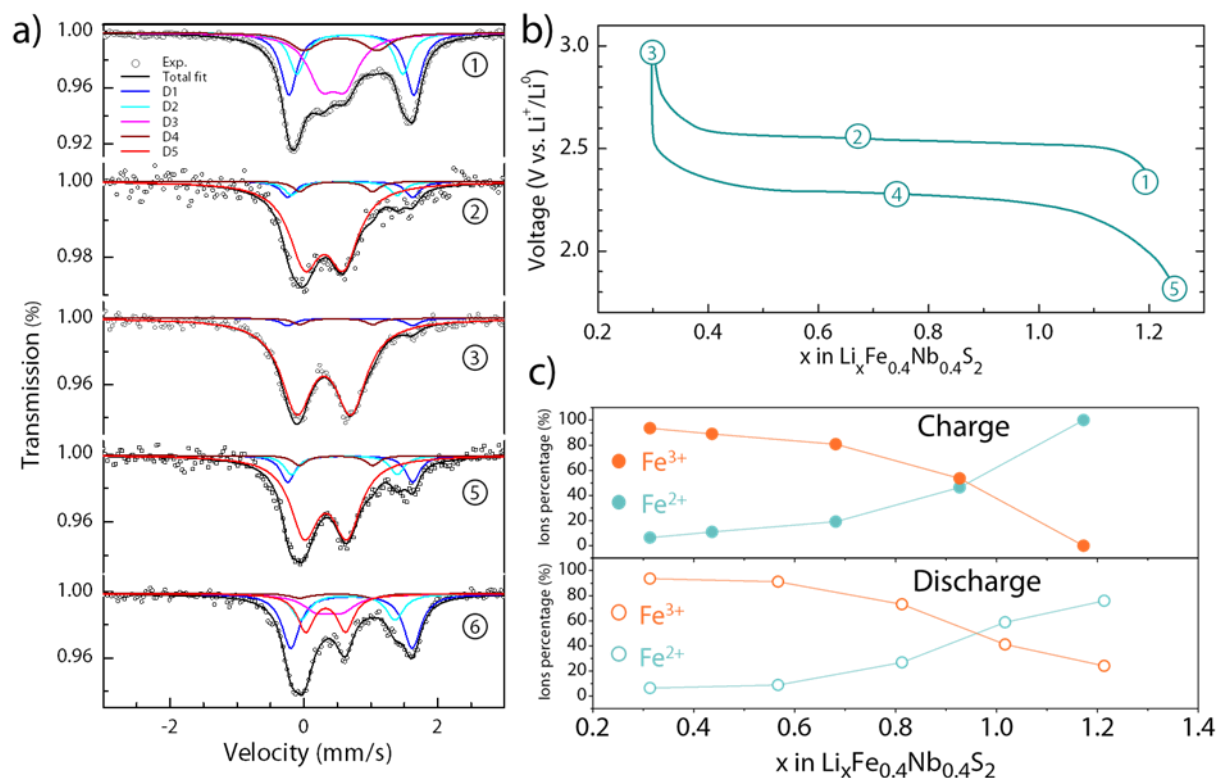


Figure III.21: (a) Mössbauer spectra of LNFS at different states of charge/discharge. To fit them four components for Fe²⁺ (D1, D2, D3 and D4) and one for Fe³⁺ (D5) are used. (b) Electrochemical curve of LNFS; the numbered points indicate the ex-situ samples prepared for XPS analysis. (c) Evolution of Fe³⁺/Fe²⁺ species during cycling species as deduced from Mössbauer spectra analysis.

The XRD pattern of the delithiated $\text{Li}_x\text{Nb}_{0.4}\text{Fe}_{0.4}\text{S}_2$ is difficult to interpret and solely the growth of a peak at lower angle than the (003) of the pristine is observed. Next, we studied the oxidation state of the iron and sulfur in the compound during cycling by Mössbauer spectroscopy (cf. figure III.21).

For iron oxidation state, the Mossbauer spectrum of the pristine compound can be interpolated using four doublets revealing a complex distribution of high and low spin Fe^{2+} as already observed for LTFS.⁸¹ All along the charge plateau, the Fe^{2+} components decrease in intensity in favor of the Fe^{3+} ones. Reversibly in discharge, the Fe^{3+} components progressively decrease in intensity and the spectrum observed at the end of the discharge is comparable to that of pristine. Moreover, it is important to note that the oxidation of iron alone is not sufficient to explain the observed capacity of the material. Hence, the participation of the sulfur redox is necessary and an XPS study is underway to verify this. Overall, both cationic and anionic redox processes are observed simultaneously throughout the cycling against the well separated cationic and anionic redox processes reported for $\text{Li}_x\text{Fe}_y\text{Ti}_{1-y}\text{S}_2$ phases.⁸¹ This could explain the observed single plateau for LNFS in contrary to the initial sloppy voltage profile followed by plateau region for LTFS. Shortly the Fe^{2+} substitution in Li_3NbS_4 leads to a layered structure while triggering the anionic redox process as is observed for different other compounds in literature.

Thus, at this point we have highlighted two ways to activate the anionic redox in Li_3NbS_4 either by disordering the cationic network or by substituting Nb with Fe. It is now important to explain these different points through more theoretical considerations.

v) *Discussion*

To understand the previous results it is first important to recall the basic criteria needed for Li-rich compounds to exhibit anionic redox process. In Li-rich compounds, when the anions are coordinated by less than three transition metal atoms, some of the sulfur (or oxygen) orbitals are little or not involved in a chemical bond with the metal, thus forming non (weakly)-bonding doublets. According to many studies, these purely anionic electrons are the only ones that can be oxidized reversibly. However, these non-bonding levels are highly localized and require some degree of hybridization with the transition metal in order to facilitate extraction of electrons. According to basic rules of quantum mechanics, in order to hybridize two orbitals

two parameters are important: the orbitals overlap, which can be deduced by symmetry considerations, and the energy difference between the two orbitals (cf. figure III.22).

From these simple rules one can understand why d^0 compounds in their ordered structure such as Li_2TiS_3 or Li_3NbS_4 have little chance to present an anionic redox activity. Indeed, considering the symmetries of the MS_6 octahedra in these systems, the atomic orbitals accounting for the free doublets of the sulfur hardly overlap the one of the metal and moreover nothing presupposes the energetic gap between these orbitals to be small. Moreover, in the case of $o\text{-Li}_3\text{NbS}_4$, the clustering of the Niobium atoms further enhances this isolation of the sulfur electrons. Indeed, preliminary theoretical results show that the $[\text{Nb}_4\text{S}_{16}]^{12-}$ unit blocks in $o\text{-Li}_3\text{NbS}_4$ can be seen as quasi-molecular objects with few inter-cluster interactions.

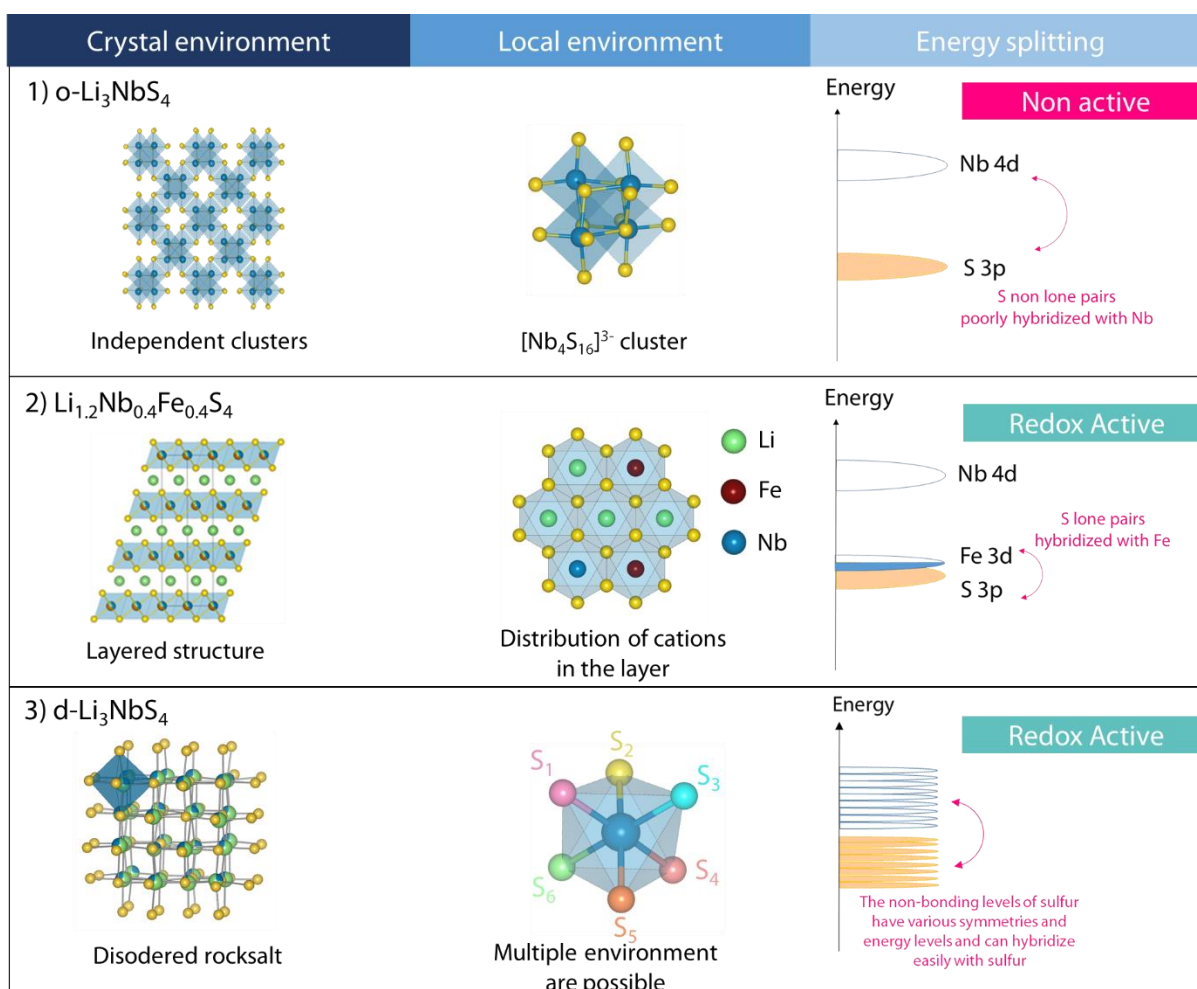


Figure III.22: Qualitative evolution of the band diagram of the compounds as a function of the symmetry of the transition metal coordination polyhedron. For Li_2TiS_3 the octahedra are perfectly regular (punctual group O_h) for $o\text{-Li}_3\text{NbS}_4$ a slight decentering of Niobium, makes S_1 and S_2 non-equivalent leading to a C_{3v} symmetry and finally in $d\text{-Li}_3\text{NbS}_4$ all sulfur atoms (S_i with $i=1-6$) are potentially different leading to many possible symmetries.

On the contrary, in the presence of a cationic redox center (i.e. not d^0) the energetic position of the cationic bands is electrochemically adjustable. Indeed, when oxidizing, the d levels of the metal decrease in energy until they potentially "meet" the free pairs of the anion, so that even a small overlap (induced by vibration for example) can induce hybridization and thus allow the removal of electrons from the sulfur. This explains the activation of the anionic redox in LNFS, as already observed in $\text{Li}_2\text{TiS}_3\text{-FeS}^{81}$ or $\text{Li}_2\text{SnS}_3\text{-FeS}^{160}$ solid solutions, where the d levels of iron must be close to the free pairs of sulfur. However, it is not necessary to introduce a cationic redox center to activate the anionic redox in a d^0 compound. Thus, it has been shown that by replacing part of the sulfur by selenium in Li_2TiS_3 it was possible to induce anionic redox activity.¹⁶¹ The substitution favors here the two important parameters of the hybridization mentioned above. Indeed, selenium is more electropositive than sulfur and allows decreasing the energetic gap between the anionic free pairs and the titanium vacancies. More importantly, this substitution induces a heteroleptic coordination of titanium by sulfur and selenium results in the formation of a $\text{TiS}_{6-y}\text{Se}_y$ polyhedra that no longer has octahedral symmetry, hence strongly reinforcing the overlap between the orbitals of the sulfur and those of the metal.

Following this reasoning can help us to understand the activation of the redox anion in the disordered compound $d\text{-Li}_3\text{NbS}_4$. In this compound and from a local point of view, the sulfur atoms are surrounded by six cations, which can be randomly lithium or niobium atoms. This allows a large number of possible sulfur environments, each with a point symmetry and a different energy. This lowering of symmetry coupled with the broadening of the energy level allows, to activate the redox anion in a compound that is nevertheless d^0 . Thus beyond the cationic or anionic substitution, this example shows that structural disorder can activate anionic redox. One practical advantage of this disorder strategy is that it does not reduce the theoretical gravimetric capacity of the material (for instance the theoretical capacity of LNFS is 244 mAh.g^{-1} vs 332 mAh.g^{-1} for Li_3NbS_4). However, this positive attribute is negated by a poor capacity retention of the material. A legitimate question, not yet answer, regards whether a cationic disorder within the transition metal layer of a lamellar compound would also allow this activation.

III.1.e Partial conclusion

In this first part we have studied the Li_3MS_4 family with M being a transition metal of the 5th group (V, Nb or Ta). From the synthetic point of view, we have seen that it was a priori not possible to synthesize the compound Li_3VS_4 by traditional methods contrary to Li_3NbS_4 and Li_3TaS_4 , which even present polymorphism depending on the synthesis method (high temperature or mechanical). Thus, if each of the processes induces the formation of a rocksalt-like structure, the mechano-synthesis leads to a complete cationic disorder whereas the ceramic process leads to an ordered structure with lithium and transition metal (Nb or Ta) occupying specific crystallographic sites.

Moreover, by studying the electrochemical activity of these compounds, we observe interestingly that the two polymorphs of Li_3NbS_4 behaved differently, the ordered compound being inactive as opposed to the disordered one. Further study shows that these differences were directly related to this cationic order and not solely to the difference in morphology between the small particles formed by mechanical grinding and the larger ones obtained at high temperature. Furthermore, a study of the charge compensation mechanism within these materials reveals that this activation with cationic order was related to the anionic nature of the oxidation process. We also managed to activate the redox process in these materials by substituting part of the niobium with iron. Altogether, these results in connection with previous reports by our group or others on Li-rich sulfides, show the importance of the hybridization of the free doublets of the anions with the transition metals' d orbitals to trigger anionic redox activity. More specifically, it suggests that cation disordering can affect this hybridization via a band structural broadening and further characterizations are underway to confirm this point.

Beyond the lithium-rich phases, the lithiated chalcogenides of 4d and 5d transition metals have been less studied than their 3d counterparts and therefore constitute a field of research conducive to the discovery of new phases. In the next section, we focus on iridium sulfides.

III.2 Study of the LiIrS_2 and IrS_2 compounds

To study the anionic redox processes in sulfides a naive idea would be to study the electrochemical behavior of phases with dimers (FeS_2 for example) but also their lithiated counterparts (Li_2FeS_2 in this case). However, transition metal sulfides containing dimers are mainly found in pyrite or marcasite crystal structures, which do not have the proper open framework for topotactic insertion/de-insertion reactions. Consequently, lithium insertion in such phases (eg., FeS_2) induces large structural changes and a loss of long-range order^{162–164} that complicate the understanding of the structure/electrochemistry interactions. Upon further digging into the literature, the iridium sulfides got our attention. Indeed, Jobic and coworkers described in 1990¹⁴⁰ IrS_2 (denoted hereafter by the moniker “Jobic’s IrS_2 ” or “J- IrS_2 ”), a compound combining both sulfur dimers¹⁶⁵ and a ramsdellite-like open framework suitable for lithium topotactic insertion. Moreover, intrigued by the possibility to form lithiated iridium sulfides, we stabilized in this study a high temperature LiIrS_2 phase isostructural to LiTiS_2 and referred to in the following text as L- IrS_2 . The structure and electrochemical behavior of these two iridium sulfide compounds is reported in this section.

III.2.a Experimental results:

NB: In this study the synchrotron XRD patterns were all collected at the 11-BM beamline of the Advanced Photon Source (Argonne National Laboratory) while the neutron diffraction patterns were then collected on the WOMBAT high-intensity neutron powder diffractometers (ANSTO, Australia)(cf. materials and methods).

i) Synthesis of the pristine materials

The synthesis of **J- IrS_2** was performed following a previously reported protocol.¹⁴⁰ In a typical synthesis, about 200 mg of IrS_2 phase was obtained by mixing in an Ar-filled glovebox, iridium powder (99.8 % Alfa Aesar) and elemental sulfur (99.998 % Sigma-Aldrich) in a 1:2.1 molar ratio. The homogeneously hand grinded mixture was then transferred into a carbon coated quartz ampoule and subsequently sealed under dynamic vacuum ($\sim 10^{-3}$ mbar). Finally, the tubes were annealed in a muffle furnace at 930°C for 60 hrs and the product was recovered and stored in Ar-filled glove box.

A similar solid-state procedure was followed to synthesize **L-LiIrS₂**. In an Ar-filled glovebox, iridium powder, elemental sulfur and lithium sulfide (99.9 % Alfa Aesar) were mixed in a 1:1.5:0.55 ratio. The mixture was then annealed under vacuum in a sealed quartz ampoule (prepared following the same procedure described above) for 60 hrs at 700 °C.

ii) *Crystal structure of the pristine materials*

The structural analyses of both materials were carried out by combined synchrotron X-ray and neutron powder diffraction pattern as well as high-resolution transmission electron microscopy analyses. The results obtained for J-IrS₂ are represented in figure III.23. The Rietveld refinement of both synchrotron X-ray and neutron powder diffraction patterns (cf. figure III.23.a and b) combined with electron diffraction patterns (cf. figure III.23.e) confirmed the previously reported orthorhombic (*Pnma*, $a = 19.8201(2)$ Å, $b = 3.5736(2)$ Å, $c = 5.6339(2)$ Å) structural model for J-IrS₂ (cf. figure III.23.c and table III.6).¹⁴⁰ In this structure, iridium atoms are octahedrally coordinated to sulfur and the formed IrS₆ octahedra share corners and edges to produce rutile-type [1x1] and ramsdellite-type [2x2] channels. A closer look into the structure, especially through dDPC-STEM picture (cf. figure III.23.d), reveals that the [1x1] channels of J-IrS₂ are distorted leading to short S-S distances of around 2.27 Å. Former Raman spectroscopy of this phase has unambiguously attributed these short distances to the presence of S₂²⁻ dimers in the structure.¹⁶⁵ Conversely, the [2x2] ramsdellite-like channels demonstrate no signs of distortion and can be ideal sites to host small cations as already demonstrated in structurally related MnO₂ polymorph.¹⁶⁶

<i>J-IrS₂</i>		<i>Pnma</i>		$R_{\text{bragg}} = 5.32\%$	$\chi^2 = 2.16$	$\text{Vol} = 399.050(2) \text{ \AA}^3$	
$a = 19.8201(2) \text{ \AA}$		$b = 3.5736(2) \text{ \AA}$		$c = 5.6339(4) \text{ \AA}$			
<i>Atom</i>	<i>Wyckoff Position</i>	x/a	y/b	z/c	$B_{\text{iso}} (\text{\AA}^2)$	<i>Occupancy</i>	
Ir1	4c	0.07692(2)	1/4	0.42453(4)	0.205(2)	1	
Ir2	4c	0.30395(2)	1/4	0.44062(4)	0.205(2)	1	
S1	4c	0.35819(7)	1/4	0.0612(3)	0.351(10)	1	
S2	4c	0.37751(7)	3/4	0.5420(3)	0.351(10)	1	
S3	4c	0.23492(8)	3/4	0.3253(3)	0.351(10)	1	
S4	4c	0.00818(7)	3/4	0.2730(3)	0.351(10)	1	

Table III.6: Crystallographic data and atomic positions for J-IrS₂ at 300 K using the complete model determined from Rietveld refinement of its synchrotron X-ray and neutron diffraction patterns.

In contrast, the L-LiIrS₂ polymorph, not reported so far to the best of our knowledge, adopts the structure displayed in figure III.24. Its X-ray synchrotron powder diffraction pattern was first indexed using the DICVOL software^{128,129} in a trigonal unit cell ($a = 3.5955(2)$ Å, $c = 5.6749(4)$ Å) and this indexation was confirmed by electron diffraction pattern shown in figure III.24.d. The similarities of this unit cell with the well-known layered transition metal chalcogenides led us to consider a structural model similar to the LiTiS₂ one ($P\bar{3}m1$) which was further validated by both SXRD and neutron powder diffraction refinements (cf. figure III.24.a and b and table III.7). In this structure, iridium atoms sit in the centres of regular IrS₆ octahedra sharing edges with each other to form CdI₂-like layers stacked along the c direction (cf. figure III.24.c).

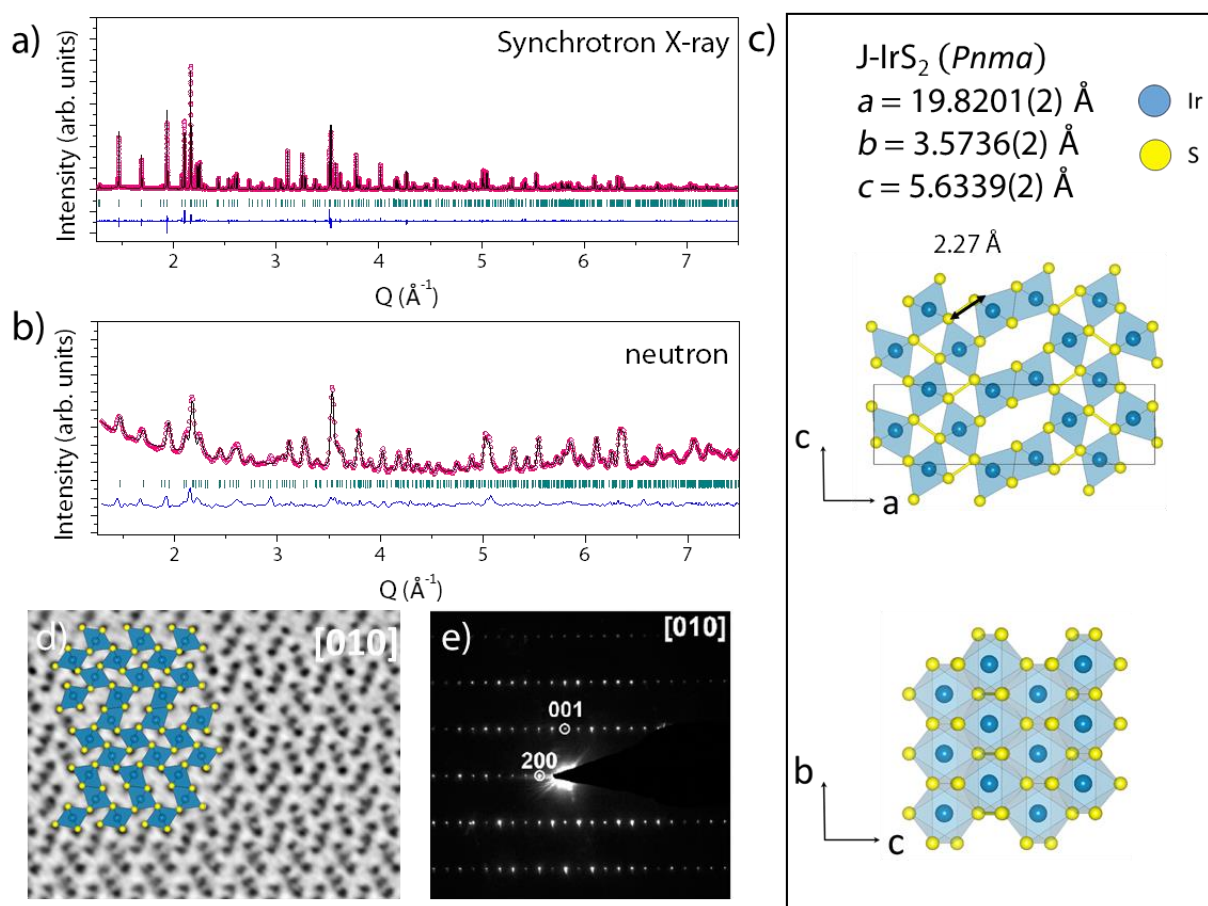


Figure III.23: (a) Synchrotron X-ray and (b) neutron Rietveld refinements of J-IrS₂ at 300 K. Wavelengths for synchrotron X-ray and neutron are $\lambda = 0.45789$ Å and $\lambda = 1.54183$ Å, respectively. The pink circles, black continuous line, and bottom blue line represent the observed, calculated, and difference patterns, respectively. Vertical green tick bars stand for the Bragg positions. Associated crystallographic data are summed up in table III.6. (c) Structure of J-IrS₂ at 300 K. (d) [010] dDPC-STEM image of J-IrS₂ with the overlaid positions of the Ir and S atoms. (e) Corresponding electron diffraction pattern of J-LiIrS₂.

The HAADF-STEM image (figure III.24.e) clearly shows that the iridium atoms from one layer to another are aligned orthogonally to the layer plane. Such a stacking is referred as O1 according to Delmas nomenclature³³ as the Li atoms are in octahedral position and the unit cell contains one MS_2 layer. The determination of the exact Li/Ir ratio with Inductively Coupled Plasma Mass Spectrometry (ICP-MS) was complicated by the insolubility of the material even in strong acidic solutions. Nevertheless, HAADF-STEM pictures show closing loops formed by the IrS_2 layers at the edge of the crystallites that could indicate a relative densification of the material on the surface hence the formation of slightly lithium deficient phase (Li_xIrS_2 where $x < 1$; $Li/Ir < 1$) as frequently observed with the synthesis of $LiMS_2$ compounds. This last assumption could also explain the $c/a=1.58$ ratio observed for this compound significantly smaller than the one observed in $LiTiS_2$ or $LiVS_2$ (1.80)

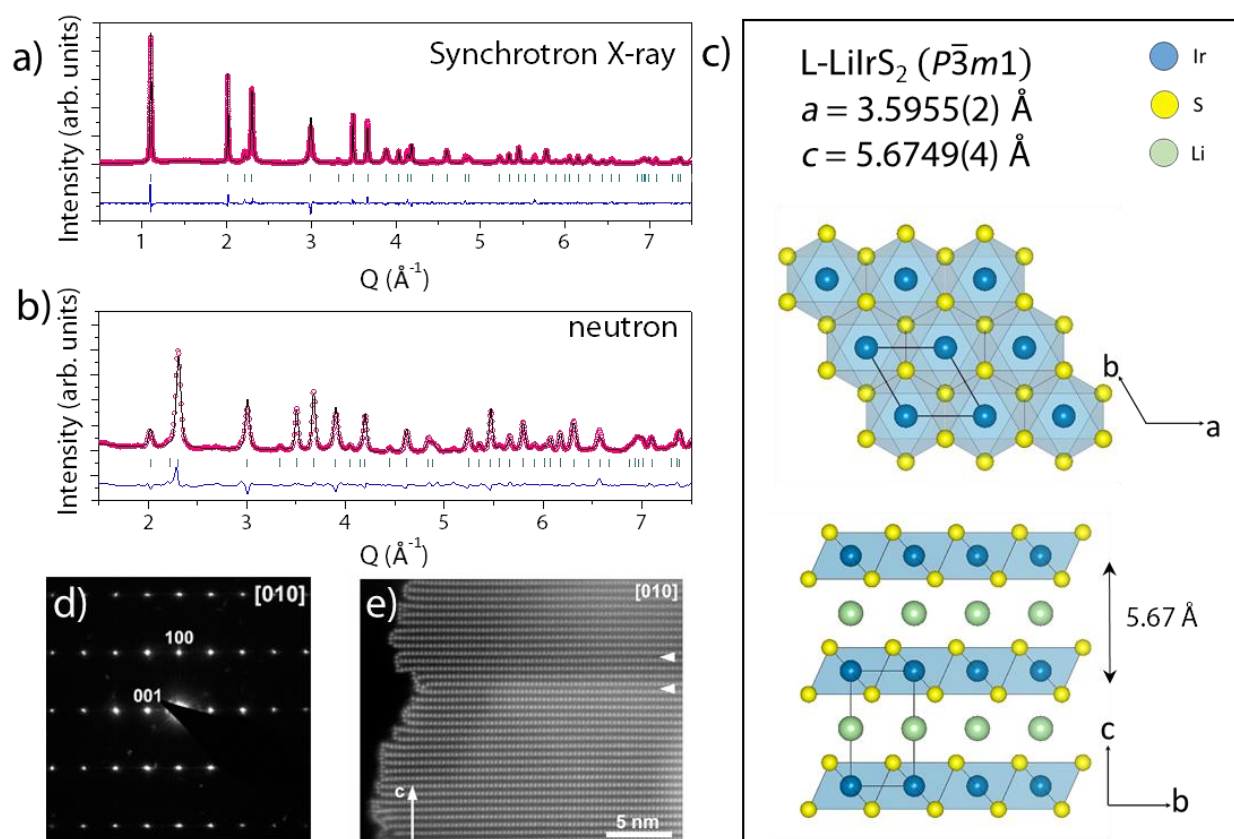


Figure III.24: (a) Synchrotron X-ray and (b) neutron Rietveld refinements of $L-LiIrS_2$ at 300 K. Wavelengths for synchrotron X-ray and neutrons are $\lambda = 0.45789 \text{ \AA}$ and $\lambda = 1.54183 \text{ \AA}$, respectively. The pink circles, black continuous line, and bottom blue line represent the observed, calculated, and difference patterns, respectively. Vertical green tick bars stand for the Bragg positions. Associated crystallographic data are summed up in table III.7. (c) Structure of $L-LiIrS_2$ at 300 K. (d) Electron diffraction pattern of $L-LiIrS_2$. (e) [010] HAADF-STEM image of $L-LiIrS_2$ showing the O1-type structure. Stacking faults are occasionally present and marked with arrowheads.

Overall, structural analyses indicate that both J-IrS₂ and L-LiIrS₂ possess either tunnels or Van der Waals layers, respectively, hence suggesting their feasibility to reversibly uptake and release Li⁺ ions as we explore next.

<i>L-LiIrS₂</i>		<i>P</i> $\bar{3}$ <i>m1</i>		<i>R</i> _{bragg} = 3.99%	χ^2 = 6.17	<i>Vol</i> = 63.535(2) Å ³	
<i>a</i> = 3.5955(2) Å		<i>c</i> = 5.6749(2) Å					
<i>Atom</i>	<i>Wyckoff Position</i>	<i>x/a</i>	<i>y/b</i>	<i>z/c</i>	<i>B</i> _{iso} (Å ²)	<i>Occupancy</i>	
Li1	1 <i>b</i>	0	0	1/2	0.429(2)	1	
Ir1	1 <i>a</i>	0	0	0	0.149(5)	1	
S1	2 <i>d</i>	1/3	2/3	0.2032(3)	0.469(3)	1	

Table III.7: Crystallographic data and atomic positions for L-LiIrS₂ at 300 K using the complete model determined from Rietveld refinement of its synchrotron X-ray and neutron diffraction patterns.

iii) *Electrochemical study*

Li half-cells were assembled for both J-IrS₂ and L-LiIrS₂ using lithium metal as counter electrode and LP30 (1M LiPF₆ in 1:1 mixture of ethylene carbonate: dimethyl carbonate) as electrolyte. The cells were cycled between different voltage cut-off and potential ranges of 1.3 -3 V for J-IrS₂ and 1.7 -3.5 V for L-LiIrS₂. These specific conditions were fixed to avoid material degradation. The cells were cycled at a C/20 rate (1 Li per unit formula removed or inserted in 20 h). The composition vs voltage plots together with the corresponding derivative curves for the first cycle are shown in figure III.25.

For J-IrS₂, the insertion and de-insertion of lithium takes place through a plateau-like profile at 1.4 and 1.5 V vs. Li⁺/Li⁰ respectively. Out of the 0.5 lithium inserted into the structure only 0.3 is removed on subsequent charge. By pushing the reduction cut-off potential to lower voltages, a new insertion process appears at 1.15 V that accounts for the insertion of almost five lithium into the structure (cf. figure III.26). However, this low voltage process is poorly reversible and accompanied by a high polarization and irreversibility on subsequent charge suggesting a possible conversion reaction.

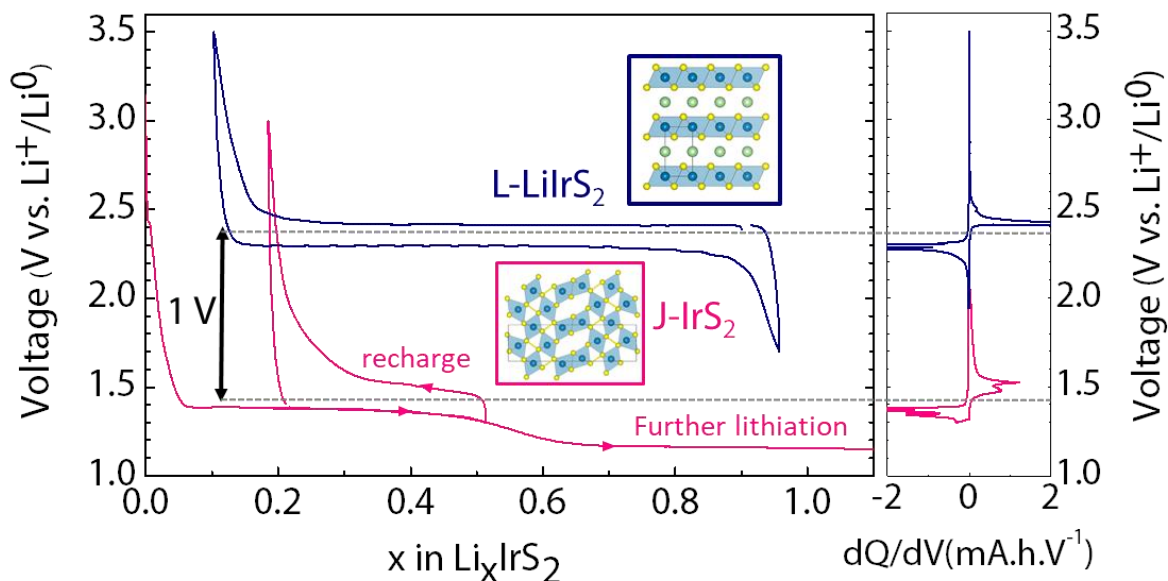


Figure III.25: First cycle voltage–composition trace (left) and derivative curves (right) of L-LiIrS₂ (blue) and J-IrS₂ (pink) cycled at C/20. The starting composition of L-LiIrS₂ is considered as Li_{0.9}IrS₂ accounting for Li-deficiency as explained in the synthesis part. The arrows on the J-IrS₂ voltage curves indicate the cycling directions. The low voltage 1.15 V discharge of J-IrS₂ extends up to ~5 Li uptake and is not shown here for clarification purpose.

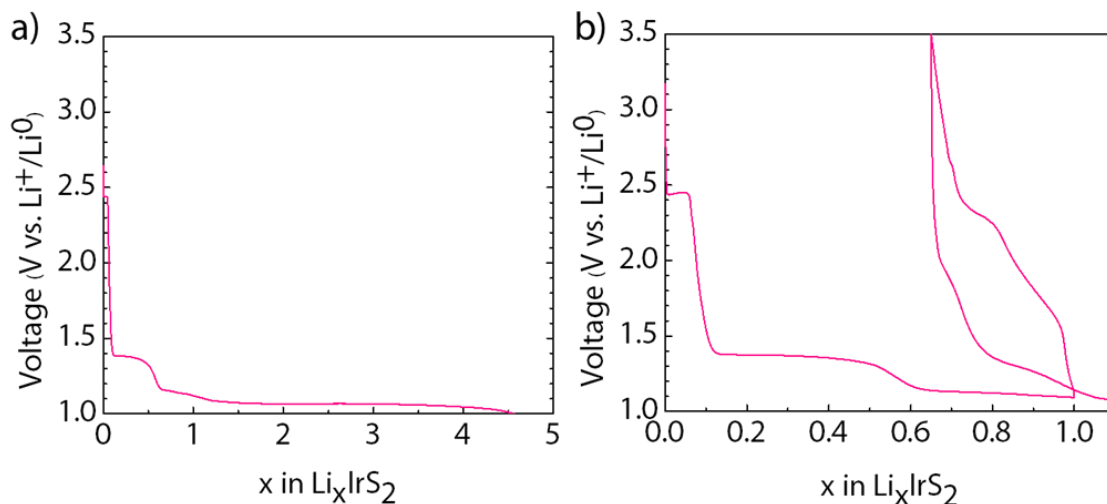


Figure III.26: (a) Voltage vs composition plot of J-IrS₂ by reducing the discharge voltage to 1 V. (b) The voltage profile when the amount of inserted lithium is limited to 1. The lithium insertion is highly irreversible upon subsequent charge indicating possible associated conversion reaction. The small 2.4 V plateau observed in the beginning of the discharge on the panel b account for some S₀ impurities in the materials.

Turning to L-LiIrS₂, strikingly the de-insertion and insertion of Li⁺ proceeds through a voltage plateau located 1V higher than for J-IrS₂ (cf. figure III.25). Interesting as well is the feasibility to insert more Li⁺ on discharge (~0.9) that it has been removed on charge (~0.8). Such difference is not fortuitous but rather suggests, based on coulomb titration, that the pristine material is slightly Li deficient (L-Li_{0.9}IrS₂). To interrogate the origin of the 1 V difference, we next investigate the crystal structure evolution of the polymorphs during Li insertion/extraction.

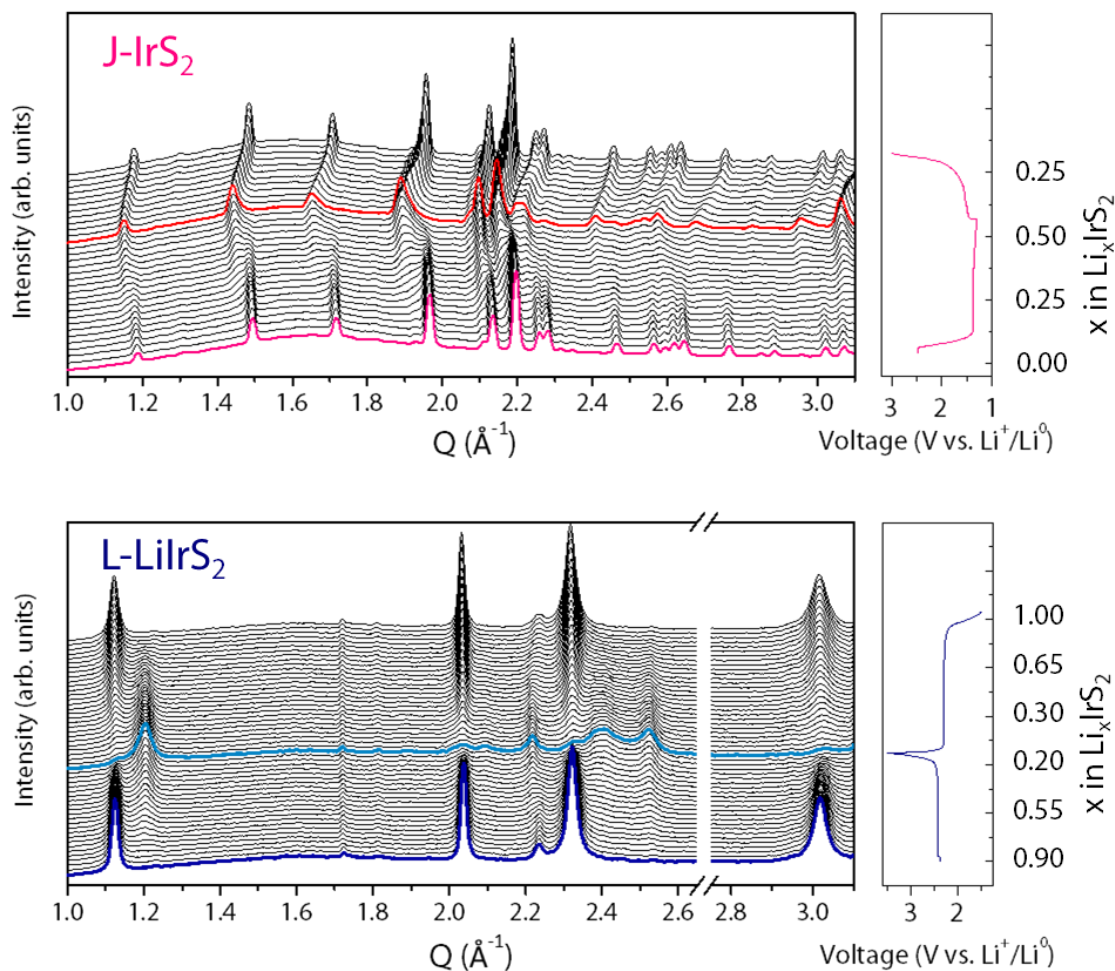


Figure III.27: Operando XRD patterns during the first cycle of J-IrS₂ (top) and L-LiIrS₂ (bottom) with the corresponding galvanostatic curves in the right panel. The compounds are cycled at C/20 and the XRD patterns were measured for every 1 h (0.05 Li insertion/removal). The XRD patterns corresponding to J-IrS₂ and J-Li_{0.5}IrS₂ in the galvanostatic curve are plotted in pink and red respectively whereas the patterns corresponding to L-LiIrS₂ and Li-IrS₂ are plotted in dark blue and light blue respectively.

Operando XRD analyses have been carried out for both J-IrS₂ and L-LiIrS₂ (cf. figure III.27). Upon lithiation, J-IrS₂ exhibits biphasic process and a nearly single phase compound was reached for the composition J-Li_{0.5}IrS₂. Upon further lithiation of J-Li_{0.5}IrS₂, a new biphasic process starts to appear and progresses till 2 lithium consumption and fades away for greater amounts of reacted Li⁺ ($2 < x < 5$) (cf. figure III.28). Similarly, L-LiIrS₂ followed biphasic delithiation and lithiation processes where the delithiated L-Li_xIrS₂ also exhibited layered structure but full refinement requires a higher resolution than lab XRD. In order to further understand these structural evolutions, we studied next the single-phase compositions by combined synchrotron XRD and TEM analyses.

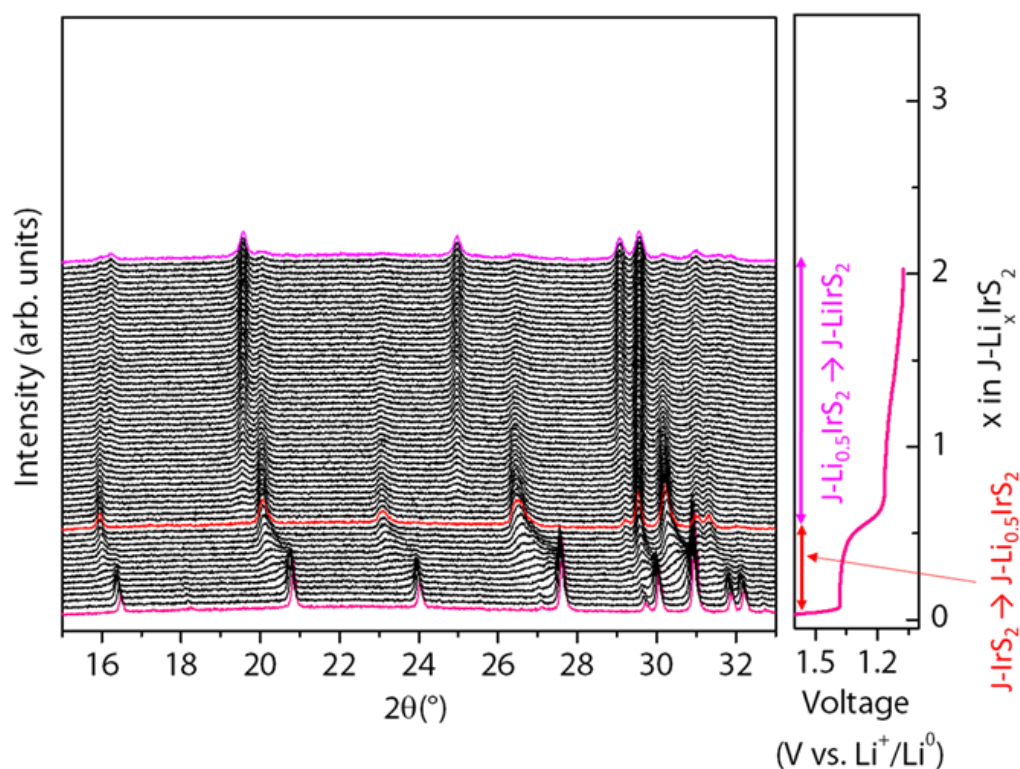


Figure III.28: Operando XRD patterns during the discharge of J-IrS₂ (left) where the discharge is controlled by the amount of reacted lithium ($x=2$). The corresponding voltage profile is shown in right. The compound is cycled at C/20 and the XRD patterns are measured for every 1 hr (0.05 lithium). On the galvanostatic curve, the patterns corresponding to J-IrS₂, J-Li_{0.5}IrS₂ and J-LiIrS₂ are plotted in magenta, red and pink respectively.

iv) *Structure of the lithiated/delithiated phases*

Both a chemical and an electrochemical procedure have been attempted to prepare **J-Li_{0.5}IrS₂** ex-situ samples. For the first one, about 500 mg of J-IrS₂ and five equivalents of n-Butyl lithium (n-BuLi; 1.6 M in hexane, Sigma-Aldrich) were mixed together in a 40 mL glass vial under Ar-atmosphere and stirred for 5 hours. The resulting powder was thoroughly rinsed with hexane to remove the n- BuLi before being dried under vacuum. To prepare the lithiated J-Li_xIrS₂ phases electrochemically, an electrode was first prepared by mixing 500 mg of IrS₂ with 20 % (in mass) of Carbon-SP, and was then discharged galvanostatically (constant current mode) at C/50 rate vs Li metal in a home-made Swagelok type cell using LP-30 (1M LiPF₆ in 1:1 by volume mixture of EC- DMC; bought from Dodochem, China) as electrolyte. The lithiated powder was then collected from the electrochemical cell under inert atmosphere and washed three times with DMC before being dried under vacuum.

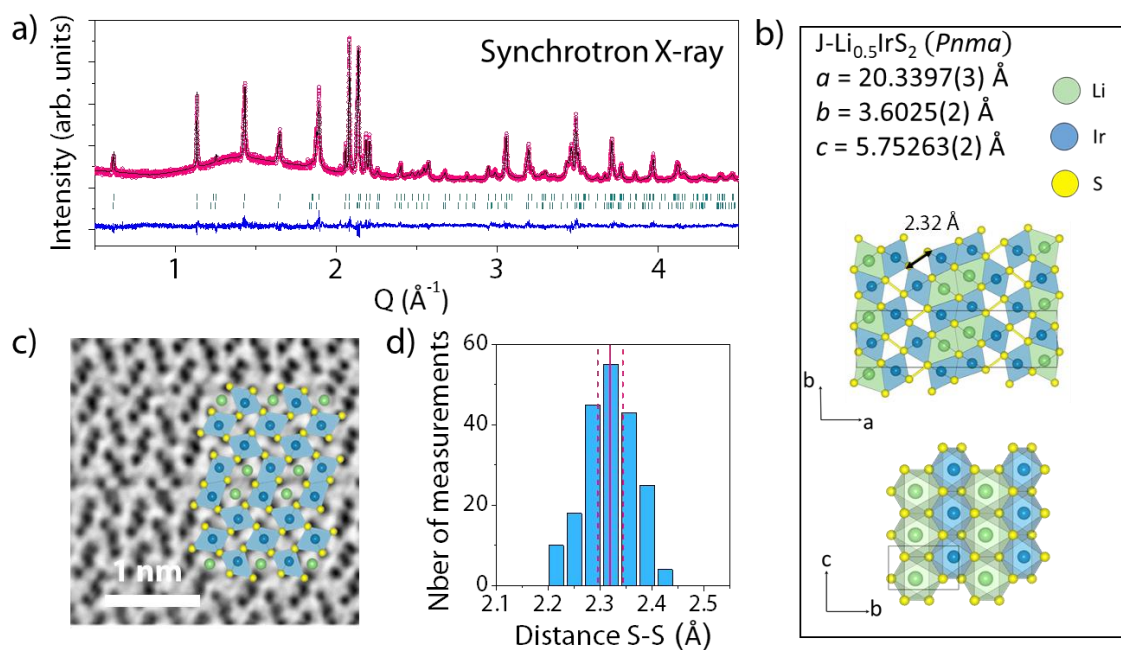


Figure III.29: (a) Synchrotron X-ray Rietveld refinement of J-Li_{0.5}IrS₂ at 300 K. The wavelength for synchrotron X-ray is $\lambda = 0.45789$ Å. The pink circles, black continuous line, and bottom blue line represent the observed, calculated, and difference patterns, respectively. Vertical green tick bars stand for the Bragg positions. Two isostructural phases with small lattice parameters have been used to index the pattern and presence of two isostructural phases is expected to be linked with inhomogeneous lithiation of the J-IrS₂ particles. (b) Structure of J-Li_{0.5}IrS₂ at 300 K. (c) [010] dDPC-STEM image of J-Li_{0.5}IrS₂ with the overlaid positions of the Li, Ir and S atoms. (d) Distribution of the S1-S3 (cf. table III.8) interatomic distances of the dimeric entities in the J-Li_{0.5}IrS₂ as measured from the [010] dDPC-STEM image.

The SXRD pattern shown in figure III.29.a is nearly alike that of J-IrS₂ and refined using the *Pnma* structural model of J-IrS₂ but with larger lattice parameters. The S-S distance is difficult to measure from XRD analyses, as the pattern is dominated by the iridium contribution, we examined the S-S distances using dDPC-STEM imaging (cf. figure III.29.c). The measured S-S average distance of 2.32(5) Å in J-Li_{0.5}IrS₂ is only slightly longer than the 2.27 Å observed in the pristine material (cf. figure III.29.d), implying that the dimers are preserved during the reduction process. Finally, the bond valence energy landscape (BVEL) calculation using the refined structure indicates that the lithium atoms in the J-Li_{0.5}IrS₂ were localized in the octahedral voids of the ramsdelite-type motifs channels. Accordingly, the final structure for J-Li_{0.5}IrS₂ is derived as shown in figure III.29.b and its structural parameters are reported in table III.8.

<i>J-Li_{0.5}IrS₂</i>		<i>Pnma</i>		$R_{\text{bragg}} = 15.1\%$	$\chi^2 = 1.59$	$\text{Vol} = 421.517(9) \text{ \AA}^3$	
$a = 20.3396(3) \text{ \AA}$		$b = 3.6023(2) \text{ \AA}$		$c = 5.7529(2) \text{ \AA}$			
Atom	Wyckoff Position	x/a	y/b	z/c	$B_{\text{iso}} (\text{Å}^2)$	Occupancy	
Ir1	4c	0.0767(2)	1/4	0.4328(3)	0.80(4)	1	
Ir2	4c	0.3035(2)	1/4	0.4391(3)	0.80(4)	1	
S1	4c	0.3568(2)	1/4	0.0450(2)	1.94(13)	1	
S2	4c	0.3781(4)	3/4	0.5737(15)	1.94(13)	1	
S3	4c	0.2354(5)	3/4	0.3068(14)	1.94(13)	1	
S4	4c	0.0134(5)	3/4	0.2706(12)	1.94(13)	1	
Li1	4c	0.0626*	3/4	0.8827*	1.00*	1	

Table III.8: Crystallographic data and atomic positions for J-Li_{0.5}IrS₂ at 300 K using the complete model determined from Rietveld refinement of its synchrotron X-ray diffraction pattern. The positions of the lithium atoms have been determined by bond valence calculations (BVS), and have not been further refined (* = non-refined parameter).

Next, we analyzed the highly lithiated J-Li_xIrS₂ phase obtained by further reducing J-Li_{0.5}IrS₂ at 1.15 V. Although the XRD pattern showed at first sight similarities with the J-IrS₂ and J-Li_{0.5}IrS₂ XRD patterns, a direct extrapolation of the structure from these models was not successful. HAADF-STEM and dDPC-STEM experiments (cf. figure III.30.a and b) were then carried out and permitted to build a structural model which was further confirmed by Rietveld refinement of the operando XRD pattern (*Pnma*, $a = 23.0886(5) \text{ \AA}$, $b = 3.6257(2) \text{ \AA}$, $c = 5.6144(2) \text{ \AA}$) (cf. figure III.30.c and table III.9). The obtained structure differs mainly from the J-IrS₂ and J-Li_{0.5}IrS₂ ones by a drastic elongation of the S-S distances previously engaged in the dimers bonding (cf. figure III.30.d) hence suggesting their breaking during the lithiation

process. Structurally speaking and as supported by BVEL calculation, this structural relaxation frees the rutile channels for lithium insertion.

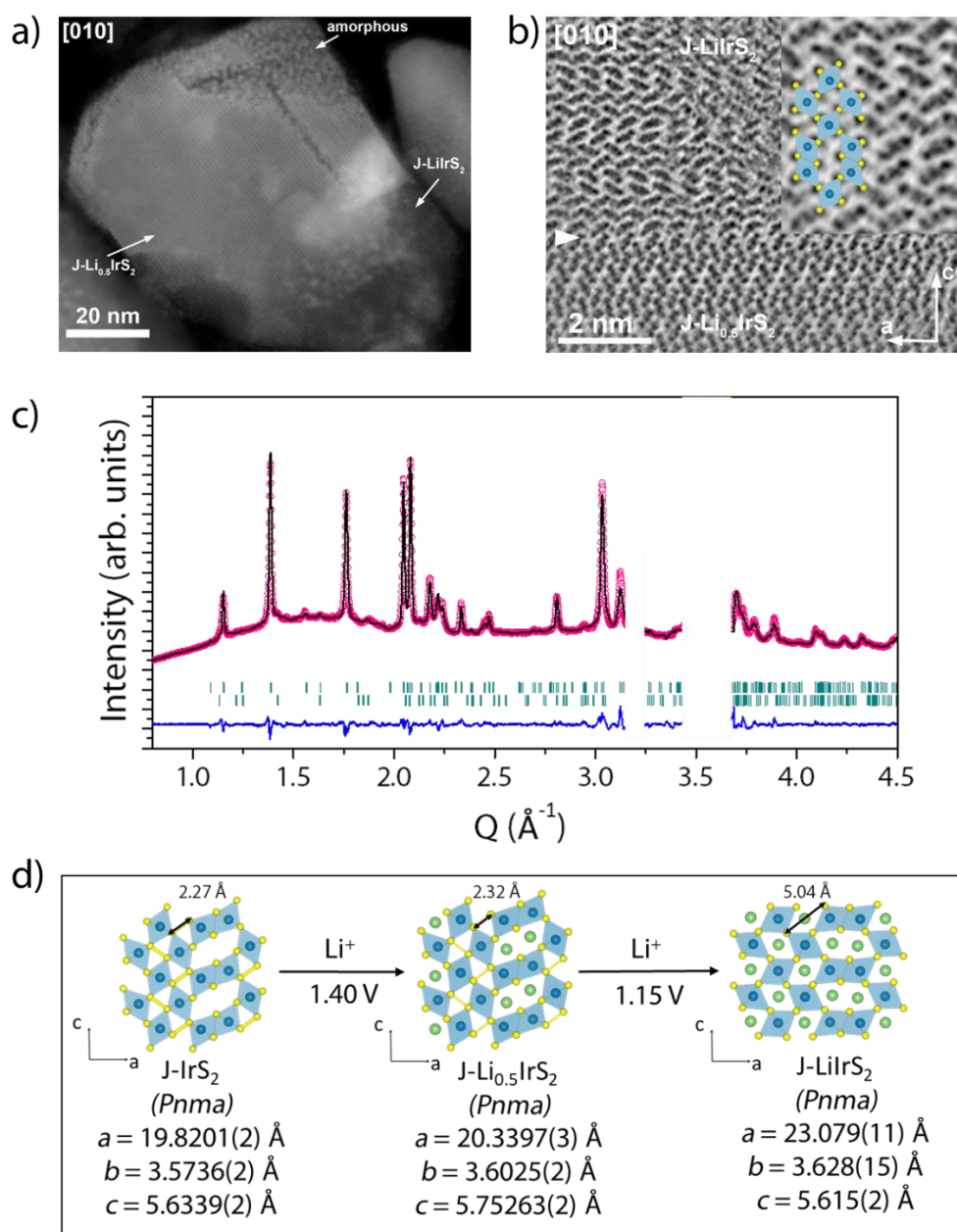


Figure III.30: (a) [010] HAADF-STEM image of highly lithiated $J\text{-Li}_x\text{IrS}_2$ showing co-existence of the $J\text{-Li}_{0.5}\text{IrS}_2$ and $J\text{-LiIrS}_2$ phases along with the amorphous products of the conversion reaction. (b) The [010] dDPC-STEM image of the interface between the $J\text{-Li}_{0.5}\text{IrS}_2$ and $J\text{-LiIrS}_2$ phases. The interface plane is marked by arrowhead. Enlarged part of the image shows the atomic details of the $J\text{-LiIrS}_2$ structure with the overlaid positions of the Ir (blue) and S (yellow) atoms. (c) Rietveld refinements of $J\text{-LiIrS}_2$ X-ray diffraction pattern at 300 K collected in situ in an electrochemical cell equipped with Be window ($\lambda = 1.54 \text{ \AA}$). The pink circles, black continuous line, and bottom blue line represent the observed, calculated, and difference patterns, respectively. Vertical green tick bars stand for the Bragg positions. Missing angular regions correspond to the Be reflections. (d) Structural evolution of $J\text{-Li}_x\text{IrS}_2$ through lithiation. The Ir-S network structure of $J\text{-LiIrS}_2$ results directly from the structural relaxation of the Ir-S network of $J\text{-IrS}_2$ with the full disappearance of the S-S dimers.

Therefore, assuming a complete filling of the octahedral vacant sites of the rutile and ramsdellite channels we propose the chemical formula J-LiIrS₂ for the phase lithiated to 1.15V. Lastly, HAADF-STEM pictures (cf. figure III.30.a) confirmed that the presence of this phase comes along with amorphous phase, which support that a concomitant conversion reaction occurs together with the formation of J-LiIrS₂.

<i>J-LiIrS₂</i>		<i>Pnma</i>		$R_{\text{bragg}} = 5.99\%$	$\chi^2 = 16.3$	$Vol = 470.000(16) \text{ \AA}^3$	
$a = 23.0886(5) \text{ \AA}$		$b = 3.6257(2) \text{ \AA}$		$c = 5.6144(2) \text{ \AA}$			
Atom	Wyckoff Position	x/a	y/b	z/c	$B_{\text{iso}} (\text{\AA}^2)$	Occupancy	
Ir1	4c	0.0676(2)	1/4	0.509(3)	0.915(4)	1	
Ir2	4c	0.3109(2)	1/4	0.504(2)	0.915(4)	1	
S1	4c	0.1515(2)	1/4	0.2431(3)	0.46(17)	1	
S2	4c	0.0960(2)	3/4	0.7634(3)	0.46(17)	1	
S3	4c	0.2270(2)	1/4	0.7411 (3)	0.46(17)	1	
S4	4c	0.0166(2)	3/4	0.2363(2)	0.46(17)	1	
Li1	4c	0.189*	3/4	0.8827*	1.00*	1	
Li2	4c	0.559*	1/4	0.476*	1.00*	1	

Table III.9: Crystallographic data and atomic positions for J-LiIrS₂ at 300 K using the complete model determined from Rietveld refinement of operando X-ray pattern. The positions of the lithium atoms have been determined by bond valence calculations (BVS), and have not been further refined (* = non-refined parameter).

Turning to the **delithiated L-Li_xIrS₂** phase (called hereafter L-IrS₂), the samples were prepared by chemical delithiation of L-LiIrS₂, by mixing in an Ar-filled glovebox one equivalent of L-LiIrS₂ with two equivalents of iodine (99+ % Alfa Aesar). The mixture was then transferred in a quartz ampoule, sealed under vacuum and subsequently annealed for 12hrs at 150°C. After the reaction, the ampoule was opened under inert atmosphere and the powder was washed with dry acetonitrile to remove excess LiI and I₂ before being dried under vacuum.

Its composition Li_{0.05}IrS₂ was determined by ICP-MS measurements. A first refinement was attempted using a layered structural model slightly distorted compared to the pristine one (*C2/m*, $a = 5.6911(4) \text{ \AA}$, $b = 3.5450(3) \text{ \AA}$, $c = 5.2375(5) \text{ \AA}$, $\beta = 89.96(14)^\circ$). Although promising, this model could not properly reproduce the intensities of several peaks (cf. figure III.31.a). Electron diffraction was then used to investigate the origin of the mismatch. It reveals the existence of a superstructure in this monoclinic model which corresponds to the $\mathbf{k} = [1/2 \ 1/2 \ 1/2]$ wave vector (cf. figure III.31.b). In parallel, HAADF-STEM image (cf. figure III.32.f) has shown that the superstructure is caused by lateral displacements of the Ir atoms creating

alternating short (~ 2.5 Å) and long (~ 3.2 Å) projected Ir-Ir distances along the Ir layers. The group theory distortion analysis lead to the construction of a triclinic super cell ($P\bar{1}$, $a = 3.3704(2)$ Å, $b = 5.9622(10)$ Å, $c = 6.2182(9)$ Å, $\alpha = 117.53(2)^\circ$, $\beta = 103.792(9)^\circ$, $\gamma = 93.865(4)^\circ$) and this model was finally confirmed by the Rietveld refinement of L-IrS₂ synchrotron X-ray (cf. figure III.32.a) powder diffraction pattern.

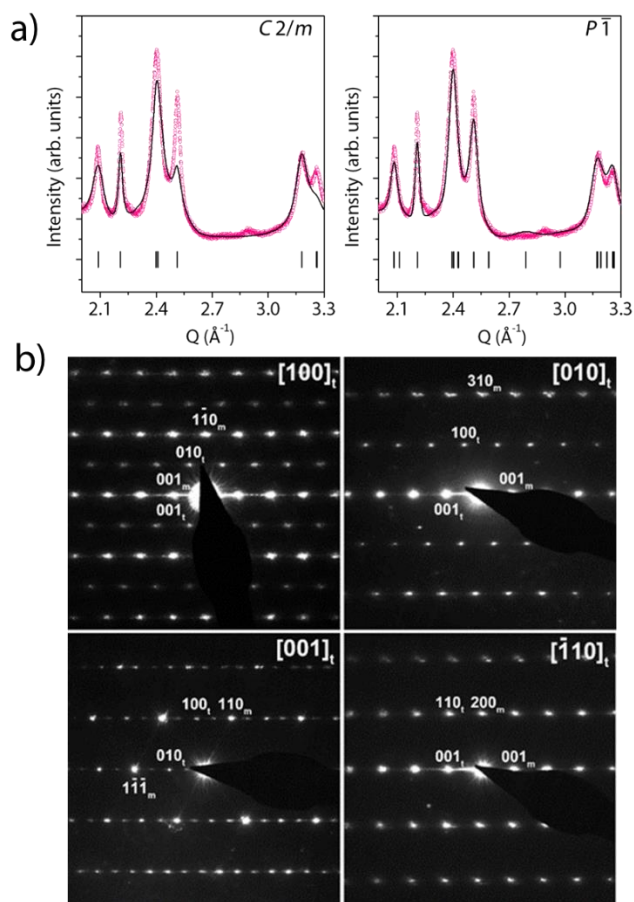


Figure III.31: (a) Comparison of the Rietveld refinements of L-IrS₂ synchrotron X-ray pattern starting with either a monoclinic ($C2/m$) structural model or triclinic ($P\bar{1}$) one. (b) ED patterns of delithiated L-IrS₂. The indexes denoted with subscript “m” belong to the monoclinically distorted C -centered subcell of the O1 structure ($a \approx 5.70$ Å, $b \approx 3.55$ Å, $c \approx 5.25$ Å, $\beta \approx 90^\circ$). The indexes denoted with subscript “t” belong to the triclinic supercell.

The obtained structure can be globally described as an O1 layered structure (cf. figure III.32.b and c and Table III.10) with however noticeable distortion inside the layers. Thus, the IrS₆ coordination polyhedra are not any longer octahedra but rather square pyramids with 5 short Ir-S bonds with an average length of 2.38 Å and a longer one at 2.93 Å (cf. figure III.32.d). This feature is later confirmed with Ir-L-edge EXAFS (cf. figure III.32.e). From the atomic point of view, this distortion induces an Ir-Ir “dimerization” observed with HAADF-STEM (cf. figure III.32.f) while sulfur atoms are split into two different sites with very different

environment (cf. figure III.33). Indeed, while S1 (cf. table III.10) positions are surrounded by three equidistant iridium atoms ($\text{Ir-S1} \approx 2.3 \text{ \AA}$), the S2 atoms develop similar short bonds with only two iridium atoms, the third neighbor being found at 2.93 \AA .

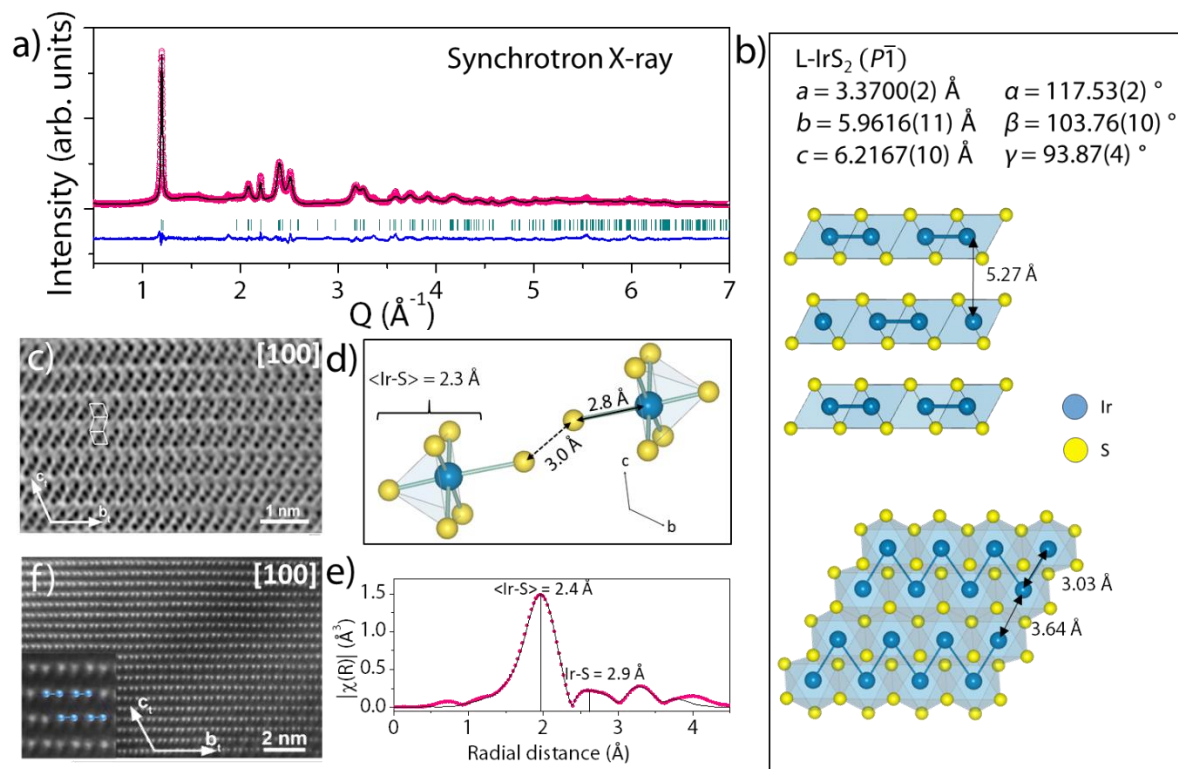


Figure III.32: (a) Synchrotron X-ray Rietveld refinements of L-IrS₂ at 300 K. Wavelengths for synchrotron X-ray is $\lambda = 0.45789 \text{ \AA}$. The pink circles, black continuous line, and bottom blue line represent the observed, calculated, and difference patterns, respectively. Vertical green tick bars stand for the Bragg positions. (b) Structure of L-IrS₂ at 300 K. (c) [100] dDPC-STEM image of L-IrS₂, the O1 stacking of the layers remains (the octahedra are traced). (d) Illustration of two IrS₆ polyhedra on both sides of the Van der Waals gap of L-IrS₂. The bi-pyramidal coordination is evidenced as well as the short S-S distances in the interlayer. (e) Magnitude of the Fourier transform of the Ir L₃-edge EXAFS oscillations on L-IrS₂ and model fitting in pink dots and black solid line, respectively. (f) [100] HAADF-STEM image of L-IrS₂. The Ir columns are shifted to form pairs with short projected intercolumn distances of $\sim 2.5 \text{ \AA}$ and long projected distances of $\sim 3.2 \text{ \AA}$ between the pairs.

Bond valence calculations suggest that this environment difference could be the sign of a charge difference between the two sulfur atoms with the S1 position more negatively charged than S2. Such a transition metal (Ir-Ir) dimerization does not come as a total surprise since it has already been spotted and described in the low temperature IrTe₂ layered structure.^{167–169} However, the origin of this distortion can be different from one compound to the other and will be detailed in the following section.

L-IrS ₂		$P\bar{1}$	$R_{\text{Bragg}} = 11.1\%$	$\chi^2 = 4.81$		
$a = 3.3700(2) \text{ \AA}$ $\alpha = 117.53(2)^\circ$		$b = 5.9616(11) \text{ \AA}$ $\beta = 103.76(10)^\circ$	$c = 6.2167(10) \text{ \AA}$ $\gamma = 93.87(4)^\circ$	Vol = 105.27(3) \AA^3		
Atom	Wyckoff Position	x/a	y/b	z/c	$B_{\text{iso}} (\text{\AA}^2)$	Occupancy
Ir1	2i	0.7629(2)	0.7160(2)	0.001(2)	0.948(9)	1
S1	2i	0.3796(4)	0.7397(3)	0.2568(2)	1.30(13)	1
S2	2i	0.8324(4)	0.2537(3)	0.2583(3)	1.30(13)	1

Table III.10: Crystallographic data and atomic positions for L-IrS₂ at 300 K using the complete model determined from Rietveld refinement of its synchrotron X-ray and neutron diffraction patterns.

Altogether, structural analyses showed that the S-S dimers are preserved during the initial uptake of Li in J-IrS₂ but are broken afterwards at high Li uptake as the lithium conversion reaction proceeds. On the other hand, L-LiIrS₂ preserved the layered structure upon delithiation and the L-IrS₂ exhibits distorted Ir-S₅₊₁ square pyramids (instead of Ir-S₆ octahedra) with short Ir-Ir distances in between. Therefore, the structural evolutions of J-IrS₂ and L-LiIrS₂ are completely different from one another and the remaining question is about the charge compensation mechanism (redox centers) in both these materials.

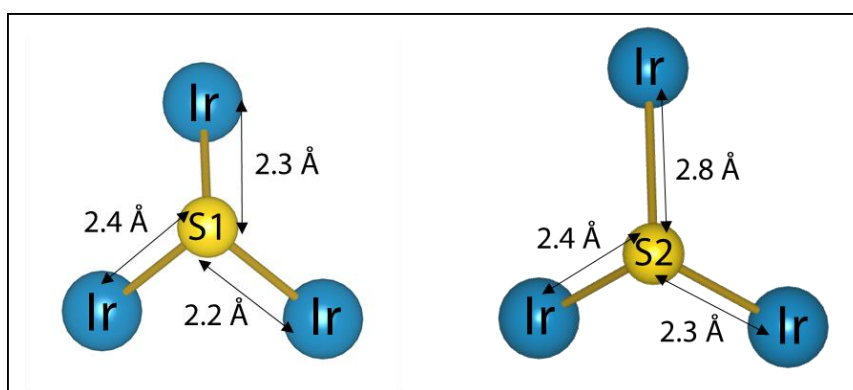


Figure III.33: Local environments of both sulfur sites (S1 and S2 according to the notations of table III.10) of L-IrS₂.

v) *Charge compensation mechanisms*

The evolution of the redox states of the iridium atoms in L-LiIrS₂, L-IrS₂, J-Li_{0.5}IrS₂ and J-IrS₂ was first investigated via Ir L₃-edge XAS (cf. figure III.35.a). At first sight the absorption spectrum shape for the four samples, look similar with only slight changes in the white line that could be indicative of different Ir environments. Hence, a small shift of the edge position can be seen in the following order $E(\text{L-LiIrS}_2) > E(\text{L-IrS}_2) = E(\text{J-Li}_{0.5}\text{IrS}_2) > E(\text{J-IrS}_2)$ that could be attributed to a slight electron density changes around this atom associated to a modification of the iono-covalency of the Ir-S bonds. To get deeper insights, iridium 4f XPS spectra were collected and the 4f_{7/2}-4f_{5/2} spin orbit components of J-Li_{0.5}IrS₂, J-IrS₂, L-IrS₂, and L-LiIrS₂ are shown in Figure III.35.b. Globally, all compounds show similar binding energy (61.7 eV for 4f_{7/2}) at the exception of the one of L-LiIrS₂ that is slightly lower (60.9 eV for 4f_{7/2}), indicative of a comparatively lower ionization state for iridium. Moreover, each 4f_{7/2} and 4f_{5/2} component (L-LiIrS₂ in Figure III.35.b) displays a fine structure with a shoulder at higher binding energy. We should note that this fine structure is not due a priori to the coexistence of two oxidation states of iridium, but rather to a multi-electron process inherent in photoemission spectroscopy, which is often observed for transition metals. For example, the Ir 4f spectrum of Li₂IrO₃ displays the same shape, although it is composed of a unique 4+ oxidation state of iridium in a unique environment.⁷⁸ Since this kind of fine structure is closely linked to the local environment of the probed atom, and therefore to the structure, the disappearance of this shouldering when moving from L-LiIrS₂ to the delithiated phase L-IrS₂ is in good agreement with our SXR/STEM results showing a significant change of crystalline structure upon Li extraction. Finally, SQUID measurements on both J-IrS₂ and L-IrS₂ (cf. figure III.34) indicates diamagnetic behavior for both these compounds. All these observations are consistent with an Ir³⁺ (i.e. a d⁶ low spin electronic configuration) with likely an effective charge (ionization degree) slightly lower for Ir in L-LiIrS₂. This indicates that while iridium is involved in the electrochemical processes of these compounds its contribution remains low and naturally questions the presence of another redox center.

Sulfur 2p XPS spectra were equally collected for the same four compositions (figure III.35.c). The J-IrS₂ spectrum can be decomposed in two components of similar intensities, the first one at low binding energy (S 2p_{3/2} at 161.8 eV) accounting for S²⁻ species and the second one at higher binding energy (163.4 eV) indicating oxidized sulfur species that can be unambiguously attributed to the (S₂)ⁿ⁻ (n≈2) dimers observed in the structure. Upon lithium insertion (J-

$\text{Li}_{0.5}\text{IrS}_2$) a significant (50%) drop of the $(\text{S}_2)^{n-}$ intensity to the benefit of S^{2-} is observed which confirms that the reduction of J-IrS_2 into $\text{J-Li}_{0.5}\text{IrS}_2$ involves mainly sulfur redox.

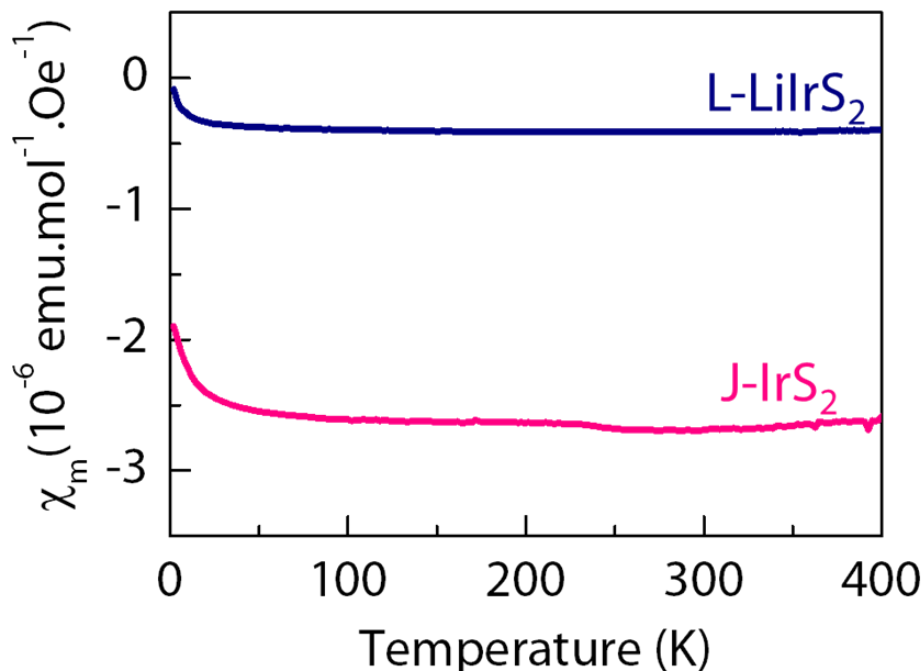


Figure III.34: Temperature dependence of the magnetic susceptibility χ of L-IrS_2 and J-IrS_2 .

Moving to the layered structures, the S 2p XPS spectrum of L-LiIrS_2 shows principally S^{2-} contribution (161.8 eV), with in addition a contribution at higher binding energy (162.8 eV). Note that the binding energy is different from $(\text{S}_2)^{n-}$ observed in J-IrS_2 phase and is attributed to oxidized sulfur specie S^{m-} ($m < 2$) that is different from S-S dimer. The presence of S^{m-} can be due to the Li/Ir off-stoichiometry of the pristine compound (estimated Li/Ir = 0.9, see above) and such average charge of the sulfur atoms lower than -2 is coherent with the relatively low c/a ratio calculated for the L-LiIrS_2 structure. This low c/a ratio might also be directly related to a partial depletion of the sp anionic band (less repulsive S...S interactions) associated with the S^{m-} ($m < 2$) electronic configuration of sulfur anions. This is also coherent with the lower ionization degree of Ir in L-LiIrS_2 previously discussed. Moreover, a slight contribution of elemental sulfur is also observed (at 164.1 eV), possibly assigned to unreacted sulfurs at the particle surface. While removing the lithium, the relative intensity of the S^{m-} peak increased compared to that of the S^{2-} (with in addition, in a smaller extent, the increase of the elemental sulfur contribution at higher binding energy). These results demonstrate the strong implication of the sulfur in the $\text{L-LiIrS}_2/\text{L-IrS}_2$ redox process, which is in line with bond valence sum calculations, indicating that L-IrS_2 is composed of sulfur atoms with two different charges referred to as S1 and S2 (see table III.10), with the latter being more oxidized. However, it is

worth noticing that the binding energy of the oxidized S atoms in L-IrS₂ is very different from the (S₂)ⁿ⁻ (n≈2) dimers in J-IrS₂, which suggests different oxidized species in line with SXRD/STEM analyses based on the S-S distances being too long (2.9 Å) to account for a S-S chemical bond in layered IrS₂. To further interrogate the nature of the oxidized sulfur species for these systems, Raman spectra of the four compounds have been collected and the results are represented in figure III.35.e.

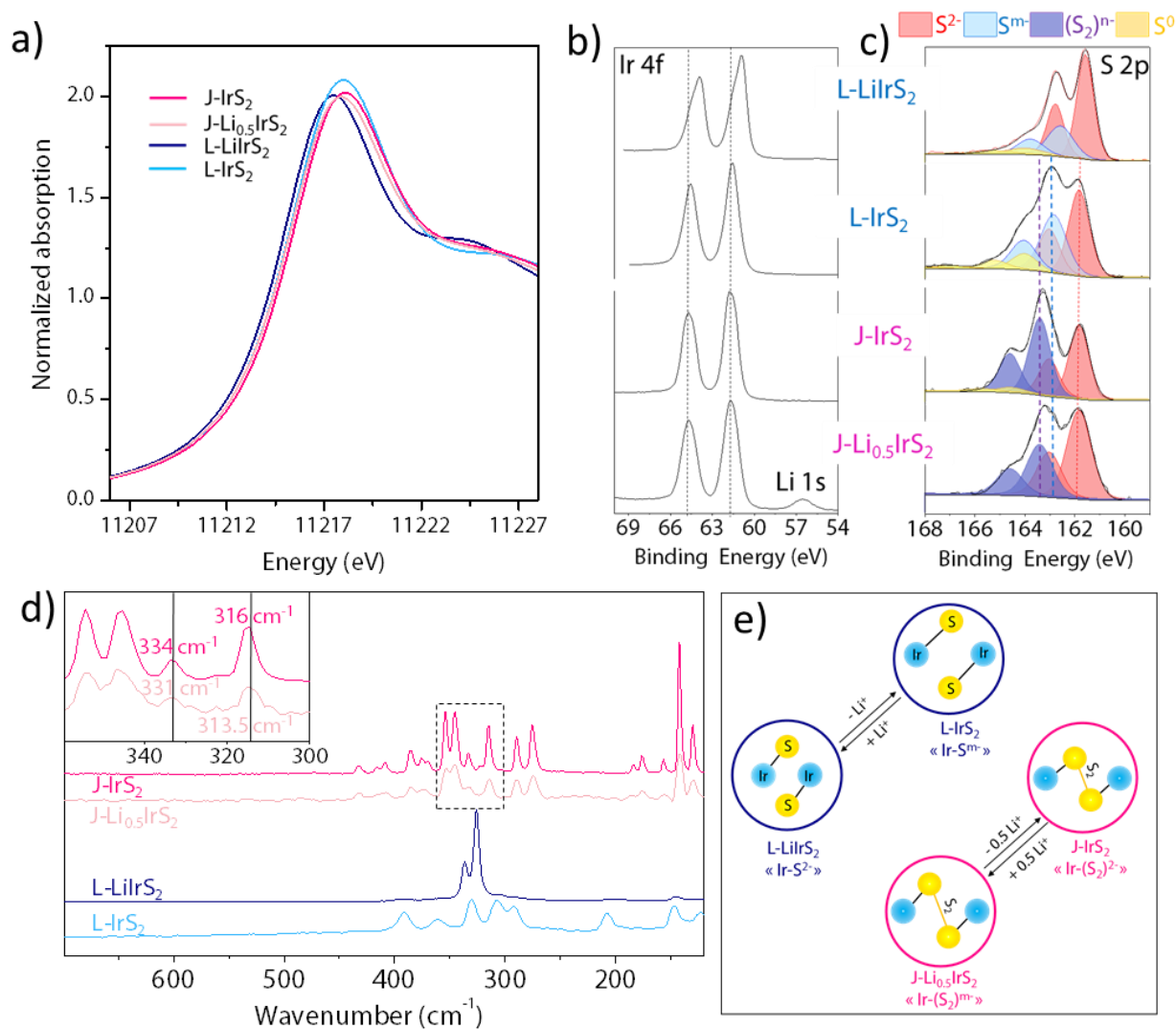


Figure III.35: (a) X-ray absorption near-edge structure of four Li_xIrS₂ compounds at Ir L₃-edge. (b-c) Ir 4f and S 2p XPS spectra. The Li 1s component observed besides the Ir 4f spectrum of J-Li_{0.5}IrS₂ mostly corresponds to residues at the surface originating from the chemical lithiation reaction used to synthesize this compound. The S 2p spectra have been decomposed in several components: S²⁻, S^{m-}, (S₂)ⁿ⁻ dimers, and a surface contribution of elemental sulfur S⁰. (d) Raman spectra of the four Li_xIrS₂. The inset is a zoom in the [360 cm⁻¹-300 cm⁻¹] region where the positions of the two peaks attributed to the S-S dimer stretching are given for both J-IrS₂ and J-Li_{0.5}IrS₂. (e) Schematic drawing of the charge compensation in both J- and L-Li_xIrS₂ polymorphs.

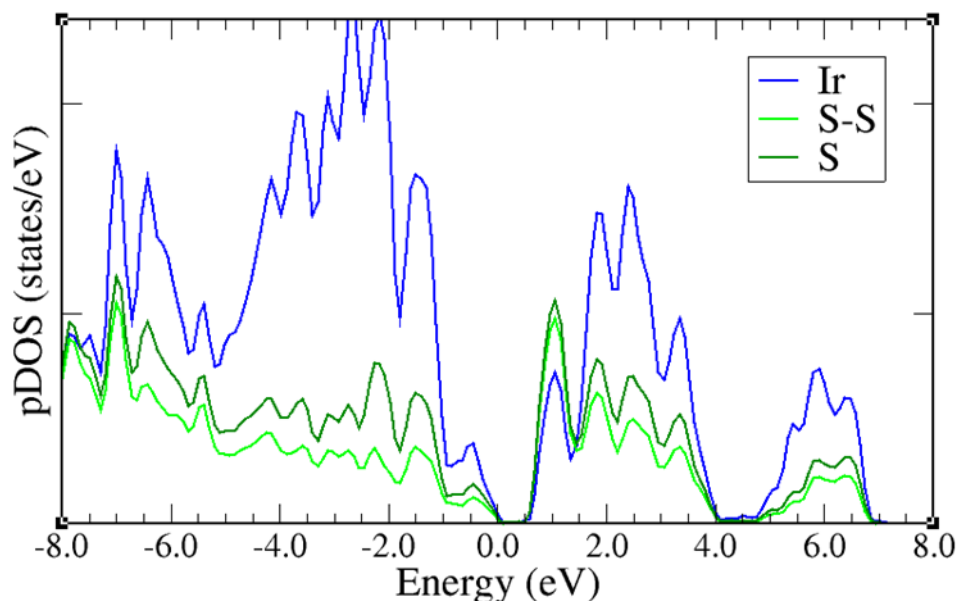


Figure III.36: pDOS as computed with VASP using the metaGGA SCAN functional for exchange and correlation potential.

The Raman spectrum measured for J-IrS₂ shows peaks related to the (S₂)ⁿ⁻ (n≈2) stretching modes at 334 and 316 cm⁻¹, indicating a 55 to 65 N.m⁻¹ bonding strength between the two sulfur atoms. Upon insertion of 0.5 Li, the overall structure of the Raman spectrum is conserved in spite of some peaks shifts. In particular the peaks related to the S-S dimers stretching are still present but they have broadened and shifted towards lower energies (331 and 313.5 cm⁻¹) indicating the retention of the S-S bond, which are however slightly weakened (50 to 60 N.m⁻¹). Such softening of the dimers corresponds to an elongation of 1 or 2 % of the S-S bonds, which is in agreement with our structural findings. At first sight such elongation of the dimer is consistent with an electrochemical reduction of this entity, however, one would expect a more significant distortion for the transition from (S₂)²⁻ to (S₂)³⁻. Nevertheless, it is important to remember that these materials are highly covalent, the electronic levels of (S₂)²⁻ of J-IrS₂ are likely strongly hybridized with the iridium ones and therefore the charge carried by the sulfur dimer is strongly delocalized explaining this small length variations. It is also possible that the structure of the material itself constrains the elongation of the dimer. At this stage, one could argue that a global reduction of the (S₂)²⁻ to (S₂)³⁻ contrasts with the XPS results since under such a scenario a shift to lower binding energy of the (S₂)²⁻ signal in the J-Li_{0.5}IrS₂ S2p spectrum is expected. However, we solely observe a change in the (S₂)²⁻/S²⁻ signal intensities ratio. Such apparent contradiction can be reconciled by considering the (S₂)³⁻ dimer as an entity evolving dynamically between (S₂)²⁻ and S²⁻. Therefore, it would be tempting to talk, alike in

organic chemistry, of mesomerism with the resonance forms being: $(S_2)^{3-} = [(S_2)^{2-} \leftrightarrow S^{2-}]$. Such a dynamic scenario could also explain in part the difficulties encountered for the theoretical simulation of these phases.

In contrast, the Raman spectra collected for the layered systems drastically differ between L-LiIrS₂ and L-IrS₂. The L-LiIrS₂ Raman spectrum ($P\bar{3}m1$) shows only two peaks (associated to A_{1g} and E_g modes) in contrast to the one of L-IrS₂ that is more complex. This difference is coherent with the symmetry lowering observed through delithiation of L-LiIrS₂, hence further supporting the existence of structural distortions in the material as previously described. However, further force field analysis would be needed to make proper attribution of the spectrum peaks.

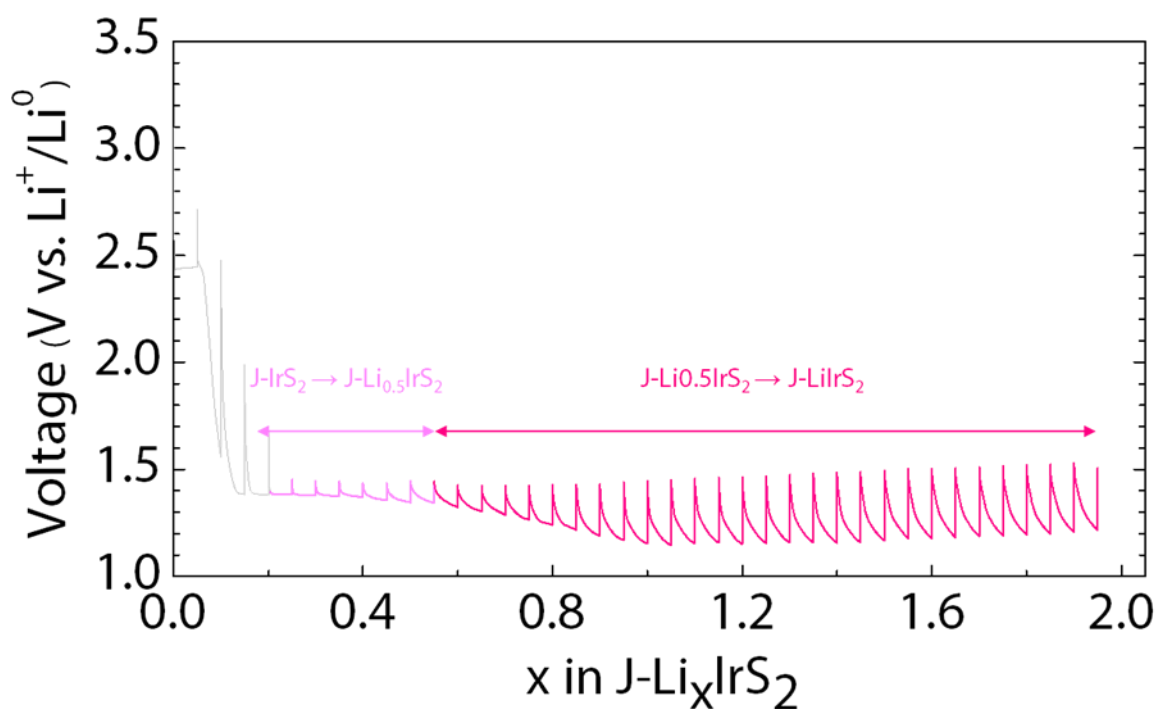


Figure III.37: Voltage profile of J-Li_xIrS₂, recorded with a GITT protocol. The cell was cycled at C/20 rate and allowed for equilibrium after every 0.05 lithium removal by keeping the cell at rest for 20 hrs. The light pink region corresponds to the formation of J-Li_{0.5}IrS₂, while the dark pink region corresponds to the formation of J-LiIrS₂. In both regions, the equilibrium potential of ~1.5 V is obtained.

Altogether these results provide an insight in the charge compensation mechanism and its interplay with the electronic structure evolution of the materials. According to the density of states of J-IrS₂ and considering a rigid band structure, the insertion of electrons in J-IrS₂ is expected to progressively fill the antibonding states of the S-S dimer hybridized with both iridium and S²⁻ sulfur (cf. figure III.36). This will first lead to a softening of the S-S bond (J-

$\text{Li}_{0.5}\text{IrS}_2$) and ultimately to its breaking (J-LiIrS_2). However, this simple band picture does not explain the voltage drop at $x = 0.5$. To gain further insight into this aspect, Galvanostatic Intermittent Titration Technique (GITT) measurements were conducted. (cf. figure III.37). They reveal a small relaxation voltage through the $\text{J-Li}_{0.5}\text{IrS}_2$ formation plateau as opposed to a strong one for the second plateau corresponding to the J-LiIrS_2 formation, but interestingly the relaxed voltage barely changes from $\text{J-Li}_{0.5}\text{IrS}_2$ to J-LiIrS_2 . This implies that the phases should form at nearly the same potential but this does not happen due to different kinetics. This kinetic limitation can be rationalized based on structural consideration by recalling that all empty ramsdelite octahedral sites are filled with lithium in $\text{J-Li}_{0.5}\text{IrS}_2$ with additionally the blocking of the rutile type-sites by S-S dimers. Thus, to uptake further Li, the structure of $\text{J-Li}_{0.5}\text{IrS}_2$ reorganizes via the breaking of the dimers and this comes with a kinetic penalty.

The charge compensation in L-IrS_2 appears more complicated although some insights can be obtained in light of reported studies on IrTe_2 . This compound adopts a room temperature O1 layered structure made of perfectly regular IrTe_6 octahedra but shows a distorted O1 layer structure at low temperature with Ir-Ir dimerization, hence bearing some resemblance to L-IrS_2 . A multicenter bond involving the iridium atoms pertaining to the dimers and the tellurium atoms joining these two iridium atoms has been proposed to account for the low temperature Ir-Ir dimerization. Thus, by analogy, the reorganization of the electronic structure in L-IrS_2 could stabilize the oxidized sulfur atoms. However, at this stage DFT calculations are strongly needed to rationalize such hypothesis and preliminary attempts have not yet been conclusive.

Finally, it is important to mention that Li_xIrS_2 is highly covalent system and is not possible to attribute a formal charge to the iridium and sulfur or to classify the redox process as strictly “cationic” or “anionic”. However, the main conclusion of this charge compensation study is that the L- and J- polymorphs follow completely different redox pathways (cf. figure III.35.f). The J- system involves an $\text{Ir-(S}_2\text{)}^{n-}$ entity ($n > 2$) while the layered system involves Ir-S^m entity ($m < 2$) in the redox process; here the prefix "Ir" suggests that the anionic levels involved in the redox are strongly hybridized by the Iridium. However, for simplification purpose, the redox couple of the J and L- system are mentioned as $(\text{S}_2)^{n-}/(\text{S}_2)^{2-}$ and S^m/S^{2-} respectively in the following discussion.

III.2.b Discussion

Altogether, we studied the Li-reactivity of two IrS₂ polymorphs: the J-IrS₂ one synthesized at high temperature which possess S-S dimers and the L-IrS₂ one obtained by delithiation of the layered LiIrS₂ and which shows oxidized sulfur anions but no S-S dimers. Our spectroscopic analyses unambiguously demonstrate that both polymorphs followed different charge compensation mechanisms through cycling. Such specific features of two polymorphs that react with Li⁺ via two different redox couples makes the IrS₂ system unique to understand the structure - charge compensation mechanism interlink.

Electrochemical reactions proceed at room temperature and usually lead to metastable phases. However, the thermodynamic reversible path for lithiation and delithiation of J-IrS₂ and L-Li_xIrS₂ can be identified by conducting reactions at higher temperatures (cf. figure III.38.a). By reacting J-IrS₂ with metallic lithium at 600 °C, L-LiIrS₂ was synthesized with a ratio Li/Ir = 1, this phase was then delithiated by an iodine (I₂) treatment at 900°C to produce J-IrS₂, hence providing a different reaction lithiation-delithiation pathway than the room temperature (electrochemical) one. These results indicate that the thermodynamically driven reaction path can be written as follows:



It is different from the room temperature electrochemical one that follows a kinetic path, as schematized in figure III.38.b. Structurally speaking, the thermodynamic reversible pathway between L-type and J-type is possible only through iridium atoms migration. Though cation migration is often reported in layered materials, studies performed on Li₂IrO₃ demonstrated that the iridium atoms are not likely to migrate during delithiation due to the strongly covalent Ir-O bond.^{78,86} On moving from oxides to sulfides the material becomes even more covalent, hence the migration of Ir is expected to be further impeded. This provides a plausible explanation to account for the different reaction pathway observed between low and high temperature. Another factor coming in play to trigger the J ⇌ L transition is the breaking and formation of S-S dimers that is associated to electronic rearrangements. Such a strong electronic reorganization is energetically costly, and therefore not the most favorable path at low temperature.

Our results thus confirm that when the activation energies required to form the thermodynamically stable phase are too high, kinetics guide the structure selection (i.e. the formation of metastable phases) along the phase transformation pathway. More importantly,

this selection of the reaction pathway directly affects the sulfur redox couple. Hence, while the thermodynamic path relies on a sulfur redox chemistry enlisting the $(S_2)^{2-}/S^{2-}$ redox couple, the room temperature kinetic pathways are constrained to those involving metastable sulfur states (i.e. $(S_2)^{n-}$ and S^{m-} with $n > 2$ and $m < 2$). Thus, the voltages differences observed for J and L (ΔE_J and ΔE_L , respectively) between the kinetic pathways and the thermodynamic one are most likely originating from the different redox potential associated to these two sulfur redox couples (cf. figure III.38.c).

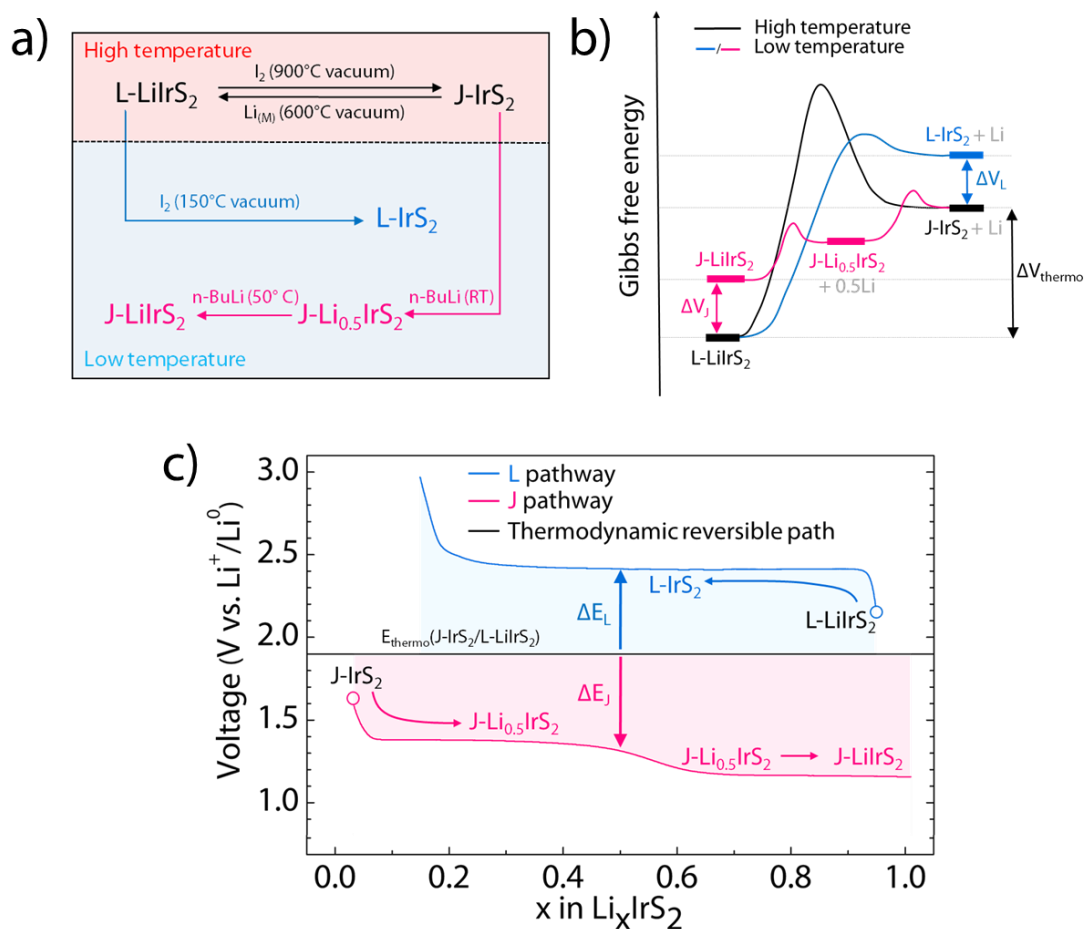


Figure III.38: a) Sum up of the chemical lithiation/delithiation products as a function of the reaction temperature. b) Schematic of the energy landscape for the Li_xIrS_2 system. In particular, it highlights the relative stability of the phases and the activation energy associated to all the reactions. c) Comparison between the experimental electrochemical curves obtained for the J and L pathways and the calculated thermodynamic potential associated to the reaction (1).

We show in this work that the crystallographic structure controls the nature of the sulfur redox couple together with its potential difference that can be as large as 1 V. A legitimate question thus arises on how such finding could provide more insights into the electrochemistry of the lithium-rich oxides. This remains an open question. Nevertheless, a parallel can be drawn

between our findings and the multistep mechanism previously hypothesized for anionic redox materials based on isothermal calorimetric measurements.⁹⁷ This proposed but unproven multistep mechanism (cf. figure III.39.a) consists of decomposing the lithiation/delithiation process into successive electrochemical steps involving minimal structural/electronic reorganization that are followed by chemical rearrangement steps (cation migration, shortening of O-O bonds or even dimer formation according to some authors). Here we nicely demonstrate that the structural differences between the charged and discharge states most presumably occur through different oxygen redox couples, which leads to the observed voltage asymmetry referred to as hysteresis (cf. figure III.39.b).

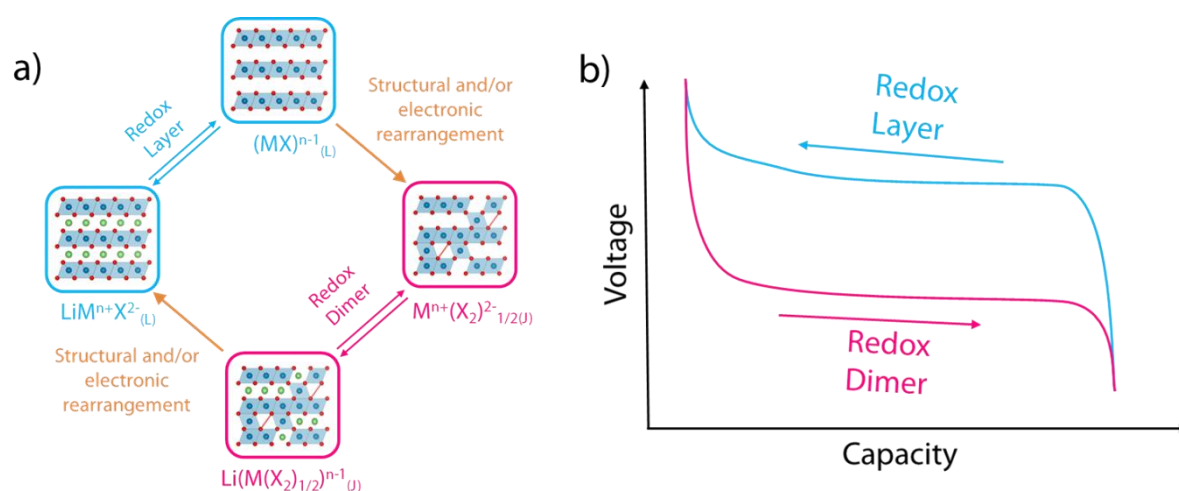


Figure III.39: a) Schematic drawing of the proposed reaction pathway within the cycling of anionic redox active material. According to this scenario, the extraction of lithium is done through a first redox process involving the anion and/ or the cation (redox layer). This metastable form then reorganizes chemically to form anionic dimers (X_2). The subsequent electrochemical process for lithium intercalation then involves the redox of the dimer (redox dimer), which at the end of the discharge can reorganizes partly/ fully to reform the pristine like material. b) The resulting (hypothetical) electrochemical curve with hysteresis due to difference in redox couples between charge (layer) and discharge (dimer). The wordings ‘layer’ and ‘dimer’ in the figure represents layered structure and the rearranged structure with dimers respectively.

Moreover, such squared mechanism suggests, at first sight, the feasibility to cure this hysteresis by preventing the reorganization steps (cf. figure III.39.a), that we have realized in this study by chemically designing these two IrS_2 polymorphs (L- IrS_2 /L- LiIrS_2 and J- IrS_2 /J- $\text{Li}_{0.5}\text{IrS}_2$ anionic redox process occurring without any hysteresis). Such strong finding is in agreement with recent studies that have correlated the absence of hysteresis in Li_2IrO_3 ¹⁰¹ or $\text{Na}_2\text{Mn}_3\text{O}_7$ ¹⁰⁰ to the lack of structural evolution concomitantly with the electrochemical reaction. Therefore, our results not only describe Li-rich sulfides but also apply to the electrochemical behavior observed for Li-rich oxides.

In summary, we have reported the chemical design of novel IrS₂ polymorphs that were used as ideal systems to understand the structurally driven reaction pathways during lithiation/delithiation of anionic redox based compounds. Combined XRD, XPS and Raman revealed that both J-IrS₂ and L-IrS₂ polymorphs, with or without S-S dimers, have asymmetric redox processes involving different reaction intermediates. Moreover, the use of such tailor-made sulfides helped in experimentally rationalizing the multistep “square scheme” model previously proposed and in turn explain the electrochemical behavior of most oxides showing anionic redox activity. Apart from providing mechanistic insights, revisiting the chalcogenide chemistry opens up a new way to predict and chemically design anionic redox based materials with mitigated hysteresis. Finally, through the report of a new IrS₂ phase, we broaden the layered chalcogenides family that constitutes a hot topic nowadays owing to unusual catalytic, optical, electronic, and spintronic properties.

Chapter conclusion

In this chapter we have synthesized lithiated transition metal chalcogenides that can present interesting properties for the study of anionic redox processes. Thus, we have been focusing on a still little-studied family of chalcogenides: the Li_3MS_4 compounds (with $\text{M} = \text{V}, \text{Nb}$ or Ta). We succeeded in synthesizing the rocksalt compounds Li_3NbS_4 and Li_3TaS_4 in two different polymorphic forms as a function of the synthesis mode (high temperature or ceramic). Interestingly, we observed that the disordered polymorph of the Li_3NbS_4 compound was electrochemically active unlike the ordered compound. This result allowed us to better understand the activation mechanisms of anionic redox processes and in particular the effect of cationic disorder in this process. Then, in a second study, we focused on the compounds LiIrS_2 and IrS_2 which, despite their identical chemical composition, present very different lithiation/delithiation mechanisms with a 1V voltage difference between the two. The detailed study of this system has highlighted the influence of the anionic dimers on the electrochemical process, thereby allowing for a better understanding of the electrochemical activity of much more complex systems such as lithium rich oxides.

These results clearly suggest that new lithiated chalcogenides remain to be discovered. For instance, it could be interesting to try to form the selenides associated with Li_3MS_4 . Our first exploratory results seem to indicate that Li_3NbSe_4 does not form contrary to Li_3TaSe_4 . Also, considering that IrS_2 and IrSe_2 are isostructural, the study of the electrochemical behavior of a tentative LiIrSe_2 is quite exciting. Finally, if the recent studies on lithium-rich chalcogenides have been focusing on the compounds of the fourth or fifth groups (Li_2MS_3 with $\text{M} = \text{Ti}, \text{Zr}$ and Hf or Li_3MS_4 with $\text{M} = \text{Nb}, \text{Ta}$ respectively), what about the sixth group? Is it possible to form Li_4MS_5 compounds (with $\text{M} = \text{Cr}, \text{Mo}$ or W) like Li_4MoO_4 and Li_4WO_4 oxides? These are just some potential ideas and many other compounds are yet to be discovered. However, it is important to remember that the electronegativity of sulfur, lower than that of oxygen, limits the high oxidation degrees of the cations. This constraint statistically decreases the number of potentially obtainable compounds and it would not be surprising if the source dried up quickly. Faced with this observation, it is important to extend the search for intercalation materials to new families of compounds that are still little or not studied: this is the purpose of the next chapter.

Chapter IV: Investigation of new chemistries

IV.0 Introduction

In the previous chapters, we have discussed the difficulties to synthesize new oxides or sulfides, these two families of compounds having already been widely exploited. Indeed, a quick check in the crystallography databases (cf. figure IV.1) clearly shows that the number of reported oxides/sulfides far exceeds that of the other monoanionic compounds (nitrides, halides etc...). If the search is extended to multi-anionic compounds (oxy-sulfides/nitrides/halides etc...) the number of possible combinations becomes infinite. However, the synthesis of these compounds is often much more complex than that of chalcogenides. In line with these observations, the aim of the next section is to investigate the electrochemical and/or magnetic properties of some oxysulfide and halide compounds.

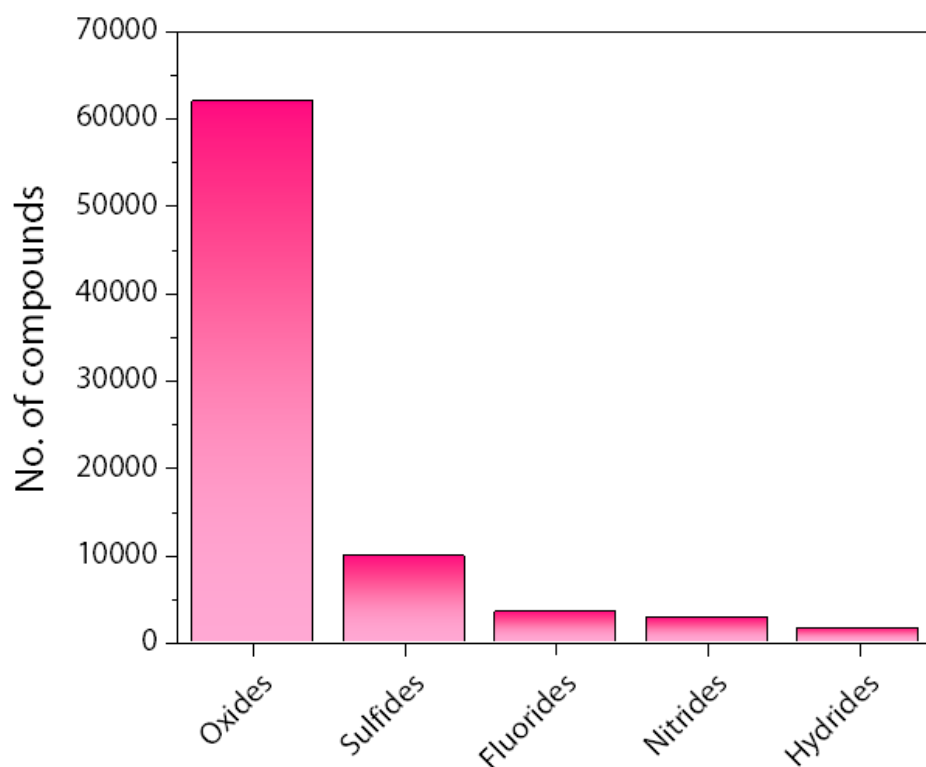


Figure IV.1: Number of single-anion compounds reported according to the Inorganic Crystal Structure Database (ICSD, <https://icsd.fiz-karlsruhe.de>), as of July 9, 2021.

IV.1 Oxysulfides

Previously, we have seen that the most common single-anion compounds studied for Li-ion batteries were oxides and sulfides. The study of oxysulfides arises then quite naturally, especially in the anionic redox context. Indeed, one naive idea would be to combine in a single compound the anionic redox stability of the sulfides with the higher potential of the oxides. The goal of this section is therefore to discuss this point after a brief introduction to the oxysulfides.

IV.1.a General Considerations

First, it is important to note that oxysulfides are quite rare in nature, indeed, in the presence of oxygen, sulfur tends to oxidize, which leads to the formation of polyanionic substructures (SO_4 , SO_3 etc. ...). Moreover, from a structural point of view, the oxysulfides slightly differ from other mixed-anion compounds such as oxynitrides or oxy-fluorides due to the bigger size of the S^{2-} anions (in IV-coordination $\text{N}^{3-} = 1.46 \text{ \AA}$, $\text{O}^{2-} = 1.38 \text{ \AA}$, $\text{F}^- = 1.31 \text{ \AA}$ and in VI-coordination $\text{S}^{2-} = 1.84 \text{ \AA}$). This size-mismatch prevents any anion-site mixing between sulfur and oxygen and leads most of the time to a long range ordering of the two anions. This segregation often takes the form of alternating layers of oxides and sulphides. For instance the LaCuOS (resp. $\text{Sr}_2\text{ZnO}_2\text{Cu}_2\text{S}_2$) structure can be described as a stacking of $[\text{LaO}]^+$ (resp. $[\text{Sr}_2\text{ZnO}_2]^{2+}$) and $[\text{CuS}]$ (resp. $[\text{Cu}_2\text{S}_2]^{2-}$) layers (cf. figure IV.2). It is worth mentioning that most of the reported oxysulfides are derivatives of the two compounds mentioned above, which are themselves related to the Ruddlesden-Popper structure.¹⁷⁰

Moreover, despite their low abundance, oxysulfides have been rather well studied as insertion materials. Indeed, Clarke's group deeply investigated the topotactical insertion of alkali cations (Li^+ , Na^+ and K^+)^{171–173} in $\text{Y}_2\text{Ti}_2\text{O}_5\text{S}_2$. Interestingly the authors demonstrated that in this compound the intercalation site was dependant on both the cation type and the chemical process. Indeed, lithium atom intercalation occurs between the oxygen layers, potassium atoms are placed between the sulfur layers and ultimately, and at low (resp. high) temperature the sodium atom insertion happens between the sulfur (resp. oxygen) slabs. Thereafter, the $\text{Sr}_2\text{MnO}_2\text{Cu}_{2m-0.5}\text{S}_{m+1}$ ($m = 1, 2, \text{ and } 3$) compounds were shown to intercalate lithium through copper/lithium displacement reactions (cf. figure IV.2).^{174–176} Following these initial studies, other oxysulfides have been studied for their alkali intercalation properties, among which we can mention CeOS ,¹⁷⁷ $\text{Na}_2\text{Fe}_2\text{OSe}_2$,¹⁷⁸ or Li_2FeOS .¹⁷⁹ The latter two in particular have been investigated as cathode compounds for Na-Ion or Li-ion batteries and the charge compensation

mechanisms have shown to occur mainly through cationic processes. However, for extended states of charge, Li_2FeOS presents an irreversible oxidation of the S^{2-} into elemental sulfur. Thus and to the best of our knowledge, the question of anionic redox processes in oxysulfides has not really been investigated yet. To fill in this gap we decided to study the $\text{Na}_3\text{VS}_{4-x}\text{O}_x$ family ($x = 0, 1$ or 2), and our results are presented below.

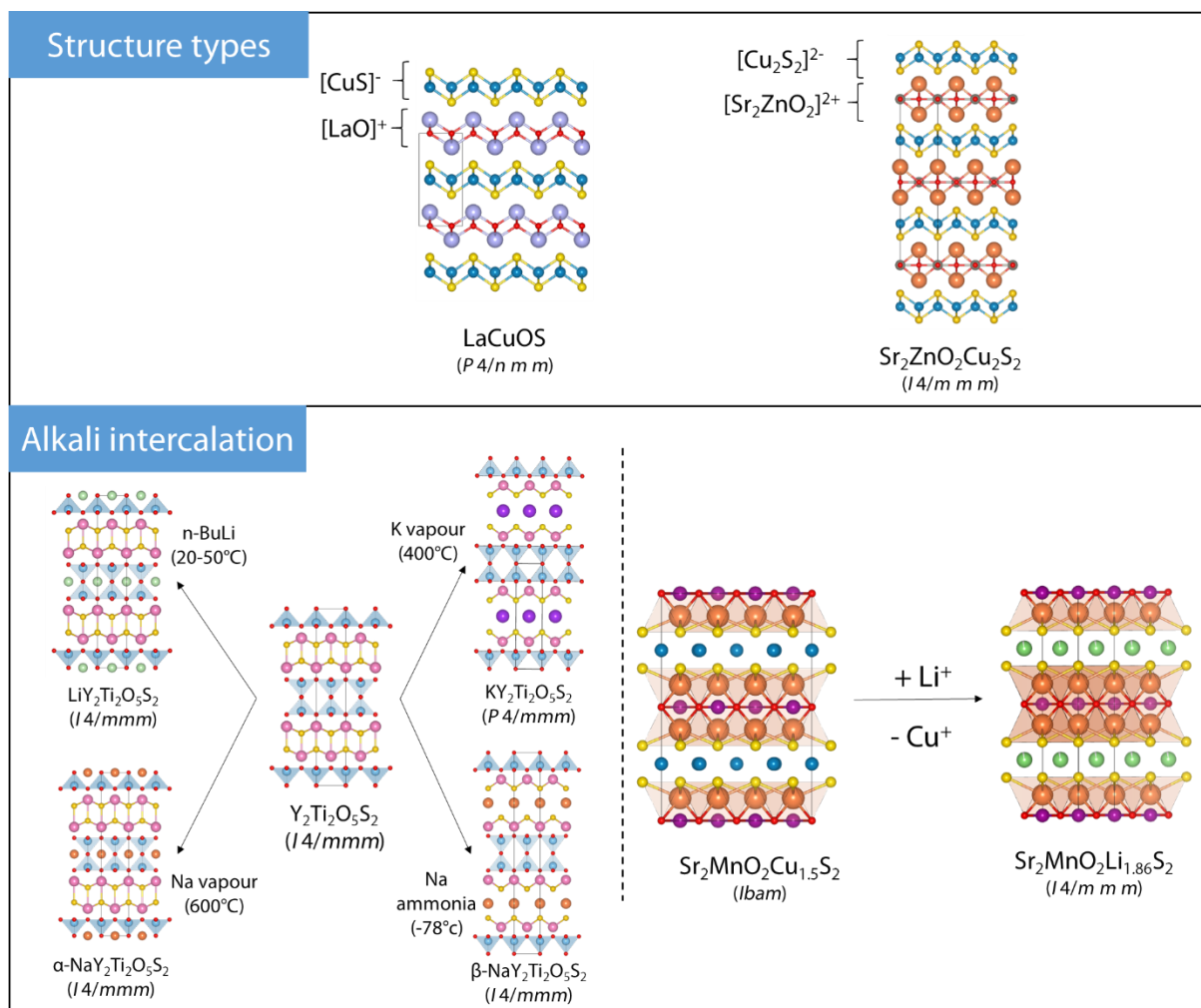


Figure IV.2: (top) schematic drawing of the two structure types dominating the known oxysulfides, (bottom) some examples of alkali intercalation in oxysulfide compounds (the left panel is inspired from ref[2])

IV.1.b $\text{Na}_3\text{VS}_{4-x}\text{O}_x$ compounds

The $\text{Na}_3\text{VS}_{4-x}\text{O}_x$ compounds ($x = 0, 1, 2, 3$ or 4) have been extensively studied by Schnabel et al.,^{154,180,181} and their structure can be described approximately (see later for further details) as independent $\text{VS}_{4-x}\text{O}_x$ octahedra dispersed in a Na^+ network. This family has particularly

attracted our attention for several reasons: first, an electronic count indicates that vanadium is supposed to be charged +5 (electronic structure d^0). We therefore expect an electrochemical participation of anions in the case of an oxidation of these compounds. Second, the vanadium is linked to both sulfur and oxygen atoms (heteroleptic polyhedron) and the ratio O/S can be controlled, thereby yielding a unique opportunity to study the influence of multi-anions on the anion redox process. We decided then to embark on the synthesis of these compounds.

i) Synthesis

As mentioned before, this family has already been described; however, most of the proposed syntheses lead to a mixture of compounds with different O/S ratios. We have then adapted the experimental procedure accordingly. For all the syntheses we have used sodium sulfide (Na_2S , Sigma-Aldrich), metallic Vanadium (Vanadium powder 99.5%, Alfa Aesar), elemental sulfur (99.998%, Sigma-Aldrich) and Vanadium (V) oxide (V_2O_5 , 99.6%) as precursors. The reactants were then homogeneously hand ground in an argon-filled glovebox following the ratio reported in table IV.1. The as-obtained mixtures were then transferred in a carbon coated quartz ampulla, which was subsequently sealed under high vacuum ($\sim 10^{-3}$ mbar). Finally, the tubes were placed in a muffle furnace and annealed at 550°C for 60 hrs. After reaction, the ampullas were opened inside a glovebox and the powder collected and stored without further processing. Following this procedure we managed to synthesize four pure compounds, namely, Na_3VS_4 , two polymorphs (α and β) of $\text{Na}_3\text{VS}_3\text{O}$ and $\text{Na}_3\text{VS}_2\text{O}_2$ found with small (unknown) impurities. It is worth noting that our attempts to obtain pure Na_3VSO_3 failed. The structures of the different compounds are described next.

	Na_3VS_4	$\alpha\text{-Na}_3\text{VS}_3\text{O}$	$\beta\text{-Na}_3\text{VS}_3\text{O}$	$\text{Na}_3\text{VS}_2\text{O}_2$
Na_2S	1.5 (1.5)	1.5 (1.5)	1.5 (1.5)	1.5 (1.5)
V	1 (1)	0.48 (0.6)	0.6 (0.6)	0.08 (0.2)
S	2.5 (2.5)	1.2 (1.5)	1.5 (1.5)	0.5 (0.5)
V_2O_5	0 (0)	0.26 (0.2)	0.2 (0.2)	0.46 (0.4)

Table IV.1: Molar ratio of the different precursors used for the synthesis. The black values correspond to the experimental ratios whereas the grey ones indicate the values expected from the compounds' stoichiometry.

ii) Structure

Prior to synchrotron XRD measurements, to avoid any decomposition in air, 0.6 mm diameter borosilicate capillaries were filled with the appropriate powders and subsequently sealed.

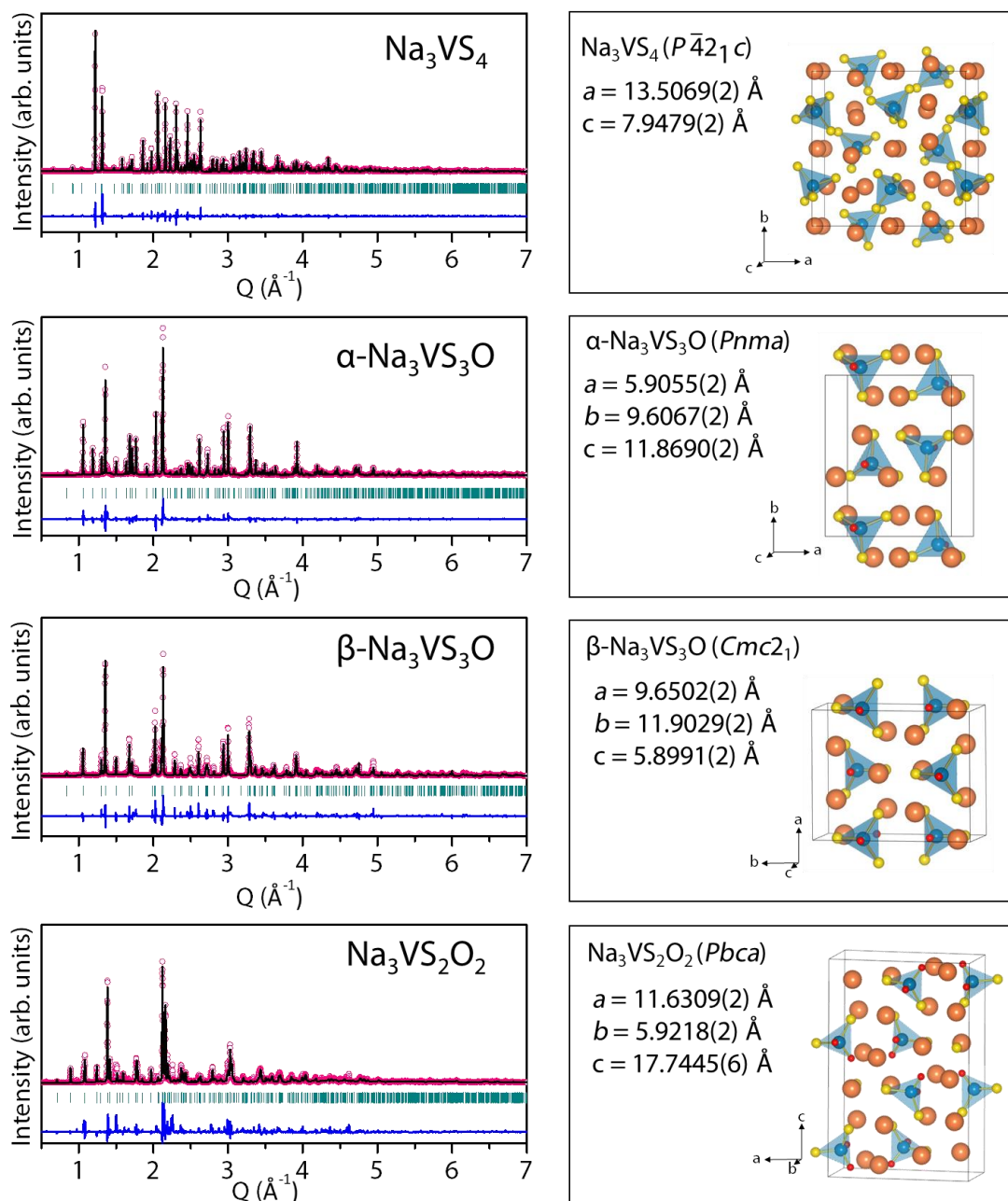


Figure IV.3: (Left) Synchrotron X-ray diffraction pattern Rietveld refinement of Na₃VS₄, α - and β -Na₃VS₃O and Na₃VS₂O₂ corresponding to the structural models reported in Table IV.2-5. Wavelength for synchrotron X-ray: $\lambda = 0.4137 \text{ \AA}$. The pink circles, black continuous line, and bottom blue line represent the observed, calculated, and difference patterns, respectively. The vertical green tick bars stand for the Bragg positions. (Right) corresponding structures. Oxygen, sulfur, vanadium and sodium atoms are represented in red, yellow, blue and orange respectively

Na_3VS_4		$P\bar{4}2_1c$	$R_{\text{Bragg}} = 5.72\%$	$\chi^2 = 6.54$		
$a = 13.5069(2) \text{ \AA}$		$c = 7.9479(2) \text{ \AA}$	$\text{Vol} = 1449.994(11) \text{ \AA}^3$			
<i>Atom</i>	<i>Wyckoff Position</i>	<i>x/a</i>	<i>y/b</i>	<i>z/c</i>	<i>B_{iso} (Å²)</i>	<i>Occupancy</i>
Na1	4d	0	1/2	0.5713(9)	3.51(8)	1
Na2	4c	1/2	1/2	0.7170(8)	3.51(8)	1
Na3	8e	0.7553(4)	0.5446(3)	0.8540(5)	3.51(8)	1
Na4	8e	0.7537(3)	0.7983(3)	0.9380(7)	3.51(8)	1
V1	8e	0.0106(2)	0.7388(2)	0.7789(2)	2.01(4)	1
S1	8e	0.6879(2)	0.5095(2)	0.5123(4)	2.46(3)	1
S2	8e	0.8710(2)	0.6898(2)	0.6799(4)	2.46(3)	1
S3	8e	0.6080(2)	0.8856(2)	0.6819(5)	2.46(3)	1
S4	8e	0.5800(2)	0.6611(3)	0.8981(4)	2.46(3)	1

Table IV.2: Crystallographic data and atomic positions of Na_3VS_4 determined from Rietveld refinement of its X-ray diffraction pattern.

$\alpha\text{-Na}_3\text{VS}_3\text{O}$		$Pnma$	$R_{\text{Bragg}} = 8.53\%$	$\chi^2 = 12.7$		
$a = 5.9055(2) \text{ \AA}$		$b = 9.6067(2) \text{ \AA}$	$c = 11.8690(2) \text{ \AA}$	$\text{Vol} = 673.354(8) \text{ \AA}^3$		
<i>Atom</i>	<i>Wyckoff Position</i>	<i>x/a</i>	<i>y/b</i>	<i>z/c</i>	<i>B_{iso} (Å²)</i>	<i>Occupancy</i>
Na1	8d	0.2543(8)	0.0424(4)	0.1305(3)	3.35(10)	1
Na2	4c	0.2546(10)	1/4	0.8708(5)	3.35(10)	1
V1	4c	0.3387(5)	1/4	0.4498(3)	3.08(8)	1
S1	4c	0.2432(7)	1/4	0.6310(3)	2.60(6)	1
S2	8d	0.2310(5)	0.0621(3)	0.3750(2)	2.60(6)	1
O1	4c	0.1401(16)	1/4	0.0530(8)	2.1(2)	1

Table IV.3: Crystallographic data and atomic positions of $\alpha\text{-Na}_3\text{VS}_3\text{O}$ determined from Rietveld refinement of its X-ray diffraction pattern.

$\beta\text{-Na}_3\text{VS}_3\text{O}$		$Cmc2_1$	$R_{\text{Bragg}} = 10.6 \%$	$\chi^2 = 23.5$		
$a = 9.6502(2) \text{ \AA}$		$b = 11.9029(2) \text{ \AA}$	$c = 5.8991(2) \text{ \AA}$		$Vol = 677.60(2) \text{ \AA}^3$	
Atom	Wyckoff Position	x/a	y/b	z/c	$B_{\text{iso}} (\text{\AA}^2)$	Occupancy
Na1	4a	0	0.8851(9)	0.152(19)	2.93(16)	1
Na2	8b	0.7956(7)	0.6146(7)	1.131(19)	2.93(16)	1
V1	4a	0	0.7065(5)	0.733(19)	1.79(12)	1
S1	4a	0	0.8788(7)	0.637(19)	1.67(8)	1
S2	8b	0.6877(5)	0.8798(5)	0.115(19)	1.67(8)	1
O1	4a	0	0.6941(14)	0.013(19)	0.5(3)	1

Table IV.4: Crystallographic data and atomic positions of $\beta\text{-Na}_3\text{VS}_3\text{O}$ determined from Rietveld refinement of its X-ray diffraction pattern.

$\text{Na}_3\text{VS}_2\text{O}_2$		$Pbca$	$R_{\text{Bragg}} = 18.3 \%$	$\chi^2 = 50.3$		
$a = 11.6309(2) \text{ \AA}$		$b = 5.9218(2) \text{ \AA}$	$c = 17.7445(6) \text{ \AA}$		$Vol = 1222.18(5) \text{ \AA}^3$	
Atom	Wyckoff Position	x/a	y/b	z/c	$B_{\text{iso}} (\text{\AA}^2)$	Occupancy
Na1	8c	0.3760(10)	0.2907(24)	0.2628(7)	2.46(20)	1
Na2	8c	0.3260(12)	0.1648(22)	0.4520(8)	2.46(20)	1
Na3	8c	0.1388(10)	0.2604(19)	0.1017(8)	2.46(20)	1
V1	8c	0.0547(5)	0.1760(12)	0.3884(5)	4.44(20)	1
S1	8c	0.3837(7)	0.2606(14)	0.1006(6)	2.57(14)	1
S2	8c	0.1238(8)	0.3046(17)	0.2865(5)	2.57(14)	1
O1	8c	0.1325(17)	0.259(3)	0.4634(12)	4.4(6)	1
O2	8c	0.4389(15)	0.367(4)	0.3766(14)	4.4(6)	1

Table IV.5: Crystallographic data and atomic positions of $\text{Na}_3\text{VS}_2\text{O}_2$ determined from Rietveld refinement of its X-ray diffraction pattern.

The different samples were then measured on the Materials Science and Powder Diffraction (MSPD) beamline of the Alba (Barcelona, Spain) synchrotron at a wavelength of 0.4137 \AA . The collected diffraction patterns were then refined using the data of the reported structural models (cf. figure IV.3). A particular attention was paid to the O/S ratio, indeed the stoichiometry used during the synthesis differed from the expected one (see table IV.1). Nevertheless, our results were consistent with the reported structures.

In short, as mentioned before, these structures are composed of independent heteroleptic VS_4-xO_x tetrahedra, where the sulfur and the oxygen atoms occupy distinct crystallographic sites. In addition, these structures differ in the spatial orientation of the coordination tetrahedra. For example, in the two Na_3VS_3O polymorphs all V-O bonds are parallel, however, in the alpha structure these bonds point in the same direction whereas in the beta structure every second tetrahedron is upside down. Finally, the sodium atoms are found in distorted vacant octahedral sites. Once these compounds were synthesized, it was possible to assemble batteries; the results of our electrochemical tests are presented next.

iii) Electrochemical tests

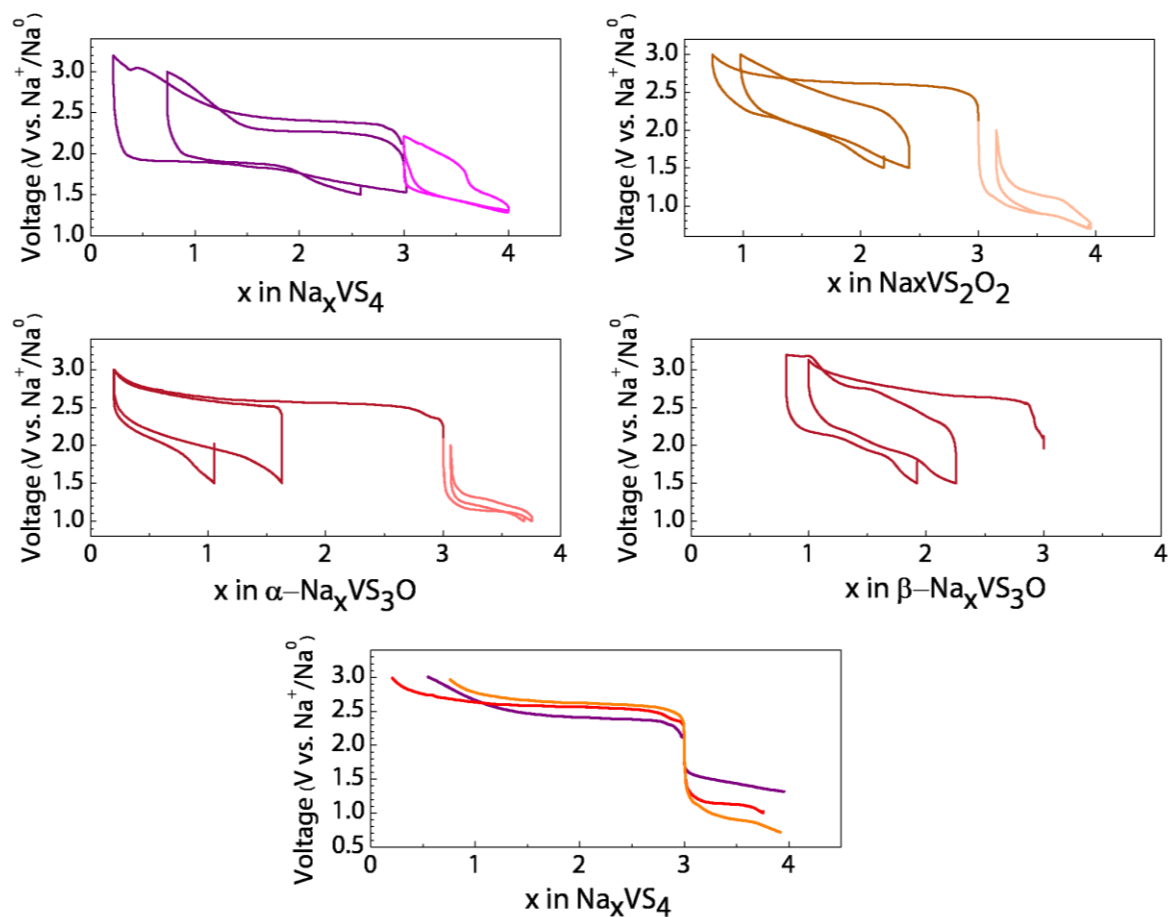


Figure IV.4: (a-d) Voltage–composition trace of (a) Na_3VS_4 , (b) $Na_3VS_2O_2$, (c) $\alpha-Na_3VS_3O$ and (d) $\beta-Na_3VS_3O$ cycled at C/20 starting with either oxidation (referred as Li-extraction) or reduction (referred as Li-insertion). (e) Comparison of potential of sodium extraction/insertion in Na_3VS_4 , $Na_3VS_2O_2$, and $\alpha-Na_3VS_3O$. The extraction (resp. insertion) potentials are those corresponding to the charge (resp. discharge) potential observed.

Swagelok-type cells were assembled using a sodium metal disk as the negative electrode and composite positive electrodes made by hand milling active compounds (either Na_3VS_4 , $\alpha\text{-Na}_3\text{VS}_3\text{O}$, $\beta\text{-Na}_3\text{VS}_3\text{O}$ or $\text{Na}_3\text{VS}_2\text{O}_2$) with 20 % in mass carbon Super P. Both positive and negative electrodes were parted with Whatmann GF/D borosilicate glass fiber sheets soaked in an electrolyte composed of a mixture of PC (polyethylene carbonate) and 1 M NaPF_6 . The cells were assembled in an argon-filled glovebox, and cycled at C/20 rate with a Biologic (MPG-2/VMP-3) cyler using a galvanostatic mode. The ability of these compounds to extract (starting with charge) or to insert (starting with discharge) sodium was tested separately. For the extraction, the cells were cycled between 3.2-1.5 V or 3.0-1.5 V, while for the insertion the cutoff limits were fixed according to the material (2.2-1.8 V for Na_3VS_4 , 2-1.0 V for $\alpha\text{-Na}_3\text{VS}_3\text{O}$ and 2.2-1.7 V for $\text{Na}_3\text{VS}_2\text{O}_2$, the insertion in $\beta\text{-Na}_3\text{VS}_3\text{O}$ has not been investigated). The composition vs voltage plots for both sodium removal and insertion are shown in Figure IV.4.a-d.

In summary, the extraction of more than two sodium atoms per formula unit is possible for each of the compounds via an electrochemical process occurring around 2.5 V. However, with the exception of Na_3VS_4 none of the compounds are able to completely reintercalate these sodium atoms and the reinsertion process occurs at a much lower potential than the insertion (voltage hysteresis). Moreover, this tendency increases cycle after cycle, and after a few cycles (around five) we observe almost no reversible capacity. Regarding the direct intercalation of sodium, each of the tested compounds demonstrated the ability to insert reversibly approximately one extra sodium per formula unit. However, in contrast to direct extraction, the potential difference between discharge and recharge is relatively small, but again the reversible capacity decreases rapidly cycle after cycle.

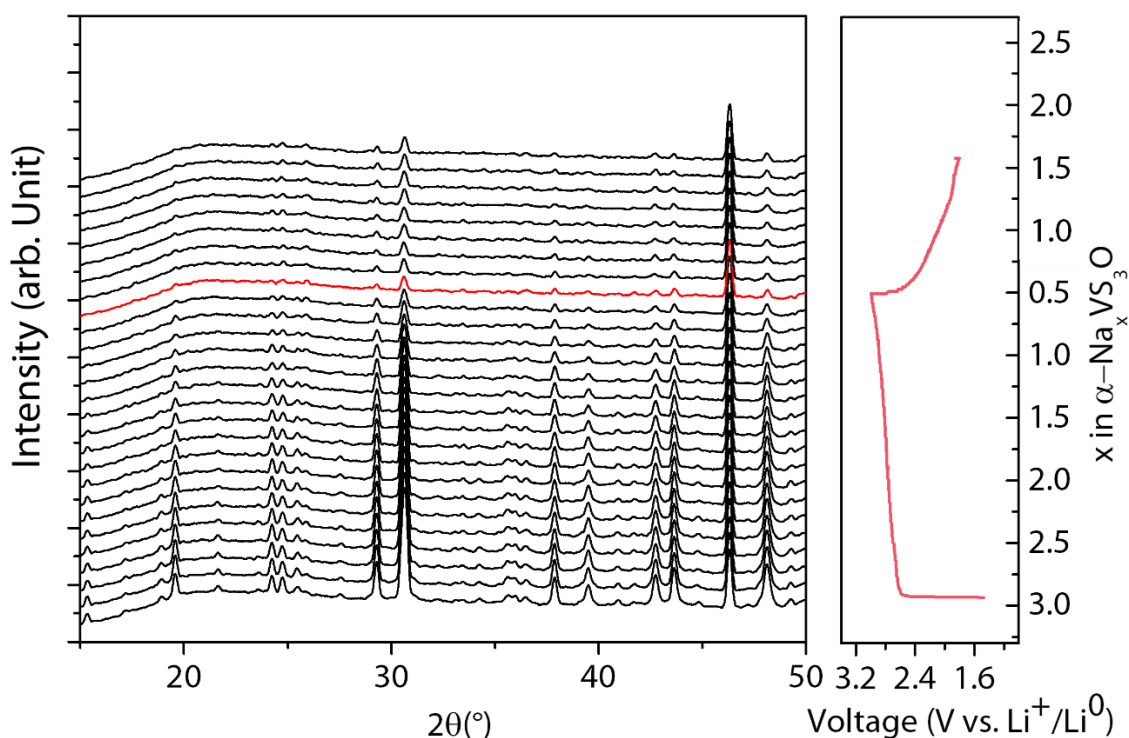


Figure IV.5: Operando XRD patterns during the first cycle of $\alpha\text{-Na}_3\text{VS}_3\text{O}$ with the corresponding galvanostatic curve. The compound is discharged at C/20 and the XRD patterns are measured for 1 h.

In order to understand the electrochemical behavior in charge, operando XRD measurements were performed on $\alpha\text{-Na}_3\text{VS}_3\text{O}$ (cf. figure IV.5). In short, upon sodium extraction the crystallinity of the materials constantly decreases and the process is irreversible. In addition, ex-situ XRD measurement on charged Na_3VS_4 and $\text{Na}_3\text{VS}_2\text{O}_2$ suggests a similar behaviour. From these data alone, it is complicated to propose a scenario explaining the electrochemical behaviour of these compounds. It is however possible to make some observations. In accordance with what has been said previously the d orbitals of vanadium are supposed to be completely empty (d^0) in these compounds. Thus, only a redox process involving sulfur and/or oxygen can participate to sodium atoms extraction. Several scenarios are then possible such as the formation of sulfur dimers throughout the material leading to the loss of long-range order as already proposed in disordered Li_2TiS_3 .¹⁸² It is also possible that this oxidation process leads to the decomposition of the compounds with a formation of elemental sulfur and/or molecular oxygen. The large structural modifications generated by either of these processes could also explain the difference in potential observed for the discharge process. Finally, the post mortem opening of the electrochemical cells clearly showed a staining of the electrolyte and the

separator, which strongly suggests a dissolution of part of the active material during cycling and could explain at least in part the loss of capacity observed cycle after cycle.

At this point, it is important to remember our initial question about the influence of the O/S ratio on the potentials of the observed electrochemical processes.

iv) Influence of the O/S ratio

In order to compare the sodium extraction and intercalation potentials, the charge and discharge voltage curves for Na_3VS_4 , $\text{Na}_3\text{VS}_2\text{O}_2$, and $\alpha\text{-Na}_3\text{VS}_3\text{O}$ have been plotted together (cf. figure IV.4.e). A first quick analysis could let us think that the Na-extraction voltage increases from Na_3VS_4 to $\alpha\text{-Na}_3\text{VS}_3\text{O}$ and $\text{Na}_3\text{VS}_2\text{O}_2$, that is, increases together with the oxygen amount as intuitively expected. It is important to note, however, that the above-plotted voltage curves correspond to the electrochemical charge. Thus, their positions do not depend only on the thermodynamic equilibrium potential associated with the oxidation reaction but also on an overpotential of kinetic origin. Indeed, if we look carefully at figure IV.4 we can see that the potential difference between the charge and the discharge also increases from Na_3VS_4 to $\text{Na}_3\text{VS}_2\text{O}_2$, thereby suggesting that the polarization also increases in that direction. It is therefore not reasonable to conclude on any evolution of the sodium extraction potential between these three compounds and a GITT analysis would be necessary to reach a conclusion. Conversely, for intercalation, as the polarization between discharge and recharge is low, it is clear that the insertion potential decreases from Na_3VS_4 to $\text{Na}_3\text{VS}_3\text{O}$ and then to $\text{Na}_3\text{VS}_2\text{O}_2$.

This trend may seem counterintuitive at first glance, since one would expect the potential to increase with the amount of oxygen. To rationalize this but also to discuss the position of the extraction potential it is possible to make a simplified model of the band structure of these compounds. Indeed, in the first chapter of this manuscript, we have proposed a method to get an idea of the band structure of a compound based on the molecular orbital diagram of the coordination polyhedron of the component transition metal. Thus, it is interesting to construct the molecular orbital diagram associated with the various studied compounds. To that end, it is necessary to first consider the punctual symmetry of all the $\text{VS}_{4-x}\text{O}_x$ polyhedra. Indeed, using the Schoenflies notations, in Na_3VS_4 , the $[\text{VS}_4]^{3-}$ tetrahedron is described by the T_d point group, in $\text{Na}_3\text{VS}_3\text{O}$, the $[\text{VS}_3\text{O}]^{3-}$ tetrahedron is described by the C_{3v} point group and lastly the $[\text{VS}_2\text{O}_2]^{3-}$ in $\text{Na}_3\text{VS}_2\text{O}_2$ is described by the C_{2v} point group. Following these symmetry considerations, taking into consideration both σ and π interactions between the vanadium center and the O/S ligands, and following the energy order proposed by Schnabel et al.,¹⁵⁴ it is possible to draw the

orbital diagram associated to the tetrahedra as presented in figure IV.6. Moreover, since the tetrahedra are totally separated from one another, the band diagram should look like the orbital diagram with narrow bands instead of discrete levels. Consequently, for the sake of simplicity we will discuss the electrochemical properties of the $\text{Na}_3\text{VS}_{4-x}\text{O}_x$ compounds using directly the molecular diagrams.

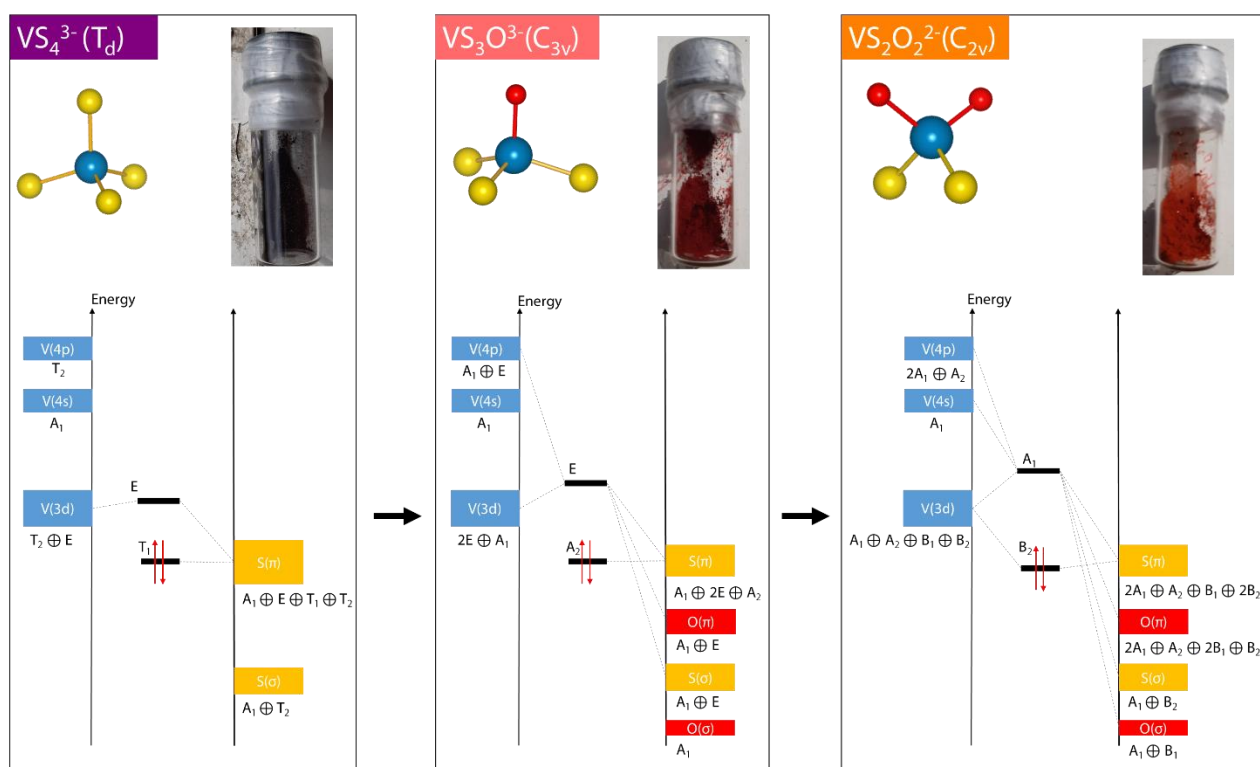


Figure IV.6: Orbital diagram of the $[\text{VS}_4]^{3-}$, $[\text{VS}_3\text{O}]^{3-}$, and $[\text{VS}_2\text{O}_2]^{3-}$ subunits considering both σ and π interactions between the vanadium center and the O/S ligands. This diagram is adapted from the work of Schnabel et al.¹⁸¹ The insets represent a picture of the corresponding $\text{Na}_3\text{VS}_{4-x}\text{O}_x$ powder.

A first interesting observation is that the highest occupied molecular orbital (HOMO) has a pure sulfur contribution and, because of symmetry considerations, is nonbonding for $[\text{VS}_4]^{3-}$ and $[\text{VS}_3\text{O}]^{3-}$ and slightly bonding for $[\text{VS}_2\text{O}_2]^{3-}$. This indicates that the energy positions of the highest energy anionic band should be the same for Na_3VS_4 , $\text{Na}_3\text{VS}_2\text{O}_2$, and $\alpha\text{-Na}_3\text{VS}_3\text{O}$ and thus (admitting a rigid band electrochemical process) their oxidation process should be the same, which is consistent with the experimental results. In other words, this indicates that in these systems the oxygen should not affect the (sulfur based) anionic redox process.

In contrast, to understand the trend observed for the potential of intercalation (reduction), one has to consider the lowest occupied molecular orbital (LUMO). We can see that while in $[\text{VS}_4]^{3-}$ (T_d) this orbital is mostly non-bonding with pure Vanadium contribution, when considering $[\text{VS}_3\text{O}]^{3-}$ and then $[\text{VS}_2\text{O}_2]^{3-}$, this orbital becomes antibonding and the increasing interactions

with the ligand orbitals pushes it at higher energies. This observation is completely in line with a diminution of the intercalation potential from Na_3VS_4 to $\text{Na}_3\text{VS}_2\text{O}_2$. Moreover, combining the stillness of the HOMO and the energy changes of the LUMO we can predict a band gap increase from Na_3VS_4 to $\text{Na}_3\text{VS}_2\text{O}_2$, which is consistent with the powder colors (cf. insert in the figure IV.6). Indeed, Na_3VS_4 is dark purple, both $\text{Na}_3\text{VS}_3\text{O}$ polymorphs are dark red and $\text{Na}_3\text{VS}_2\text{O}_2$ is orange.

In conclusion, we have reproduced the synthesis of four $\text{Na}_3\text{VS}_{4-x}\text{O}_x$ compounds, and demonstrated the possibility to extract/insert sodium from/in their structures. However, the anionic redox process that we believe to occur and that would explain the oxidation of these compounds is not reversible, which induces poor cyclability. Finally, based on both experiments and basic theoretical models, we have proposed that the O/S ratio does not affect the anionic redox process voltage. On the contrary, the insertion voltage increases when the O/S ratio decreases. Finally, given these results and the difficulty to synthesize oxysulfides with the necessary characteristics for a cathode material, I believe it would be interesting to study theoretically the influence of the O/S ratio on the anionic potential for other coordination polyhedra (octahedra) to avoid wasting time and energy pursuing pipe dreams. The following section addresses whether the same ending will apply to the halide chemistry.

IV.2 Vanadium halides

At this point of the manuscript, there is no doubt in the reader's mind that the lamellar structures observed for TiS_2 or LiCoO_2 are perfectly adapted to the insertion of lithium ions. It may therefore seem strange at first sight that the family of transition metal halides (MX_2 or MX_3 with M being a transition metal and $\text{X} = \text{Cl}^-$, Br^- or I^-), in which many compounds share this lamellar structure, has hardly ever been studied for lithium intercalation. Moreover, several of these compounds, that were early on investigated for their superconducting or charge density waves properties, are regaining interest for their exotic magnetic properties. We then decided to focus on the VX_3 family in particular, for several reasons. On the one hand the V(III)/V(II) couple should be active, and on the other hand it has been shown that VI_3 is ferromagnetic below 50 K. These specifications make it an ideal candidate for a proof of concept. In this section, we will first describe the synthesis and the structure of the different VX_3 compounds with a special emphasis on VI_3 , which is still the subject of intense debates and the source of contradictory reports^{183–185}. Moreover, upon cooling, VI_3 undergoes two successive phase transitions at around 76 K^{183,185} and 32 K¹⁸⁶ whose crystallographic structures have not been fully determined until now. Then, the electrochemical behaviors and the associated structural evolutions of these compounds will be briefly described. Lastly, the magnetic properties of VX_3 will be presented with once again special emphasis on VI_3 .

IV.2.a Synthesis

VCl_3 is commercially available (Sigma-Aldrich, 97 %) and was used as such. Pure VI_3 and VBr_3 powders were obtained through iodine and bromine vapor transport in quartz tubes under high vacuum as already described elsewhere.¹⁸³ Vanadium metal powder (Alfa Aesar, 99.9 %) was mixed with a slight excess of iodine (99+%, Alfa Aesar) (1:1.1 molar ratio) or liquid bromine (Sigma-Aldrich) inside an argon filled glovebox, the mixtures were then poured in a quartz tube subsequently sealed under high vacuum (10^{-6} bar). To prevent evaporation of the liquid bromine during sealing, the tubes were previously frozen in liquid nitrogen. The ampullas were then placed in a tubular furnace in such a way that one end of the tube was at room temperature whereas the other one was positioned in the middle of the furnace and heated at either 450°C (VI_3) or 400°C (VBr_3) for 72 hrs. After reaction, the tube was opened inside a

glovebox and the powder was placed in a Schlenk flask and purified under dynamic vacuum at 200 °C.

LiVX₃ powders were prepared by stirring the corresponding VX₃ powder in an excess (1:3 molar ratio) of n-Butyl Lithium (2.5 M in hexane, Sigma Aldrich) under argon atmosphere. After 1-hour reaction, the suspension was centrifuged and rinsed three times with hexane before being dried under dynamic vacuum.

IV.2.b Structure

i) VCl₃ and VBr₃

These materials have been previously reported and are known to adopt a BI₃-type structure^{187,188} ($R\bar{3}$ space group). In this framework the edge-sharing VX₆ are forming honeycomb layers stacked together along the c direction with an A-B-C sequence (cf. figure IV.7 b and d). Moreover, it worth mentioning that in these structures the halide layers are themselves stacked with an AB periodicity (O1 type according to Delmas nomenclature).³³

Ex-situ samples of each compounds were prepared by filling 0.6 mm Borosilicate capillaries inside an Ar-filled glovebox subsequently sealed before synchrotron measurement. An indexation of the VCl₃ SXRD pattern was done using the dicvol program of the FullProf suite and is in line with the literature ($R\bar{3}$ $a = 6.055$ Å, $b = 17.498$ Å). However, further refinement for this phase were made impossible due to large peak shape anisotropy originating from stacking faults (cf. figure IV.7.a). On the contrary, Rietveld refinement was done on VBr₃ using the FullProf program (cf. figure IV.7.c). VBr₃ was found to adopt as expected the BiI₃ structure ($R\bar{3}$ $a = 6.9269(2)$ Å, $b = 19.9418(2)$ Å) with however, the honeycomb order partially suppressed as 29% of the vanadium is found in the honeycomb voids (cf. table IV.6). This latter observation have been already made by Cava and co workers¹⁸⁷ who explained it by a misinterpretation of stacking fault by the Rietveld method rather than an actual disorder in the transition metal layer.

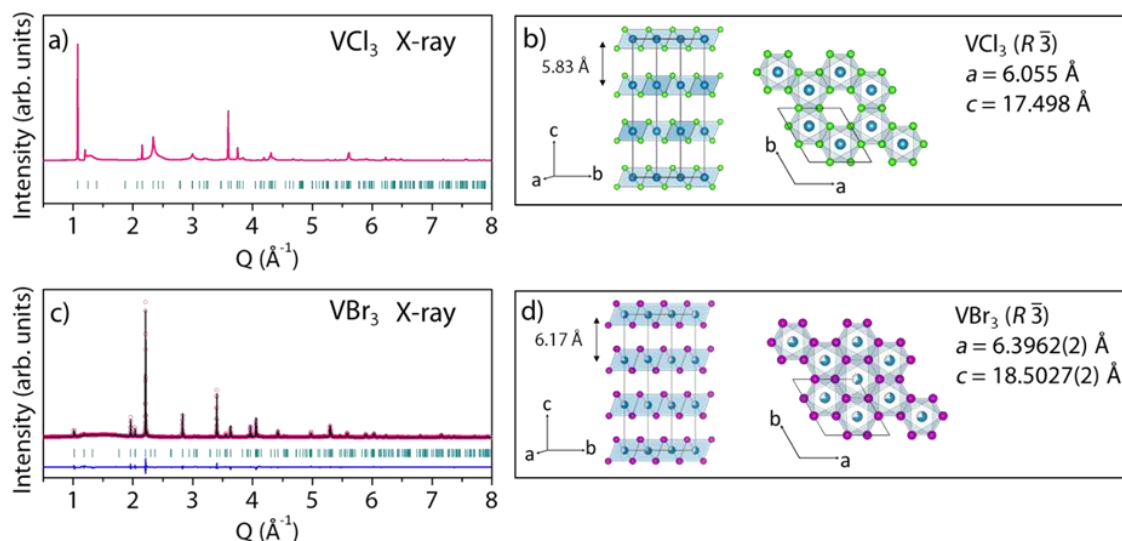


Figure IV.7: (a) Peak indexation of the synchrotron XRD pattern of VCl_3 where vertical green tick bars stand for the Bragg positions. (c) Synchrotron XRD ($\lambda = 0.41378 \text{ \AA}$) Rietveld refinement of VBr_3 corresponding of the structural model reported in the table IV.6. The pink circles, black continuous line, and bottom blue line represent the observed, calculated, and difference patterns, respectively. Vertical green tick bars stand for the Bragg positions. Structure of VCl_3 (b), VBr_3 (d). Vanadium, chlorine and bromine atoms are colored in blue, green and purple respectively.

VBr_3		$R\bar{3}$	$R_{\text{Bragg}} = 3.63 \%$	$\chi^2 = 19.7$		
$a = 6.3962(2) \text{ \AA}$		$c = 18.5027(2) \text{ \AA}$		$\text{Vol} = 655.551(7) \text{ \AA}^3$		
Atom	Wyckoff Position	x/a	y/b	z/c	$B_{\text{iso}} (\text{\AA}^2)$	Occupancy
Br	18f	0.0000(3)	0.3448(3)	0.07998(9)	2.258(16)	1
V	6c	0	0	0.3376(6)	1.000(2)	0.71(16)
V	3a	0	0	0	1.000(2)	0.58(16)

Table IV.6: Crystallographic data and atomic positions of VBr_3 determined from Rietveld refinement of its synchrotron X-ray pattern.

ii) VI_3 Room temperature structure

VI_3 have long been reported to adopt a BI_3 -type structure¹⁸⁹ analogous to VCl_3 and VBr_3 with the $R\bar{3}$ space group, but recent publications have challenged this assignment with reports of alternative $P\bar{3}1c$ ¹⁸⁵ or $C2/m$ ¹⁸⁴ space groups.

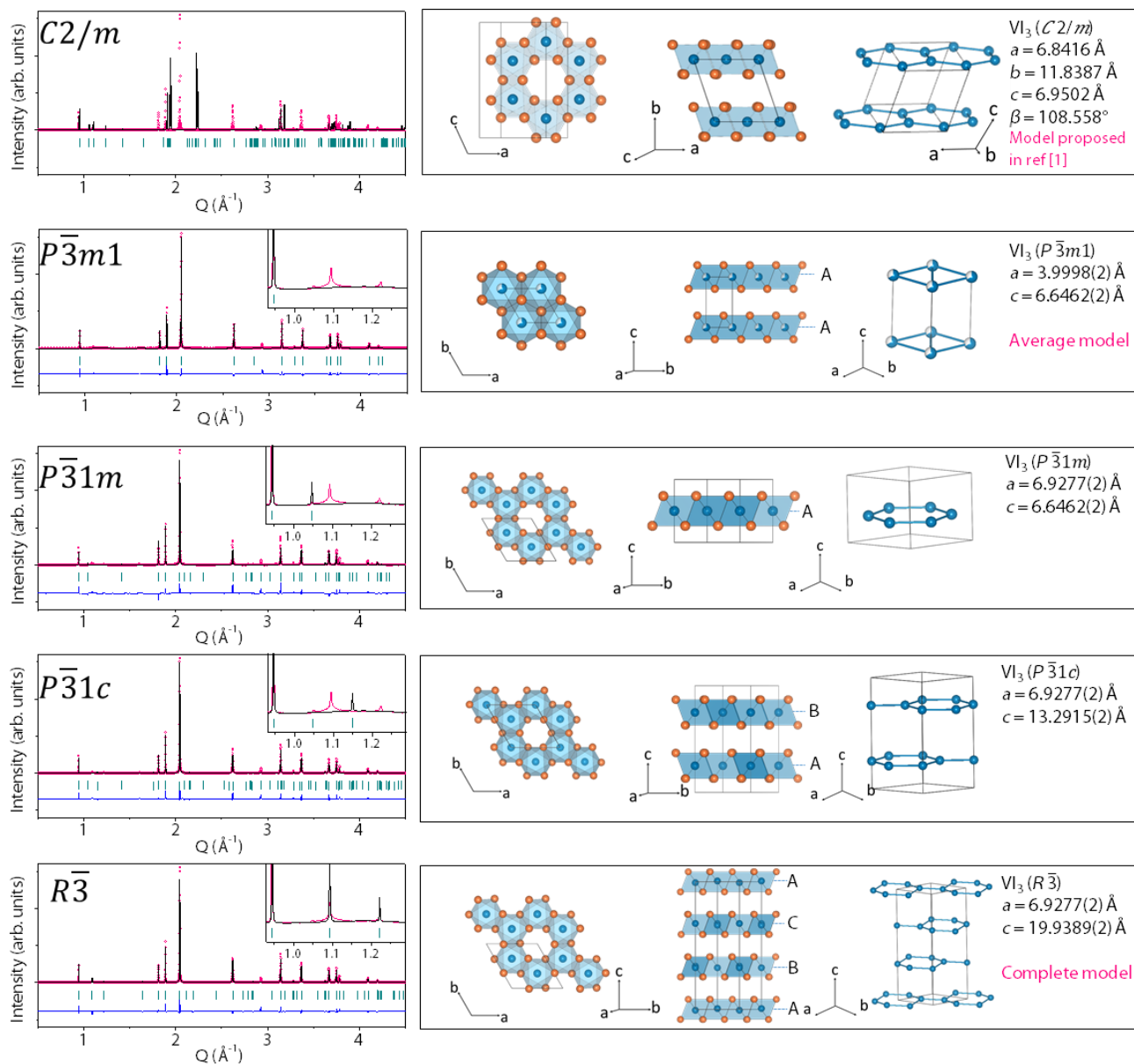


Figure IV.8: Comparison of the Rietveld refinement (left) of the VI_3 synchrotron XRD pattern using different structural models with the corresponding structure (right). The $C2/m$ model is described in ref [184]. The inset highlights the superstructure peaks Q region.

These different models commonly agree that VI_6 octahedra share edges to form layers into which vanadium atoms fill 2/3 of the octahedral positions to form a honeycomb pattern. These honeycomb layers are then stacked one above the other, and layers are separated by a van der Waals gap. Their discrepancies are nested in the different stacking sequences of the VI_3 layers along the c -axis. For instance, the $C2/m$ model proposed by Tian et al. implies an ABC stacking of the iodine atoms in opposition to an ABAB one for both the $R\bar{3}$ and the $P\bar{3}1c$ models. The difference between the two latter is more subtle and originates from different honeycomb stackings, which result in only minute variations in the X-ray powder diffraction patterns. In order to clarify the VI_3 room temperature structure, we tried to refine the experimental synchrotron powder pattern collected at room temperature with those different models (cf. Figure IV.8). While the $C2/m$ model (ABC stacking of iodine layers) is clearly inadequate to index our pattern, the other models (ABAB stacking of iodine layers) led to decent fits, and solely the indexation of small low angle reflections specific to the vanadium honeycomb superstructure allowed discriminating them. The only space group able to index all these peaks was $R\bar{3}$, with lattice parameters $a = 6.9277(2) \text{ \AA}$, $c = 19.9389(2) \text{ \AA}$ and this model led to the best refinement (Figure IV.9.a and b and Table IV.7).

VI_3 300 K (complete model)		$R\bar{3}$					$R_{\text{Bragg}} = 15.5\%$, $\chi^2 = 18.5$	
hexagonal axes								
$a = 6.9277(2) \text{ \AA}$		$c = 19.9389(2) \text{ \AA}$			$Vol = 828.730(4) \text{ \AA}^3$			
Atom	Wyckoff Positions	x/a	y/b	z/c	$B_{iso} (\text{\AA}^2)$	Occupancy		
I	18f	0.0115(2)	0.344(2)	0.0789(2)	0.916(11)	1		
V	6c	0	0	0.3266(3)	0.57(4)	1		
rhombohedral axes								
$a = 7.7570(2) \text{ \AA}$		$\alpha = 53.0447(2)^\circ$			$Vol = 276.241(4) \text{ \AA}^3$			
Atom	Wyckoff Positions	x/a	y/b	z/c	$B_{iso} (\text{\AA}^2)$	Occupancy		
I	6f	0.0904(2)	0.4111(2)	0.73512(2)	0.916(11)	1		
V	2c	0.3266(3)	0.3266(3)	0.3266(3)	0.57(4)	1		

Table IV.7: Crystallographic data and atomic positions for VI_3 at 300 K using the complete model determined from Rietveld refinement of its synchrotron X-ray pattern using the hexagonal and rhombohedral axes.

In this structure, the iodine layers are stacked in an ABAB manner (O1 type) whereas the vanadium honeycomb motifs adopt an ABC sequence. This structural model assignment from powder diffraction is supported by single crystal diffraction,¹⁸³ where the differences between these trigonal space groups are easier to spot, provided that good quality single crystal are available.

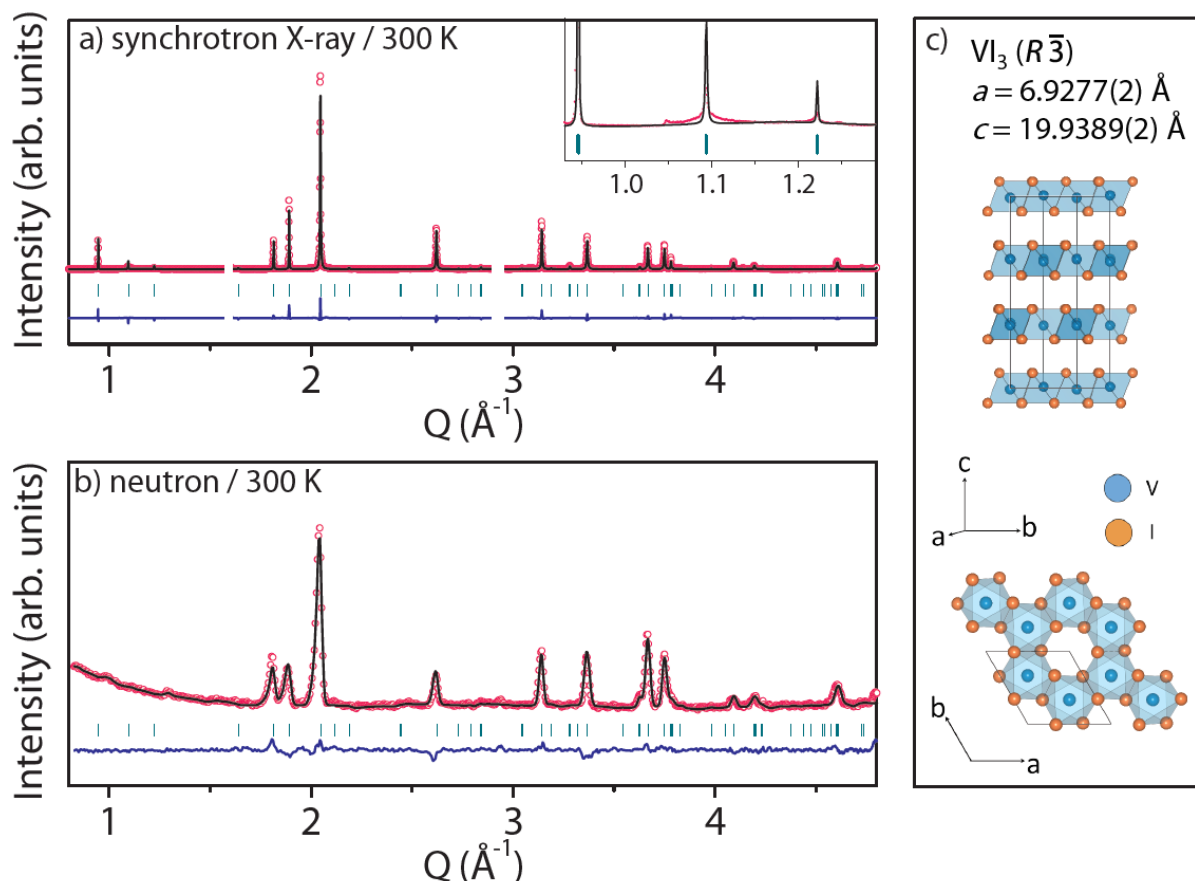


Figure IV.9: Synchrotron X-ray (a) and neutron (b) Rietveld refinements of VI_3 at 300 K. Wavelengths for synchrotron X-rays and neutrons are $\lambda = 0.3869$ Å and $\lambda = 2.4184$ Å, respectively. The pink circles, black continuous line, and bottom blue line represent the observed, calculated, and difference patterns, respectively. Vertical green tick bars stand for the Bragg positions. Two regions were excluded due to minute amount of impurities. The inset in a) highlights the indexation of the superstructure peaks c) Structure of VI_3 at 300 K.

It is worth mentioning that a good refinement can also be obtained in a nine-fold smaller unit cell with $a = 3.9998(2)$ Å, $c = 6.6462(2)$ Å ($P\bar{3}m1$ space group) (cf. Figure IV.8 and Table IV.8). This cell indexes all peaks, except the superstructure ones associated with the honeycomb ordering, and corresponds to a structural model in which vanadium sits in a $1a$ Wyckoff site with a $2/3$ occupancy. For the rest of the manuscript this model will be referred as “the average model” as opposed to the “complete model” taking into account the vanadium honeycomb

ordering. Considering the lattice centering translations in $R\bar{3}$, the complete model is therefore a threefold superstructure of the average model.

VI ₃ 300 K (average model) $a = 3.9998(2)$ Å		$P\bar{3}m1$ $c = 6.6462(2)$ Å	$R_{\text{Bragg}} = 15.0$ %	$\chi^2 = 54.6$	Vol = 92.081(2) Å ³	
Atom	Wyckoff Position	x/a	y/b	z/c	B_{iso} (Å ²)	Occupancy
I	2d	1/3	2/3	0.2359(2)	1.031(12)	1
V	1a	0	0	0	1.17(11)	2/3

Table IV.8: Crystallographic data and atomic positions for VI₃ at 300 K using the average model determined from Rietveld refinement of its synchrotron X-ray pattern.

Low temperature structures

The structural evolution of VI₃ upon cooling was explored by high-angular resolution synchrotron X-ray powder diffraction. From RT to 80 K the structure described above is preserved with however a contraction of the lattice parameters. When further lowering the temperature, the SXRD patterns show a first abrupt splitting of peaks (cf. Figure IV.10) at 76 K and a second one less drastic at temperatures around 32 K. Such features are in agreement with the reported first and second order phase transitions at $T_1 \approx 76$ K^{183–185,190} and $T_2 = 32$ K,¹⁹⁰ respectively. Nevertheless and to the best of our knowledge, no structural models have ever been proposed for the lowest temperature phase. For the intermediate phase, the only model reported in literature¹⁸⁵ was deduced from a X-ray powder pattern showing a strong preferred orientation, and whose RT analog was refined in $P\bar{3}1c$, a space group we excluded as discussed earlier. Thus, we embarked on solving the structure of these two low temperature phases using high-angular resolution SXRD. Diffraction patterns were collected at 60 K and 9 K in Debye-Scherrer geometry (powder filled in glass capillaries) to avoid preferred orientation effects. At a first approach, the structures were solved without considering the vanadium honeycomb superstructure (“average models”), and in a second time a more complex but realistic structural description was built by adding the honeycomb vanadium superstructure to the average model (“complete models”).

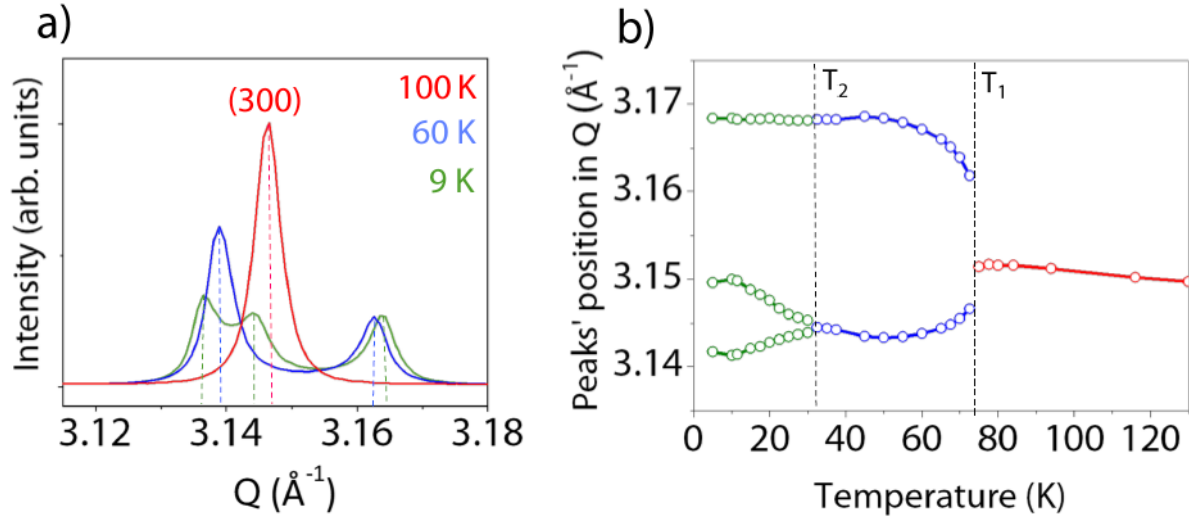


Figure IV.10: Evolution of selected reflections with temperature a) evolution of the (300) peak (indexes refer to the $R\bar{3}$ cell) b) evolution of the peaks' positions.

Average model:

The 60 K SXR pattern (excluding the superstructure peaks) can be indexed in a monoclinic unit cell with $a = 6.9395(2) \text{\AA}$, $b = 3.9671(2) \text{\AA}$, $c = 6.5960(2) \text{\AA}$, $\beta = 90.4539(4)^\circ$, that is related to the RT average cell using the following transformation:

$$(a_m \quad b_m \quad c_m) = (a_h \quad b_h \quad c_h) \begin{pmatrix} 2 & 0 & 0 \\ 1 & 1 & 0 \\ 0 & 0 & 1 \end{pmatrix}.$$

Where the m and h subscripts stand for monoclinic and hexagonal ($P\bar{3}m1$ space group) cells, respectively. It is worth mentioning that this transformation is the one commonly used to relate the trigonal/hexagonal cell to the C-centered ortho-hexagonal cell, therefore the distortion from room temperature to 60 K corresponds solely to a change of the ortho-hexagonal β angle from 90° (RT) to $\beta = 90.4539(4)^\circ$ (60 K).

Then, the pattern was refined via the Rietveld method using the space group $C2/m$ confirming the plausibility of the model (cf. Figure IV.11 and Table IV.9). At 9 K, the symmetry was further lowered to the $P\bar{1}$ space group without changing the unit cell metrics and the model was refined against the SXR pattern (cf. Figure IV.11 and Table IV.10). A decent fit of the SXR pattern, which gave a satisfactory representation of the structure, was obtained with the average model. However, although contributing only to a limited extent to the diffraction

pattern intensity, the superstructure peaks are of prime importance to understand the physical properties of the material and have to be considered.

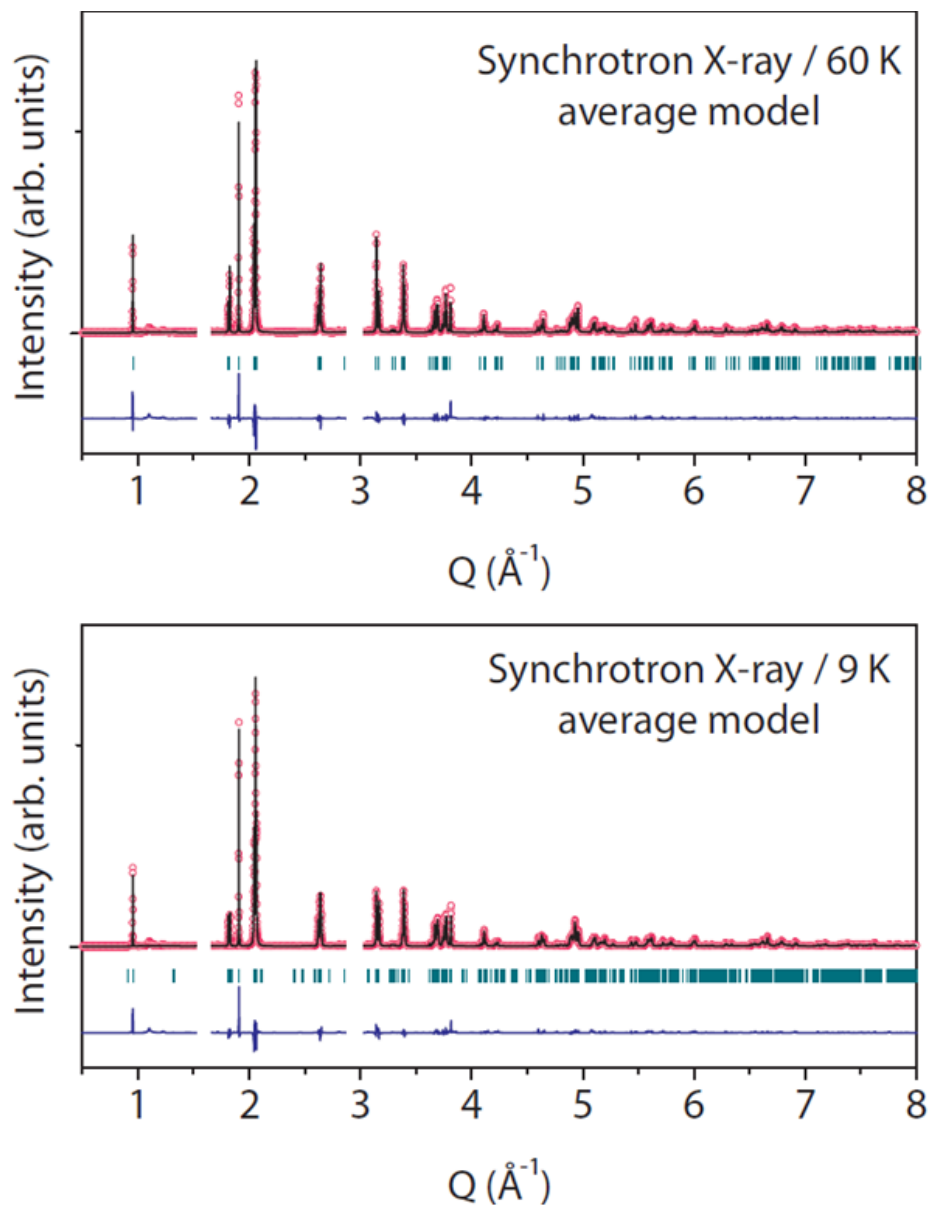


Figure IV.11: Synchrotron XRD Rietveld refinement of VI_3 at 60 K (top) and 9 K (bottom). Wavelength for synchrotron X-ray is $\lambda = 0.3869 \text{ \AA}$. The pink circles, black continuous line, and bottom blue line represent the observed, calculated, and difference patterns, respectively. Vertical green tick bars stand for the Bragg positions. Some regions have been excluded due to minute amount of impurities.

VI ₃ 60 K (average model)		C2/m		R _{Bragg} = 6.94 %	χ ² = 62.3		
a = 6.9395(2) Å		b = 3.9671(2) Å		c = 6.5960(2) Å	β = 90.4539(4)°	Vol = 181.578(2) Å ³	
Atom	Wyckoff Position	x/a	y/b	z/c	B _{iso} (Å ²)	Occupancy	
I	4i	0.1669(2)	1/2	0.2402(2)	0.774(8)	1	
V	2a	0	0	0	0.53(7)	2/3	

Table IV.9: Crystallographic data and atomic positions for VI₃ at 60 K using the average model determined from Rietveld refinement of its synchrotron X-ray pattern.

VI ₃ 9 K (average model)		P $\bar{1}$		R _{Bragg} = 8.06 %	χ ² = 81.3		
a = 6.9353(2) Å		b = 3.9655(2) Å		c = 6.5910(2) Å		Vol = 181.259(2) Å ³	
α = 90.1044(6)°		β = 90.3956(5)°		γ = 90.1495(5)°			
Atom	Wyckoff Position	x/a	y/b	z/c	B _{iso} (Å ²)	Occupancy	
I1	2i	0.1663(8)	0.5062(6)	0.2495(8)	0.691(9)	1	
I2	2i	0.6668(8)	0.9945(6)	0.2373(8)	0.691(9)	1	
V1	1a	0	0	0	0.48(7)	2/3	
V2	1e	1/2	1/2	0	0.48(7)	2/3	

Table IV.10: Crystallographic data and atomic positions for VI₃ at 9 K using the average model determined from Rietveld refinement of its synchrotron X-ray pattern.

Complete model

Assuming that the vanadium superstructure observed at RT (honeycomb layers stacked in a ABC sequence) is preserved in the low temperature phases, a supercell was built from the average model with the following transformation:

$$(a_s \ b_s \ c_s) = (a_a \ b_a \ c_a) \begin{pmatrix} -1/2 & 1/2 & 0 \\ 1/2 & 1/2 & -1 \\ 1 & 1 & 1 \end{pmatrix}$$

Here the *s* and *a* subscripts stand for supercell and average cell, respectively. At room temperature, this supercell represented in figure IV.12 corresponds to the rhombohedral cell of the $R\bar{3}$ model ($a = b = c = 7.7570(2)$ Å and $\alpha = \beta = \gamma = 53.0447(2)^\circ$, see table IV.7).

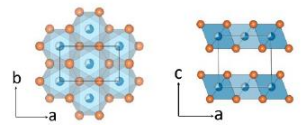
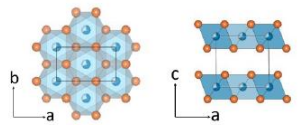
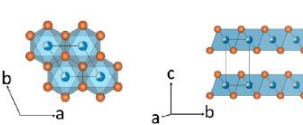
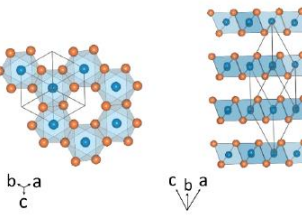
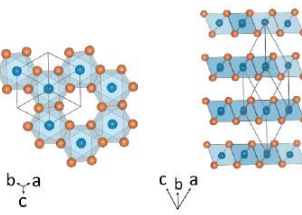
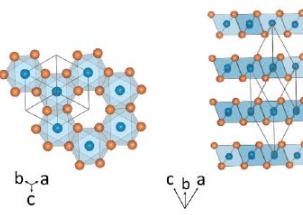
	9 K	60 K	300 K
Average model (without superstructure)	$P\bar{1}$ $a = 6.9353(2) \text{ \AA}$ $\alpha = 90.1044(6)^\circ$ $b = 3.9655(2) \text{ \AA}$ $\beta = 90.3956(5)^\circ$ $c = 6.5910(2) \text{ \AA}$ $\gamma = 90.1495(5)^\circ$ 	$C2/m$ $a = 6.9395(2) \text{ \AA}$ $\beta = 90.4539(4)^\circ$ $b = 3.9671(2) \text{ \AA}$ $c = 6.5960(2) \text{ \AA}$ 	$P\bar{3}m1$ (Hexagonal cell) $a = 3.9998(2) \text{ \AA}$ $c = 6.6462(2) \text{ \AA}$ 
Complete model (with superstructure)	$P\bar{1}$ $a = 7.7268(2) \text{ \AA}$ $\alpha = 53.1280(2)^\circ$ $b = 7.6808(2) \text{ \AA}$ $\beta = 53.0863(3)^\circ$ $c = 7.6985(2) \text{ \AA}$ $\gamma = 53.5022(3)^\circ$ 	$P\bar{1}$ $a = 7.7359(2) \text{ \AA}$ $\alpha = 53.1933(5)^\circ$ $b = 7.6886(2) \text{ \AA}$ $\beta = 53.0168(7)^\circ$ $c = 7.6968(2) \text{ \AA}$ $\gamma = 53.4732(7)^\circ$ 	$R\bar{3}$ (Hexagonal cell) $a = 6.9277(2) \text{ \AA}$ $c = 19.9389(2) \text{ \AA}$ $R\bar{3}$ (Rhombohedral cell) $a = 7.7570(2) \text{ \AA}$ $\alpha = 53.0447(2)^\circ$ 

Figure IV.12: Overview of the different structural models at 9 K, 60 K and 300 K. The upper row presents the “average models” where the honeycomb vanadium superstructure is not taken into account. The lower row presents the “complete models” including the vanadium superstructure.

Then, Rietveld refinements of the 60 K and 9 K patterns using this model led to a good indexation of the superstructure peaks splitting observed on cooling (cf. Figure IV.13 and Table IV.11 and IV.12). The visible shape mismatch between the calculated and the measured superstructure peaks likely accounts for the presence of stacking faults as commonly encountered in such layered materials¹⁹¹ and strain developing across the phase transitions. Finally, this two-step refinement process enabled to derivate the atomic positions and lattice parameters from the average model which prevented our refinements to diverge with such a large amount of refined parameters. All complete and average structural models for VI_3 are summarized in Figure IV.14 together with the corresponding transformation matrixes.

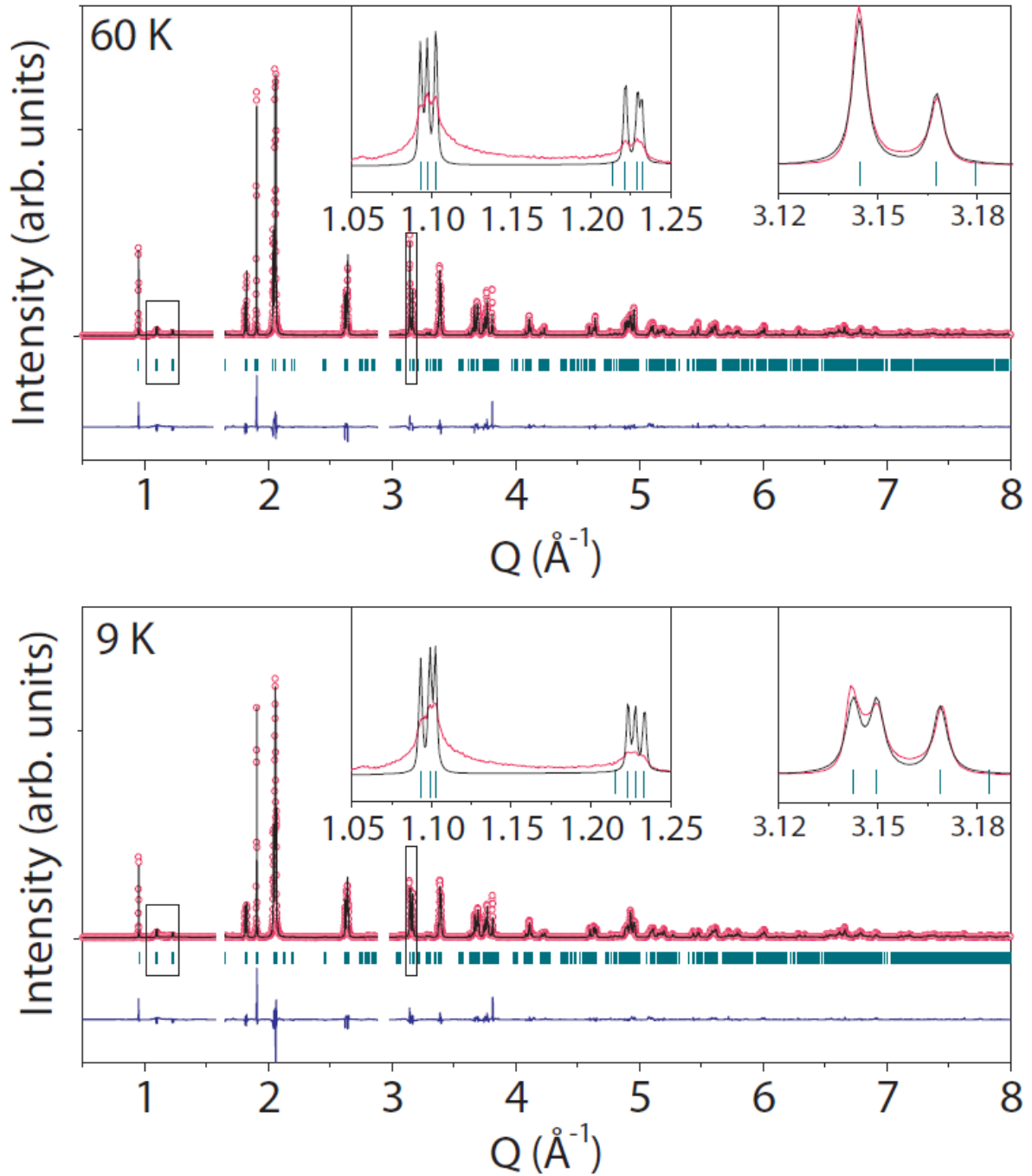


Figure IV.13: Synchrotron XRD Rietveld refinement of VI_3 at 60 K (top) and 9 K (bottom) using the “complete model” in $P\bar{1}$ space group reported in Tables IV.11 and IV.12. Wavelength for synchrotron X-ray is $\lambda = 0.3869 \text{ \AA}$. The pink circles, black continuous line, and bottom blue line represent the observed, calculated, and difference patterns, respectively. Vertical green tick bars stand for the Bragg positions. Some regions were excluded due to minute amount of impurities. The insets in each figure refer to a zoom of the angular regions shown by a black rectangle in the main figure. The middle inset highlights the indexation of the superstructure peaks whereas the right one highlights the Q range represented in Figure IV.10.a.

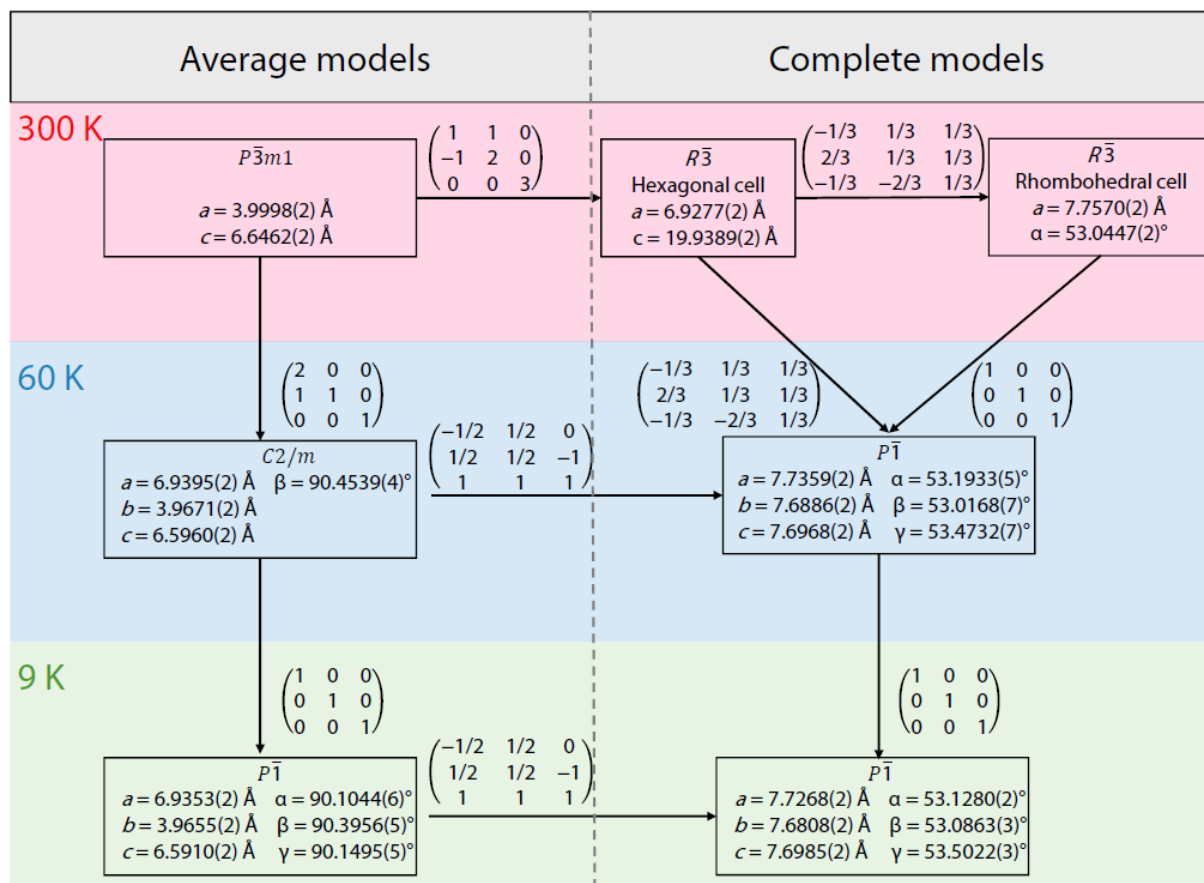


Figure IV.14: Summary of the different structural models of VI_3 and the associated transformation matrixes.

To further understand the origin of the observed distortions we represent in Figure IV.15 the evolution of the V-V distances in the honeycomb layers. Above 76 K, vanadium atoms describe regular hexagons in the layers. In contrast, below this temperature, a contraction of one of the V-V distances leads to the formation of vanadium dimers. This finding contradicts the vanadium anti-dimerization deduced by Son et al.¹⁸⁵ Finally, below 32 K, the honeycomb framework is further distorted leading to three distinct V-V distances inside the layer. Similar behaviors have been reported for other transition metal trichlorides MCl_3 (namely TiCl_3 , MoCl_3 or TcCl_3), with however a larger difference between long and short M-Cl distances.¹⁹²

VI ₃ 60 K (complete model)		$P\bar{1}$	$R_{\text{Bragg}} = 9.42\%$	$\chi^2 = 81.3$			
$a = 7.7359(2) \text{ \AA}$ $\alpha = 53.1933(5)^\circ$		$b = 7.6886(2) \text{ \AA}$ $\beta = 53.0168(7)^\circ$	$c = 7.6968(2) \text{ \AA}$ $\gamma = 53.4732(7)^\circ$				Vol = 272.356(7) \AA^3
Atom	Wyckoff Position	x/a	y/b	z/c	$B_{\text{iso}} (\text{\AA}^2)$	Occupancy	
I1	2i	0.0852(5)	0.4199(6)	0.7357(6)	0.577(8)	1	
I2	2i	0.4157(5)	0.7471(6)	0.0771(7)	0.577(8)	1	
I3	2i	0.7483(5)	0.0824(6)	0.4097(7)	0.577(8)	1	
V1	2i	0.3337(2)	0.3332(2)	0.3332(2)	0.47(6)	1	

Table IV.11: Crystallographic data and atomic positions for VI₃ at 60 K using the complete model determined from Rietveld refinement of its synchrotron X-ray pattern.

VI ₃ 9 K (complete model)		$P\bar{1}$	$R_{\text{Bragg}} = 9.44\%$	$\chi^2 = 86.3$			
$a = 7.7268(2) \text{ \AA}$ $\alpha = 53.1280(2)^\circ$		$b = 7.6808(2) \text{ \AA}$ $\beta = 53.0863(3)^\circ$	$c = 7.6985(2) \text{ \AA}$ $\gamma = 53.5022(3)^\circ$				Vol = 271.901(3) \AA^3
Atom	Wyckoff Position	x/a	y/b	z/c	$B_{\text{iso}} (\text{\AA}^2)$	Occupancy	
I1	2i	0.0822(5)	0.4148(6)	0.7438(6)	0.664(9)	1	
I2	2i	0.4140(5)	0.7451(5)	0.0811(6)	0.664(9)	1	
I3	2i	0.7459(5)	0.0807(5)	0.4153(6)	0.664(9)	1	
V1	2i	0.3335(2)	0.3335(2)	0.3334(2)	0.73(7)	1	

Table IV.12: Crystallographic data and atomic positions for VI₃ at 9 K using the complete model determined from Rietveld refinement of its synchrotron X-ray pattern.

At this stage, it is important to consider the connection between those complex structural transitions and the onset of ferromagnetic order at $T_C = 50 \text{ K}$ in VI₃ that we confirm in our homemade sample (cf. following section). Obviously, the 76 K structural phase transition that occurs far above T_C (50 K) is free of magnetic effects. Between T_1 (76 K) and T_2 (32 K), it is worth noting that the evolution of the lattice parameters and characteristic distances in the VI₃ structure are not monotonous (cf. Figure IV.16). More specifically, we observe that the V-V and interlayer (van der Waals) distances (cf. Figure IV.16.a and b) increase from 76 K to 50 K while they decrease upon further cooling. This anomaly is directly linked to the establishment of a magnetic order in the structure and is strongly indicative of a magnetostriction phenomenon already suggested by Dolezal et al.¹⁹⁰ Finally, the origin of the low temperature structural phase transition at $T_2 = 32 \text{ K}$ still remains to be explained in conjunction with the magnetic ordering at 50 K.

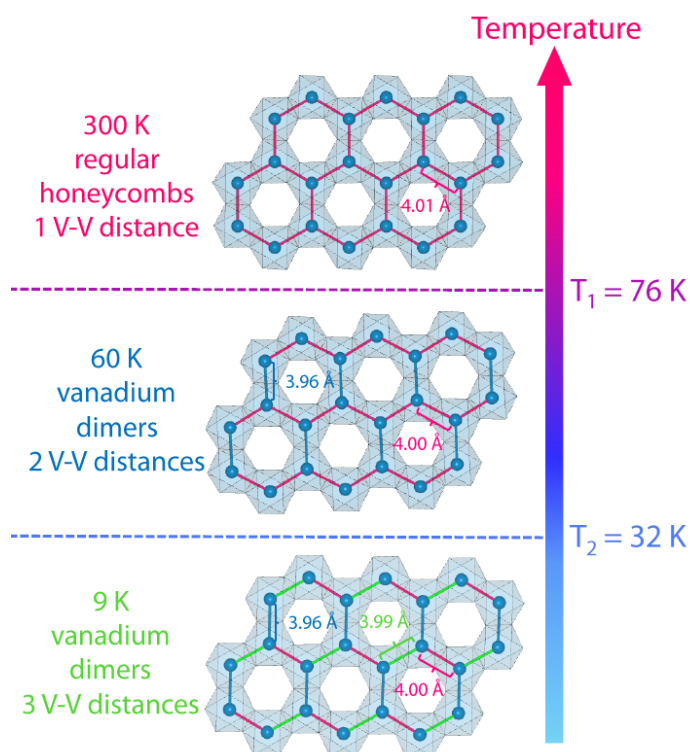


Figure IV.15: Evolution of the V-V distances in the honeycomb motifs at 300 K, 60 K and 9 K, deduced from the complete structural models reported in Table IV.7, IV.11 and IV.12.

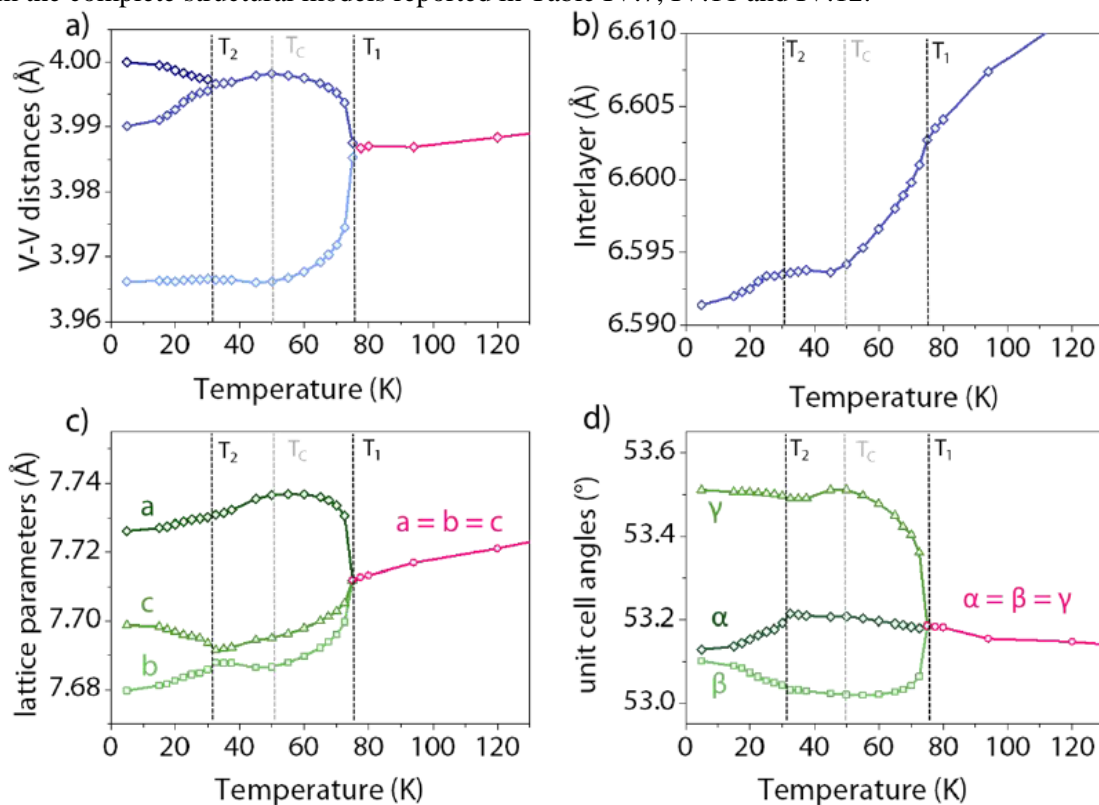


Figure IV.16: Evolution of a) the vanadium-vanadium distances, b) the interlayer distance (defined as the distance between two vanadium layers) and c), d) lattice parameters of VI_3 from 10 K to 140 K. These parameters are given using the complete model settings described in Figure IV.12, and the high temperature phase is described in the rhombohedral primitive cell of $R\bar{3}$.

IV.2.c Lithium intercalation

To interrogate the feasibility of these phases towards Li-insertion, we assembled electrochemical cells, using VX_3 mixed with carbon super-P (in a 7/3 ratio) as cathode, lithium metal as the anode and the state-of-the-art Li-ion batteries electrolyte: LP30 (1 M $LiPF_6$ in a 1:1 EC/DMC mixture). The results are presented on the left panel of the figure IV.17 and whatever the compounds small discharged capacity is observed with in addition, no reversibility. Moreover, post mortem opening of the cells clearly indicates dissolution of the electrode materials. This result was in fact predictable, the VX_3 compounds being very soluble salts and it explains that in spite of a favorable structure these compounds have never been studied so far for lithium atoms intercalation. We have contour this long lasting difficulty by the use of superconcentrated electrolytes. Figure IV.17 (right panel) shows that the use of 5M LiFSI in the DMC allows obtaining a reversible cycling over a few cycles. Rather than going further into the electrochemistry of these compounds, that were detailed by another PhD group student (Nicolas DUBOUIS) in his thesis manuscript, we will next focus on the structural evolution of VX_3 during lithiation.

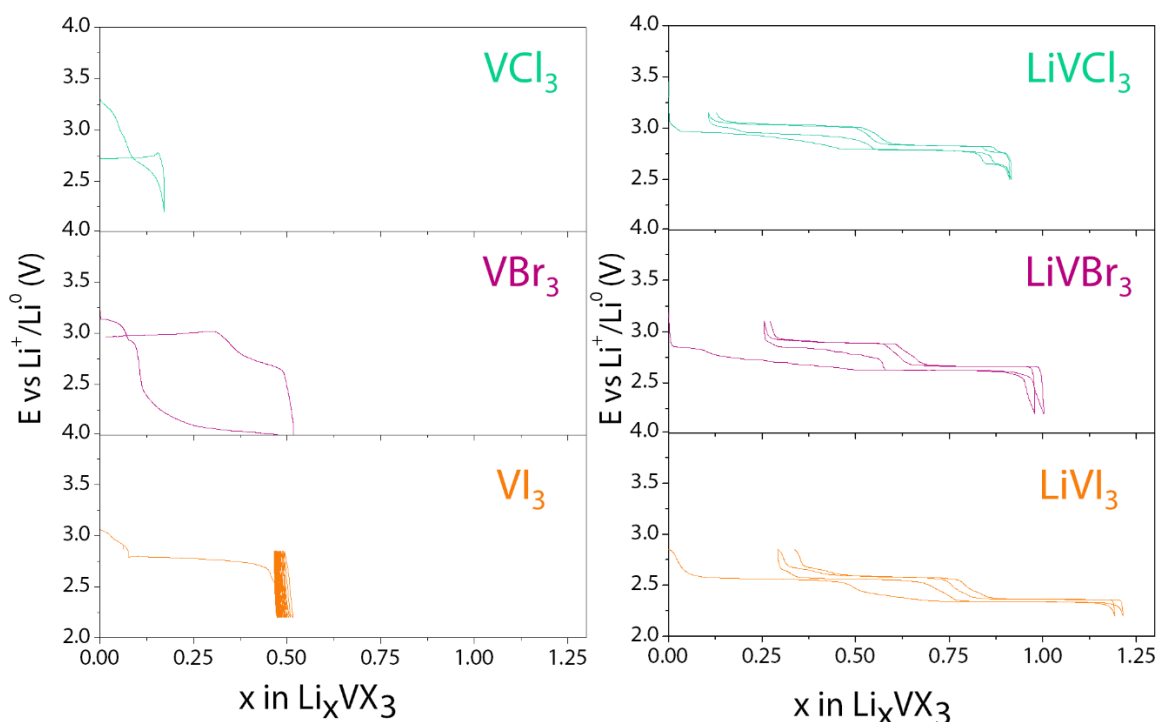


Figure IV.17: (left) galvanostatic cycling of VCl_3 (green), VBr_3 (purple) and VI_3 (orange) at C/40 using LP30 electrolyte and metallic lithium as negative electrode. (right) galvanostatic cycling of VCl_3 (green), VBr_3 (purple) and VI_3 (orange) at C/40 using a superconcentrated (5 M LiFSI in DMC) and metallic lithium as negative electrode. For this last panel the first two cycles are plotted.

To question the behavior of VX_3 compounds upon lithium atoms intercalation, operando synchrotron XRD experiments has been performed (cf. figure IV.18) in the MSPD line of the Alba synchrotron (cf. annexe for details). Whatever the halide, the lithium intercalation translates electrochemically into two successive plateau on the voltage curves, which is in line with two-biphasic processes observed in XRD. Moreover, on charge these processes are found reversible. Hence, upon intercalation two lithiated phases are form successively for each VX_3 compound: an intermediate phase (named $Li_{0.5}VX_3$ for sake of simplicity) and a “final” phase corresponding to $LiVX_3$. Now we propose to describe the structures of these phases.

i) Structure of the intermediate phases: “ $Li_{0.5}VX_3$ ”

In line with VCl_3 the $Li_{0.5}VCl_3$ pattern presents large shape anisotropy, which prevents any full refinement. A peak indexation of the pattern is however compatible with the pristine structural model (Figure IV.19 a and b) with solely an increase of the lattice parameters ($a = 6.055 \text{ \AA}$, $b = 17.498 \text{ \AA}$). The similarities existing between the $Li_{0.5}VI_3$ (resp. $Li_{0.5}Br_3$) and the VI_3 (resp. VBr_3) patterns led us to use a similar structural model, with however, larger lattice parameters. Rietveld refinements validate a posteriori this intuition (Figure IV.19 c and e) and confirm both that the honeycomb superstructure is kept for $Li_{0.5}VI_3$ (cf. table IV.14) and the presence of vanadium atoms in the honeycomb void (26 %) for $Li_{0.5}Br_3$ (cf. table IV.13) which suggests that stacking faults are still present in this material. Finally, as the intermediate phases cannot be easily produced in sufficient quantity to carry out neutron diffraction, the position of the lithium could not be refined. Instead, for the models proposed in the tables IV.13 and IV.14, the lithium atoms were simply positioned in the octahedral sites of the interlayer.

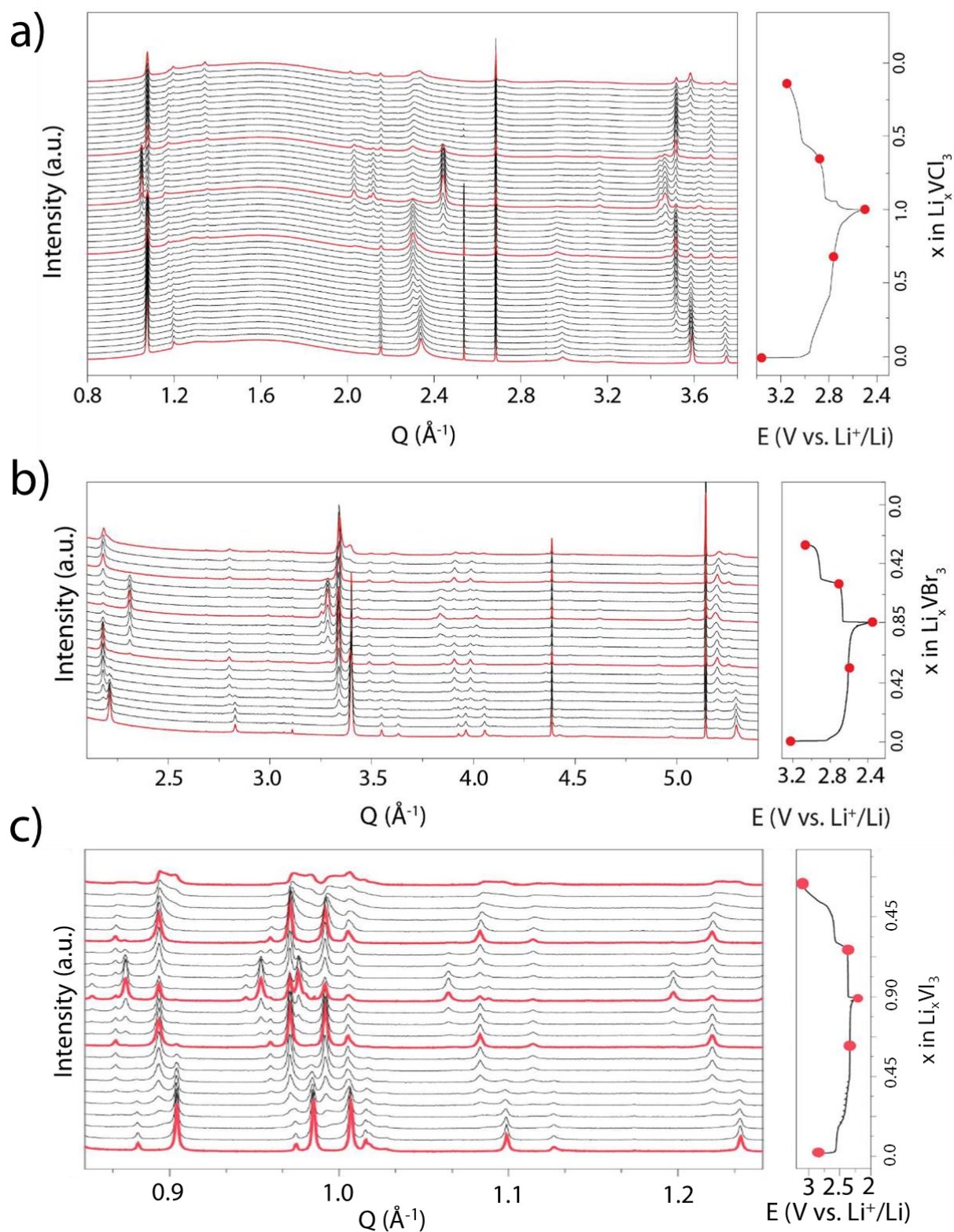


Figure IV.18: Operando synchrotron X-Ray diffraction patterns recorded for VCl_3 (a), VBr_3 (b) and VI_3 (c) upon cycling (left). The electrochemistry was conducted at C/20. The potential profile recorded during the operando measurement is plotted on the right panel.

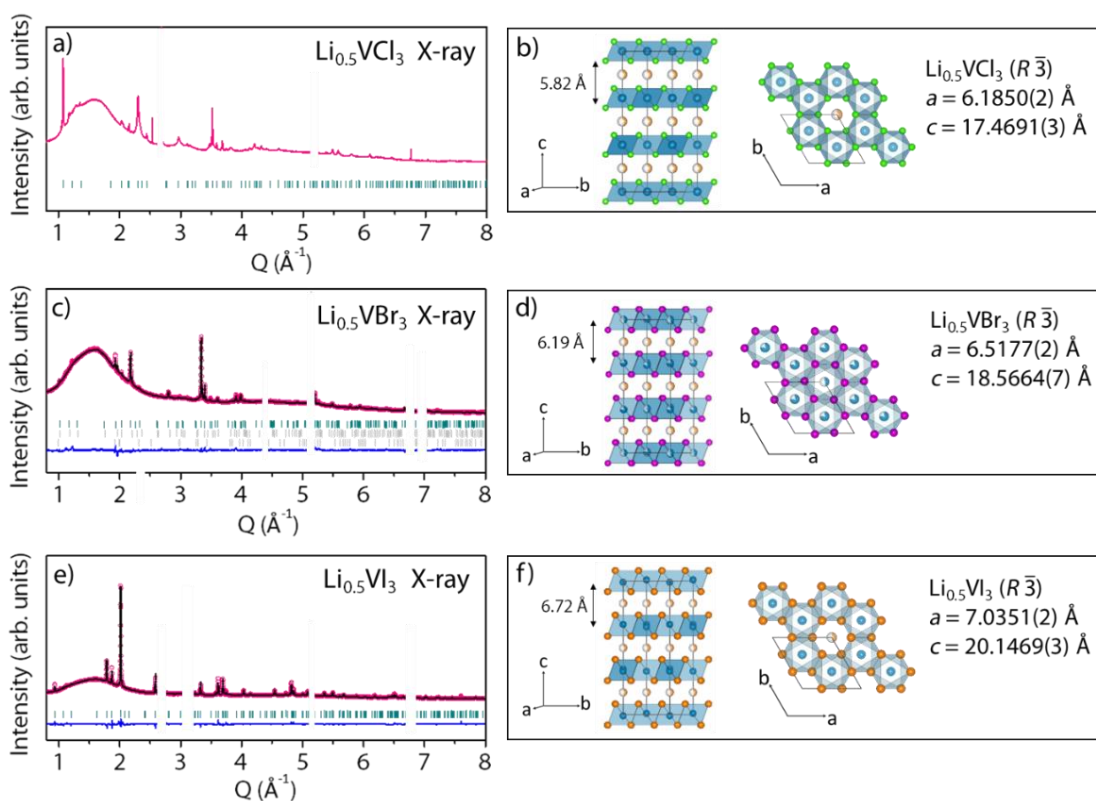


Figure IV.19: a) Indexed synchrotron XRD ($\lambda = 0.41378 \text{ \AA}$) pattern for $\text{Li}_{0.5}\text{VCl}_3$ where vertical green tick bars stand for the Bragg positions. b) Rietveld refinement for $\text{Li}_{0.5}\text{VBr}_3$ and c) $\text{Li}_{0.5}\text{VI}_3$ synchrotron XRD patterns ($\lambda = 0.41378 \text{ \AA}$), corresponding to the structural model reported in the Tables IV.13 and IV.14. The pink circles, black continuous line, and bottom blue line represent the observed, calculated, and difference patterns, respectively. Vertical green tick bars stand for the Bragg positions. Structure of d) $\text{Li}_{0.5}\text{VCl}_3$, e) $\text{Li}_{0.5}\text{VBr}_3$ and f) $\text{Li}_{0.5}\text{VI}_3$. Vanadium, chlorine, bromine, iodine and lithium atoms are represented in blue, green, purple, orange and yellow, respectively. Some parts of the pattern have been excluded due to the presence of Li or Be diffraction peaks

$\text{Li}_{0.5}\text{VBr}_3$		$R\bar{3}$	$R_{\text{Bragg}} = 15.76 \%$	$\chi^2 = 2.54$		
$a = 6.5177(2) \text{ \AA}$		$c = 18.5664(7) \text{ \AA}$		$\text{Vol} = 683.05(3) \text{ \AA}^3$		
Atom	Wyckoff Position	x/a	y/b	z/c	$B_{\text{iso}} (\text{\AA}^2)$	Occupancy
Br	18f	0.0155(9)	0.3447(10)	0.0776(4)	1.04(4)	1
V	6c	0	0	0.337(6)	3.7(3)	0.74(16)
V	3a	0	0	0	3.7(3)	0.52(16)
Li	3b	0	0	0.5	1*	1/3*
Li	6c	0	0	0.16667*	1*	1/3*

Table IV.13: Crystallographic data and atomic positions for $\text{Li}_{0.5}\text{VBr}_3$ determined from Rietveld refinement of its synchrotron X-ray pattern. The “*” symbol indicates that these parameters have not been refined. For the Vanadium atoms the B_{iso} parameters have been constrained in the refinement to be the same.

$\text{Li}_{0.5}\text{VI}_3$		$R\bar{3}$	$R_{\text{Bragg}} = 6.84\%$	$\chi^2 = 8.17$		
$a = 7.0351(2) \text{ \AA}$		$c = 20.1469(3) \text{ \AA}$		$\text{Vol} = 863.525(16) \text{ \AA}^3$		
Atom	Wyckoff Position	x/a	y/b	z/c	$B_{\text{iso}} (\text{Å}^2)$	Occupancy
I	18f	0.0008(9)	0.329(8)	0.07905(13)	1.665(19)	1
V	6c	0	0	0.3241(11)	3.1(3)	1
Li	3b	0	0	0.5	1*	1/3*
Li	6c	0	0	0.16667*	1*	1/3*

Table IV.14: Crystallographic data and atomic positions of $\text{Li}_{0.5}\text{VI}_3$ determined from Rietveld refinement of its synchrotron X-ray pattern. The “*” symbol indicates that these parameters have not been refined.

ii) *Structure of the final phase: “ LiVX_3 ”*

Contrary to the intermediate phases, we found the possibility to synthesize chemically the final phases using n-butyl-lithium in hexane (apolar solvent). The structure of the as-prepared phases were found by XRD to match those prepared by electrochemistry.

Alike for $\text{Li}_{0.5}\text{VI}_3$, the LiVI_3 structural determination was straightforward as the pattern can be indexed using the VI_3 structural model, only increasing the lattice parameters ($R\bar{3}$, $a = 7.1439(2) \text{ \AA}$, $c = 20.6642(2) \text{ \AA}$) (cf. figure IV.20 and table IV.17). Unlike for LiVI_3 , for both LiVCl_3 and LiVBr_3 the indexation of the pattern was not compatible with their pristine framework. The first attempts to solve these structures were based on a previous study reporting a spinel-like LiVCl_3 obtained at high temperature.¹⁹³ However, although this cubic model showed encouraging results at first sight, further examination revealed the presence of non-indexed peaks. A complete fitting of the pattern was finally possible using a hexagonal unit cell, suggesting a O3-type layered oxides ($R\bar{3}m$) which was later validated by Rietveld refinement for both LiVCl_3 ($R\bar{3}m$, $a = 3.6273(2) \text{ \AA}$, $c = 17.9394(5) \text{ \AA}$) and LiVBr_3 ($R\bar{3}m$, $a = 3.8225(2) \text{ \AA}$, $c = 19.0100(3) \text{ \AA}$) (cf. figure IV.20 and table IV.15 and IV.16). This new packing differs from the pristine one only by layer gliding, with the halides sequence switching from AB (O1 type) in the pristine materials to ABC (O3 type) in the lithiated phases (cf. figure IV.20).

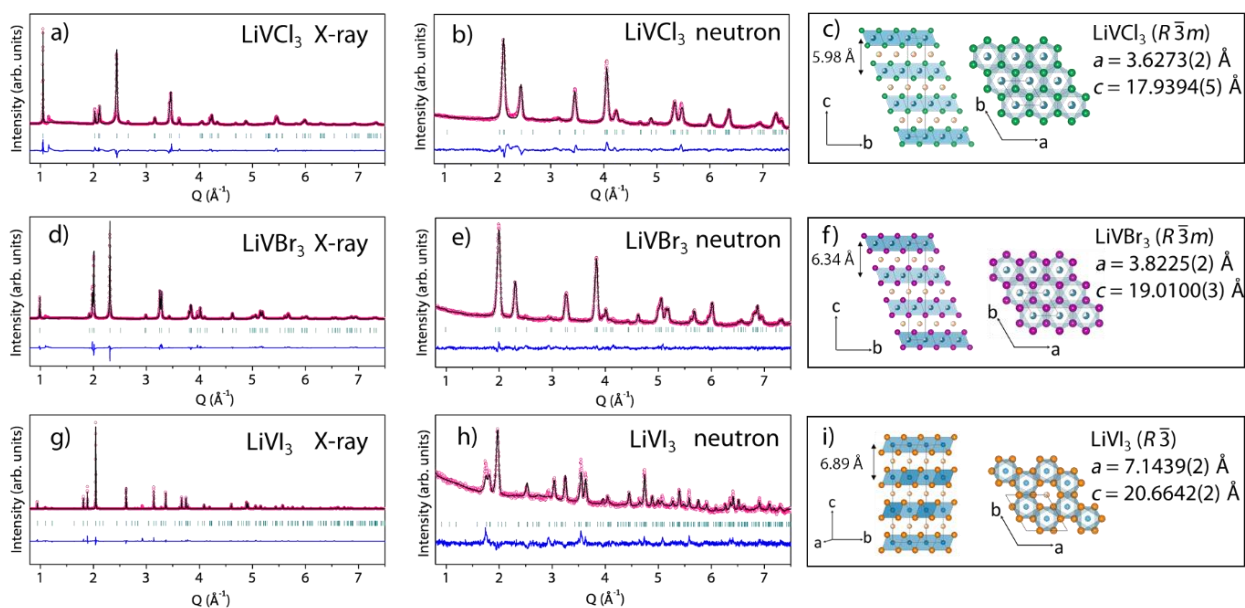


Figure IV.20: a) Synchrotron XRD ($\lambda = 0.41378 \text{ \AA}$) Rietveld refinement for LiVCl_3 , b) LiVBr_3 and c) LiVI_3 . d) Neutron diffraction ($\lambda = 1.6220 \text{ \AA}$) Rietveld refinement for LiVCl_3 , e) LiVBr_3 and f) LiVI_3 . The corresponding structural models are reported in the Tables IV.15, IV.16 and IV.17. The pink circles, black continuous line, and bottom blue line represent the observed, calculated, and difference patterns, respectively. Vertical green tick bars stand for the Bragg positions. g) Structure of LiVCl_3 , h) LiVBr_3 , i) LiVI_3 . The vanadium, chlorine, bromine, iodine and lithium atoms are represented in blue, green, purple, orange and yellow, respectively.

However, some unindexed broad peaks with diffuse scattering can be observed at greater angle than the (003) reflection peak (cf. figure IV.21) for both LiVCl_3 and LiVBr_3 . Such structural features are commonly observed in A_2MO_3 honeycomb ordered layered materials.¹⁹¹ A symmetry reduction from $R\bar{3}m$ to $C2/m$ was then undertaken to introduce such ordering in the transition metal layer with, however, no improvement of the refinement (cf. figure IV.21). This unsatisfactory fitting does not question the presence of a superstructure but is rather imputable to the presence of stacking faults that would need specific treatment. Nevertheless, for the sake of simplicity, the “average” $R\bar{3}m$ model was kept to report the structures in this manuscript. Finally, neutron diffraction patterns were collected for the three lithiated phases, allowing us to locate the lithium atoms. For both LiVCl_3 and LiVBr_3 , the lithium cations occupy the octahedral vacant sites of the interlayer (in position $3b$). For LiVI_3 , the octahedral sites of the interlayer are split into two different positions: $3b$ or $6c$. Rietveld refinement of the neutron diffraction patterns confirms the presence of lithium in these sites with no clear evidence of any preferred occupancy between them.

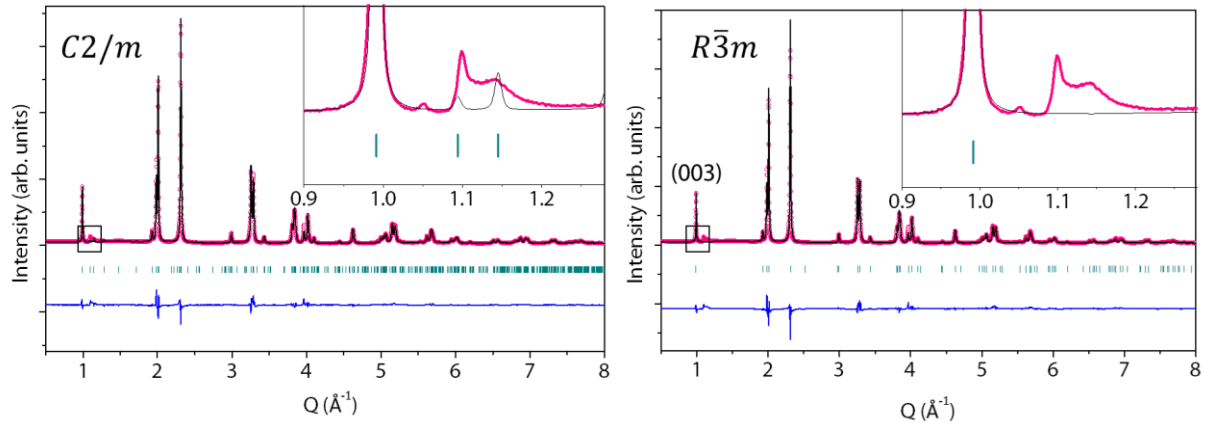


Figure IV.21: Refinement of LiVBr_3 synchrotron XRD pattern ($\lambda = 0.41378 \text{ \AA}$) using either $C2/m$ (left) or $R\bar{3}m$ (right) structural models. The pink circles, black continuous line, and bottom blue line represent the observed, calculated, and difference patterns, respectively. Vertical green tick bars stand for the Bragg positions. The inset in each picture refers to a zoom in the 0.9-1.3 \AA^{-1} region. The $C2/m$ model introduces honeycomb ordering in the TM layer that is not taken into account in the $R\bar{3}m$ model. Nevertheless, despite using the $C2/m$ model allows to grow intensity corresponding to the 1.1-1.2 \AA broad peak, this region cannot be fitted properly, probably due to stacking faults.

LiVCl_3		$R\bar{3}m$	$R_{\text{Bragg}} = 4.07 \%$	$\chi^2 = 24.7$		
$a = 3.6273(2) \text{ \AA}$		$c = 17.9394(5) \text{ \AA}$		$\text{Vol} = 204.415(6) \text{ \AA}^3$		
Atom	Wyckoff Position	x/a	y/b	z/c	$B_{\text{iso}} (\text{\AA}^2)$	Occupancy
Cl	6c	0	0	0.2570(6)	0.94(3)	1
V	3a	0	0	0	0.83(4)	2/3
Li	3b	0	0	0.5	3.3(3)	2/3

Table IV.15: Crystallographic data and atomic positions for LiVCl_3 determined from Rietveld refinement of both its synchrotron X-ray and neutron patterns.

LiVBr_3		$R\bar{3}m$	$R_{\text{Bragg}} = 3.17 \%$	$\chi^2 = 28.3$		
$a = 3.8225(2) \text{ \AA}$		$c = 19.0100(3) \text{ \AA}$		$\text{Vol} = 240.510(10) \text{ \AA}^3$		
Atom	Wyckoff Position	x/a	y/b	z/c	$B_{\text{iso}} (\text{\AA}^2)$	Occupancy
Br	6c	0	0	0.2545(4)	1.805(11)	1
V	3a	0	0	0	1.89(5)	2/3
Li	3b	0	0	0.5	1.27(9)	2/3

Table IV.16: Crystallographic data and atomic positions for LiVBr_3 determined from Rietveld refinement of both its synchrotron X-ray and neutron patterns.

LiVI ₃		$R\bar{3}$	$R_{\text{Bragg}} = 1.91\%$	$\chi^2 = 83.2$		
$a = 7.1439(2) \text{ \AA}$		$c = 20.6642(2) \text{ \AA}$		$\text{Vol} = 913.306(12) \text{ \AA}^3$		
<i>Atom</i>	<i>Wyckoff Position</i>	x/a	y/b	z/c	$B_{\text{iso}} (\text{\AA}^2)$	<i>Occupancy</i>
I	18f	0.0022(2)	0.3337(3)	0.0788(5)	1.964(13)	1
V	6c	0	0	0.3326(4)	2.61(11)	1
Li	3b	0	0	0.5	1.1(3)	2/3
Li	6c	0	0	0.1511(11)	1.1(3)	2/3

Table IV.17: Crystallographic data and atomic positions for LiVI₃ determined from Rietveld refinement of both its synchrotron X-ray and neutron patterns.

We have just seen that it was possible to lithiate the VX₃ phases, we are now interested in the influence of this lithiation on the magnetic properties of these compounds.

IV.2.d Magnetic properties of the Li_xVX_3 phases (with $x = 0$ or 1)

Magnetic susceptibility measurements were performed on the LiVX_3 phases under zero field cooled (ZFC) condition between 2 K and 400 K with an applied magnetic field of 10 kOe (Figure IV.22, IV.23 and IV.24) and on the VX_3 for sake of comparison. We will first look at VBr_3 , VCl_3 , and the corresponding lithiated compounds. As shown in figures IV.22 (a and b) and IV.23 (a and b) and in accordance with previous studies,^{187,192} vanadium trichloride (resp. tribromide) is antiferromagnetic with a Néel temperature of 25 K (resp. 30 K). The effective moment is found to be $2.81 \mu_B$ (resp. $2.61 \mu_B$) (cf. table IV.18) close to the $2.83 \mu_B$ moment expected for a spin-1 configuration of V^{3+} . Through lithiation the antiferromagnetic behavior of VBr_3 is conserved (cf. figure IV.23.b and d) with however, a shift of the Néel temperature to the higher temperature ($T_N = 60$ K). It is worth mentioning moreover, that the magnetic transition is found much broader for LiVBr_3 than for VBr_3 . The LiVCl_3 behavior is found more complicated with possibly two broad antiferromagnetic transitions found at high temperature than VCl_3 ($T_{N1} = 35$ K and $T_{N2} = 85$ K). In addition Curie-Weiss fitting performed on LiVCl_3 (resp. LiVBr_3) lead to an effective moment of $3.59 \mu_B$ (resp. $3.68 \mu_B$) confirming V^{2+} oxidation states in these compounds (the moment expected for a spin-1 V^{2+} being $3.87 \mu_B$).

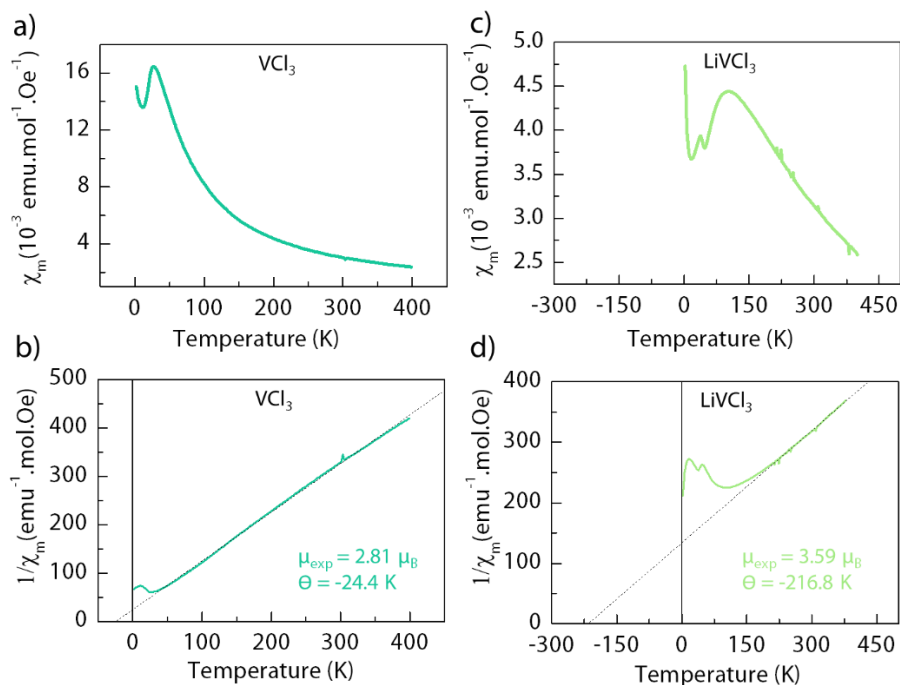


Figure IV.22: Temperature dependence of the magnetic susceptibility χ of VCl_3 (a), and LiVCl_3 (c). Temperature dependence of the inverse of the magnetic susceptibility $1/\chi$ of VCl_3 (b) and LiVCl_3 (d), measured in zero-field-cooled (ZFC) conditions. The curves follow at high temperature an ideal Curie-Weiss behavior represented by the dashed line (Curie Weiss fit).

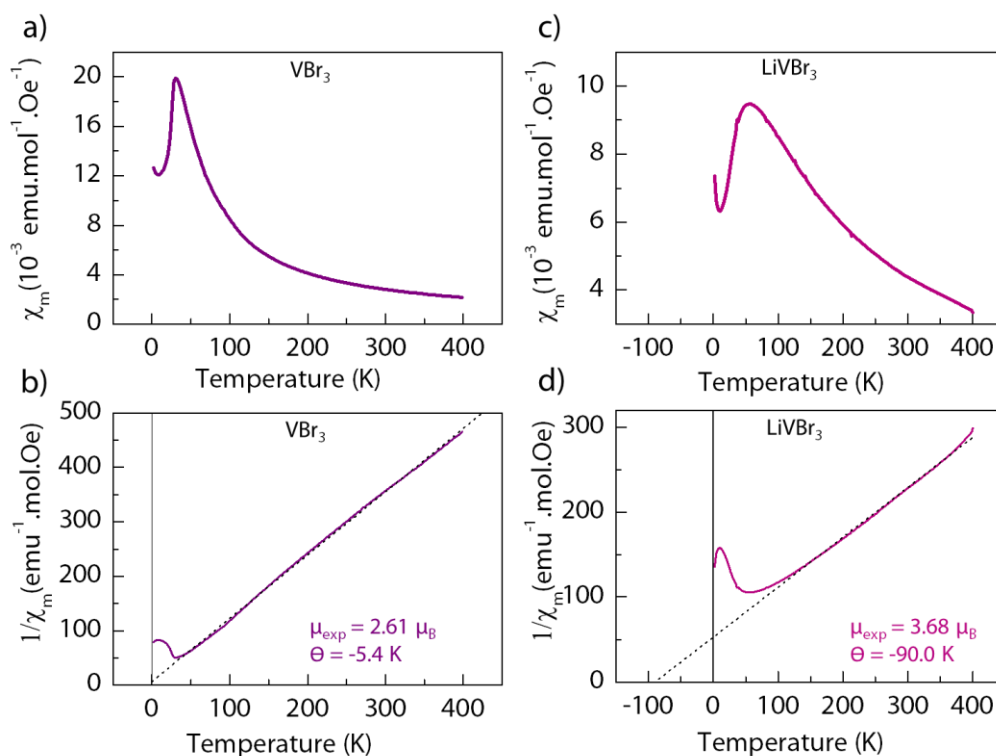


Figure IV.23: Temperature dependence of the magnetic susceptibility χ of VBr_3 (a), and LiVBr_3 (c). Temperature dependence of the inverse of the magnetic susceptibility $1/\chi$ of VBr_3 (b) and LiVBr_3 (d), measured in zero-field-cooled (ZFC) conditions. The curves follow at high temperature an ideal Curie-Weiss behavior represented by the dashed line (Curie Weiss fit).

The understanding of the evolution of the magnetic properties of these compounds with lithiation is delicate without more data (especially theoretical simulation). Indeed, beyond the oxidation degree of vanadium, the stacking of the honeycomb planes changes between VX_3 and LiVX_3 ($\text{X} = \text{Cl}$ or Br), each of these phenomena being able to induce complex changes of the magnetic properties.¹⁹⁴ However, the broadening of the magnetic transition and the appearance of a second transition for LiVCl_3 can be potentially attributed to stacking faults as already observed for $\alpha\text{-RuCl}_3$.¹⁹⁵

Similarly for VI_3 , in line with precedent investigations^{183–185,190} a ferromagnetic order at around 50 K (cf. Figure IV.24.a) was found. The interpolation of the high temperature part of the susceptibility with a Curie-Weiss law indicates an effective moment of $2.28 \mu_{\text{B}}$ per vanadium atom, slightly lower than the one expected for the spin configuration of V^{3+} ($2.83 \mu_{\text{B}}$) and an interpolated Weiss temperature of $+43.7 \text{ K}$ (cf. Figure IV.24.b) suggesting predominant ferromagnetic interactions. Moreover, magnetization curves were collected at 2 K in a $[-70 \text{ kOe}; 70 \text{ kOe}]$ range and demonstrate a clear hysteresis loop accounting for a 10 kOe coercitive field (cf. Figure IV.24.c), which confirmed the ferromagnetism in VI_3 . On the contrary, LiVI_3

shows an antiferromagnetic order below $T_N = 12$ K with a Curie Weiss temperature $\theta = -18.7$ K and an effective moment of $3.55 \mu_B$ per vanadium, (i.e. a value a bit lower than the $3.87 \mu_B$ expected). This ferromagnetic to antiferromagnetic transition puzzled us and to better understand it we interrogate the presence of a long-range magnetic ordering in both VI_3 and LiVI_3 using neutron diffraction.

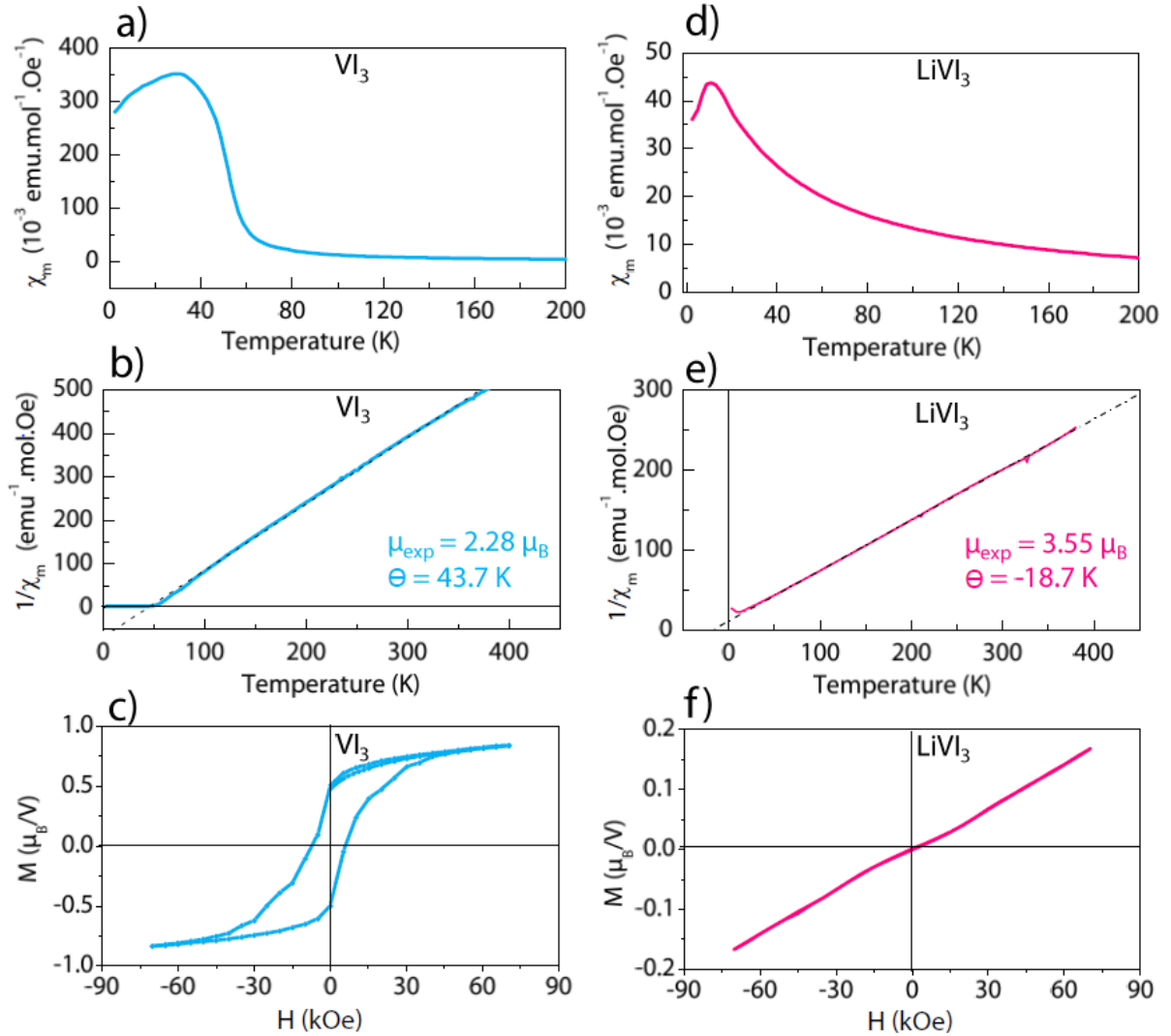


Figure IV.24: Temperature dependence of the magnetic susceptibility χ of VI_3 (a), and LiVI_3 (d). Temperature dependence of the inverse of the magnetic susceptibility $1/\chi$ of VI_3 (b) and LiVI_3 (e), measured in zero-field-cooled (ZFC) conditions. The curves follow at high temperature an ideal Curie-Weiss behavior represented by the dashed line (CW fit). Magnetization curve of VI_3 (c) and LiVI_3 (f) as a function of the applied field measured at 2 K.

	Cl	Br	I
VX ₃	Antiferromagnetic T _N ≈ 25 K C = 0.99 Θ = -24.4 K DO(V) = 3.02	Antiferromagnetic T _N ≈ 30 K C = 0.86 Θ = -5.4 K DO(V) = 3.20	Ferromagnetic T _C ≈ 50 K C = 0.66 Θ = 43.7 K DO(V) = 3.51
LiVX ₃	Antiferromagnetic T _{N1} ≈ 35 K T _{N2} ≈ 85 K C = 1.62 Θ = -216.8 K DO(V) = 2.28	Antiferromagnetic T _N ≈ 60 K C = 1.7 Θ = -90.0 K DO(V) = 2.19	Antiferromagnetic T _N ≈ 12 K C = 1.59 Θ = -18.7 K DO(V) = 2.31

Table IV.18: Magnetic information on the VX₃ and LiVX₃ phases

i) Magnetic structure of VI₃

To investigate an eventual magnetic transition in VI₃ we collected neutron diffraction patterns between 3 K and 100 K. The patterns are reported in Figure IV.25a and confirm the occurrence of structural phase transitions at T₁ = 76 K and T₂ = 32 K, previously spotted by X-rays. The latter is however barely observable because of the lower resolution of the neutron diffractometer compared to the synchrotron XRD one. The magnetic signature related to the ferromagnetic ordering is even more difficult to observe. Nevertheless some hints can be spotted by comparing the 60 K (above T_c), 40 K and 9 K (both below T_c) patterns. They show a subtle intensity evolution of the (110) peak (at Q = 1.84 Å⁻¹, here (hkl) indices refer to the R $\bar{3}$ hexagonal cell) (cf. Figure IV.25.c and d) with no further visible evolution of this peak's intensity down to the lowest measured temperature. An increase of the (110) peaks is expected with a ferromagnetic order with magnetic moments oriented perpendicular to the honeycomb vanadium layers (along [001]) (cf. Figure IV.25b), as deduced from simulations of ferromagnetic contributions along different directions (cf. Figure IV.26). However, if of magnetic origin, this subtle intensity increase would correspond to an ordered magnetic moment of maximum 0.2 μ_B, which is ten-fold smaller than expected for V³⁺ (2 μ_B, S = 1 for V³⁺) and is of the order of magnitude of the standard deviation obtained on the Rietveld refinement. Such an observation indicates that the macroscopic ferromagnetic ordering along [001] evidenced by magnetic susceptibility on single crystals¹⁸³ does not translate into a long-range complete ordering.

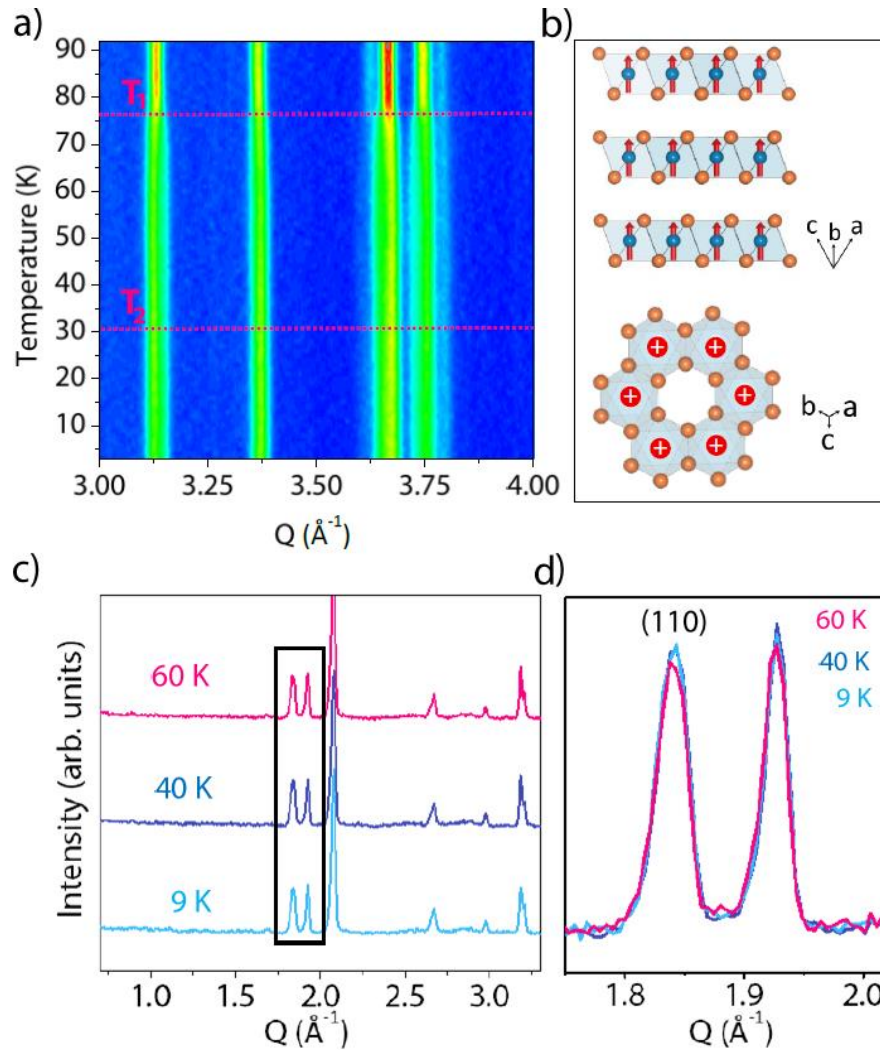


Figure IV.25: a) Evolution of the neutron diffraction patterns with temperature between 3 K and 92 K. It is worth noticing that the neutron instrument resolution is not high enough to clearly distinguish the structural transition at T_2 b) Hypothetical magnetic structure of VI_3 (vanadium and iodine atoms are in blue and orange respectively). The spin orientations are represented with red arrows or by a '+' sign indicating that the spins are pointing orthogonally to the view. c) Comparison of the 60 K, 40 K and 9 K neutron diffraction pattern in the $[0.7 \text{ \AA}^{-1}; 3.3 \text{ \AA}^{-1}]$ Q range, d) zoom in the $[1.7 \text{ \AA}^{-1}; 2.05 \text{ \AA}^{-1}]$ Q range to highlight the magnetic contribution to the (110) reflection (with (hkl) indices referring to the $R\bar{3}$ hexagonal cell).

This almost-undistinguishable ordered moment may arise from a reduced coherence length in the magnetic structure, which may be due to the presence of defects in the vanadium honeycomb pattern, stacking faults and weakness of the magnetic interactions across the van der Waals gap. Still, this is not supported by our neutron data since no signs of diffuse magnetic scattering in the patterns is observed at low scattering angles. The existence of an ordered magnetic structure can therefore be questioned, and the small increase in the (110) reflection could just be due to another origin. The apparent contradiction with the macroscopic magnetic measurements that

clearly indicates a ferromagnetic behavior still needs to be clarified, and a field-induced ferromagnetic ordering should be further explored as the origin for this contradiction.

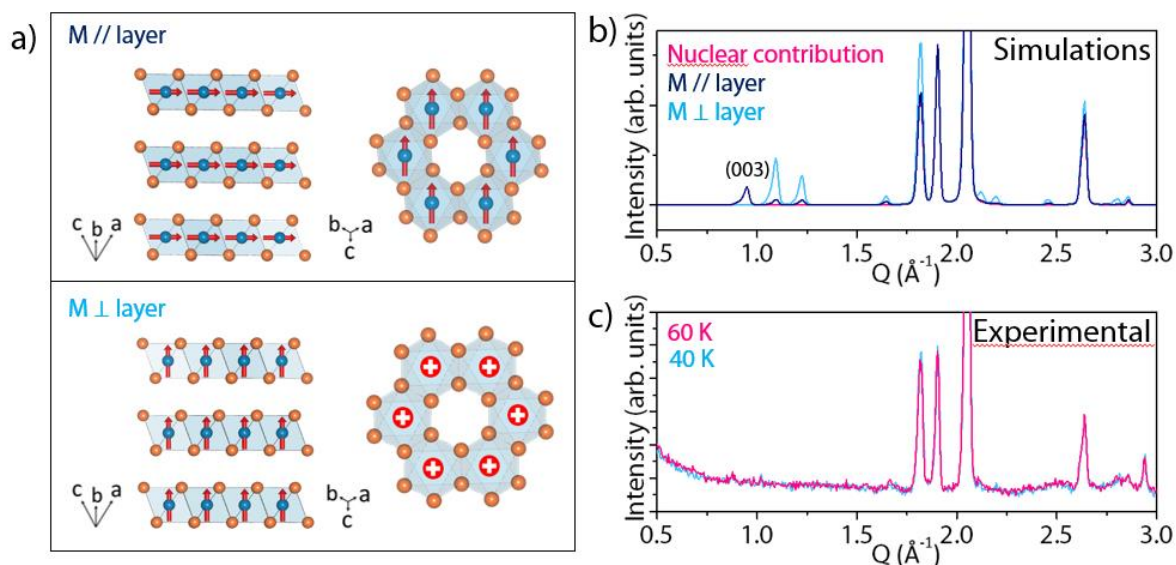


Figure IV.26: a) Magnetic structure of VI_3 (vanadium and Iodine atoms are in blue and orange respectively) with spin oriented either parallel (top) or perpendicular (bottom) to the honeycomb layers. The spin orientations are represented with red arrows or by a '+' sign indicating that the spins are pointing orthogonally to the view b) Simulated neutron diffraction patterns with different spin configurations c) comparison of the 60 K and 40 K experimental neutron diffraction pattern in the $[0.5 \text{ \AA}^{-1}; 3 \text{ \AA}^{-1}]$ Q range.

ii) *Magnetic structure of $LiVI_3$*

Neutron diffraction patterns collected between 25 K and 3 K for $LiVI_3$ show the emergence of extra magnetic peaks at low angle (cf. Figure IV.27.a). Altogether, these observations combined with the magnetic behavior described above, suggest the formation of a long-range magnetic structure at low temperature. Further exploiting the NPD patterns, we could index the extra reflections using a $\mathbf{k} = (0, 0, 0)$ propagation vector and determine the associated magnetic structure using the Isodistort program^{132,133}. The 3 K neutron diffraction pattern was successfully refined in the $R\bar{3}'$ magnetic space group (cf. Figure IV.27.c and Table IV.19), where all the magnetic moment are found to be oriented in the $[001]$ direction with both intra- and interlayer adjacent vanadium atoms being antiferromagnetically coupled (cf. Figure IV.27.b). Surprisingly, the refined magnetic moment was found to be equal to $1.68(6) \mu_B$ i.e. lower than the expected $3 \mu_B$ value for a d^3 ion. Such a difference could arise from a reduced coherence length induced by defect such as stacking faults and weakness of interlayer interaction.

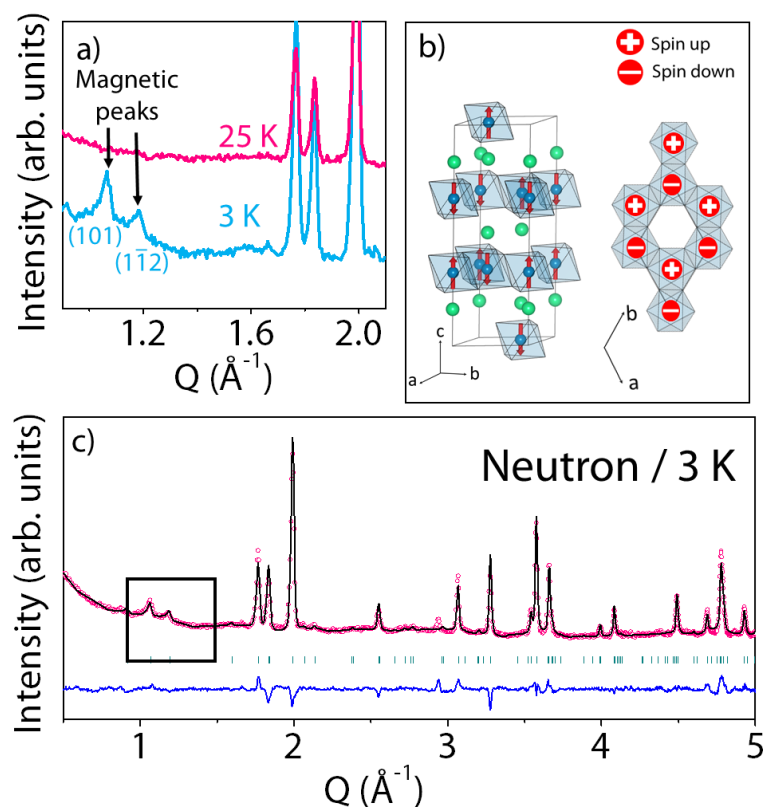


Figure IV.27: a) Neutron powder diffraction patterns of LiVI_3 at 25 K and 3 K b) magnetic structure of LiVI_3 spin orientations are represented with red arrows, the right panel represents the spin organization in a single layer c) Rietveld refinements of LiVI_3 at 3 K ($\lambda = 2.4395 \text{ \AA}$). The pink circles, black continuous line, and bottom blue line represent the observed, calculated, and difference patterns, respectively. Vertical green tick bars stand for the Bragg positions.

Understanding this Li-driven ferromagnetic to antiferromagnetic transition calls for a comparison of both VI_3 and LiVI_3 in terms of crystal and electronic structures. Firstly, the redox state of vanadium changes from V^{3+} (d^2) to V^{2+} (d^3) leading to half-filled t_{2g} electronic states i.e. similarly to that of ferromagnetic CrI_3 . Besides, although CrI_3 and LiVI_3 share exactly the same $R\bar{3}$ structure at low temperature, they differ by longer M-I bond lengths as well as larger interlayer distances ($\text{V-I} = 2.90 \text{ \AA}$, interlayer = 6.84 \AA , at 100 K) for LiVI_3 as compared to CrI_3 ($\text{Cr-I} = 2.73 \text{ \AA}$, interlayer = 6.60 \AA , at 90 K). Moreover, it is worth reminding that several first principle calculation investigations^{194,196} on bulk CrI_3 revealed a strong intralayer ferromagnetic exchange as opposed to a weaker ferromagnetic interlayer coupling. Thus, presently, the increase of the interlayer and M-M distances (where M stands for transition metal) from CrI_3 to LiVI_3 may change the competing nature of the interlayer and intralayer couplings and consequently explain the antiferromagnetic interaction observed for LiVI_3 . However, further theoretical investigations are needed to support our explanation and to better understand how

the intra vs inter M-M distance variation impacts the magnetic properties of layered van der Waals materials.

LiVI ₃ 3 K		Shubnikov group: $R\bar{3}'$		$R_{\text{Bragg}} = 12.0$ %	$\chi^2 = 8.05$	$R_{\text{mag}} = 16.1$ %	
$a = 7.0956(2)$ Å		$c = 20.4980(5)$ Å		Vol = 893.82(4) Å ³			
Atom	Wyckoff Position	x/a	y/b	z/c	B_{iso} (Å ²)	Occupancy	M_z
I	18f	0.0007(14)	0.328(2)	0.0792(4)	0.70(9)	1	/
V	6c	0	0	0.327(6)	0.42(4)	1	1.68(6) μ _B
Li1	3b	0	0	1/2	2.122(12)	2/3	/
Li2	6c	0	0	0.1641(7)	2.122(12)	2/3	/

Table IV.19: Crystallographic and magnetic structures data and atomic positions for LiVI₃ at 3 K determined from Rietveld refinement of its neutron diffraction pattern

Finally, in this section we have demonstrated the possibility to intercalate topotactically lithium in the layered vanadium halides compounds (VCl₃, VBr₃ or VI₃) and studied deeply their crystallographic structures with particular attention paid to the VI₃ phase. Indeed, we confirm that the room temperature $R\bar{3}'$ VI₃ phase undergoes two structural transitions upon cooling at 76 K and 32 K together with a ferromagnetic ordering at 50 K. Moreover, we provide a structural model of this compound in the whole temperature range and demonstrate that the 76 K and 32 K phase transitions are solely due to distortion of the vanadium honeycomb networks with minute changes of the V-V distances. In a second time we studied the effect of the lithiation the magnetic properties of the VX₃ compounds. For both VCl₃ and VBr₃ this lithiation conserves the antiferromagnetic ordering solely shifting the Néel temperature to the higher temperatures. In contrast, the lithiation of the VI₃ ferromagnet leads to LiVI₃ which is antiferromagnetic. Altogether all these results calls for deeper investigation of the lithiation of transition metal halides for both energy storage and magnetism applications.

Chapter conclusion

The aim of this chapter was to discuss the interest of exploring new chemistries in view of isolating new alkali metal intercalation materials. Firstly, we have examined the case of oxysulfides within the context of anionic redox with the hope to combine the advantages of oxides (high potential) and those of sulfides (stability of the oxidation process). Among the few possible candidates we chose to focus on the $\text{Na}_3\text{VS}_{4-x}\text{O}_x$ family ($x = 0, 1$ or 2) where the vanadium atoms are heteroleptically bonded to sulfur and oxygen to highlight the influence of the O/S ratio on the oxidation potential (theoretically purely anionic). Unfortunately, although they present an electrochemical activity, the process is poorly reversible with little deviation in their oxidation potentials. Nevertheless, the use of simplified model of the electronic structure based on the $[\text{VS}_{4-x}\text{O}_x]^{3-}$ tetrahedron molecular orbital diagram suggests that the anionic redox would come only from the sulfur atoms with almost no participation of oxygen, thereby questioning the interest of such compositions as cathodes for metal ion batteries.

Secondly, we established for the first time the possibility of using layered vanadium halides (VCl_3 , VBr_3 or VI_3) as lithium intercalation materials. The structures of these compounds as well as their lithiated counterparts were determined. Although they do not exhibit (as such) outstanding cycling properties, we hope this preliminary study to pave the way for the exploration of a whole family of materials. On that basis one can reasonably ask the question of the activity of rich halides such as Li_2MnCl_4 (254 mAh.g^{-1} theoretically) or Li_6VCl_8 (218 mAh.g^{-1} theoretically). Moreover, as expected, we have seen that the lithiation of these compounds allows to modify their magnetic properties, thereby opening a new dimension to tune the physical properties of these compounds.

Altogether, it is clear that new cathode materials can be found in unexploited areas of chemistry, but their discovery is tedious. Because the lack of theoretical guidance intuition based on simple chemical considerations must still prevail. Nevertheless, one should not fall into easy pessimism as the examples reported herein are widening the range of applications of intercalation materials beyond energy storage issues with additional impact in the field of spintronic and others. Thus, optimism must prevail among solid state chemists as new exotic compounds are still waiting to be uncovered.

Conclusion and future work

Over the last forty years, the development of new alkali-ion intercalation compounds has been a major focus of metal-ion battery research. Indeed, the discovery of better performing materials or "model" compounds (i.e. specifically designed to better understand the intercalation mechanisms) have strongly contributed to making Li-ion batteries the leading technology in electrochemical energy storage. While the growing need for improved energy density in these cells still requires the discovery of new compounds, intensive research on the subject has exhausted most of the possibilities and the description of new intercalation structures in the literature has declined significantly in recent years. In this context, the aim of this thesis was to explore new synthetic leads to obtain original compositions.

Thus, by noting that the synthesis of most intercalation materials was mainly done using high temperature routes (therefore leading mainly to thermodynamically stable compounds), it was natural to explore low temperature processes in order to obtain metastable compositions. For this purpose, we focused on the family of ruthenium oxides, which has been widely explored for their magnetic or catalytic properties and more recently as intercalation materials. We have shown that by reducing a strongly oxidized salt of ruthenium ($\text{KRu}^{\text{VII}}\text{O}_4$) in the presence of strongly complexing cations (Ba^{2+} , Sr^{2+}) in water at only 200°C it was possible to obtain original and metastable ruthenium oxides. In addition, this process was shown to be very dependent on the physico-chemical conditions of the reaction medium (pH, temperature) and moreover, by playing on these parameters, it was possible to synthesize a whole family of new ternary Ba(Sr)-Ru-O oxides. This example gives a good idea of the potential of low temperature processes, in particular when they are solution based, to reach a fine and precise control of the reaction path during the synthesis. Thus, one can dream that by using such processes it will be possible one day to obtain a plethora of metastable materials as is done in organic chemistry. However, there is still a long way to go before we reach this state of affairs. Indeed great challenges are to be met in order to understand in detail the complex formation mechanisms of these materials in solution. On a more realistic timescale, it would be interesting to show that the synthesis process used here can be extended to other cations than ruthenium. Manganese is a natural candidate for this as KMnO_4 , similarly to KRuO_4 , can be reduced by water at high temperature. In addition, beyond the synthesis process itself, some of the compounds obtained, namely SrRu_2O_6 and BaRu_2O_6 , have shown interesting electrochemical and magnetic properties. Thus, these two lamellar structures are antiferromagnetic with Néel temperatures

among the highest described for 4d metal oxides, and allow the topotactic insertion of lithium ions. Moreover, preliminary results suggest that the magnetic order temperature in SrRu_2O_6 is lithiation dependent. This observation reminds us that beyond the application to energy storage, the topotactic intercalation of cations allows for a controlled modification of the structure, thereby opening the door to the fine tuning of their physical properties.

While low temperature synthesis is without any doubt one of the most promising ways to obtain new materials, it is still possible to obtain new intercalation materials via a ceramic process by focusing on chemical compositions that are still little explored such as chalcogenides. Indeed, if these materials were the first to be studied for lithium intercalation, oxides quickly supplanted them. Today, however, the stability of the anionic redox process in these materials, contrary to oxides, tends to put them back in the spotlight. This new problematic opens the way to the synthesis of sulfides that have been ignored until now, such as lithium-rich sulfides or lithiated sulfides based on 4d or 5d metals. Thus, in order to study the anionic redox process in lithium-rich structures, we first studied the two polymorphs of Li_3NbS_4 . Surprisingly, the comparison of the electrochemical behavior of these two materials allowed us to highlight the importance of the dimensionality of the transition metal network in the electrochemical activity. Moreover, the systematic search for lithiated sulfides led us to the discovery of the lamellar compound L-LiIrS_2 , which is isostructural to LiTiS_2 . Interestingly, the non-lithiated compound J-IrS_2 obtained by ceramic route presents a non-lamellar structure with S-S dimers. Along with these structural differences, these two materials present different electrochemical behaviors with 1 V difference between the delithiation of L-LiIrS_2 and the lithiation of J-IrS_2 . Using a wide range of characterization techniques, we have shown that the anionic redox couple of the two polymorphs was different depending on whether or not the S-S dimer was present. In a global way, this result allows to better understand the reaction pathways followed by the materials during the anionic redox and to propose an explanation for the hysteresis phenomenon observed in the so-called "Li-rich" oxides. However, beyond these results, it is natural to wonder if the search for new lithium chalcogenides is an ephemeral theme or if it can constitute a major research axis in the field of Li-ion batteries. First, regarding the industrial applicability of sulfides, it is interesting to calculate an order of magnitude of the maximum performances of such compounds. The lithiated sulfide with the highest theoretical gravimetric capacity being Li_2TiS_3 (340 mAh.g^{-1}), and since the voltage associated with the lithium withdrawal does not exceed 2.5 V in a sulfide, we obtain a maximum theoretical energy density of 850 Wh.kg^{-1} , which is barely higher than the practical energy density of commercial NMC 811. Thus, even

pushed to their maximum these materials would be at the level of the market standards, and then do not seem to be the most promising cathode materials. What about using them as model materials for a better understanding of anionic redox? Although it is impossible to predict future discoveries, it is safe to say that this use of sulfides promises interesting future studies. However, it is important to note that due to the higher energy position of the 3p-bands of sulfur compared to the 2p-bands of oxygen, the maximum oxidation state of the transition metals is lower in sulfides than in oxides. Therefore, the number of possible lithiated transition metal sulfides must be accordingly lower than that of oxygen. Thus, if discoveries of new chalcogenide phases are highly probable, it is likely that this unexplored reserve of materials will be rapidly exhausted and it is therefore necessary to find other strategies.

One last idea would of course be to focus on still-unexplored chemical families. However, after so many years of research, the compounds that have been little explored are those difficult to synthesize or apply in a battery. We have first studied oxysulfides with the idea of combining in a single compound the advantages of oxides (high energy density) and those of sulfides (stability of anionic redox processes). Thus, we focused on $\text{Na}_3\text{VS}_{4-x}\text{O}_x$ compounds, which seemed ideal to study the question of anionic redox in multi-anionic compounds. Our initial electrochemical results coupled with a simplified electronic structure analysis of the materials do not seem to indicate much change in the anionic redox potentials along with the S/O ratio. These results suggest that the anion mixture will probably not allow us to obtain the “miracle material”, the one operating at high potential with a stable anionic redox. Thus, in view of the great difficulty of synthesizing these compounds, it could be interesting to verify these results from a theoretical point of view or to be open to the study of these materials beyond their application to energy storage. In a second step, we turned to the study of transition metal trihalides. Contrary to oxysulfides, these compounds are quite common, particularly well-studied for their magnetic properties and have for the most part a lamellar structure, which is ideal for the intercalation of transition metals. However, due to their high solubility in polar solvents they have almost never been studied as intercalation materials. This difficulty was overcome by engineering the electrolyte, which confirmed the possibility of reversibly intercalating lithium ions in VX_3 compounds ($\text{X} = \text{Cl}, \text{Br}$ or I). This result illustrates that the choice of cathode material is limited not only by solid-state chemistry but also by the constraints inherent to the battery system. Thus, beyond the solubility problems raised by our study, many cathode materials could not be studied because of the electrochemical window of the electrolyte and, paradoxically, the future of the search for cathode materials depends in part on the progress

of research in electrolytes. Finally, although the electrochemical performance of VX_3 compounds do not make them promising materials for large scale energy storage applications, we have shown that their lithiation allows a modification of their magnetic properties. This opens the way to a better understanding of the already widely studied two-dimensional magnetism of these compounds.

In the end, what is the general message carried by these results? First, it is clear that the control of low-temperature synthesis processes as well as the search for new chemistry constitute the most exciting future challenges in solid-state chemistry. However, in low temperature chemistry, if the promises are huge, the road will be long before having a controlled access to the infinity of the promised metastable compounds. It seems to me that on a short timescale the search for multi-anionic compounds is one of the most promising because the possibilities are very large and the investigations still rare. From the more limited point of view of lithium intercalating materials, it is unlikely that a revolution will come from these new chemistries and if a "miracle" material is to be discovered, it is likely to be an oxide. Indeed, the discovery of $Na_2Mn_3O_7$ allows us to dream of 3d metal oxides with a stable redox anion. In a less hypothetical way, the greatest hope of the field is probably a significant improvement of the electrochemical window of the electrolyte, which would allow studying high-voltage compounds, among which some have already been discovered. Finally, even if the search for new cathode materials would come to an end, the possibilities offered by topotactic cation intercalation chemistry for other research fields (magnetism and others) would remain immense and still promise great discoveries.

Materials and methods

A) Synthesis methods

A.1 Precursor grinding

Grinding of powders was done initially with a mortar and a pestle made of agate under a fume hood. For some syntheses (as mentioned for each example specifically in the manuscript), a more efficient mixing of the precursors was necessary. For this purpose, two different ball mills apparatus were used:

-A high-energy ball mill (SPEX 8000M series) equipped with 30 mL stainless steel jars and 11.9 mm diameter (6.9 g) steel balls. For all the synthesis, three balls were used for about 1 g of reaction mixture for 60 min of grinding.

-A planetary mill type pulverisette 7, equipped with a 45 mL zirconia jar and 10 mm diameter zirconia balls. During the synthesis of Li_3NbS_4 10, balls were used with about 1 g of reaction mixture and ground for 60 hours at 550 rpm.

A.2 Hydrothermal methods

The hydrothermal synthesis reported in chapter II were performed using either homemade Teflon-Line stainless steel 2 mL autoclaves (cf. figure A.1 a) or commercial (Anton-Paar) 20 mL ones (cf. figure A.1 b).

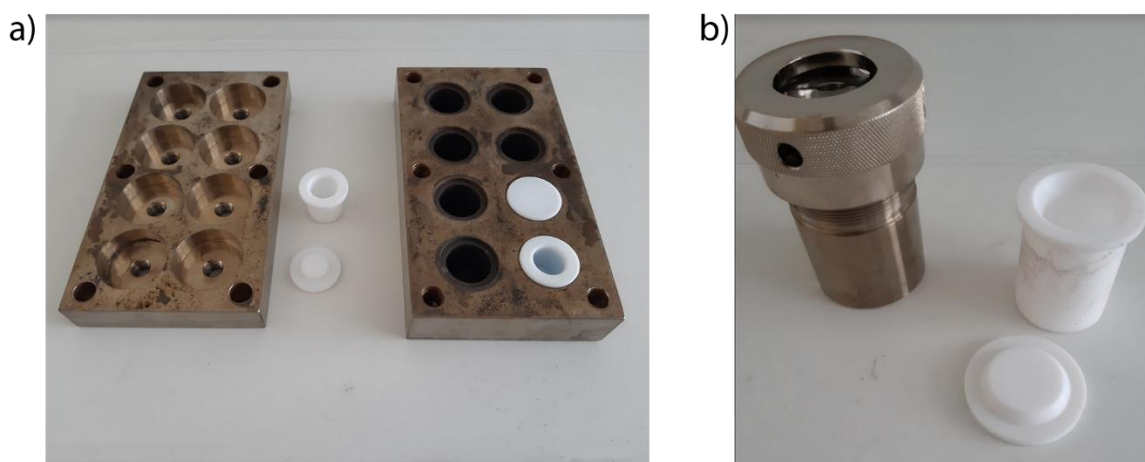


Figure A.1: a) Homemade Teflon-Line stainless steel 2 mL autoclaves. This setup allows up to 8 vessels to be heated simultaneously. b) Commercial (Anton-Paar) Teflon-Line stainless steel 20 mL autoclaves.

In contrast, BaRu_2O_6 was specifically synthesized in a microwave oven with silicon carbide (SiC) vessels (10 ml microwave flask). The tubes were heated at 200°C for three hours (final temperature is reached after 2 minutes).

A.3 Sealed tubes

High temperature syntheses under inert atmosphere were performed in sealed quartz tubes under high vacuum. For this purpose, the precursors were premixed and introduced into the tube (most often this step was performed in a glove box filled with argon). The tube was then connected to a high vacuum pump (see Figure A.2 a) and finally sealed. To avoid any reaction of the reagents with the wall of the tube, it is possible to place the reagents in an alumina crucible or to make a carbon coating on the surface of the tube (see figure A.2 b).

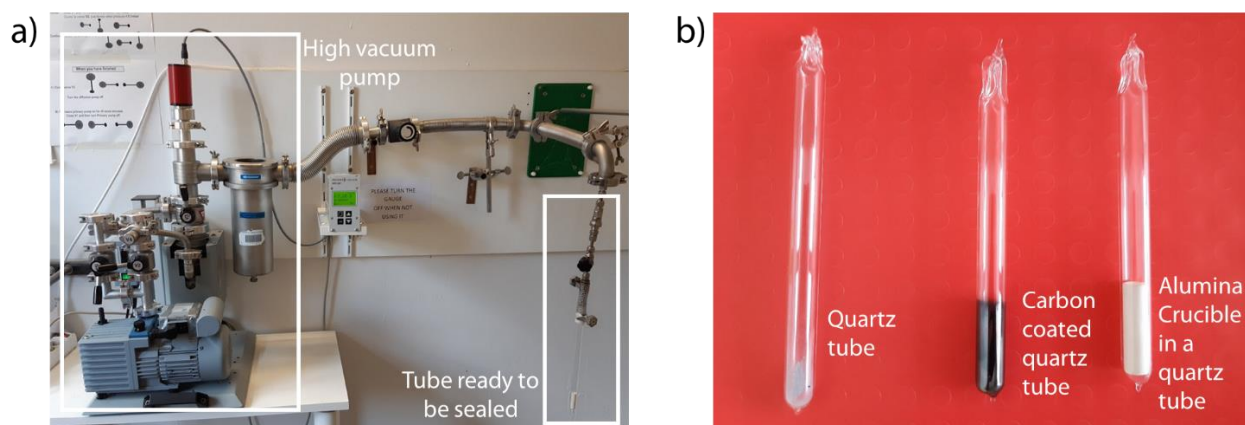


Figure A.2: a) Tube sealing setup. b) The different ways to prepare a sealed tube.

B) Structural characterizations

B.1 Laboratory X-ray powder Diffraction (XRD)

Laboratory powder XRD measurements were performed with a Bruker D8 Advance diffractometer operating in the Bragg-Brentano geometry with $\text{Cu K}\alpha$ radiations ($\lambda(\text{K}\alpha_1) = 1.54056 \text{ \AA}$, $\lambda(\text{K}\alpha_2) = 1.54439 \text{ \AA}$) and a Lynxeye XE detector.

For air-sensitive measurements, the samples were prepared in an Ar-filled Glovebox and using two different airtight samples holders. The first one is an home-made holder assembled with a Kapton window and the second one is an electrochemical cell equipped with a beryllium window as described by Leriche et al.¹⁹⁷ (cf. figure A.3)

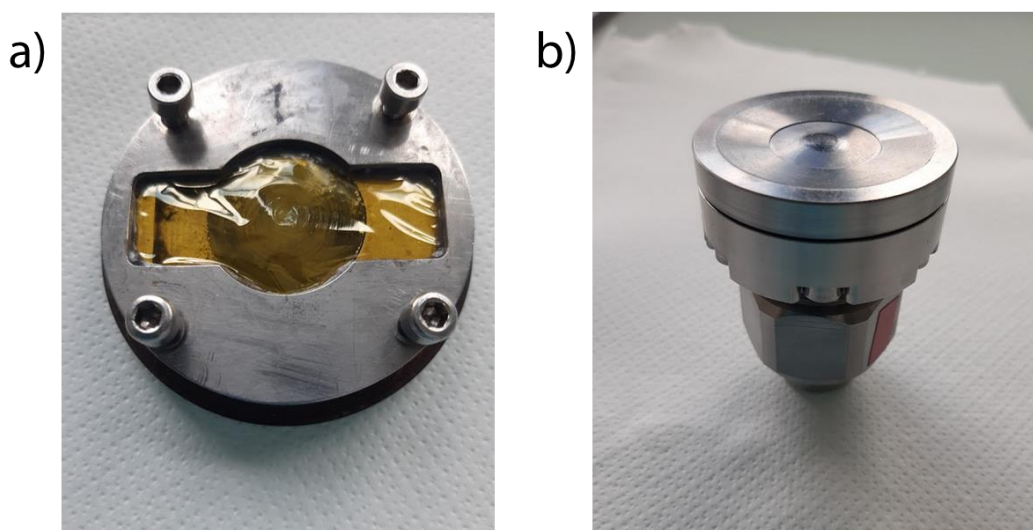


Figure A.3: a) Homemade airtight XRD sample holder made with a Kapton foil. B) Homemade cell equipped with Be window as described by Leriche et al.¹⁹⁷ This cell can also be used to perform operando electrochemical/XRD experiments.

B.2 Synchrotron X-ray powder Diffraction (SXRD)

X-ray powder diffraction (SXRD) patterns were measured either on the 11-BM beamline of the Advanced Photon Source (Argonne National Laboratory) or on the MSPD beamline of the ALBA synchrotron (Barcelona, Spain).

-For 11-BM measurements, powders were first mixed with the appropriate amount of amorphous silica (to limit absorption) before being placed in 0.7 mm diameter kapton capillaries. For air-sensitive compounds, the powders were first placed in 0.6 mm diameter borosilicate capillaries inside an Ar-filled glovebox and then sealed.

-On the ALBA synchrotron MSPD beamline, the powders were sealed in an Ar glovebox inside a 0.6 mm diameter borosilicate capillary prior to the measurements. Low temperature measurements were performed by transferring the capillaries to the Dynaflo liquid helium flow cryostat. In this case, the MAD (Multi Analyzer Detection) configuration was used, providing the highest possible instrumental angular resolution, $\Delta(2\theta) < 0.006^\circ$ in the range 0-35°.^{198,199}

The wavelengths used for each measurement may change from experiment to experiment and are reported individually in each chapter. These measurements were performed at ALBA with the help of François Fauth.

B.3 Neutron powder Diffraction (NPD)

Neutron powder diffraction experiments have been carried out either in the institut Laue Langevin (ILL, Grenoble, France), or at the Australian center for Neutron Scattering (ANSTO, Lucas Heights, Australia).

At the ILL facility neutron diffraction pattern (NPD) were collected on either the high-intensity D1B diffractometer ($\lambda = 2.5297 \text{ \AA}$) with the help of Claire Colin or the high angular-resolution D2B diffractometer ($\lambda = 1.5940 \text{ \AA}$) with the help of Thomas Hansen. The NPD patterns were recorded in transmission mode with the powder sample placed in vanadium cans of 8 mm diameter (for air sensitive samples, the cans were loaded in an argon-filled glovebox and sealed with an indium wire).

At the ANSTO facilities, Maxim Avdeev performed the measurement. Constant wavelength neutron powder diffraction (NPD) data were collected on the ECHIDNA high-resolution and WOMBAT high-intensity neutron powder diffractometers^{200,201} using the wavelengths of 2.4395 \AA and 2.4184 \AA , respectively. To prevent reaction of the samples with ambient atmosphere, the samples were loaded into 9 mm diameter cylindrical vanadium cans in Ar glove box and sealed with an indium wire.

B.4 Single crystal X-ray diffraction (SCXRD)

Single crystal X-ray diffraction (SCXRD) data were collected at the X-ray diffraction platform of IMPMC and analysed by Benoît Baptiste, on a Rigaku MM007HF diffractometer equipped with a RAXIS4++ image plate detector, a Mo rotating anode ($\lambda = 0.71073 \text{ \AA}$, Varimax multilayer optics) at 293 K. Following an equivalent procedure as described by A. Rothkirch et al.,²⁰² the collected images were converted to the esperanto format with an in-house program (not published). Then, data reduction, cell refinement, space group determination, scaling and empirical absorption correction were performed using CrysAlisPro software (CrysAlisPro 1.171.38.46, Rigaku Oxford Diffraction, 2015).

The structure was solved using SHELXT²⁰³ implemented in Olex2 program.²⁰⁴ The refinement was then carried out with SHELXL, by full-matrix least squares minimization and difference Fourier methods. All atoms were refined with anisotropic displacement parameters.

B.5 Structure determination from powders

Rietveld Refinement

Rietveld refinements of XRD, SXRD and NPD patterns were performed using the FullProf program.²⁰⁵ The magnetic structure refinements were also carried out using this tool.

Other Refinements

To take into account stacking faults and intergrowth we used the FAULTS program.¹²⁷ This software allows describing structures as a stack of layers by defining as input the structure of the different layers, the stacking vectors between these layers and the probabilities for these stacking to occur.

B.4 Bond valence calculations

Bond valence energy landscape maps (BVEL) were obtained using the BondSTR program implemented in the FullProf Suite following the method developed by Adams.²⁰⁶

B.5 Structures database and visualization

Throughout this thesis the crystallographic structures were visualized with the VESTA software,²⁰⁷ and the crystallographic data reported in the literature were extracted from the ICSD database.

C) Electrochemistry

C.1 Electrodes preparation

All the active materials were grinded in a mortar with 20% in mass carbon SP in an Ar-filled glovebox and used as such.

C.2 Electrochemical cells

All the electrochemical tests were performed in swagelok-type electrochemical cells (cf. figure A.4) assembled in Ar-filled glovebox. The anode was a metallic Li/Na foil deposited on a stainless steel current collector. Whatmann borosilicate glass fiber sheets were used as separators. For lithium batteries, unless otherwise stated either LP30 (1M LiPF₆ in 1/1 EC/DMC) or LP100 (1/1/3 EC/PC/DMC) were used as electrolyte while 1M NaPF₆ in PC was used for Na-ion batteries.

In situ XRD experiments were carried out using the beryllium window equipped cell described in the “Laboratory X-ray powder Diffraction (XRD)” section and shown on the figure A.3 b.

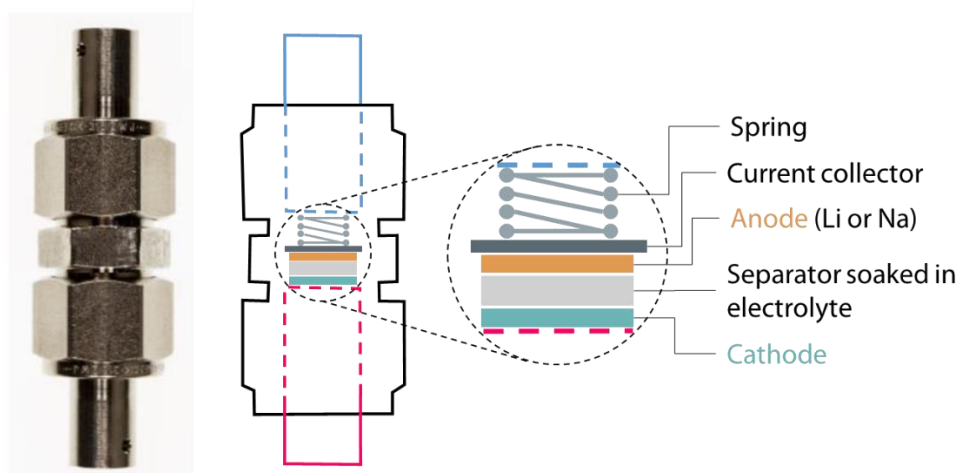


Figure A.4: Swagelok-type electrochemical cell

C.3 Electrochemical techniques

All the electrochemical experiments were performed using a VMP3 potentiostat/galvanostat (Biologic, S.A.). The standard battery tests were performed in galvanostatic mode i.e. by imposing a constant current in the cell and by measuring the potential variation at its terminals. Galvanostatic Intermittant Titration Technique (GITT) consists in alternating galvanostatic cycling with open circuit voltage (OCV) periods.

D) Magnetism

D.1 Magnetic measurements

The evolution of the magnetic susceptibility with temperature was measured using a SQUID (XL, Quantum Design) at the Sorbonne Université low temperature physics platform.

E) Electronic Microscopy

E.1 Scanning Electron Microscopy (SEM)

Scanning electronic microscopy and EDX analysis were performed using an SEM-FEG Hitachi SU-70 microscope coupled with an Oxford X-Max 50 mm² energy dispersive X-ray (EDX) spectrometer. Pierre Lemaire and Daniel Alves Dalla Corte are warmly thanked for these measurements.

E.2 Transmission Electron Microscopy (TEM)

For Transmission Electron Microscopy (TEM) investigations not sensitive to air (resp. air sensitive) samples were prepared in air (resp. inside Ar-filled glovebox) by crushing the crystals in a mortar in anhydrous ethanol (resp. DMC) and depositing drops of suspension onto holey carbon grids. Electron diffraction (ED) patterns, high angle annular dark field scanning transmission electron microscopy (HAADF-STEM) and annular bright field STEM (ABF-STEM) images were obtained with an aberration-corrected Titan Themis Z electron microscope operated at 200 kV. These analysis were performed by Artem Abakumov at the Center for Energy Science and Technology of the Skolkovo Institute of Science and Technology (Moscow, Russia).

F) Additional characterizations

F.1 Thermogravimetric analysis

Thermogravimetric analysis (TGA) were performed using a Metler Toledo TGA/DSC 3+ (LF1100°C) under argon atmosphere in order to determine the changes in sample weight with

increasing temperature and to evaluate the decomposition temperature of the different compounds synthesized. For this, a heating ramp from 25°C to 800°C was imposed, with a heating rate of 5°C per minute.

F.2 Mossbauer spectroscopy

Moulay Tahar Sougrati performed Mossbauer experiment in Montpellier at the Institut Charles Gerhardt (ICGM). Room temperature standard and in situ ^{57}Fe Mossbauer analyses were carried out in the transmission geometry in the constant acceleration mode and with a $^{57}\text{Co}(\text{Rh})$ source with an radioactivity of 350 MBq. The velocity scale ($\pm 4 \text{ mm s}^{-1}$) was calibrated at room temperature with $\alpha\text{-Fe}$ foil. Regarding the low amount of iron in the sample, 80 mg of powder were needed to get a good spectrum in 72 hours. During cycling, spectra were collected for 24hrs at selected voltages. The used electrodes contain 30 mg/cm² mixed with 25% of carbon black and 5% of PFTE. The hyperfine parameters IS (isomer shift) and QS (quadrupole splitting) were determined by fitting Lorentzian lines to the experimental data. The in situ cell used was described here.²⁰⁸ Note that the spectra consist of many doublets highlighting the fact that iron environments are not identical as can be expected regarding the distribution of iron's nearest-next neighbors (Fe, Nb, Li). This nearest-next neighbors effect was responsible of the spectra broadening.

F.3 Raman spectroscopy

Raman spectra of the Li_xIrS_2 samples were collected with a Renishaw's InVia Reflex Raman system using a microscope confocal InVia Reflex device. The instrument was equipped with a double edge filter to eliminate the Rayleigh scattering, and with a CCD camera working at a temperature of 220 K with a 1024 X 256 pixels array. Laser excitations were at 488 nm, 514 nm, 633 nm and 785 nm. Only the excitation at 785 nm enabled us to record the spectra of all the samples without destroying them and without making them evolve under a laser. The setup was composed of a confocal microscope that was equipped with an automated XYZ table allowing us to position the capillaries containing the samples away from the environment in the focal plane of the optical microscope. The spectral resolution achieved with the use of gratings of 2400 or 1200 grooves per mm was between 3 and 5 cm^{-1} depending on the excitation wavelength. The focused power of the laser beam on the powders inside the capillaries was also

checked for each wavelength to avoid any transformation or heating of the samples. Accordingly, the surface power density was kept below $15 \mu\text{W} \mu\text{m}^{-2}$ with the magnitudes 50X of the long distance working objective being selected after a series of tests. These measurements were performed and analysed by Bernard Humbert and Jean-Yves Mevellec at the Institut des matériaux Jean Rouxel (IMN, Nantes, France).

F.3 X-ray absorption spectroscopy

Ex situ XAS measurements at the Ir L_3 -edge of Li_xIrS_2 samples were performed in transmission mode at the ROCK beamline²⁰⁹ of synchrotron SOLEIL (France) by Antonella Iadecola. A Si(111) channel-cut quick-XAS monochromatic with an energy resolution of 1.1 eV at 11 keV was used. The intensity of the monochromatic X-ray beam was measured with three consecutive ionization chambers filled with 40 mL of N_2 . A pellet of $\alpha\text{-Li}_2\text{IrO}_3$ was placed between the second and the third ionization chamber to ensure the energy calibration. For each compound, 8 mm diameter pellet was prepared in an Ar-filled glovebox by mixing 5 mg of sample with almost 30 mg of dried cellulose, embedded in kapton tape and sealed in plastic bag to avoid any air exposure during the XAS measurements. The data was treated using the Demeter package for energy calibration and normalization.²¹⁰ The EXAFS oscillations of the Li_xIrS_2 compounds (chapter III) were fitted using the Artemis software. The Fourier transforms of EXAFS oscillations were carried out in k -range from 3.5 \AA^{-1} to 15.9 and the fitting was performed in R -range from 1.0 to 3.9 \AA using k^3 weight. EXAFS amplitudes and phase-shifts were calculated by FEFF7 with a starting model derived from XRD and ND (Table S5). Except the radial distance (R) and the Debye-Waller factor (σ^2), all other parameters were kept constant (N_i , E_0 , S_0^2) in the conventional least squares modelling using the phase and amplitude factors calculated by the FEFF7.

F.3 X-ray photoelectron spectroscopy

X-ray photoemission spectroscopy (XPS) measurements were carried out with a THERMO Escalab spectrometer, using focused monochromatic Al $K\alpha$ radiation ($h\nu = 1486.6 \text{ eV}$) and equipped with an argon-filled glove box allowing to preserve the samples from moisture and air at all times from their preparation to their analysis. Peaks were recorded with constant pass energy of 20 eV. The pressure in the analysis chamber was around 5×10^{-8} mbar. The binding

energy scale was calibrated using the C 1s peak at 285.0 eV from the hydrocarbon contamination present at the samples surface. The spectra were fitted using a minimum number of components. Several spectra were recorded at different times to check that the samples were not subjected to degradation during the X-ray irradiation. These measurements have been performed at the institut des sciences analytiques et de physico-chimie pour l'environnement et les matériaux (IPREM, Pau, France) by Dominique Foix and Rémi Dedryvere.

Glossary

ABF	Annular Bright Field
Ar	Argon
Be	Beryllium
DFT	Density Functional Theory
DMC	Dimethyl Carbonate
DSC	Differential Scanning Calorimetry
EC	Ethylene Carbonate
EDX	Energy-Dispersive X-ray (spectroscopy)
EXAFS	Extended X-ray Absorption Fine Structure
FEG	Field Emission Gun
GITT	Galvanostatic Intermittent Titration Technique
HAADF	High Angle Annular Dark-Field
HOMO	Highest Occupied Molecular Orbital
ICP-MS	Inductively Coupled Plasma Mass Spectrometry
LCO	Lithium Cobalt Oxide (LiCoO ₂)
Li	Lithium
LFP	Lithium ferrophosphate (LiFePO ₄)
LUMO	Mower Unoccupied Molecular Orbital
Na	Sodium
NMC	LiNi _x Mn _y Co _z O ₂
NPD	Neutron Powder Diffraction
OCV	Open Circuit Voltage
SCXRD	Single Crystal X-ray Diffraction
SEM	Scanning Electron Microscopy
Si	Silicon
SiC	Silicon Carbide
SQUID	Superconducting QUantum Interference Device
STEM	Scanning Transmission Electron Microscopy

Glossary

SXRD	Synchrotron X-ray powder Diffraction
TEM	Transmission Electron Microscopy
TGA	Thermogravimetric Analysis
XANES	X-ray Absorption Near Edge Structure
XAS	X-Ray Absorption Spectroscopy
XPS	X-Ray photoelectron Spectroscopy
XRD	X-Ray Diffraction

References

- (1) Pauling, L. The Principles Determining the Structure of Complex Ionic Crystals. *J. Am. Chem. Soc.* **1929**, *51*, 1010–1026. <https://doi.org/10.1021/ja01379a006>.
- (2) Tulsy, E. G.; Long, J. R. Dimensional Reduction: A Practical Formalism for Manipulating Solid Structures. *Chem. Mater.* **2001**, *13* (4), 1149–1166. <https://doi.org/10.1021/cm0007858>.
- (3) Materials, I. L. *Intercalated Layered Materials*; 1979. <https://doi.org/10.1007/978-94-009-9415-7>.
- (4) Rüdorff, W.; Hofmann, U. Über Graphitsalze. *Zeitschrift für Anorg. und Allg. Chemie* **1938**, *238* (1). <https://doi.org/10.1002/zaac.19382380102>.
- (5) Hayward, M. A.; Green, M. A.; Rosseinsky, M. J.; Sloan, J. Sodium Hydride as a Powerful Reducing Agent for Topotactic Oxide Deintercalation: Synthesis and Characterization of the Nickel(I) Oxide LaNiO_2 . *J. Am. Chem. Soc.* **1999**, *121* (38), 8843–8854. <https://doi.org/10.1021/ja991573i>.
- (6) Sasaki, S.; Caldes, M. T.; Guillot-Deudon, C.; Braems, I.; Steciuk, G.; Palatinus, L.; Gautron, E.; Frapper, G.; Janod, E.; Corraze, B.; Jobic, S.; Cario, L. Design of Metastable Oxychalcogenide Phases by Topochemical (de)Intercalation of Sulfur in $\text{La}_2\text{O}_2\text{S}_2$. *Nat. Commun.* **2021**, *12* (1), 1–9. <https://doi.org/10.1038/s41467-021-23677-w>.
- (7) Wang, H.; Yuan, H.; Sae Hong, S.; Li, Y.; Cui, Y. Physical and Chemical Tuning of Two-Dimensional Transition Metal Dichalcogenides. *Chem. Soc. Rev.* **2015**, *44* (9), 2664–2680. <https://doi.org/10.1039/c4cs00287c>.
- (8) Wan, J.; Lacey, S. D.; Dai, J.; Bao, W.; Fuhrer, M. S.; Hu, L. Tuning Two-Dimensional Nanomaterials by Intercalation: Materials, Properties and Applications. *Chem. Soc. Rev.* **2016**, *45* (24), 6742–6765. <https://doi.org/10.1039/c5cs00758e>.
- (9) Berthier, C.; Y, C.; P, S.; Chevalier, P.; Trichet, L.; Le Mehaute, A. Semiconductor-Metal Transition upon Intercalation in Li_xZrSe_2 . *Solid State Ionics* **1981**, *5*, 379–382. [https://doi.org/10.1016/0167-2738\(81\)90272-1](https://doi.org/10.1016/0167-2738(81)90272-1).
- (10) Ahmad, M.; Müller, E.; Habenicht, C.; Schuster, R.; Knupfer, M.; Büchner, B. Semiconductor-to-Metal Transition in the Bulk of WSe_2 upon Potassium Intercalation. *J. Phys. Condens. Matter* **2017**, *29* (16). <https://doi.org/10.1088/1361-648X/aa63a7>.
- (11) Morosan, E.; Zandbergen, H. W.; Dennis, B. S.; Bos, J. W. G.; Onose, Y.; Klimczuk, T.; Ramirez, A. P.; Ong, N. P.; Cava, R. J. Superconductivity in Cu_xTiSe_2 . *Nat. Phys.* **2006**, *2* (8), 544–550. <https://doi.org/10.1038/nphys360>.
- (12) Guo, J.; Jin, S.; Wang, G.; Wang, S.; Zhu, K.; Zhou, T.; He, M.; Chen, X. Superconductivity in the Iron Selenide $\text{K}_x\text{Fe}_2\text{Se}_2$ ($0 \leq x \leq 1.0$). *Phys. Rev. B - Condens. Matter Mater. Phys.* **2010**, *82* (18), 3–6. <https://doi.org/10.1103/PhysRevB.82.180520>.
- (13) Kriener, M.; Segawa, K.; Ren, Z.; Sasaki, S.; Wada, S.; Kuwabata, S.; Ando, Y. Electrochemical Synthesis and Superconducting Phase Diagram of $\text{Cu}_x\text{Bi}_2\text{Se}_3$. *Phys. Rev. B - Condens. Matter Mater. Phys.* **2011**, *84* (5), 1–5. <https://doi.org/10.1103/PhysRevB.84.054513>.
- (14) Yao, J.; Koski, K. J.; Luo, W.; Cha, J. J.; Hu, L.; Kong, D.; Narasimhan, V. K.; Huo, K.; Cui, Y. Optical Transmission Enhancement through Chemically Tuned Two-Dimensional Bismuth Chalcogenide Nanoplates. *Nat. Commun.* **2014**, *5*, 1–7. <https://doi.org/10.1038/ncomms6670>.

References

- (15) Nah, Y. C.; Ghicov, A.; Kim, D.; Schmuki, P. Enhanced Electrochromic Properties of Self-Organized Nanoporous WO_3 . *Electrochem. commun.* **2008**, *10* (11), 1777–1780. <https://doi.org/10.1016/j.elecom.2008.09.017>.
- (16) Rouse, G.; Rodriguez-Carvajal, J.; Patoux, S.; Masquelier, C. Magnetic Structures of the Triphylite LiFePO_4 and of Its Delithiated Form FePO_4 . *Chem. Mater.* **2003**, *15* (21), 4082–4090. <https://doi.org/10.1021/cm0300462>.
- (17) Di Salvo, F. J.; Hull, G. W.; Schwartz, L. H.; Voorhoeve, J. M.; Waszczak, J. V. Metal Intercalation Compounds of TaS_2 : Preparation and Properties. **1973**, *1922* (59). <https://doi.org/10.1063/1.1680277>.
- (18) Wan, C.; Gu, X.; Dang, F.; Itoh, T.; Wang, Y.; Sasaki, H.; Kondo, M.; Koga, K.; Yabuki, K.; Snyder, G. J.; Yang, R.; Koumoto, K. Flexible N-Type Thermoelectric Materials by Organic Intercalation of Layered Transition Metal Dichalcogenide TiS_2 . *Nat. Mater.* **2015**, *14* (6), 622–627. <https://doi.org/10.1038/nmat4251>.
- (19) Reddy, M. V.; Mauger, A.; Julien, C. M.; Paoletta, A.; Zaghbi, K. Brief History of Early Lithium-Battery Development. *Materials (Basel)*. **2020**, *13* (8), 1–9. <https://doi.org/10.3390/MA13081884>.
- (20) Armand, J.-M. T. & M. Issues and Challenges Facing Rechargeable Lithium Batteries. *Nature* **2001**, *414* (November), 359–367. <https://doi.org/10.1038/35104644>.
- (21) Rouxel, J.; Danot, M.; Bichon, M. Les Composites Intercalaires de Na_xTiS_2 . Etude Générale Des Phases Na_xTiS_2 et K_xTiS_2 . *Bull. Soc. Chim* **1971**, *11*, 3930–3936.
- (22) Whittingham, M. S. Electrical Energy Storage and Intercalation Chemistry. *Science (80-.)*. **1976**, *192* (4244), 1126–1127. <https://doi.org/10.1088/1751-8113/44/8/085201>.
- (23) Lazzari, M.; Scrosati, B. A Cyclable Lithium Organic Electrolyte Cell Based on Two Intercalation Electrodes. *J. Electrochem. Soc.* **1980**, *127* (3), 773–774. <https://doi.org/10.1149/1.2129753>.
- (24) Yazami, R.; Touzain, P. A Reversible Graphite-Lithium Negative Electrode for Electrochemical Generators. *J. Power Sources* **1983**, *9* (3), 365–371. [https://doi.org/10.1016/0378-7753\(83\)87040-2](https://doi.org/10.1016/0378-7753(83)87040-2).
- (25) Ruysink, A. F. J.; Kadijk, F.; Wagner, A. J.; Jellinek, F. Preparation, Structure and Properties of Triniobium Tetrasulphide, Nb_3S_4 . *Acta Crystallogr. Sect. B Struct. Crystallogr. Cryst. Chem.* **1968**, *24* (12), 1614–1619. <https://doi.org/10.1107/s0567740868004723>.
- (26) Andersson, A. S.; Kalska, B.; Häggström, L.; Thomas, J. O. Lithium Extraction/Insertion in LiFePO_4 : An X-Ray Diffraction and Moessbauer Spectroscopy Study. *Solid State Ionics* **2000**, *130* (1), 41–52. [https://doi.org/10.1016/S0167-2738\(00\)00311-8](https://doi.org/10.1016/S0167-2738(00)00311-8).
- (27) Chianelli, R. ; Scanlon, J. C.; Thompson, A. H. Structure Refinement of Stoichiometric TiS_2 . *Mater. Res. Bull.* **1975**, *10*, 1379–1382.
- (28) Hahn, V.; Harder, B. On the Crystal Structure of Titanium Sulfides. *Zeitschrift für Anorg. und allgemeine Chemie* **1956**, *288* (1928), 241–348.
- (29) Alexander, A.; Battle, P. D.; Burley, J. C.; Gallon, D. J.; Grey, P.; Kim, S. H. Structural and Magnetic Properties of Li_3RuO_4 . **2003**, 0–4. <https://doi.org/10.1039/b305220f>.
- (30) Jacquet, Q.; Perez, A.; Batuk, D.; Van Tendeloo, G.; Rouse, G.; Tarascon, J.-M. The $\text{Li}_3\text{Ru}_y\text{Nb}_{1-y}\text{O}_4$ ($0 \leq y \leq 1$) System: Structural Diversity and Li Insertion and Extraction Capabilities. *Chem. Mater.* **2017**, *29* (12), 5331–5343. <https://doi.org/10.1021/acs.chemmater.7b01511>.
- (31) Manthiram, A. A Reflection on Lithium-Ion Battery Cathode Chemistry. *Nat. Commun.* **2020**, *11* (1), 1–

9. <https://doi.org/10.1038/s41467-020-15355-0>.
- (32) Jacquet, Q.; Iadecola, A.; Saubanère, M.; Lemarquais, L.; Berg, E. J.; Alves Dalla Corte, D.; Rouse, G.; Doublet, M. L.; Tarascon, J. M. Competition between Metal Dissolution and Gas Release in Li-Rich $\text{Li}_3\text{Ru}_y\text{Ir}_{1-y}\text{O}_4$ Model Compounds Showing Anionic Redox. *Chem. Mater.* **2018**, *30* (21), 7682–7690. <https://doi.org/10.1021/acs.chemmater.8b02955>.
- (33) Mendiboure, A.; Delmas, C.; Hagemuller, P. Electrochemical Intercalation and Deintercalation of Na_xMnO_2 Bronzes. *J. Solid State Chem.* **1985**, *57* (3), 323–331. [https://doi.org/10.1016/0022-4596\(85\)90194-X](https://doi.org/10.1016/0022-4596(85)90194-X).
- (34) Thackeray, M. M.; Johnson, P. J.; de Picciotto, L. A.; Bruce, P. G.; Goodenough, J. B. Electrochemical Extraction of Lithium from LiMn_2O_4 . *Mater. Res. Bull.* **1984**, *19* (2), 179–187. [https://doi.org/10.1016/0025-5408\(84\)90088-6](https://doi.org/10.1016/0025-5408(84)90088-6).
- (35) Huang, Y.; Dong, Y.; Li, S.; Lee, J.; Wang, C.; Zhu, Z.; Xue, W.; Li, Y.; Li, J. Lithium Manganese Spinel Cathodes for Lithium-Ion Batteries. *Adv. Energy Mater.* **2021**, *11* (2), 1–21. <https://doi.org/10.1002/aenm.202000997>.
- (36) Clément, R. J.; Lun, Z.; Ceder, G. Cation-Disordered Rocksalt Transition Metal Oxides and Oxyfluorides for High Energy Lithium-Ion Cathodes. *Energy Environ. Sci.* **2020**, *13* (2), 345–373. <https://doi.org/10.1039/c9ee02803j>.
- (37) Ji, H.; Urban, A.; Kitchaev, D. A.; Kwon, D. H.; Artrith, N.; Ophus, C.; Huang, W.; Cai, Z.; Shi, T.; Kim, J. C.; Kim, H.; Ceder, G. Hidden Structural and Chemical Order Controls Lithium Transport in Cation-Disordered Oxides for Rechargeable Batteries. *Nat. Commun.* **2019**, *10* (1). <https://doi.org/10.1038/s41467-019-08490-w>.
- (38) Reynaud, M.; Rouse, G.; Chotard, J. N.; Rodríguez-Carvajal, J.; Tarascon, J. M. Marinite $\text{Li}_2\text{M}(\text{SO}_4)_2$ (M = Co, Fe, Mn) and $\text{Li}_1\text{Fe}(\text{SO}_4)_2$: Model Compounds for Super-Super-Exchange Magnetic Interactions. *Inorg. Chem.* **2013**, *52* (18), 10456–10466. <https://doi.org/10.1021/ic401280e>.
- (39) Melot, B. C.; Rouse, G.; Chotard, J. N.; Ati, M.; Rodríguez-Carvajal, J.; Kemei, M. C.; Tarascon, J. M. Magnetic Structure and Properties of the Li-Ion Battery Materials FeSO_4F and LiFeSO_4F . *Chem. Mater.* **2011**, *23* (11), 2922–2930. <https://doi.org/10.1021/cm200465u>.
- (40) Nytén, A.; Abouimrane, A.; Armand, M.; Gustafsson, T.; Thomas, J. O. Electrochemical Performance of $\text{Li}_2\text{FeSiO}_4$ as a New Li-Battery Cathode Material. *Electrochem. commun.* **2005**, *7* (2), 156–160. <https://doi.org/10.1016/j.elecom.2004.11.008>.
- (41) Legagneur, V.; An, Y.; Mosbah, A.; Portal, R.; Le Gal La Salle, A.; Verbaere, A.; Guyomard, D.; Piffard, Y. LiMBO_3 (M = Mn, Fe, Co): Synthesis, Crystal Structure and Lithium Deinsertion/Insertion Properties. *Solid State Ionics* **2001**, *139* (1–2), 37–46. [https://doi.org/10.1016/S0167-2738\(00\)00813-4](https://doi.org/10.1016/S0167-2738(00)00813-4).
- (42) Rouse, G.; Rodríguez-Carvajal, J.; Wurm, C.; Masquelier, C. A Neutron Diffraction Study of the Antiferromagnetic Diphosphate LiFeP_2O_7 . *Solid State Sci.* **2002**, *4* (7), 973–978. [https://doi.org/10.1016/S1293-2558\(02\)01347-X](https://doi.org/10.1016/S1293-2558(02)01347-X).
- (43) Ellis, B. L.; Ramesh, T. N.; Davis, L. J. M.; Goward, G. R.; Nazar, L. F. Structure and Electrochemistry of Two-Electron Redox Couples in Lithium Metal Fluorophosphates Based on the Tavorite Structure. *Chem. Mater.* **2011**, *23* (23), 5138–5148. <https://doi.org/10.1021/cm201773n>.
- (44) Padhi, A. K.; Nanjundaswamy, K. S.; Goodenough, J. B. Phospho-olivines as Positive-Electrode Materials

References

- for Rechargeable Lithium Batteries. *J. Electrochem. Soc.* **1997**, *144* (4), 1188–1194.
- (45) Gong, Z.; Yang, Y. Recent Advances in the Research of Polyanion-Type Cathode Materials for Li-Ion Batteries. *Energy Environ. Sci.* **2011**, *4* (9), 3223–3242. <https://doi.org/10.1039/c0ee00713g>.
- (46) Rouse, G.; Tarascon, J. M. Sulfate-Based Polyanionic Compounds for Li-Ion Batteries: Synthesis, Crystal Chemistry, and Electrochemistry Aspects. *Chem. Mater.* **2014**, *26* (1), 394–406. <https://doi.org/10.1021/cm4022358>.
- (47) Lander, L.; Tarascon, J.; Yamada, A. Sulfate-Based Cathode Materials for Li- and Na-Ion Batteries. 1–40. <https://doi.org/10.1002/tcr.201800071>.
- (48) Mariyappan, S.; Wang, Q.; Tarascon, J. M. Will Sodium Layered Oxides Ever Be Competitive for Sodium Ion Battery Applications? *J. Electrochem. Soc.* **2018**, *165* (16), A3714–A3722. <https://doi.org/10.1149/2.0201816jes>.
- (49) Aydinol, M.; Kohan, A.; Ceder, G.; Cho, K.; Joannopoulos, J. Ab Initio Study of Lithium Intercalation in Metal Oxides and Metal Dichalcogenides. *Phys. Rev. B - Condens. Matter Mater. Phys.* **1997**, *56* (3), 1354–1365. <https://doi.org/10.1103/PhysRevB.56.1354>.
- (50) McKinnon, W. R.; Haering, R. R. *Physical Mechanisms of Intercalation.*; 1983. https://doi.org/10.1007/978-1-4615-7461-3_4.
- (51) Saubanère, M.; Yahia, M. Ben; Lebègue, S.; Doublet, M. L. An Intuitive and Efficient Method for Cell Voltage Prediction of Lithium and Sodium-Ion Batteries. *Nat. Commun.* **2014**, *5*, 1–7. <https://doi.org/10.1038/ncomms6559>.
- (52) Hoffmann, R. How Chemistry and Physics Meet in the Solid State. *Angew. Chemie Int. Ed. English* **1987**, *26* (9), 846–878. <https://doi.org/10.1002/anie.198708461>.
- (53) Okada, S.; Sawa, S.; Egashira, M.; Yamaki, J. I.; Tabuchi, M.; Kageyama, H.; Konishi, T.; Yoshino, A. Cathode Properties of Phospho-Olivine LiMPO_4 for Lithium Secondary Batteries. In *Journal of Power Sources*; 2001; Vol. 97–98, pp 430–432. [https://doi.org/10.1016/S0378-7753\(01\)00631-0](https://doi.org/10.1016/S0378-7753(01)00631-0).
- (54) Li, G.; Azuma, H.; Tohda, M. LiMnPO_4 as the Cathode for Lithium Batteries. *J. Electrochem. Soc.* **2002**, 136–138. <https://doi.org/10.1149/1.1475195>.
- (55) Wolfenstine, J.; Allen, J. $\text{Ni}^{3+}/\text{Ni}^{2+}$ Redox Potential in LiNiPO_4 . *J. Power Sources* **2005**, *142*, 389–390. <https://doi.org/10.1016/j.jpowsour.2004.11.024>.
- (56) Mizushima, K.; Jones, P. C.; Wiseman, P. J.; Goodenough, J. B. Li_xCoO_2 ($0 < x < 1$): A New Cathode Material for Batteries of High Energy Density. *Solid State Ionics* **1981**, *4*, 171–174. [https://doi.org/10.1016/0025-5408\(80\)90012-4](https://doi.org/10.1016/0025-5408(80)90012-4).
- (57) Lander, L.; Reynaud, M.; Rouse, G.; Sougrati, M. T.; Laberty-Robert, C.; Messinger, R. J.; Deschamps, M.; Tarascon, J. M. Synthesis and Electrochemical Performance of the Orthorhombic $\text{Li}_2\text{Fe}(\text{SO}_4)_2$ Polymorph for Li-Ion Batteries. *Chem. Mater.* **2014**, *26* (14), 4178–4189. <https://doi.org/10.1021/cm5012845>.
- (58) Ohzuku, T.; Kitagawa, M.; Hirai, T. Electrochemistry of Manganese Dioxide in Lithium Nonaqueous Cell: I. X-Ray Diffractational Study on the Reduction of Electrolytic Manganese Dioxide. *J. Electrochem. Soc.* **1989**, *136* (11), 3169–3174. <https://doi.org/10.1149/1.2096421>.
- (59) Xu, K. Nonaqueous Liquid Electrolytes for Lithium-Based Rechargeable Batteries. **2004**.
- (60) Yabuuchi, N.; Ohzuku, T. Novel Lithium Insertion Material of $\text{LiCo}_{1/3}\text{Ni}_{1/3}\text{Mn}_{1/3}\text{O}_2$ for Advanced Lithium-

- Ion Batteries. *J. Power Sources* **2003**, *119–121*, 171–174. [https://doi.org/10.1016/S0378-7753\(03\)00173-3](https://doi.org/10.1016/S0378-7753(03)00173-3).
- (61) Wu, S.-L.; Zhang, W.; Song, X.; Shukla, A. K.; Liu, G.; Battaglia, V.; Srinivasan, V. High Rate Capability of $\text{Li}(\text{Ni}_{1/3}\text{Mn}_{1/3}\text{Co}_{1/3})\text{O}_2$ Electrode for Li-Ion Batteries. *J. Electrochem. Soc.* **2012**, *159* (4), A438–A444. <https://doi.org/10.1149/2.062204jes>.
- (62) Dou, S. Review and Prospect of Layered Lithium Nickel Manganese Oxide as Cathode Materials for Li-Ion Batteries. *J. Solid State Electrochem.* **2013**, *17* (4), 911–926. <https://doi.org/10.1007/s10008-012-1977-z>.
- (63) Lu, Z.; Dahn, J. R. Understanding the Anomalous Capacity of $\text{Li}/\text{Li}[\text{Ni}_x\text{Li}_{(1/3-2x/3)}\text{Mn}_{(2/3-x/3)}]\text{O}_2$ Cells Using In Situ X-Ray Diffraction and Electrochemical Studies. *J. Electrochem. Soc.* **2002**, *149* (7), A815. <https://doi.org/10.1149/1.1480014>.
- (64) Perez, A. J.; Jacquet, Q.; Batuk, D.; Iadecola, A.; Saubanère, M.; Rousse, G.; Larcher, D.; Vezin, H.; Doublet, M. L.; Tarascon, J. M. Approaching the Limits of Cationic and Anionic Electrochemical Activity with the Li-Rich Layered Rocksalt Li_3IrO_4 . *Nat. Energy* **2017**, *2* (12), 954–962. <https://doi.org/10.1038/s41560-017-0042-7>.
- (65) Kalyani, P.; Chitra, S.; Mohan, T.; Gopukumar, S. Lithium Metal Rechargeable Cells Using Li_2MnO_3 as the Positive Electrode. *J. Power Sources* **1999**, *80* (1–2), 103–106. [https://doi.org/10.1016/S0378-7753\(99\)00066-X](https://doi.org/10.1016/S0378-7753(99)00066-X).
- (66) James, A. C. W. P.; Goodenough, J. B. Structure and Bonding in Li_2MoO_3 and $\text{Li}_{2-x}\text{MoO}_3$ ($0 \leq x \leq 1.7$). *J. Solid State Chem.* **1988**, *76* (1), 87–96. [https://doi.org/10.1016/0022-4596\(88\)90194-6](https://doi.org/10.1016/0022-4596(88)90194-6).
- (67) James, A. C. W. P.; Goodenough, J. B. Structure and Bonding in Lithium Ruthenate, Li_2RuO_3 . *J. Solid State Chem.* **1988**, *74* (2), 287–294. [https://doi.org/10.1016/0022-4596\(88\)90357-X](https://doi.org/10.1016/0022-4596(88)90357-X).
- (68) Assat, G.; Foix, D.; Delacourt, C.; Iadecola, A.; Dedryvère, R.; Tarascon, J. Of Lithium-Rich Cathodes. *Nat. Commun.* <https://doi.org/10.1038/s41467-017-02291-9>.
- (69) Assat, G.; Tarascon, J. M. Fundamental Understanding and Practical Challenges of Anionic Redox Activity in Li-Ion Batteries. *Nat. Energy* **2018**, *3* (5), 373–386. <https://doi.org/10.1038/s41560-018-0097-0>.
- (70) Johnson, C. S.; Li, N.; Vaughey, J. T.; Hackney, S. A.; Thackeray, M. M. Lithium-Manganese Oxide Electrodes with Layered-Spinel Composite Structures $x\text{Li}_2\text{MnO}_3 \cdot (1-x)\text{Li}_{1+y}\text{Mn}_{2-y}\text{O}_4$ ($0 < x < 1$, $0 \leq y \leq 0.33$) for Lithium Batteries. *Electrochem. commun.* **2005**, *7* (5), 528–536. <https://doi.org/10.1016/j.elecom.2005.02.027>.
- (71) Armstrong, A. R.; Holzapfel, M.; Novák, P.; Johnson, C. S.; Kang, S. H.; Thackeray, M. M.; Bruce, P. G. Demonstrating Oxygen Loss and Associated Structural Reorganization in the Lithium Battery Cathode $\text{Li}[\text{Ni}_{0.2}\text{Li}_{0.2}\text{Mn}_{0.6}]\text{O}_2$. *J. Am. Chem. Soc.* **2006**, *128* (26), 8694–8698. <https://doi.org/10.1021/ja062027+>.
- (72) Koga, H.; Croguennec, L.; Ménétrier, M.; Douhil, K.; Belin, S.; Bourgeois, L.; Suard, E.; Weill, F.; Delmas, C. Reversible Oxygen Participation to the Redox Processes Revealed for $\text{Li}_{1.20}\text{Mn}_{0.54}\text{Co}_{0.13}\text{Ni}_{0.13}\text{O}_2$. *J. Electrochem. Soc.* **2013**, *160* (6), A786–A792. <https://doi.org/10.1149/2.038306jes>.
- (73) Tarascon, J. M.; Disalvo, F. J.; Eibschutz, M.; Murphy, D. W.; Waszczak, J. V. Preparation and Chemical and Physical Properties of the New Layered Phases $\text{Li}_x\text{Ti}_{1-y}\text{M}_y\text{S}_2$ with $\text{M}=\text{V}, \text{Cr}$ or Fe . *Phys. Rev. B* **1983**,

References

- 28 (11), 6397–6406. <https://doi.org/10.1103/PhysRevB.28.6397>.
- (74) Tarascon, J. M.; Vaughan, G.; Chabre, Y.; Seguin, L.; Anne, M.; Strobel, P.; Amatucci, G. In Situ Structural and Electrochemical Study of $\text{Ni}_{1-x}\text{Co}_x\text{O}_2$ Metastable Oxides Prepared by Soft Chemistry. *J. Solid State Chem.* **1999**, *147* (1), 410–420. <https://doi.org/10.1006/jssc.1999.8465>.
- (75) Sathiya, M.; Rouse, G.; Ramesha, K.; Laisa, C. P.; Vezin, H.; Sougrati, M. T.; Doublet, M.; Foix, D.; Gonbeau, D.; Walker, W.; Prakash, A. S.; Hassine, M. Ben; Dupont, L. High-Capacity Layered-Oxide Electrodes. *Nat. Mater.* **2013**, *12* (7), 1–9. <https://doi.org/10.1038/nmat3699>.
- (76) Li, B.; Shao, R.; Yan, H.; An, L.; Zhang, B.; Wei, H.; Ma, J.; Xia, D.; Han, X. Understanding the Stability for Li-Rich Layered Oxide Li_2RuO_3 Cathode. *Adv. Funct. Mater.* **2016**, *26* (9), 1330–1337. <https://doi.org/10.1002/adfm.201504836>.
- (77) McCalla, E.; Abakumov, A. M.; Saubanère, M.; Foix, D.; Berg, E. J.; Rouse, G.; Doublet, M. L.; Gonbeau, D.; Novák, P.; Van Tendeloo, G.; Dominko, R.; Tarascon, J. M. Visualization of O-O Peroxo-like Dimers in High-Capacity Layered Oxides for Li-Ion Batteries. *Science* (80-.). **2015**, *350* (6267), 1516–1521. <https://doi.org/10.1126/science.aac8260>.
- (78) Pearce, P. E.; Perez, A. J.; Rouse, G.; Saubanère, M.; Batuk, D.; Foix, D.; McCalla, E.; Abakumov, A. M.; Van Tendeloo, G.; Doublet, M. L.; Tarascon, J. M. Evidence for Anionic Redox Activity in a Tridimensional-Ordered Li-Rich Positive Electrode $\beta\text{-Li}_2\text{IrO}_3$. *Nat. Mater.* **2017**, *16* (5), 580–586. <https://doi.org/10.1038/nmat4864>.
- (79) Li, B.; Jiang, N.; Huang, W.; Yan, H.; Zuo, Y.; Xia, D. Thermodynamic Activation of Charge Transfer in Anionic Redox Process for Li-Ion Batteries. *Adv. Funct. Mater.* **2018**, *28* (4), 1–11. <https://doi.org/10.1002/adfm.201704864>.
- (80) Flamary-Mespoulie, F.; Boulineau, A.; Martinez, H.; Suchomel, M. R.; Delmas, C.; Pecquenard, B.; Le Cras, F. Lithium-Rich Layered Titanium Sulfides: Cobalt- and Nickel-Free High Capacity Cathode Materials for Lithium-Ion Batteries. *Energy Storage Mater.* **2020**, *26*, 213–222. <https://doi.org/10.1016/j.ensm.2019.12.033>.
- (81) Saha, S.; Assat, G.; Sougrati, M. T.; Foix, D.; Li, H.; Vergnet, J.; Turi, S.; Ha, Y.; Yang, W.; Cabana, J.; Rouse, G.; Abakumov, A. M.; Tarascon, J. M. Exploring the Bottlenecks of Anionic Redox in Li-Rich Layered Sulfides. *Nat. Energy* **2019**, *4* (11), 977–987. <https://doi.org/10.1038/s41560-019-0493-0>.
- (82) Assat, G.; Iadecola, A.; Delacourt, C.; Dedryvère, R.; Tarascon, J. M. Decoupling Cationic-Anionic Redox Processes in a Model Li-Rich Cathode via Operando X-Ray Absorption Spectroscopy. *Chem. Mater.* **2017**, *29* (22), 9714–9724. <https://doi.org/10.1021/acs.chemmater.7b03434>.
- (83) Taylor, Z. N.; Perez, A. J.; Coca-Clemente, J. A.; Braga, F.; Drewett, N. E.; Pitcher, M. J.; Thomas, W. J.; Dyer, M. S.; Collins, C.; Zanella, M.; Johnson, T.; Day, S.; Tang, C.; Dhanak, V. R.; Claridge, J. B.; Hardwick, L. J.; Rosseinsky, M. J. Stabilization of O-O Bonds by d^0 Cations in $\text{Li}_{4+x}\text{Ni}_{1-x}\text{WO}_6$ ($0 \leq x \leq 0.25$) Rock Salt Oxides as the Origin of Large Voltage Hysteresis. *J. Am. Chem. Soc.* **2019**, *141* (18), 7333–7346. <https://doi.org/10.1021/jacs.8b13633>.
- (84) Gent, W. E.; Lim, K.; Liang, Y.; Li, Q.; Barnes, T.; Ahn, S. J.; Stone, K. H.; McIntire, M.; Hong, J.; Song, J. H.; Li, Y.; Mehta, A.; Ermon, S.; Tylliszczak, T.; Kilcoyne, D.; Vine, D.; Park, J. H.; Doo, S. K.; Toney, M. F.; Yang, W.; Prendergast, D.; Chueh, W. C. Coupling between Oxygen Redox and Cation Migration Explains Unusual Electrochemistry in Lithium-Rich Layered Oxides. *Nat. Commun.* **2017**, *8* (1).

- <https://doi.org/10.1038/s41467-017-02041-x>.
- (85) Saubanère, M.; McCalla, E.; Tarascon, J. M.; Doublet, M. L. The Intriguing Question of Anionic Redox in High-Energy Density Cathodes for Li-Ion Batteries. *Energy Environ. Sci.* **2016**, *9* (3), 984–991. <https://doi.org/10.1039/c5ee03048j>.
- (86) Hong, J.; Gent, W. E.; Xiao, P.; Lim, K.; Seo, D.; Wu, J.; Csernica, P. M.; Takacs, C. J.; Nordlund, D.; Sun, C.; Stone, K. H.; Passarello, D.; Yang, W.; Prendergast, D.; Ceder, G.; Toney, M. F.; Chueh, W. C. Metal–Oxygen Decoordination Stabilizes Anion Redox in Li-Rich Oxides. *Nat. Mater.* **2019**, *18* (3), 256–265. <https://doi.org/10.1038/s41563-018-0276-1>.
- (87) Yabuuchi, N.; Nakayama, M.; Takeuchi, M.; Komaba, S.; Hashimoto, Y.; Mukai, T.; Shiiba, H.; Sato, K.; Kobayashi, Y.; Nakao, A.; Yonemura, M.; Yamanaka, K.; Mitsuhara, K.; Ohta, T. Origin of Stabilization and Destabilization in Solid-State Redox Reaction of Oxide Ions for Lithium-Ion Batteries. *Nat. Commun.* **2016**, *7* (May), 1–10. <https://doi.org/10.1038/ncomms13814>.
- (88) Luo, K.; Roberts, M. R.; Hao, R.; Guerrini, N.; Pickup, D. M.; Liu, Y.; Edström, K.; Guo, J.; Chadwick, A. V.; Duda, L. C.; Bruce, P. G. Generation of Localized Electron Holes on Oxygen. *Nat. Chem.* **2016**, *8* (7), 684–691. <https://doi.org/10.1038/nchem.2471>.
- (89) House, R. A.; Maitra, U.; Pérez-Osorio, M. A.; Lozano, J. G.; Jin, L.; Somerville, J. W.; Duda, L. C.; Nag, A.; Walters, A.; Zhou, K. J.; Roberts, M. R.; Bruce, P. G. Superstructure Control of First-Cycle Voltage Hysteresis in Oxygen-Redox Cathodes. *Nature* **2020**, *577* (7791), 502–508. <https://doi.org/10.1038/s41586-019-1854-3>.
- (90) Grimaud, A.; Hong, W. T.; Shao-Horn, Y.; Tarascon, J. M. Anionic Redox Processes for Electrochemical Devices. *Nat. Mater.* **2016**, *15* (2), 121–126. <https://doi.org/10.1038/nmat4551>.
- (91) Seo, D. H.; Lee, J.; Urban, A.; Malik, R.; Kang, S.; Ceder, G. The Structural and Chemical Origin of the Oxygen Redox Activity in Layered and Cation-Disordered Li-Excess Cathode Materials. *Nat. Chem.* **2016**, *8* (7), 692–697. <https://doi.org/10.1038/nchem.2524>.
- (92) Ben Yahia, M.; Vergnet, J.; Saubanère, M.; Doublet, M. L. Unified Picture of Anionic Redox in Li/Na-Ion Batteries. *Nat. Mater.* **2019**, *18* (5), 496–502. <https://doi.org/10.1038/s41563-019-0318-3>.
- (93) Radin, M. D.; Vinckeviciute, J.; Seshadri, R.; Van der Ven, A. Manganese Oxidation as the Origin of the Anomalous Capacity of Mn-Containing Li-Excess Cathode Materials. *Nat. Energy* **2019**, *4* (8), 639–646. <https://doi.org/10.1038/s41560-019-0439-6>.
- (94) Gent, W. E.; Abate, I. I.; Yang, W.; Nazar, L. F.; Chueh, W. C. Li Perspective Design Rules for High-Valent Redox in Intercalation Electrodes. *Joule* **2020**, 1–29. <https://doi.org/10.1016/j.joule.2020.05.004>.
- (95) Komaba, S.; Takei, C.; Nakayama, T.; Ogata, A.; Yabuuchi, N. Electrochemical Intercalation Activity of Layered NaCrO₂ vs. LiCrO₂. *Electrochem. commun.* **2010**, *12* (3), 355–358. <https://doi.org/10.1016/j.elecom.2009.12.033>.
- (96) Lyu, Y.; Ben, L.; Sun, Y.; Tang, D.; Xu, K.; Gu, L.; Xiao, R.; Li, H.; Chen, L.; Huang, X. Atomic Insight into Electrochemical Inactivity of Lithium Chromate (LiCrO₂): Irreversible Migration of Chromium into Lithium Layers in Surface Regions. *J. Power Sources* **2015**, *273*, 1218–1225. <https://doi.org/10.1016/j.jpowsour.2014.09.082>.
- (97) Assat, G.; Glazier, S. L.; Delacourt, C.; Tarascon, J.-M. Probing the Thermal Effects of Voltage Hysteresis in Anionic Redox-Based Lithium-Rich Cathodes Using Isothermal Calorimetry. *Nat. Energy* **2019**.

References

- <https://doi.org/10.1038/s41560-019-0410-6>.
- (98) Koper, M. T. M. Theory of Multiple Proton-Electron Transfer Reactions and Its Implications for Electrocatalysis. *Chem. Sci.* **2013**, *4* (7), 2710–2723. <https://doi.org/10.1039/c3sc50205h>.
- (99) Sano, M.; Taube, H. “Molecular Hysteresis” in an Electrochemical System Revisited. *Inorg. Chem.* **1994**, *33* (4), 705–709. <https://doi.org/10.1021/ic00082a014>.
- (100) Tsuchimoto, A.; Shi, X. M.; Kawai, K.; Mortemard de Boisse, B.; Kikkawa, J.; Asakura, D.; Okubo, M.; Yamada, A. Nonpolarizing Oxygen-Redox Capacity without O-O Dimerization in Na₂Mn₃O₇. *Nat. Commun.* **2021**, *12* (1), 1–7. <https://doi.org/10.1038/s41467-020-20643-w>.
- (101) Kitchaev, D. A.; Vinckeviciute, J.; Van Der Ven, A. Delocalized Metal-Oxygen π -Redox Is the Origin of Anomalous Nonhysteretic Capacity in Li-Ion and Na-Ion Cathode Materials. *J. Am. Chem. Soc.* **2021**, *143* (4), 1908–1916. <https://doi.org/10.1021/jacs.0c10704>.
- (102) Gamble, F. R.; Disalvo, F. J.; Klemm, R. A.; Geballe, T. H. Superconductivity in Layered Structure Organometallic Crystals. *Science* (80-.). **1970**, *168*, 568–570. <https://doi.org/10.1126/science.168.3931.568>.
- (103) Jolivet J-P., Henry M., Livage J., and B. E. Metal Oxide Chemistry and Synthesis. 2000, p 318.
- (104) Ranade, M. R.; Navrotsky, A.; Zhang, H. Z.; Banfield, J. F.; Elder, S. H.; Zaban, A.; Borse, P. H.; Kulkarni, S. K.; Doran, G. S.; Whitfield, H. J. Energetics of Nanocrystalline TiO₂. *Proc. Natl. Acad. Sci.* **2002**, *99* (Supplement 2), 6476–6481. <https://doi.org/10.1073/pnas.251534898>.
- (105) Kitchaev, D. A.; Ceder, G. Evaluating Structure Selection in the Hydrothermal Growth of FeS₂ Pyrite and Marcasite. *Nat. Commun.* **2016**, *7*, 1–7. <https://doi.org/10.1038/ncomms13799>.
- (106) Sathiya, M.; Rouse, G.; Ramesha, K.; Laisa, C. P.; Vezin, H.; Sougrati, M. T.; Doublet, M. L.; Foix, D.; Gonbeau, D.; Walker, W.; Prakash, A. S.; Ben Hassine, M.; Dupont, L.; Tarascon, J. M. Reversible Anionic Redox Chemistry in High-Capacity Layered-Oxide Electrodes. *Nat. Mater.* **2013**, *12* (9), 827–835. <https://doi.org/10.1038/nmat3699>.
- (107) Sathiya, M.; Abakumov, A. M.; Foix, D.; Rouse, G.; Ramesha, K.; Saubanère, M.; Doublet, M. L.; Vezin, H.; Laisa, C. P.; Prakash, A. S.; Gonbeau, D.; Vantendloo, G.; Tarascon, J. M. Origin of Voltage Decay in High-Capacity Layered Oxide Electrodes. *Nat. Mater.* **2015**, *14* (2), 230–238. <https://doi.org/10.1038/nmat4137>.
- (108) Sathiya, M.; Ramesha, K.; Rouse, G.; Foix, D.; Gonbeau, D.; Prakash, A. S.; Doublet, M. L.; Hemalatha, K.; Tarascon, J. M. High Performance Li₂Ru_{1-y}Mn_yO₃ (0.2 ≤ y ≤ 0.8) Cathode Materials for Rechargeable Lithium-Ion Batteries: Their Understanding. *Chem. Mater.* **2013**, *25* (7), 1121–1131. <https://doi.org/10.1021/cm400193m>.
- (109) Jacquet, Q.; Perez, A.; Batuk, D.; Van Tendeloo, G.; Rouse, G.; Tarascon, J. M. The Li₃Ru_yNb_{1-y}O₄ (0 ≤ y ≤ 1) System: Structural Diversity and Li Insertion and Extraction Capabilities. *Chem. Mater.* **2017**, *29* (12), 5331–5343. <https://doi.org/10.1021/acs.chemmater.7b01511>.
- (110) Jacquet, Q.; Rouse, G.; Iadecola, A.; Saubanère, M.; Doublet, M. L.; Tarascon, J. M. Electrostatic Interactions versus Second Order Jahn-Teller Distortion as the Source of Structural Diversity in Li₃MO₄ Compounds (M = Ru, Nb, Sb and Ta). *Chem. Mater.* **2018**, *30* (2), 392–402. <https://doi.org/10.1021/acs.chemmater.7b04117>.
- (111) Lee, Y.; Suntivich, J.; May, K. J.; Perry, E. E.; Shao-Horn, Y. Synthesis and Activities of Rutile IrO₂ and

- RuO₂ Nanoparticles for Oxygen Evolution in Acid and Alkaline Solutions. *J. Phys. Chem. Lett.* **2012**, *3* (3), 399–404. <https://doi.org/10.1021/jz2016507>.
- (112) Ishida, K.; Mukuda, H.; Kitaoka, Y.; Asayama, K.; Mao, Z. Q.; Mori, Y.; Maeno, Y. Spin-Triplet Superconductivity in Sr₂RuO₄ Identified by ¹⁷O Knight Shift. *Nature* **1998**, *396* (6712), 658–660. <https://doi.org/10.1038/25315>.
- (113) Hiley, C. I.; Scanlon, D. O.; Sokol, A. A.; Woodley, S. M.; Ganose, A. M.; Sangiao, S.; De Teresa, J. M.; Manuel, P.; Khalyavin, D. D.; Walker, M.; Lees, M. R.; Walton, R. I. Antiferromagnetism at T > 500 K in the Layered Hexagonal Ruthenate SrRu₂O₆. *Phys. Rev. B - Condens. Matter Mater. Phys.* **2015**, *92* (10), 1–7. <https://doi.org/10.1103/PhysRevB.92.104413>.
- (114) Renard, C.; Abraham, F. High-Pressure Synthesis and Crystal Structure of a New Strontium Ruthenium Oxide: Sr₂Ru₃O₁₀. **1999**, *272*, 266–272. <https://doi.org/10.1006/jssc.1998.8105>.
- (115) Munenaka, T.; Sato, H. A Novel Pyrochlore Ruthenate: Ca₂Ru₂O₇. *J. Phys. Soc. Japan* **2006**, *75* (10), 5–8. <https://doi.org/10.1143/JPSJ.75.103801>.
- (116) Hiley, C. I.; Lees, M. R.; Fisher, J. M.; Thompsett, D.; Agrestini, S.; Smith, R. I.; Walton, R. I. Ruthenium(V) Oxides from Low-Temperature Hydrothermal Synthesis. *Angew. Chemie - Int. Ed.* **2014**, *53* (17), 4423–4427. <https://doi.org/10.1002/anie.201310110>.
- (117) Hiley, C. I.; Lees, M. R.; Hammond, D. L.; Kashtiban, R. J.; Sloan, J.; Smith, R. I.; Walton, R. I. Ba₄Ru₃O_{10.2}(OH)_{1.8}: A New Member of the Layered Hexagonal Perovskite Family Crystallised from Water. *Chem. Commun.* **2016**, *52* (38), 6375–6378. <https://doi.org/10.1039/C6CC02121B>.
- (118) Prasad, B. E.; Kazin, P.; Komarek, A. C.; Felser, C.; Jansen, M. β-Ag₃RuO₄, a Ruthenate(V) Featuring Spin Tetramers on a Two-Dimensional Trigonal Lattice. *Angew. Chemie - Int. Ed.* **2016**, *55* (14), 4467–4471. <https://doi.org/10.1002/anie.201510576>.
- (119) Prasad, B. E.; Kanungo, S.; Jansen, M.; Komarek, A. C.; Yan, B.; Manuel, P.; Felser, C. AgRuO₃, a Strongly Exchange-Coupled Honeycomb Compound Lacking Long-Range Magnetic Order. *Chem. - A Eur. J.* **2017**, *23* (19), 4680–4686. <https://doi.org/10.1002/chem.201606057>.
- (120) Battle, P. D.; Kim, S. H.; Powell, A. V. The Crystal Structure and Electronic Properties of Ba₄Ru₃MO₁₂ (M = Li, Na, Mg, Zn). *J. Solid State Chem.* **1992**, *101* (1), 161–172. [https://doi.org/10.1016/0022-4596\(92\)90212-E](https://doi.org/10.1016/0022-4596(92)90212-E).
- (121) Povar, I.; Spinu, O. Ruthenium Redox Equilibria: 3. Pourbaix Diagrams for the Systems Ru-H₂O and Ru-Cl-H₂O. *J. Electrochem. Sci. Eng.* **2016**, *6* (1), 145. <https://doi.org/10.5599/jese.229>.
- (122) Burnett, D. L.; Petrucco, E.; Rigg, K. M.; Zalitis, C. M.; Lok, J. G.; Kashtiban, R. J.; Lees, M. R.; Sharman, J. D. B.; Walton, R. I. (M,Ru)O₂ (M = Mg, Zn, Cu, Ni, Co) Rutiles and Their Use as Oxygen Evolution Electrocatalysts in Membrane Electrode Assemblies under Acidic Conditions. **2020**. <https://doi.org/10.1021/acs.chemmater.0c01884>.
- (123) Haraguchi, Y.; Michioka, C.; Matsuo, A.; Kindo, K.; Ueda, H.; Yoshimura, K. Magnetic Ordering with an XY-like Anisotropy in the Honeycomb Lattice Iridates ZnIrO₃ and MgIrO₃ Synthesized via a Metathesis Reaction. *Phys. Rev. Mater.* **2018**, *2* (5), 054411. <https://doi.org/10.1103/PhysRevMaterials.2.054411>.
- (124) Haraguchi, Y.; Nawa, K.; Michioka, C.; Ueda, H.; Matsuo, A.; Kindo, K.; Avdeev, M.; Sato, T. J.; Yoshimura, K. Frustrated Magnetism in the J1-J2 Honeycomb Lattice Compounds MgMnO₃ and ZnMn

References

- O₃ Synthesized via a Metathesis Reaction. *Phys. Rev. Mater.* **2019**, *3* (12). <https://doi.org/10.1103/PhysRevMaterials.3.124406>.
- (125) Ogawa, T.; Sato, H. New Ternary Barium Ruthenates: 10H-Type BaRuO₃ and Ba₂Ru₇O₁₈. *J. Alloys Compd.* **2004**, *383* (1–2), 313–318. <https://doi.org/10.1016/j.jallcom.2004.04.035>.
- (126) Hong, S.-T.; Sleight, A. W. Crystal Structure of 4H BaRuO₃: High Pressure Phase Prepared at Ambient Pressure. *J. Solid State Chem.* **1997**, *128* (128), 251–255. <https://doi.org/10.1006/jssc.1996.7200>.
- (127) Casas-Cabanas, M.; Reynaud, M.; Rikarte, J.; Horbach, P.; Rodríguez-Carvajal, J. FAULTS: A Program for Refinement of Structures with Extended Defects. *J. Appl. Crystallogr.* **2016**, *49* (6), 2259–2269. <https://doi.org/10.1107/s1600576716014473>.
- (128) Boulton, A.; Louer, D. Indexing of Powder Diffraction Patterns for Low-Symmetry Lattices by the Successive Dichotomy Method. *J. Appl. Crystallogr.* **1991**, *24* (pt 6), 987–993. <https://doi.org/10.1107/S0021889891006441>.
- (129) Boulton, A. History of the Dichotomy Method for Powder Pattern Indexing. *Powder Diffr.* **2005**, *20* (04), 284–287. <https://doi.org/10.1154/1.2135307>.
- (130) Lee, E.; Lu, J.; Ren, Y.; Luo, X.; Zhang, X.; Wen, J.; Miller, D.; DeWahl, A.; Hackney, S.; Key, B.; Kim, D.; Slater, M. D.; Johnson, C. S. Layered P2/O3 Intergrowth Cathode: Toward High Power Na-Ion Batteries. *Adv. Energy Mater.* **2014**, *4* (17), 1–8. <https://doi.org/10.1002/aenm.201400458>.
- (131) Thomas Marchandier, Claire Colin, Gwenaëlle Rouse, S. S. Determination of the Magnetic Structure of BaRu₂O₆. Institut Laue-Langevin (ILL). **2019**. <https://doi.org/10.5291/ILL-DATA.CRG-2581>.
- (132) Campbell, B. J.; Stokes, H. T.; Tanner, D. E.; Hatch, D. M. ISODISPLACE: A Web-Based Tool for Exploring Structural Distortions. *J. Appl. Crystallogr.* **2006**, *39* (4), 607–614. <https://doi.org/10.1107/S0021889806014075>.
- (133) H. T. Stokes, D. M. Hatch, and B. J. Campbell. ISODISTORT, ISOTROPY Software Suite, Iso.Byu.Edu.
- (134) Tian, W.; Svoboda, C.; Ochi, M.; Matsuda, M.; Cao, H. B.; Cheng, J. G.; Sales, B. C.; Mandrus, D. G.; Arita, R.; Trivedi, N.; Yan, J. Q. High Antiferromagnetic Transition Temperature of the Honeycomb Compound SrRu₂O₆. *Phys. Rev. B - Condens. Matter Mater. Phys.* **2015**, *92* (10). <https://doi.org/10.1103/PhysRevB.92.100404>.
- (135) Amatucci, G. G.; Badway, F.; Singhal, A.; Beaudoin, B.; Skandan, G.; Bowmer, T.; Plitz, I.; Pereira, N.; Chapman, T.; Jaworski, R. Investigation of Yttrium and Polyvalent Ion Intercalation into Nanocrystalline Vanadium Oxide. *J. Electrochem. Soc.* **2001**, *148* (8), A940. <https://doi.org/10.1149/1.1383777>.
- (136) Tamaru, M.; Wang, X.; Okubo, M.; Yamada, A. Layered Na₂RuO₃ as a Cathode Material for Na-Ion Batteries. *Electrochem. Commun.* **2013**, *33*, 23–26. <https://doi.org/10.1016/j.elecom.2013.04.011>.
- (137) Perez, A. J.; Batuk, D.; Saubanère, M.; Rouse, G.; Foix, D.; McCalla, E.; Berg, E. J.; Dugas, R.; Van Den Bos, K. H. W.; Doublet, M. L.; Gonbeau, D.; Abakumov, A. M.; Van Tendeloo, G.; Tarascon, J. M. Strong Oxygen Participation in the Redox Governing the Structural and Electrochemical Properties of Na-Rich Layered Oxide Na₂IrO₃. *Chem. Mater.* **2016**, *28* (22), 8278–8288. <https://doi.org/10.1021/acs.chemmater.6b03338>.
- (138) Portehault, D.; Cassaignon, S.; Jolivet, J. Structural and Morphological Control of Manganese Oxide Nanoparticles upon Soft Aqueous Precipitation through MnO⁴⁺/Mn²⁺ Reaction. **2009**, 2407–2416. <https://doi.org/10.1039/b816348k>.

- (139) Rouxel, J. Anion-Cation Redox Competition and the Formation of New Compounds in Highly Covalent Systems. *Chem. - A Eur. J.* **1996**, *2* (9), 1053–1059. <https://doi.org/10.1002/chem.19960020904>.
- (140) Jobic, S.; Deniard, P.; Brec, R.; Rouxel, J.; Drew, M. G. B.; David, W. I. F. Properties of the Transition Metal Dichalcogenides: The Case of IrS₂ and IrSe₂. *J. Solid State Chem.* **1990**, *89*, 315–327. [https://doi.org/10.1016/0022-4596\(90\)90273-Z](https://doi.org/10.1016/0022-4596(90)90273-Z).
- (141) Yabuuchi, N.; Takeuchi, M.; Nakayama, M.; Shiiba, H.; Ogawa, M.; Nakayama, K.; Ohta, T.; Endo, D.; Ozaki, T.; Inamasu, T.; Sato, K.; Komaba, S. High-Capacity Electrode Materials for Rechargeable Lithium Batteries: Li₃NbO₄-Based System with Cation-Disordered Rocksalt Structure. *Proc. Natl. Acad. Sci. U. S. A.* **2015**, *112* (25), 7650–7655. <https://doi.org/10.1073/pnas.1504901112>.
- (142) Jacquet, Q.; Iadecola, A.; Saubanère, M.; Li, H.; Berg, E. J.; Rouse, G.; Cabana, J.; Doublet, M. L.; Tarascon, J. M. Charge Transfer Band Gap as an Indicator of Hysteresis in Li-Disordered Rock Salt Cathodes for Li-Ion Batteries. *J. Am. Chem. Soc.* **2019**, *141* (29), 11452–11464. <https://doi.org/10.1021/jacs.8b11413>.
- (143) Lee, J.; Seo, D. H.; Balasubramanian, M.; Twu, N.; Li, X.; Ceder, G. A New Class of High Capacity Cation-Disordered Oxides for Rechargeable Lithium Batteries: Li-Ni-Ti-Mo Oxides. *Energy Environ. Sci.* **2015**, *8* (11), 3255–3265. <https://doi.org/10.1039/c5ee02329g>.
- (144) Hansen, C. J.; Zak, J. J.; Martinolich, A. J.; Ko, J. S.; Bashian, N. H.; Kaboudvand, F.; Van Der Ven, A.; Melot, B. C.; Nelson Weker, J.; See, K. A. Multielectron, Cation and Anion Redox in Lithium-Rich Iron Sulfide Cathodes. *J. Am. Chem. Soc.* **2020**. <https://doi.org/10.1021/jacs.0c00909>.
- (145) Martinolich, A. J.; Zak, J. J.; Agyeman-budu, D. N.; Kim, S. S.; Bashian, N. H.; Irshad, A.; Narayan, S. R.; Melot, B. C.; Weker, J. N.; See, K. A. Controlling Covalency and Anion Redox Potentials through Anion Substitution in Li-Rich Chalcogenides. **2020**. <https://doi.org/10.1021/acs.chemmater.0c04164>.
- (146) Barker, J.; Kendrick, E. The Electrochemical Insertion and Safety Properties of the Low-Cost Li-Ion Active Material, Li₂FeS₂. *J. Power Sources* **2011**, *196* (16), 6960–6963. <https://doi.org/10.1016/j.jpowsour.2010.11.051>.
- (147) Dugast, A.; Brec, R.; Ouvrard, G.; Rouxel, J. Li₂FeS₂, a Cathodic Material for Lithium Secondary Battery. *Solid State Ionics* **1981**, *5* (C), 375–378. [https://doi.org/10.1016/0167-2738\(81\)90271-X](https://doi.org/10.1016/0167-2738(81)90271-X).
- (148) Brec, R.; Prouzet, E.; Ouvrard, G. Redox Processes in the Li_xFeS₂/Li Electrochemical System Studied through Crystal, Mössbauer, and EXAFS Analyses. *J. Power Sources* **1989**, *26* (3–4), 325–332. [https://doi.org/10.1016/0378-7753\(89\)80142-9](https://doi.org/10.1016/0378-7753(89)80142-9).
- (149) Brec, R.; Dugast, A.; Le Mehauté, A. Chemical and Electrochemical Study of the Li_xFeS₂ Cathodic System (0 < x ≤ 2). *Mater. Res. Bull.* **1980**, *15* (5), 619–625. [https://doi.org/10.1016/0025-5408\(80\)90142-7](https://doi.org/10.1016/0025-5408(80)90142-7).
- (150) Le Mehaute, A.; Brec, R.; Dugast, A.; Rouxel, J. The Li_xFeS₂ Electrochemical System. *Solid State Ionics* **1981**, *3–4* (C), 185–189. [https://doi.org/10.1016/0167-2738\(81\)90080-1](https://doi.org/10.1016/0167-2738(81)90080-1).
- (151) Shannon, R. D.; Calvo, C. Refinement of the Crystal Structure of Low Temperature Li₃VO₄ and Analysis of Mean Bond Lengths in Phosphates, Arsenates, and Vanadates. *J. Solid State Chem.* **1973**, *6* (4), 538–549. [https://doi.org/10.1016/S0022-4596\(73\)80012-X](https://doi.org/10.1016/S0022-4596(73)80012-X).
- (152) Ukei, K.; Suzuki, H.; Shishido, T.; Fukuda, T. Li₃NbO₄. *Acta Crystallogr. Sect. C Cryst. Struct. Commun.* **1994**, *50* (5), 655–656. <https://doi.org/10.1107/s010827019300890x>.
- (153) Zocchi, M.; Gatti, M.; Santoro, A.; Roth, R. S. Neutron and X-Ray Diffraction Study on Polymorphism in

References

- Lithium Orthotantalate, Li_3TaO_4 . *J. Solid State Chem.* **1983**, *48* (3), 420–430. [https://doi.org/10.1016/0022-4596\(83\)90101-9](https://doi.org/10.1016/0022-4596(83)90101-9).
- (154) Schnabel, S. Strukturchemie, Elektronische Strukturen Und Spektroskopische Eigenschaften Der Alkalimetallthiooxovanadate (V) $\text{A}_3\text{VS}_x\text{O}_{4-x}$. **2008**, No. V, 1–138.
- (155) Niewa, R.; Vajenine, G. V.; DiSalvo, F. J. Synthesis and Crystal Structure of Ternary Sulfides A_3MS_4 with $\text{A}=\text{Na}$, Rb and $\text{M}=\text{Nb}$, Ta . *J. Solid State Chem.* **1998**, *139* (2), 404–411. <https://doi.org/10.1006/jssc.1998.7872>.
- (156) Sakuda, A.; Takeuchi, T.; Kobayashi, H.; Sakaebe, H.; Tatsumi, K.; Ogumi, Z. Preparation of Novel Electrode Materials Based on Lithium Niobium Sulfides. *Electrochemistry* **2014**, *82* (10), 880–883. <https://doi.org/10.5796/electrochemistry.82.880>.
- (157) Britto, S.; Leskes, M.; Hua, X.; Hébert, C. A.; Shin, H. S.; Clarke, S.; Borkiewicz, O.; Chapman, K. W.; Seshadri, R.; Cho, J.; Grey, C. P. Multiple Redox Modes in the Reversible Lithiation of High-Capacity, Peierls-Distorted Vanadium Sulfide. *J. Am. Chem. Soc.* **2015**, *137* (26), 8499–8508. <https://doi.org/10.1021/jacs.5b03395>.
- (158) Jacquet, Q.; Perez, A.; Batuk, D.; Van Tendeloo, G.; Rouse, G.; Tarascon, J. M. The $\text{Li}_3\text{Ru}_y\text{Nb}_{1-y}\text{O}_4$ ($0 \leq y \leq 1$) System: Structural Diversity and Li Insertion and Extraction Capabilities. *Chem. Mater.* **2017**, *29* (12), 5331–5343. <https://doi.org/10.1021/acs.chemmater.7b01511>.
- (159) Sakuda, A.; Takeuchi, T.; Okamura, K.; Kobayashi, H.; Sakaebe, H.; Tatsumi, K.; Ogumi, Z. Rock-Salt-Type Lithium Metal Sulphides as Novel Positive-Electrode Materials. *Sci. Rep.* **2014**, *4*, 2–6. <https://doi.org/10.1038/srep04883>.
- (160) Nagarajan, S.; Hwang, S.; Balasubramanian, M.; Thangavel, N. K.; Arava, L. M. R. Mixed Cationic and Anionic Redox in Ni and Co Free Chalcogen-Based Cathode Chemistry for Li-Ion Batteries. *J. Am. Chem. Soc.* **2021**. <https://doi.org/10.1021/jacs.1c06828>.
- (161) Leube, B. T.; Robert, C.; Foix, D.; Porcheron, B.; Dedryvère, R.; Rouse, G.; Salager, E.; Cabelguen, P.-E.; Abakumov, A. M.; Vezin, H.; Doublet, M.-L.; Tarascon, J.-M. Activation of Anionic Redox in D0 Transition Metal Chalcogenides by Anion Doping. *Nat. Commun.* **2021**, *12* (1), 5485. <https://doi.org/10.1038/s41467-021-25760-8>.
- (162) Tomczuk, Z.; Tani, B.; Otto, N. C.; Roche, M. F.; Vissers, D. R. Phase Relationships in Positive Electrodes of High Temperature Li - Al / LiCl - KCl / FeS_2 Cells. *J. Electrochem. Soc.* **1982**, *129* (5), 925–931. <https://doi.org/10.1149/1.2124067>.
- (163) Shao-horn, Y.; Osmialowski, S.; Horn, Q. C. Reinvestigation of Lithium Reaction Mechanisms in FeS_2 Pyrite at Ambient Temperature. *J. Electrochem. Soc.* **2002**, 1547–1555. <https://doi.org/10.1149/1.1516772>.
- (164) Cells, L. F.; Butala, M. M.; Mayo, M.; Doan-nguyen, V. V. T.; Lumley, M. A.; Go, C.; Wiaderek, K. M.; Borkiewicz, O. J.; Chapman, K. W.; Chupas, P. J.; Balasubramanian, M.; Laurita, G.; Britto, S.; Morris, A. J.; Grey, C. P.; Seshadri, R. Local Structure Evolution and Modes of Charge Storage in Secondary Li – FeS_2 Cells. **2017**. <https://doi.org/10.1021/acs.chemmater.7b00070>.
- (165) Sourisseau, C.; Cavagnat, R.; Fouassier, M.; Jolic, S.; Deniard, P.; Brec, R.; Rouxel, J. The Vibrational Resonance Raman Spectra and the Valence Force Field of Iridium Dichalcogenides, IrS_2 and IrSe_2 . *J. Solid State Chem.* **1991**, *91* (1), 153–172. [https://doi.org/10.1016/0022-4596\(91\)90069-T](https://doi.org/10.1016/0022-4596(91)90069-T).

- (166) Levi, E.; Zinigrad, E.; Teller, H.; Levi, M. D.; Aurbach, D. The Structure of a 3 V Li_xMnO_2 Cathode and Its Change upon Electrochemical Lithiation. *J. Electrochem. Soc.* **1998**, *145* (10), 3440–3443. <https://doi.org/10.1149/1.1838824>.
- (167) Saleh, G.; Artyukhin, S. First-Principles Theory of Phase Transitions in IrTe_2 . *J. Phys. Chem. Lett.* **2020**, *11* (6), 2127–2132. <https://doi.org/10.1021/acs.jpcclett.0c00012>.
- (168) Oh, Y. S.; Yang, J. J.; Horibe, Y.; Cheong, S. W. Anionic Depolymerization Transition in IrTe_2 . *Phys. Rev. Lett.* **2013**, *110* (12), 1–5. <https://doi.org/10.1103/PhysRevLett.110.127209>.
- (169) Joseph, B.; Bendele, M.; Simonelli, L.; Maugeri, L.; Pyon, S.; Kudo, K.; Nohara, M.; Mizokawa, T.; Saini, N. L. Local Structural Displacements across the Structural Phase Transition in IrTe_2 : Order-Disorder of Dimers and Role of Ir-Te Correlations. *Phys. Rev. B* **2013**, *224109*, 3–6. <https://doi.org/10.1103/PhysRevB.88.224109>.
- (170) Clarke, S. J.; Adamson, P.; Herkelrath, S. J. C.; Rutt, O. J.; Parker, D. R.; Pitcher, M. J.; Smura, C. F. Structures, Physical Properties, and Chemistry of Layered Oxychalcogenides and Oxypnictides. *Inorg. Chem.* **2008**, *47* (19), 8473–8486. <https://doi.org/10.1021/ic8009964>.
- (171) Hyett, G.; Rutt, O. J.; Gál, Z. A.; Denis, S. G.; Hayward, M. A.; Clarke, S. J. Electronically Driven Structural Distortions in Lithium Intercalates of the $n = 2$ Ruddlesden-Popper-Type Host $\text{Y}_2\text{Ti}_2\text{O}_5\text{S}_2$: Synthesis, Structure, and Properties of $\text{Li}_x\text{Y}_2\text{Ti}_2\text{O}_5\text{S}_2$ ($0 < x < 2$). *J. Am. Chem. Soc.* **2004**, *126* (7), 1980–1991. <https://doi.org/10.1021/ja037763h>.
- (172) Rutt, O. J.; Hill, T. L.; Gál, Z. A.; Hayward, M. A.; Clarke, S. J. The Cation-Deficient Ruddlesden-Popper Oxysulfide $\text{Y}_2\text{Ti}_2\text{O}_5\text{S}_2$ as a Layered Sulfide: Topotactic Potassium Intercalation to Form $\text{KY}_2\text{Ti}_2\text{O}_5\text{S}_2$. *Inorg. Chem.* **2003**, *42* (24), 7906–7911. <https://doi.org/10.1021/ic0301730>.
- (173) Clarke, S. J.; Denis, S. G.; Rutt, O. J.; Hill, T. L.; Hayward, M. A.; Hyett, G.; Gál, Z. A. Sodium Intercalation into the $n = 2$ Ruddlesden-Popper Type Host $\text{Y}_2\text{Ti}_2\text{O}_5\text{S}_2$: Synthesis, Structure, and Properties of $\alpha\text{-Na}_x\text{Y}_2\text{Ti}_2\text{O}_5\text{S}_2$ ($0 < x \leq 1$). *Chem. Mater.* **2003**, *15* (26), 5065–5072. <https://doi.org/10.1021/cm034762f>.
- (174) Indris, S.; Cabana, J.; Rutt, O. J.; Clarke, S. J.; Grey, C. P. Layered Oxysulfides $\text{Sr}_2\text{MnO}_2\text{Cu}_{2m-0.5}\text{S}_{m+1}$ ($m = 1, 2$, and 3) as Insertion Hosts for Li Ion Batteries. *J. Am. Chem. Soc.* **2006**, *128* (41), 13354–13355. <https://doi.org/10.1021/ja064961a>.
- (175) Rutt, O. J.; Williams, G. R.; Clarke, S. J. Reversible Lithium Insertion and Copper Extrusion in Layered Oxysulfides. *Chem. Commun.* **2006**, 88 (27), 2869–2871. <https://doi.org/10.1039/b605105g>.
- (176) Dey, S.; Zeng, D.; Adamson, P.; Cabana, J.; Indris, S.; Lu, J.; Clarke, S. J.; Grey, C. P. Structural Evolution of Layered Manganese Oxysulfides during Reversible Electrochemical Lithium Insertion and Copper Extrusion. *Chem. Mater.* **2021**, *33* (11), 3989–4005. <https://doi.org/10.1021/acs.chemmater.1c00375>.
- (177) Cassidy, S. J.; Pitcher, M. J.; Lim, J. J. K.; Hadermann, J.; Allen, J. P.; Watson, G. W.; Britto, S.; Chong, E. J.; Free, D. G.; Grey, C. P.; Clarke, S. J. Layered CeSO and LiCeSO Oxide Chalcogenides Obtained via Topotactic Oxidative and Reductive Transformations. *Inorg. Chem.* **2019**, *58*, acs.inorgchem.8b03485. <https://doi.org/10.1021/acs.inorgchem.8b03485>.
- (178) Gamon, J.; Perez, A. J.; Jones, L. A. H.; Zanella, M.; Daniels, L. M.; Morris, R. E.; Tang, C. C.; Veal, T. D.; Hardwick, L. J.; Dyer, M. S.; Claridge, B.; Rosseinsky, M. J. $\text{Na}_2\text{Fe}_2\text{O}_5\text{S}_2$, a New Earth Abundant Cathode Material for Na-Ion Batteries †. **2020**, 20553–20569. <https://doi.org/10.1039/d0ta07966a>.

References

- (179) Lai, K. T.; Antonyshyn, I.; Prots, Y.; Valldor, M. Anti -Perovskite Li-Battery Cathode Materials. *J. Am. Chem. Soc.* **2017**, *139* (28), 9645–9649. <https://doi.org/10.1021/jacs.7b04444>.
- (180) Schnabel, S.; Röhr, C. Kalium-Thio/Oxo-Vanadate(V) $K_3[VS_xO_{4-x}]$ ($x = 1-4$) Und $Na_3[VS_3O_3]$: Synthese, Strukturchemie, Eigenschaften. *Zeitschrift für Naturforsch. B* **2008**, *63* (7), 819–833. <https://doi.org/10.1515/znb-2008-0704>.
- (181) Schnabel, S.; Röhr, C. Gemischte Thio/Oxo-Orthovanadate $Na_3[VS_xO_{4-x}]$ ($x = 2, 3$): Darstellung – Strukturen – Eigenschaften. *Zeitschrift für Naturforsch. B* **2005**, *60* (5), 479–490. <https://doi.org/10.1515/znb-2005-0501>.
- (182) Sakuda, A.; Ohara, K.; Kawaguchi, T.; Fukuda, K.; Nakanishi, K.; Arai, H.; Uchimoto, Y.; Ohta, T.; Matsubara, E.; Ogumi, Z.; Kuratani, K.; Kobayashi, H.; Shikano, M.; Takeuchi, T.; Sakaebe, H. A Reversible Rocksalt to Amorphous Phase Transition Involving Anion Redox. *Sci. Rep.* **2018**, *8* (1), 8–13. <https://doi.org/10.1038/s41598-018-33518-4>.
- (183) Kong, T.; Stolze, K.; Timmons, E. I.; Tao, J.; Ni, D.; Guo, S.; Yang, Z.; Prozorov, R.; Cava, R. J. VI_3 — a New Layered Ferromagnetic Semiconductor. *Adv. Mater.* **2019**, *31* (17), 1–7. <https://doi.org/10.1002/adma.201808074>.
- (184) Tian, S.; Zhang, J. F.; Li, C.; Ying, T.; Li, S.; Zhang, X.; Liu, K.; Lei, H. Ferromagnetic van Der Waals Crystal VI_3 . *J. Am. Chem. Soc.* **2019**, *141* (13), 5326–5333. <https://doi.org/10.1021/jacs.8b13584>.
- (185) Son, S.; Coak, M. J.; Lee, N.; Kim, J.; Kim, T. Y.; Hamidov, H.; Cho, H.; Liu, C.; Jarvis, D. M.; Brown, P. A. C.; Kim, J. H.; Park, C. H.; Khomskii, D. I.; Saxena, S. S.; Park, J. G. Bulk Properties of the van Der Waals Hard Ferromagnet VI_3 . *Phys. Rev. B* **2019**, *99* (4), 1–9. <https://doi.org/10.1103/PhysRevB.99.041402>.
- (186) Doležal, P.; Kratochvílová, M.; Holý, V.; Čermák, P.; Sechovský, V.; Dušek, M.; Míšek, M.; Chakraborty, T.; Noda, Y.; Son, S.; Park, J.-G. Crystal Structures and Phase Transitions of the van Der Waals Ferromagnet VI_3 . *Phys. Rev. Mater.* **2019**, *3* (12), 121401. <https://doi.org/10.1103/PhysRevMaterials.3.121401>.
- (187) Kong, T.; Guo, S.; Ni, D.; Cava, R. J. Crystal Structure and Magnetic Properties of the Layered van Der Waals Compound VBr_3 . *Phys. Rev. Mater.* **2019**, *3* (8), 1–5. <https://doi.org/10.1103/PhysRevMaterials.3.084419>.
- (188) Klemm, W.; Krose, E. Die Kristallstrukturen von $ScCl_3$, $TiCl_3$ Und VCl_3 . *Zeitschrift für Anorg. Chemie Anorg. Chemie* **1947**, *253* (3–4), 218–225. <https://doi.org/10.1002/zaac.19472530313>.
- (189) Juza, D.; Giegling, D.; Schäfer, H. Über Die Vanadinjodide VJ_2 Und VJ_3 . *Zeitschrift für Anorg. und Allg. Chemie Anorg. und Allg. Chemie* **1969**, *366* (3–4), 121–129. <https://doi.org/10.1002/zaac.19693660303>.
- (190) Vi, F. Crystal Structures and Phase Transitions of the Van-Der-Waals. *Phys. Rev. Mater.* **2019**, *3*, 1–22.
- (191) Boisse, B. M. De; Reynaud, M.; Ma, J.; Kikkawa, J.; Nishimura, S.; Casas-cabanas, M.; Delmas, C.; Okubo, M.; Yamada, A. Coulombic Self-Ordering upon Charging a Large-Capacity Layered Cathode Material for Rechargeable Batteries. *Nat. Commun.* **2019**, *10*, 2185. <https://doi.org/10.1038/s41467-019-09409-1>.
- (192) McGuire, M. Crystal and Magnetic Structures in Layered, Transition Metal Dihalides and Trihalides. *Crystals* **2017**, *7* (5), 121. <https://doi.org/10.3390/cryst7050121>.
- (193) Soubeyroux, J. L.; Cros, C.; Gang, W.; Kanno, R.; Pouchard, M. Neutron Diffraction Investigation of the

- Cationic Distribution in the Structure of the Spinel-Type Solid Solutions $\text{Li}_{2-2x}\text{M}_{1+x}\text{Cl}_4$ ($\text{M} = \text{Mg}, \text{V}$): Correlation with the Ionic Conductivity and NMR Data. *Solid State Ionics* **1985**, *15* (4), 293–300. [https://doi.org/10.1016/0167-2738\(85\)90132-8](https://doi.org/10.1016/0167-2738(85)90132-8).
- (194) Sivadas, N.; Okamoto, S.; Xu, X.; Fennie, C. J.; Xiao, D. Stacking-Dependent Magnetism in Bilayer CrI_3 . *Nano Lett.* **2018**, *18* (12), 7658–7664. <https://doi.org/10.1021/acs.nanolett.8b03321>.
- (195) Cao, H. B.; Banerjee, A.; Yan, J. Q.; Bridges, C. A.; Lumsden, M. D.; Mandrus, D. G.; Tennant, D. A.; Chakoumakos, B. C.; Nagler, S. E. Low-Temperature Crystal and Magnetic Structure of $\alpha\text{-RuCl}_3$. *Phys. Rev. B* **2016**, *93* (13), 1–8. <https://doi.org/10.1103/PhysRevB.93.134423>.
- (196) Jiang, P.; Wang, C.; Chen, D.; Zhong, Z.; Yuan, Z.; Lu, Z.-Y.; Ji, W. Stacking Tunable Interlayer Magnetism in Bilayer CrI_3 . *Phys. Rev. B* **2019**, *99* (14), 144401. <https://doi.org/10.1103/PhysRevB.99.144401>.
- (197) Leriche, J. B.; Hamelet, S.; Shu, J.; Morcrette, M.; Masquelier, C.; Ouvrard, G.; Zerrouki, M.; Soudan, P.; Belin, S.; Elkaïm, E.; Baudelet, F. An Electrochemical Cell for Operando Study of Lithium Batteries Using Synchrotron Radiation. *J. Electrochem. Soc.* **2010**, *157* (5), A606. <https://doi.org/10.1149/1.3355977>.
- (198) Fauth, F.; Boer, R.; Gil-Ortiz, F.; Popescu, C.; Vallcorba, O.; Peral, I.; Fullà, D.; Benach, J.; Juanhuix, J. The Crystallography Stations at the Alba Synchrotron. *Eur. Phys. J. Plus* **2015**, *130* (8). <https://doi.org/10.1140/epjp/i2015-15160-y>.
- (199) Fauth, F.; Peral, I.; Popescu, C.; Knapp, M. S360 Vol. 28, No.S2, September 2013. *Powder Diffr.* **2013**, *28* (September), 360–370.
- (200) Avdeev, M.; Hester, J. R. ECHIDNA: A Decade of High-Resolution Neutron Powder Diffraction at OPAL. *J. Appl. Crystallogr.* **2018**, *51* (6), 1597–1604. <https://doi.org/10.1107/S1600576718014048>.
- (201) Frontzek, M. D.; Whitfield, R.; Andrews, K. M.; Jones, A. B.; Bobrek, M.; Vodopivec, K.; Chakoumakos, B. C.; Fernandez-Baca, J. A. WAND2 - A Versatile Wide Angle Neutron Powder/Single Crystal Diffractometer. *Rev. Sci. Instrum.* **2018**, *89* (9). <https://doi.org/10.1063/1.5033900>.
- (202) Rothkirch, A.; Gatta, G. D.; Meyer, M.; Merkel, S.; Merlini, M.; Liermann, H.-P. Single-Crystal Diffraction at the Extreme Conditions Beamline P02.2: Procedure for Collecting and Analyzing High-Pressure Single-Crystal Data. *J. Synchrotron Radiat.* **2013**, *20* (5), 711–720. <https://doi.org/10.1107/s0909049513018621>.
- (203) Sheldrick, G. M. SHELXT - Integrated Space-Group and Crystal-Structure Determination. *Acta Crystallogr. Sect. A Found. Crystallogr.* **2015**, *71* (1), 3–8. <https://doi.org/10.1107/S2053273314026370>.
- (204) Dolomanov, O. V.; Bourhis, L. J.; Gildea, R. J.; Howard, J. A. K.; Puschmann, H. OLEX2 : A Complete Structure Solution, Refinement and Analysis Program . *J. Appl. Crystallogr.* **2009**, *42* (2), 339–341. <https://doi.org/10.1107/s0021889808042726>.
- (205) Rodríguez-Carvajal, J. Recent Advances in Magnetic Structure Determination by Neutron Powder Diffraction. *Phys. B Phys. Condens. Matter* **1993**, *192* (1–2), 55–69. [https://doi.org/10.1016/0921-4526\(93\)90108-I](https://doi.org/10.1016/0921-4526(93)90108-I).
- (206) Adams, S. From Bond Valence Maps to Energy Landscapes for Mobile Ions in Ion-Conducting Solids. *Solid State Ionics* **2006**, *177* (19-25 SPEC. ISS.), 1625–1630. <https://doi.org/10.1016/j.ssi.2006.03.054>.
- (207) Momma, K.; Izumi, F. VESTA 3 for Three-Dimensional Visualization of Crystal , Volumetric and Morphology Data. *J. Appl. Crystallogr.* **2011**, 1272–1276. <https://doi.org/10.1107/S0021889811038970>.

References

- (208) Chamas, M.; Sougrati, M. T.; Reibel, C.; Lippens, P. E. Quantitative Analysis of the Initial Restructuring Step of Nanostructured FeSn₂-Based Anodes for Li-Ion Batteries. *Chem. Mater.* **2013**, *25* (12), 2410–2420. <https://doi.org/10.1021/cm400253a>.
- (209) Briois, V.; La Fontaine, C.; Belin, S.; Barthe, L.; Moreno, T.; Pinty, V.; Carcy, A.; Girardot, A.; Fonda, E. ROCK: The New Quick-EXAFS Beamline at SOLEIL. *J. Phys. Conf. Ser.* **2016**, *712*, 012149. <https://doi.org/10.1088/1742-6596/712/1/012149>.
- (210) Ravel, B.; Newville, M. ATHENA , ARTEMIS , HEPHAESTUS : Data Analysis for X-Ray Absorption Spectroscopy Using IFEFFIT. *J. Synchrotron Radiat.* **2005**, *12*, 537–541. <https://doi.org/10.1107/S0909049505012719>.

Synthèse, caractérisation et étude des propriétés de nouveaux composés exotiques d'intercalation des ions lithium

Résumé:

Le réchauffement climatique est sans aucun doute l'un des défis majeurs de 21^{ème} siècle. Pour parvenir à le juguler, une modification drastique de notre mix énergétique est nécessaire. Cependant, la plupart des sources d'énergies renouvelables (solaire, éolien etc...) sont intermittentes et des dispositifs de stockage performants doivent être développés. La technologie Li-ion, qui s'est déjà imposée sur le marché de l'électronique portable et de la voiture électrique, figure parmi les solutions les plus intéressantes. Toutefois, la demande de densité d'énergie toujours plus grande nécessite une amélioration continue de ces systèmes. Ainsi, l'un des éléments les plus limitants de cette capacité énergétique se trouve être l'électrode positive ce qui a mené au cours des 40 dernières années à une recherche effrénée dans le domaine. Pourtant, bien que l'enthousiasme sur le sujet soit toujours plus que jamais d'actualité, la plupart des matériaux d'intercalation du lithium répertoriés dans les bases de données ont été explorés et les idées viennent à manquer. Pour autant, il n'est pas question de laisser la place à un quelconque pessimisme et le but de ce travail de thèse est d'explorer différentes voies permettant de synthétiser de nouveaux composés d'insertion du lithium.

Ainsi, dans un premier temps nous nous sommes intéressés au potentiel des voies de synthèse basse température pour obtenir des matériaux originaux. En effet, la plupart des synthèses traditionnelles se font à haute température et mènent seulement aux composés thermodynamiquement les plus stables laissant l'immensité des composés métastables inaccessibles. Aussi, nous avons étudié un procédé de synthèse hydrothermale d'oxydes de ruthénium qui nous a permis d'obtenir plusieurs nouveaux composés dont certains présentent des propriétés électrochimiques et/ou magnétiques intéressantes. Dans une deuxième partie, nous avons ré-exploré la chimie des sulfures lithiés laissée en jachère depuis de nombreuses années. Nous avons ainsi montré qu'il reste dans cette famille des compositions inexplorées et que leur étude peut de plus aider à la compréhension de mécanismes électrochimiques complexes observés dans les oxydes. Enfin, à la recherche de familles chimiques inexploitées pour l'insertion du lithium, nous avons étudié tour à tour les propriétés électrochimiques de composés oxysulfures et halogénures. Cette dernière étude confirme que de belles découvertes de matériaux d'intercalation restent à faire et rappelle le potentiel de cette chimie d'insertion bien au-delà du stockage de l'énergie.

Mots clés: Chimie du Solide, Cristallographie, Li-ion batteries.

Synthesis, characterization and study of the properties of new exotic lithium ion intercalation compounds.

Abstract:

Global warming is undoubtedly one of the major challenges of the 21st century. In order to curb it, a drastic change in our energy mix is necessary. However, most renewable energy sources (solar, wind, etc.) are intermittent and efficient storage devices must be developed. Li-ion technology, which has already established itself in the portable electronics and electric car markets, is among the most interesting solutions. However, the demand for ever greater energy density requires continuous improvement of these systems. One of the most limiting elements of this energy capacity is the positive electrode, which has led to a frantic research in this field over the last 40 years. However, while enthusiasm for the subject is as high as ever, most of the lithium intercalation materials listed in the databases have been explored and ideas are running out. However, it is not a question of giving way to any pessimism and the aim of this thesis is to explore different ways to synthesize new lithium insertion compounds.

Thus, in a first step we are interested in the potential of low temperature synthesis routes to obtain original materials. Indeed, most of the traditional syntheses are done at high temperature and lead only to the most thermodynamically stable compounds leaving the vastness of metastable compounds inaccessible. Thus, we have studied a hydrothermal synthesis process of ruthenium oxides which allowed us to obtain several new compounds, some of which present interesting electrochemical and/or magnetic properties. In a second part we have re-explored the chemistry of lithium sulfides left fallow for many years. We have shown that there are still unexplored compositions in this family and that their study can help to understand complex electrochemical mechanisms observed in oxides. Finally, in search of unexplored chemical families for lithium insertion we have studied in turn the electrochemical properties of oxysulfide and halide compounds. This last study confirms that great discoveries of intercalation materials are still to be made and reminds us of the potential of this insertion chemistry far beyond energy storage.

Keywords: Solid state chemistry, crystallography, Li-ion batteries